Three-Dimensional CT Imaging and Microstructural Mechanical Modeling of Corrosion and Freeze-Thaw Damage of Concrete

by

Mustafa A. Alhusain

A thesis
presented to the University of Waterloo
in the fulfillment of the
thesis requirement for the degree of
Doctor of Philosophy
in
Mechanical and Mechatronics Engineering

Waterloo, Ontario, Canada, 2022

Examining Committee Membership

The following served on the Examining Committee for this thesis. The decision of the Examining Committee is by majority vote.

External Examiner:	Dr. Karl Peterson Associate Professor, Dept. of Civil and Mineral Engineering University of Toronto
Supervisor:	Dr. Adil Al-Mayah Associate Professor, Dept. of Civil and Environmental Engineering, University of Waterloo
Internal Members:	Dr. Ehsan Toyserkani Professor, Dept. of Mechanical & Mechatronics Engineering, University of Waterloo
	Dr. Duane Cronin Professor, Dept. of Mechanical & Mechatronics Engineering, University of Waterloo
Internal-External Member:	Dr. Hassan Baaj Professor, Dept. of Civil and Environmental Engineering, University of Waterloo

Author's Declaration

This thesis consists of material all of which I authored or co-authored: see Statement of Contributions included in the thesis. This is a true copy of the thesis, including any required final revisions, as accepted by my examiners.

I understand that my thesis may be made electronically available to the public.

Statement of Contributions

Mustafa Alhusain was the sole author of the thesis, which was written under the supervision of Dr. Adil Al-Mayah. This dissertation contributed the following first-authored materials that have or will be published in academic journals and conference proceedings:

1. Alhusain M, Al-Mayah A. Three dimensional imaging of reinforcement corrosion using micro-computed tomography: Literature review. Construction and Build Materials Journal 2021;284:122813.
2. Alhusain M, Al-Mayah A. Three-Dimensional μCT Imaging of Pore Morphology and Freeze-Thaw Damage Mechanisms of Different Concrete Mixing Proportions. Royal Society Open Science Journal. 2022. [Submitted]
3. Alhusain M, Al-Mayah A. Three-Dimensional Imaging of Natural Reinforcement Corrosion using Micro-Computed Tomography. Construction and Building Materials Journal 2022. [Submitted]
4. Alhusain M, Al-Mayah A. Microscale Damage Characterization of Concrete under Coupled Freeze-Thaw and Sulfate Attack Conditions Using Micro-Computed Tomography. Materials and Structures Journal 2022. [Submitted]
5. Alhusain M, Al-Mayah A. Microstructural Finite Element Model of Freeze-Thaw Damage of Concrete 2022. [In the Submission Process]
6. Alhusain M, Al-Mayah A. Micro-Computed Tomography Imaging of Freeze-Thaw Damage in Concrete: Literature Review 2022. [In the Submission Process]
7. Alhusain, M., Quayle, T.G., Al-Mayah, A., 2022. Three-Dimensional Characterization of Naturally Corroded Steel-Reinforced Concrete Using Computed Tomography, in: Ilki,

A., Ispir, M., Inci, P. (Eds.), 10th International Conference on FRP Composites in Civil Engineering, Lecture Notes in Civil Engineering. Springer International Publishing, Cham, pp. 706–713.

8. Alhusain, M., Al-Mayah, A., 2022. Three Dimensional CT Imaging Analysis of Concrete: Effects of Water and Sand Contents on Pore Characteristics, in: 8th International Conference on Advanced Composite Materials in Bridges and Structures, Lecture Notes in Civil Engineering. Springer International Publishing.
9. Alhusain, M., Al-Mayah, A., 2022. Three-Dimensional Micro-Scale Analysis of Natural Corrosion and Damage Mechanisms Using μCT Imaging of Various Concrete Mixtures, in: 11th International Conference on Short and Medium Span Bridges, Lecture Notes in Civil Engineering. Springer International Publishing.
10. Alhusain, M., Al-Mayah, A., 2022. Microstructural Investigation of Coupled Sulfate and Freeze-Thaw Damage of Concrete Using Micro-Computed Tomography, in: Annual Conference of the Canadian Society for Civil Engineering, Lecture Notes in Civil Engineering. Springer International Publishing.
11. Alhusain, M., Al-Mayah, A., 2022. Toward Image-Based Microstructural Finite Element (FE) Modeling of Reinforcement Corrosion, in: 11th International Conference on Short and Medium Span Bridges, Lecture Notes in Civil Engineering. Springer International Publishing.
12. Alhusain, M., Al-Mayah, A., 2022. Image-Based Microstructural Finite Element Model of Concrete Subjected to Freeze-Thaw Cycles, in: Annual Conference of the Canadian Society for Civil Engineering, Lecture Notes in Civil Engineering. Springer International Publishing.

Abstract

Corrosion and freeze-thaw can cause detrimental damage to concrete structures. Understanding concrete damage mechanisms at the micro-level can play an essential role in implementing effective preventive measures and efficient repair methods. Among various non-destructive testing technologies, high-resolution micro-computed tomography (μCT) imaging has been gaining popularity due to its ability to provide three-dimensional (3D) reconstructions of concrete's internal structure and analyze its damage mechanisms. Despite its unique capabilities, the full potential of using CT imaging to investigate the general microscale damage of concrete has yet to be realized. Also, limited research has been conducted to investigate the 3D microstructural concrete damage caused by corrosion and freeze-thaw conditions.

Therefore, the main objective of this research is to attain a better understanding of the effects of concrete composition and surrounding environments on the severity and mechanisms of corrosion and freeze-thaw damage. This objective was complimented by integrating mechanical characterization using CT imaging into image-based microstructural finite element (FE) modeling. Furthermore, the full potential of CT imaging was examined by investigating the accuracy of corrosion detection using an unprecedentedly large naturally corroded concrete element.

The effects of mixture proportions on the mechanisms of corrosion and freeze-thaw damage were examined by investigating internal structures of concrete, such as pore characteristics. The specimens were imaged before being subjected to corrosion and freeze-thaw conditions to determine the impact of concrete composition on its pore properties, after which the corrosion specimens were exposed to 120 wet-dry cycles in salt water with a concentration of 3.5%, whereas the freeze-thaw samples were subjected to 40 cycles. The pore properties were analyzed before and after testing, and the concrete damage mechanisms were investigated.

Also, the full potential of CT imaging was examined by investigating the corrosion of a 50-year-old naturally corroded concrete element that is 12 cm wide, 6 cm thick, and 17 cm high. The detected corrosion products were compared to the corrosion of the actual concrete specimen to investigate the accuracy of corrosion detection. A method for improving corrosion detection accuracy was proposed and tested. Moreover, the damage mechanisms were determined by analyzing the pore structure of the concrete element.

The effects of the surrounding environment on the severity and mechanisms of freeze-thaw damage were investigated by subjecting concrete specimens of the same composition to 80 freeze-thaw cycles in distinct sulfate environments with different concentrations. The mass loss data and pore characteristics, including porosity, pore size, and pore accessibility, were analyzed throughout the applied cycles to determine the impact of the sulfate salt and concentration on the severity of frost damage. On the other hand, freeze-thaw damage mechanisms under the different sulfate environments were investigated using 3D reconstructions of concrete's pore microstructure.

Also, novel image-based microstructural FE models were developed to investigate concrete damage under corrosion and freeze-thaw conditions. Three-dimensional reconstructions of the FE elements, including the aggregates, air pores, and cement mortar, were created by thresholding and stacking the CT images. The corrosion FE model was modeled by subjecting the steel reinforcement to experiment-based uniform corrosion. On the other hand, the freeze-thaw FE models were simulated by filling the air pores with freezing water and applying the temperatures of the actual freeze-thaw cycles. The interaction between the different elements was examined by studying the internal stress distribution throughout the applied corrosion and freeze-thaw conditions. Also, the accuracy of the FE models was investigated by comparing the severity and mechanisms of the FE models to the CT data of the actual concrete specimens.

Acknowledgements

I would like to express my sincere appreciation and gratitude to my mother and father for their continuous support, guidance, and encouragement throughout my life. I wouldn't have accomplished a thing if it wasn't for them. I owe them my endless gratitude that I would never be able to pay back.

I would also like to express my deepest gratitude to my supervisor, Professor Adil Al-Mayah, for his dedication, encouragement, humbleness, and support. Publishing in high-impact journals wouldn't have been possible without his guidance. I will always cherish the valuable lessons learned from him and the precious memories made throughout my graduate studies.

I would also like to express my sincere gratitude to Dr. Ali Algarny, the former Dean of the College of Engineering at King Faisal University. May Allah rest his soul in eternal peace and grant him the highest place in Aljannah. I have learned priceless lessons from him that I have been applying throughout my life.

I would also like to thank the technicians Peter Volcic, Douglas Hirst, Richard Morrison, and Jorge Cruz from the Civil Engineering Laboratories and the Engineering Machine Shop. I would also like to thank my friend Ahmed Aljimiai for the informative discussions and continuous support.

Special thanks to my sponsor, King Faisal University, and to the College of Engineering at King Faisal University for giving me the chance to pursue graduate studies. I would also like to thank the Saudi Arabian Cultural Bureau for its support throughout the scholarship.

To MY Parents and Family

Table of Contents

Examining Committee Membership ii

Author's Declaration iii

Statement of Contributions iv

Abstract vi

Acknowledgements viii

Dedication ix

List of Figures xvi

List of Tables xxv

Chapter 1: Introduction 1

1.1. General Background 1

1.2. Research Objectives 3

1.3. Thesis Structure 4

Chapter 2: Literature Review 6

2.1. Introduction 6

2.2. Micro-Computed Tomography (μCT) Imaging 9

2.2.1. Imaging Principles 9

2.2.2. CT Imaging Parameters 10

2.3. CT Imaging of Corrosion 13

2.3.1. Corrosion Induction Methods 13
2.3.2. Corrosion Diffusion 15
2.3.3. Damage Propagation 17
2.3.4. Mass Loss 19
2.3.5. Effect of Impressed Current Densities 21
2.3.6. Effect of Steel Reinforcement Material 23
2.3.7. Effect of Voids 26
2.3.8. Effect of Confinement 28
2.4. CT Imaging of Freeze-Thaw Damage 31
2.4.1. Test Methodologies 31
2.4.2. Damage Propagation 32
2.4.3. Effect of Mixture Proportions 34
2.4.4. Effect of Sulfate Salts 35
2.4.5. Effect of Air Entrainment 37
2.4.6. Effect of Nano-Additives 39
2.4.7. Effect of Saturation Level 41
2.5. Conclusions and Research Gaps 44
Chapter 3: 3D CT Imaging of Corrosion and Freeze-Thaw Damage of Concrete of Different Mixing Proportions 46
3.1. Introduction 46

3.2. Materials and Methodologies 49
3.2.1. Specimen Preparation 49
3.2.2. CT Imaging 51
3.2.3. Wet-Dry Cycles 52
3.2.4. Freeze-Thaw Cycles 53
3.3. Results and Discussion 54
3.3.1. Corrosion Damage 54
3.3.1.1. General 54
3.3.1.2. Porosity of Corrosion Specimens 54
3.3.1.3. Weight Measurement of Corrosion Specimens 57
3.3.1.4. Corrosion Mechanisms 59
3.3.2. Freeze-Thaw Damage 62
3.3.2.1. General 62
3.3.2.2. Porosity of Freeze-Thaw Specimens 66
3.3.2.3. Pore Accessibility of Freeze-Thaw Specimens 69
3.3.2.4. Pore Size of Freeze-Thaw Specimens 71
3.3.2.5. Pore Shape of Freeze-Thaw Specimens 73
3.3.2.6. Pore Distribution of Freeze-Thaw Specimens 76
3.3.2.7. Severity and Mechanisms of Freeze-Thaw Damage 78
3.4. Conclusions 81

Chapter 4: CT Imaging of Large Naturally Corroded Reinforced Concrete Element 83
4.1. Introduction 83
4.2. Materials and Methodologies 85
4.2.1. Specimen 85
4.2.2. CT Imaging 86
4.2.3. Post-Processing of CT Images 86
4.3. Results and Discussion 88
4.3.1. General 88
4.3.2. Corrosion Damage 91
4.3.3. Corrosion Distribution and Detection Accuracy 94
4.4. Conclusions 96
Chapter 5: 98
Chapter 5: CT Imaging of Concrete Damage under Coupled Freeze-Thaw and Sulfate Attack Conditions 98
5.1. Introduction 98
5.2. Materials and Methodologies 100
5.2.1. Specimens 100
5.2.2. Cyclic Freeze-Thaw Exposure 101
5.2.3. μCT Imaging 103
5.3. Results and Discussion 103

5.3.1. General 103
5.3.2. Mass Loss 106
5.3.3. Frost Damage Characterization Using Pore Properties 108
5.3.3.1. Porosity 108
5.3.3.2. Pore Size 110
5.3.3.3. Surface Pore 113
5.3.4. Frost Damage Mechanisms 116
5.4. Conclusions 120
Chapter 6: Image-Based Microstructural Finite Element (FE) Modelling of Corrosion and Freeze-Thaw Damage 121
6.1. Introduction 121
6.2. Finite Element (FE) Model 122
6.2.1. General 122
6.2.2. Mechanical Properties 127
6.2.3. Contact Characteristics 129
6.2.4. Reinforcement Corrosion 130
6.2.5. Freeze-Thaw Cycles 131
6.3. Results and Discussion 132
6.3.1. Corrosion Damage 132
6.3.1.1. General 132

6.3.1.2. Stress Distribution of Corrosion FE Model 133
6.3.1.3. Corrosion Damage Mechanisms 135
6.3.1.4. Preliminary Accuracy Analysis of Corrosion FE Model 137
6.3.2. Freeze-Thaw Damage 138
6.3.2.1. General 138
6.3.2.2. Stress Distribution of Freeze-Thaw FE Model 139
6.3.2.3. Severity of Freeze-Thaw Damage 141
6.3.2.4. Freeze-Thaw Damage Progression 143
6.4. Conclusions 145
Chapter 7: Conclusions and Recommendations 147
7.1. General 147
7.2. Corrosion and Freeze-Thaw Damage of Concrete of Different Mixing Proportions 147
7.3. Naturally Corroded Reinforced Concrete Element 149
7.4. Concrete Damage under Coupled Freeze-Thaw and Sulfate Attack Conditions 150
7.5. Image-Based Microstructural Finite Element (FE) Modeling of Corrosion and Freeze-Thaw Damage 151
References 154

List of Figures

Figure 1.1. Thesis Structure.....5

Figure 2.1. Literature Search Process 8

Figure 2.2. (A) Main Components of Micro-Computed Tomography (μCT) Imaging System, and (B) 3D Stacking of CT Images 9

Figure 2.3. CT Image of Concrete Element (A) before and after (B) Median Filtration (3×3×3 Pixels), (C) Material Segmentation, and (D) Void Detection 10

Figure 2.4. Corrosion Level at Different Phases of Corrosion Process. Recreated from Chen and Mahadevan [135] with Permission from Elsevier. 16

Figure 2.5. CT Imaging of a 2.5 mm Rebar (White), Rust (Red), and a 10×10×10 mm^3Concrete at Different Phases of Corrosion. Reproduced from Dong et al. [55] with Permission from Elsevier. 17

Figure 2.6. CT Images of Corrosion-Induced Crack of a Mortar Specimen of a 36 mm Diameter Reinforced with a 6 mm Steel Reinforcement: (A) Top View, and (B) Side View. Reproduced from Van Steen et al. [100] with Permission from Elsevier. 18

Figure 2.7. CT Image of Preferred Path of Concrete Cracking due to Corrosion of a 12 mm Rebar. Reproduced from Wang et al. [144] with Permission from Elsevier. 19

Figure 2.8. Reinforcement Mass Loss Data Attained Using CT Imaging, Gravimetric Test, and Faraday's Law. Reproduced from Hong et al. [94] with Permission from Elsevier. 20

Figure 2.9. Corrosion-Induced Mortar Cracking with Reinforcement Exposed to Different Levels of Impressed Current Density. Reproduced from Hong et al. [98] with Permission from Elsevier. 22

Figure 2.10. Corroded Steel Reinforcement after Exposure to Current Densities of 0.2, 1.5, and 6 $\mu A/mm^2$. Reproduced from Hong et al. [56] with Permission from Elsevier. 23

Figure 2.11. Enlarged Images of Corroded (A) Low Alloy Steel, and (B) Low Carbon Steel Reinforcements with a Diameter of 10 mm. Reproduced from Shi et al. [103] with Permission from Elsevier. 25

Figure 2.12. Corrosion-Induced Crack of Mortar (5 mm in Diameter) with embedded (A) Carbon Steel, and (B) Stainless Steel Reinforcements with a Diameter of 0.5 mm. Reproduced from Itty et al. [90] with Permission from Elsevier. 25

Figure 2.13. Corrosion of Steel Reinforcement Exposed to Different Interfacial Defects. Reproduced from Rossi et al. [40] with Permission from Elsevier. 27

Figure 2.14. Corrosion Distribution and Cracking of Mortar with (A) Interfacial, (B) Midsection, and (C) External Surface Defects. Reproduced from Zhang et al. [44] with Permission from Elsevier. 28

Figure 2.15. Corroded Steel Reinforcement (A) without FRP Confinement, and (B) with FRP Confinement. Reproduced from Zhou et al. [119] with Permission from Elsevier. 30

Figure 2.16. Longitudinal and Lateral Corrosion-Induced Cracks within Mortar Cover of Eccentric Reinforcement. Reproduced from Xi and Yang [99] with Permission from Elsevier. .30

Figure 2.17. Progression of Damage of a Concrete Element with a Diameter of 75 mm Induced by (A) 0, (B) 12, (C) 18, (D) 24, (E) 30, and (F) 36 Freeze-Thaw Cycles. Reproduced from Jie Yuan et al. [153] with Permission from Hindawi.....33

Figure 2.18. Mass Loss Resulted from Exposure to Freeze-Thaw Cycles. Reproduced from Li et al. [154] with Permission from Elsevier.....34

Figure 2.19. CT Imaging of Concrete Voids/Cracks of a 70.7×70.7×210 mm^3 Element after Exposure to (A) 0, (B)75, (C) 250, and (D) 450 Freeze-Thaw Cycles. Reproduced from Liu et al. [57] with Permission from Elsevier. 37

Figure 2.20. Material Formation within (A) nAE, and (B) AE Mortar Specimens after Freeze-Thaw Testing. Reproduced from Sokhansefat et al. [29] with Permission from Elsevier. 39

Figure 2.21. Post-Test CT Images of Concrete Specimens with (A) 0.6% 15 nm SiO_2 NPs, (B) 0.4% 30 nm SiO_2 NPs, and (C) 0.6% 30 nm TiO_2 NPs. Reproduced from Liu et al. [58] with Permission from MDPI. 41

Figure 2.22. Freeze-Thaw Damage within Mortar Specimen under 100% Water Saturation. Reproduced from Sokhansefat et al. [29] with Permission from Elsevier. 42

Figure 2.23. Freeze-Thaw Damage within Concrete Specimens of (A) 75%, (B) 90%, (C) 95%, and (D) 100% Saturation levels. Reproduced from Shields et al. [59] with Permission from Elsevier. 43

Figure 3.1. Concrete Element (A) before Reinforcement Corrosion, (B) after Filling Interfacial Voids with Corrosion Products (Red), and (C) after Cracking by the Expansive Internal Pressure 48

Figure 3.2. Concrete (A) before Freezing, (B) while Freezing, and (C) after Freeze-Thaw Damage.....48

Figure 3.3. Concrete Specimens (A) CW4, (B) CW5/CS10, (C) CW6, (D) CW7, (E) CW8, (F) CS5, (G) CS20, (H) CS30, (I) FW4, (J) FW5/FS10, (K) FW6, (L) FW7, (M) FW8, (N) FW9, (O) FS5, (P) FS20, and (Q) FS30 before Testing 50

Figure 3.4. (A) μCT Imaging System, (B) Specimen's Region of Interest, and (C) Three-Dimensional Reconstruction of Detected Air Pores 52

Figure 3.5. Temperature of Controlled Environment throughout Each Freeze-Thaw Cycle.....53

Figure 3.6. Porosity (%) of (A) W/C, and (B) S/C Concrete Specimens after Applying 120 Wet-Dry Cycles 56

Figure 3.7. Mass Gain (%) of (A) W/C, and (B) S/C Concrete Specimens after Applying Wet-Dry Cycles 58

Figure 3.8. Detected Corrosion Products (Red and Yellow Highlights) within the 36 mm Midsection of Specimens (A) CW4, (B) CW5/CS10, (C) CW6, (D) CW7, (E) CW8, (F) CS5, (G) CS20, and (H) CS30 60

Figure 3.9. 3D Reconstructions of Pore Structures of Specimens (A) CW4, (B) CW5/CS10, (C) CW6, (D) CW7, (E) CW8, (F) CS5, (G) CS20, and (H) CS30 before (Left) and after (Right) 120 Wet-Dry Cycles 61

Figure 3.10. Cumulative Porosity vs. Pore Size for Concrete Specimens with different (A) W/C and (B) S/C Ratios before Freeze-Thaw Exposure.....62

Figure 3.11. 3D Reconstructions of Pore Structures of Specimens (A) FW4, (B) FW5/FS10, (C) FW6, (D) FW7, (E) FW8, (F) FW9, (G) FS5, (H) FS20, and (I) FS30 before Freeze-Thaw Test. 65

Figure 3.12. Damaged Concrete Specimens (A) FW8, and (B) FW9 after 40 Freeze-Thaw Cycles 66

Figure 3.13. Porosity of Concrete Specimens with Different (A) W/C, and (B) S/C Ratios before and after Freeze-Thaw Cycles 68

Figure 3.14. Open-Pore Ratio (%) of Concrete Specimens with Different (A) W/C, and (B) S/C Ratios before and after Testing.....70

Figure 3.15. Large-Pore (>1.18×10^6 μm^3) Ratio (%) of Concrete Specimens with Different (A) W/C, and (B) S/C Ratios before and after Testing 73

Figure 3.16. High-Sphericity (>0.5) Ratio (%) of Concrete Specimens with Different (A) W/C, and (B) S/C Ratios before and after Testing.....75

Figure 3.17. Average Pore Gap of Concrete Specimens with Different (A) W/C, and (B) S/C Ratios before and after Testing.....77

Figure 3.18. Mass Loss of Concrete Specimens of Different (A) W/C, and (B) S/C Ratios 79

Figure 3.19. 2D Section of Specimens (A) FW4, (B) FW5/FS10. (C) FW6, (D) FW7, (E) FS5, (F) FS20, and (G) FS30 before (Left) and after (Right) Exposure to 40 Freeze-Thaw Cycles.....80

Figure 4.1. Naturally Corroded Reinforced Concrete before Cutting (A), and after Cutting (B) .85

Figure 4.2. Three-dimensional (A) Image Stacking, and (B) Reconstruction of the Concrete Specimen 87

Figure 4.3. Steps of Post-Processing the CT Images 87

Figure 4.4. 3D Reconstructions of (A) Corroded Concrete Specimen, (B) Detected Rust, and (C) Exposed Surface of Steel Reinforcement.....90

Figure 4.5. 3D Reconstructions of (A) the Exposed Side of Steel Reinforcement, and (B) the Covered Side of Steel Reinforcement.....92

Figure 4.6. Detected Air Pores and the Analysis Direction of Accumulated Pore Volume 93

Figure 4.7. Accumulative Pore Volume along the Concrete Width 93

Figure 4.8. Detected Corrosion Products 95

Figure 4.9. Top-View Section of the Specimen Showing the Uncorroded Rebar (Blue), Corrosion Products (Red), and Falsely Detected Aggregates (Highlighted).....95

Figure 4.10. Comparison between (A) Detected Corrosion Products, and (B) Actual Rust ..96

Figure 5.1. (A) Control, (B) PS-5%, (C) PS-10%, (D) MS-5%, and (E) MS-10% Concrete Specimens 101

Figure 5.2. Temperature of Controlled Environment throughout Each Freeze-Thaw Cycle [217] 102

Figure 5.3. (A) Control, (B) MS-5%, (C) MS-10%, (D) PS-5%, and (E) PS-10% Concrete Specimens after 40 Freeze-Thaw Cycles 105

Figure 5.4. (A) Control, (B) MS-5%, (C) MS-10%, (D) PS-5%, and (E) PS-10% Concrete Specimens after 80 Freeze-Thaw Cycles 105

Figure 5.5. 2D CT Images of Specimens (A) PS-10%, and (B) MS-10% before (Left) and after 40 (Right) Freeze-Thaw Cycles 106

Figure 5.6. Frost-Induced Mass Loss (%) of Concrete Specimens 107

Figure 5.7. Surface Pores of Specimen MS-5% (A) before, and (B) after 40 Freeze-Thaw Cycles 108

Figure 5.8. Porosity (%) of Concrete Specimens before and after the Freeze-Thaw Cycles 109

Figure 5.9. Large-Pore Ratio (%) of Concrete Specimens before and after the Frost Cycles 111

Figure 5.10. Large Pores of Specimens (A) Control, (B) PS-5%, (C) MS-5%, (D) PS-10%, and (E) MS-10% before (Left) and after 40 (Middle) and 80 (Right) Freeze-Thaw Cycles 112

Figure 5.11. Open-Pore Ratio (%) of Concrete Specimens before and after the Freeze-Thaw Cycles 114

Figure 5.12. Surface (Open) Pores of Specimens (A) Control, (B) PS-5%, (C) MS-5%, (D) PS-10%, and (E) MS-10% before (Left) and after 40 (Middle) and 80 (Right) Freeze-Thaw Cycles 115

Figure 5.13. 2D Sections of Specimens (A) Control, (B) PS-5%, (C) PS-10%, (D) MS-5%, and (E) MS-10% before (Left) and after 40 (Middle) and 80 (Right) Freeze-Thaw Cycles 118

Figure 5.14. 3D Pore Structure of Specimens (A) Control, (B) PS-5%, (C) MS-5%, (D) PS-10%, and (E) MS-10% before (Left) and after 40 (Middle) and 80 (Right) Freeze-Thaw Cycles 119

Figure 6.1. (A) Corrosion Specimen, and (B) Freeze-Thaw Specimens 1 (Left) and 2 (Right) .123

Figure 6.2. 3D Models of (A) Aggregates, (B) Air Voids, (C) Steel Reinforcement, and (D) Cement Mortar 125

Figure 6.3. 3D Models of (A) Aggregates, (B) Ice (Voids), and (C) Cement Mortar of Specimens 1 (Left) and 2 (Right) 126

Figure 6.4. (A) Modulus of Elasticity, (B) Thermal Expansion Coefficient, (C) Density, and (D) Poisson's Ratio of Ice at Different Freezing Temperatures. Recreated from [252–255].....128

Figure 6.5. (A) Compressive and (B) Tensile Stress-Strain Curves of Cement Mortar 129

Figure 6.6. The Controlled Environment Temperature of a Single Freeze-Thaw Cycle [217]...131

Figure 6.7. Temperature of the Applied Freeze-Thaw Cycles 132

Figure 6.8. von Mises Stress (MPa) Distribution within the Cement Mortar at (A) 0.6%, (B) 3%, and (C) 6% of the Reinforcement Expansion 134

Figure 6.9. 2D Propagation of Concrete Damage (A) before, and after (B) 1.2%, (C) 2.4%, (D) 3.6%, (E) 4.8%, and (F) 6% of Reinforcement Expansion 136

Figure 6.10. Comparison between (A) the Actual Concrete Damage and (B) the Simulated Concrete Damage at 1.5% of Reinforcement Expansion 137

Figure 6.11. Concrete Specimen #1 (A) before and (B) after 40 Freeze-Thaw Cycles.....138

Figure 6.12. von Mises Stress Distribution within the Concrete Specimen #1 (A) before and after (B) 5, (C) 20, and (D) 40 Freeze-Thaw Cycles 140

Figure 6.13. Volume Loss of (A) Specimen #1, and (B) Specimen #2 after 40 Freeze-Thaw Cycles 142

Figure 6.14. Freeze-Thaw Damage of the Modeled Concrete after (A) 5, (B) 20, and (C) 40 Freeze-Thaw Cycles.....144

Figure 6.15. Internal Pore Structures of Specimen #1 (A) before and (B) after 40 Freeze-Thaw Cycles, and (C) the Frost Damage of the FE Model.....145

List of Tables

Table 2.1. Micro-Computed Tomography (μCT) Imaging Parameters Utilized in the Literature 12

Table 2.2. Conditions of Applied Wet-Dry Cycles.....14

Table 2.3. Freeze-Thaw Conditions Applied in the Literature.....31

Table 3.1. Composition of Concrete Specimens.....50

Table 5.1. Chemical Composition of Portland Cement [234].....101

Table 5.2. Composition of Freeze-Thaw Solution.....102

Table 6.1. Mechanical Properties of Cement Mortar, Aggregates, and Steel Reinforcement 127

Table 6.2. Parameters of Concrete Damage Plasticity Model.....129

Table 6.3. Contact Conditions of the Mortar-Aggregate, Mortar-Steel, Aggregate-Steel, Mortar-Ice, and Aggregate-Ice Interfaces.....130

Chapter 1: Introduction

1.1. General Background

Concrete durability is defined by its ability to retain its strength and serviceability by resisting various deterioration processes caused by environmental conditions. For example, prolonged exposure to wet and cold environments can cause detrimental corrosion and freeze-thaw damage within concrete structures.

Reinforcement corrosion is the leading cause of concrete damage [1–4], which resulted in structural catastrophes, including the Silver Bridge in 1967, the Genoa bridge in 1979, the Mianus River Bridge in 1983, and the Kinzua Bridge in 2003 [5–8]. According to the National Association of Corrosion Engineers (NACE) International report, repair of corrosion-induced infrastructural damage annually costs the United States about $22.6 billion [9]. This is due to the fact that the total volume occupied by steel reinforcement increases once corroded because of rust expansion. Consequently, substantial concrete cracking can be caused by the resulted high expansive pressure between the steel reinforcement and the surrounding concrete [10–13]. Also, the corrosion can severely disintegrate the steel reinforcement and considerably degrade the bond between concrete and its steel reinforcement, causing a sudden fracture of concrete structures [14–20].

On the other hand, continuous or frequent exposure to sub-zero temperatures makes concrete prone to frost damage by freezing the water retained within its capillaries [21–24]. The freeze-thaw damage results from a combination of a crystallization pressure induced by ice expansion, an internal hydraulic pressure produced by compression of retained water, and interfacial stress created by the mismatching thermal expansion coefficients of the concrete materials [25–28]. Concrete cracking occurs when the stress induced by the expansive internal pressure exceeds its

tensile strength, likely when the degree of saturation exceeds its critical threshold ranging from about 50% to about 90% [29–34]. In addition to deteriorating the concrete strength, frost-induced cracks considerably accelerate the ingress of water, chloride, and CO_2 by increasing the permeability of concrete, leading to faster freeze-thaw and corrosion damage [35–37].

The severity of corrosion and freeze-thaw damage can be impacted by concrete's pore characteristics, including permeability, porosity, pore size, and pore distribution [38–40]. Permeable concrete is vulnerable to corrosion and freeze-thaw conditions due to the associated increase in water ingress [41–43]. Also, increasing the concrete porosity can weaken its strength, making concrete more prone to cracking. Likewise, while uniformly distributed microvoids can mitigate corrosion and freeze-thaw damages, large and clustered pores can cause stress concentration, resulting in faster cracking [44,45]. Thus, a deep understanding of the effects of concrete composition and surrounding environments on its pore properties and the severity and mechanisms of the corrosion and freeze-thaw damage is imperative for implementing preventive measures and applying effective rehabilitation.

Different non-destructive technologies are employed in the literature to evaluate concrete damage, including the acoustic emission test [46–48], the permeability test [49–51], and the electrical resistivity measurement [52–54]. However, little details were provided on concrete's pore morphology and damage mechanisms under corrosion and freeze-thaw conditions. Hence, high-resolution micro-computed tomography (μCT) imaging has been getting more attention as it can provide a three-dimensional reconstruction of concrete's internal microstructure and precisely monitor its damage mechanisms [55–59]. Also, image-based microstructural finite element (FE) models can be developed using CT images. Thus, CT imaging is utilized in this research to analyze concrete's pore characteristics and damage mechanisms under corrosion and freeze-thaw

conditions and to calculate internal stress distribution by developing image-based sample-specific microstructural FE models.

1.2. Research Objectives

General Objective

The main objective of this research is to gain a deeper understanding of the effects of concrete composition and surrounding environments on the severity and mechanisms of corrosion and freeze-thaw damage by integrating mechanical characterization using CT imaging into image-based microstructural FE modeling.

Specific Objectives

- Investigate the effects of mixture proportions on the pore properties, including pore size, shape, and distribution, and the microstructural damage of concrete subjected to corrosion and freeze-thaw conditions. [Chapter 3]
- Examine the distribution of the natural corrosion products and damage mechanisms of large concrete elements. [Chapter 4]
- Study the impact of different sulfate environments on the severity and mechanisms of microstructural freeze-thaw damage. [Chapter 5]
- Investigate concrete's internal stress distribution caused by corrosion and freeze-thaw damage using novel image-based microstructural FE models. [Chapter 6]

1.3. Thesis Structure

Chapter 1 presents the general background, objectives, methodologies, and structure of this research, shown in Figure 1.1.

In Chapter 2, a comprehensive literature review of corrosion and freeze-thaw damage of concrete using CT imaging is presented. The utilized imaging parameters were listed, and the reported severity and mechanisms of concrete damage under different corrosion and freeze-thaw conditions were discussed. Also, the research gaps were identified for further investigation.

In Chapter 3, the microscale impact of concrete composition on its pore properties and damage mechanisms under corrosion and freeze-thaw conditions was investigated. Wet-dry cycles were applied to the corrosion specimens, whereas the freeze-thaw samples were exposed to freeze-thaw cycles. The pore characteristics, including the porosity and pore size, shape, and distribution, were analyzed before and after testing, and the concrete damage mechanisms were discussed.

Chapter 4 presents an investigation of corrosion distribution within a naturally corroded large concrete element using CT imaging. The 3D distribution of corrosion products within a large 50-year-old naturally corroded concrete element was investigated, and the concrete damage mechanisms were studied by analyzing its pore structure. Also, the accuracy of corrosion detection was verified by comparing the captured rust with the corrosion products of the concrete element.

In Chapter 5, the effects of different sulfate salts and concentrations on the severity and mechanisms of freeze-thaw damage are examined. Concrete specimens of the same composition were subjected to freeze-thaw cycles in distinct solutions: water, magnesium sulfate, and potassium sulfate, with concentrations of 5% and 10%. The severity of frost damage was

determined from the mass loss and porosity expansion data, whereas the damage mechanisms were investigated by monitoring the changes in the internal microstructure of concrete.

Chapter 6 presents the development of two image-based microstructural finite element models of corrosion and freeze-thaw damage of concrete. Three-dimensional reconstructions of the cement mortar, aggregates, and air pores were created using the CT image. Also, while the corrosion FE model consisted of the steel reinforcement that was subjected to uniform corrosion, the freeze-thaw model was simulated by filling the voids with freezing water and exposing the concrete element to freeze-thaw cycles. The internal stress distribution was investigated by analyzing the interaction between the cement mortar, aggregates, and corroding steel reinforcement. Also, the severity and mechanisms of the simulated concrete damage were compared to experimental data.

In Chapter 7, the conclusions and recommendations for future work are presented. Overall, this research contributed six journal articles and six conference papers, most of which were published or submitted for publication.

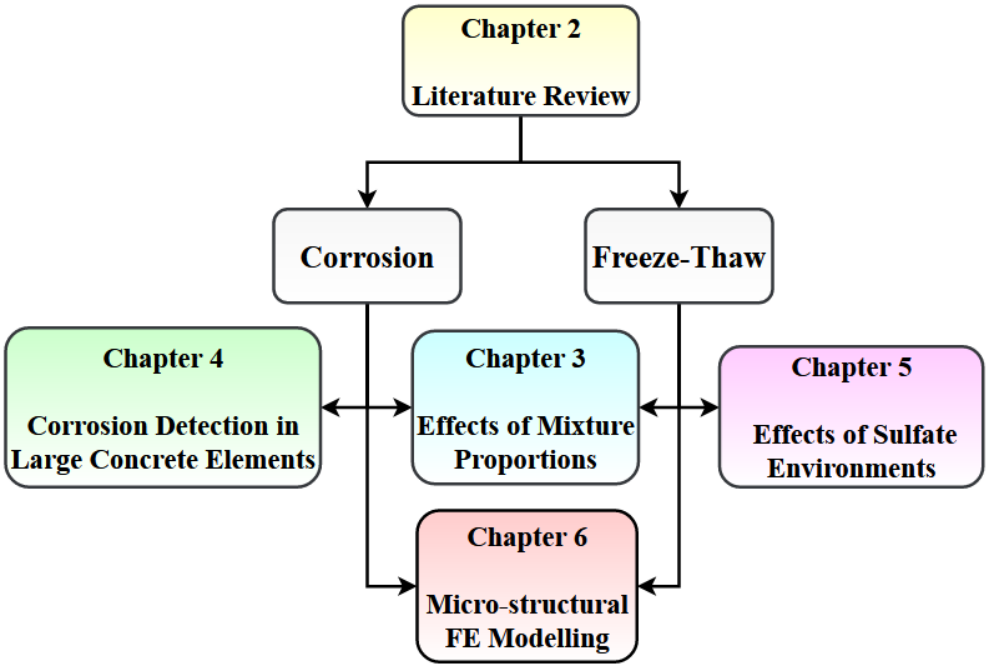

Figure 1.1. Thesis Structure

Chapter 2: Literature Review

This chapter provides a comprehensive review of microstructural imaging of corrosion and freeze-thaw damage of concrete using non-destructive micro-computed tomography (μCT). It also presents the utilized imaging parameters and discusses the reported observations of concrete damage under different testing and degradation conditions.

2.1. Introduction

Repair of concrete damage is anticipated to cost the United States alone about $2 trillion by 2025, as indicated in the American Society of Civil Engineering (ASCE) report (2017) [60]. Reinforcement corrosion and freeze-thaw damage are two leading causes of concrete degradation [1,3,4,59,61]. Hence, extensive research has been conducted to better understand the severity and mechanisms of concrete damage under different corrosion and freeze-thaw conditions.

Prior to corrosion, steel reinforcement is, to a certain limit, protected from the environment by a ferric oxide (Fe_2O_3) layer [62–66]. This protective layer can deteriorate once subjected to a threshold of chloride ions or an acidic (low pH) environment, leading to corrosion of the exposed steel reinforcement [67–69]. Reinforcement corrosion not only disintegrates the steel rebars, reducing their area and making them weaker and more vulnerable to fracture, but also produces a high internal expansive pressure within reinforced concrete structures, resulting in excessive concrete cracking [18–20,70,71]. Also, corrosion can cause substantial degradation of the bond between concrete and its steel reinforcement, leading to sudden fracture of concrete structures [14–17]. Unless monitored and repaired, the corrosion damage can cause structural catastrophes, such

as the Silver Bridge in 1967, the Genoa bridge in 1979, the Mianus River Bridge in 1983, and the Kinzua Bridge in 2003 [5–8].

On the other hand, concrete structures in cold regions are susceptible to freeze-thaw damage due to the expansion of freezing water retained within the concrete capillaries, which can cause irreversible pore enlargement, and concrete spalling and cracking [59,61,72]. Concrete cracking occurs when the stress induced by the expansive internal pressure exceeds the tensile strength of concrete, which is more likely to occur when the degree of saturation exceeds its critical threshold of 50–90% [29–34]. Also, the temperature fluctuation between cold and warm environments can produce thermal stress within the interfacial transition zone at the aggregate-mortar interface, attributed to the mismatching thermal expansion coefficients of the mortar and aggregates [73–75]. These conditions result in concrete cracking, particularly within the interfacial transition zone because of its low strength and surface asperities that can cause stress concentration [26,27,76]. In addition to deteriorating the strength of concrete structures, concrete cracks increase water ingress, accelerating carbonation, corrosion, and further frost damage [77,78].

Researchers have employed various technologies to investigate concrete damage, including the acoustic emission test [46–48,79–81], ultrasonic waves [82,83], the permeability test [49–51], and the electrical resistivity measurement [52–54]. However, to obtain more information, researchers have recently explored using advanced and non-destructive micro-computed tomography (μCT) imaging systems to thoroughly investigate the corrosion and freeze-thaw damage mechanisms. Using CT imaging, researchers are able to produce precise three-dimensional reconstructions of concrete's internal pore structure and monitor the severity and mechanisms of concrete damage. However, the full potential of CT imaging has yet to be fully realized despite its promising outcomes.

Thus, this literature review provides a comprehensive insight into the current research progress in this field by reviewing the specifications of examined specimens, the applied testing conditions, and the utilized CT scanning parameters for attaining high-resolution images. This review was conducted using the keywords “computed tomography”, “corrosion”, “concrete”, “cement”, “freeze-thaw”, “frost”, and “mortar”. Over 1,300 research articles were reviewed, but only a small number of scientific papers used CT imaging to examine concrete’s corrosion and freeze-thaw damage, as illustrated in Figure 2.1.

The reported corrosion diffusion and crack propagation mechanisms were synthesized, and the accuracy of CT measurements of reinforcement mass loss was investigated by comparing its results to the data of gravimetric testing and Faraday’s law. Also, the effects of impressed current, type of steel reinforcement, structural defects, and confinement on the corrosion and cracking mechanisms were discussed. Similarly, the published observations of freeze-thaw damage mechanisms were described. Also, the effects of mixture proportions (e.g., water/cement and sand/cement ratios), air entrainment, nano-additives, saturation level, and sulfate environments on the severity and mechanisms of freeze-thaw damage were discussed.

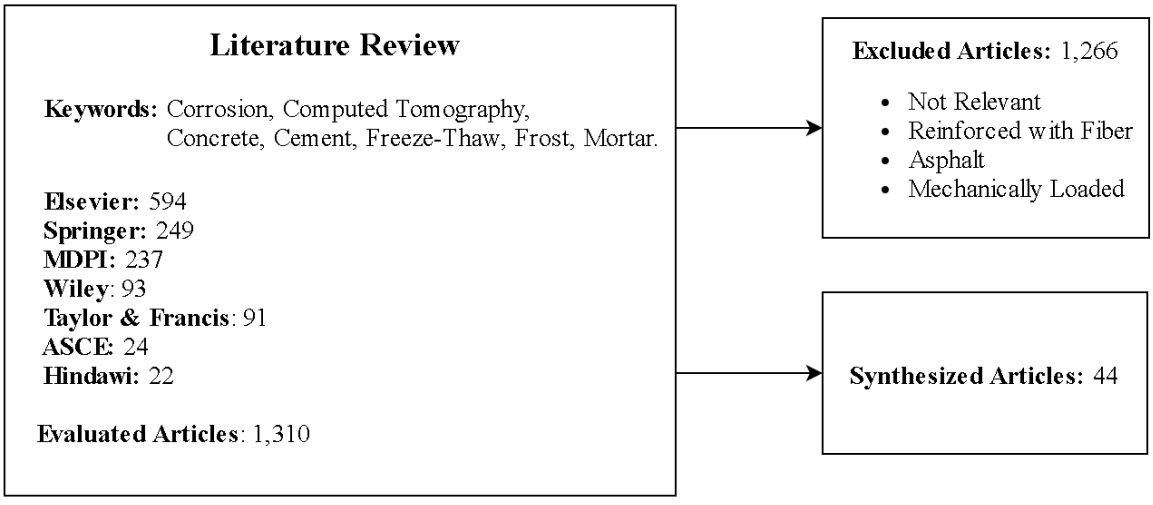

Figure 2.1. Literature Search Process

2.2. Micro-Computed Tomography (µCT) Imaging

2.2.1. Imaging Principles

Micro-computed tomography (µCT) is a non-destructive imaging system that employs an X-ray to scan materials' internal microstructure (e.g., concrete). Photons are emitted from the X-ray source toward the specimen, part of which penetrates through the rotating sample and reaches the detector [84], as illustrated in Figure 2.2 (A). Due to the variation of X-ray attenuation within the specimen, the detected photons have a spectrum of energy and density through which CT images with distinguishable contrast are generated [85]. The collected CT images are then stacked to create a 3D model, as shown in Figure 2.2 (B). Further image post-processing, such as filtration, can be performed to minimize imaging artifacts, as shown in Figure 2.3 (B). Also, material segmentation can be used to segment different components of the element, such as the intact steel reinforcement (blue highlight) and corrosion products (red highlight) demonstrated in Figure 2.3 (C). Similarly, void detection can be applied to capture and highlight the air pores within the element, as illustrated in Figure 2.3 (D).

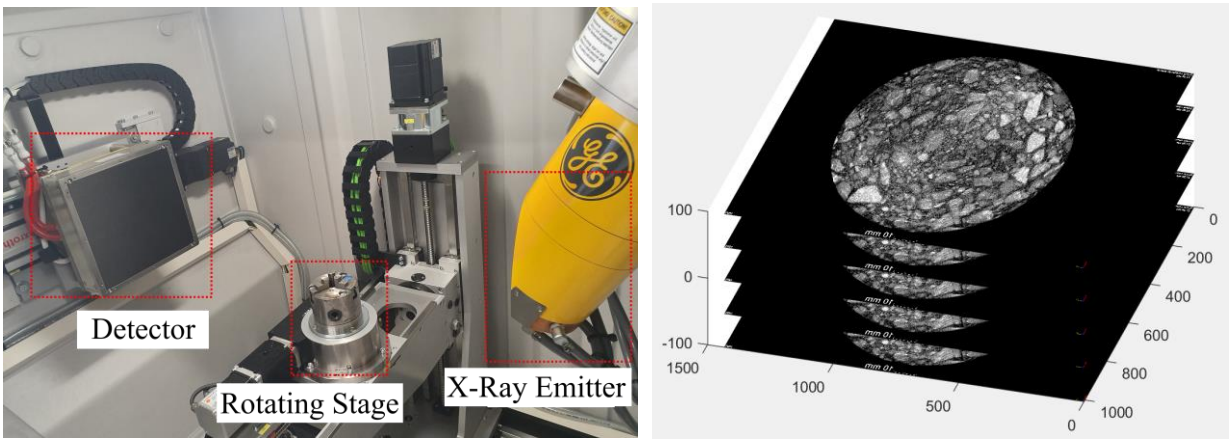

(A) (B)

Figure 2.2. (A) Main Components of Micro-Computed Tomography (µCT) Imaging System, and (B) 3D Stacking of CT Images

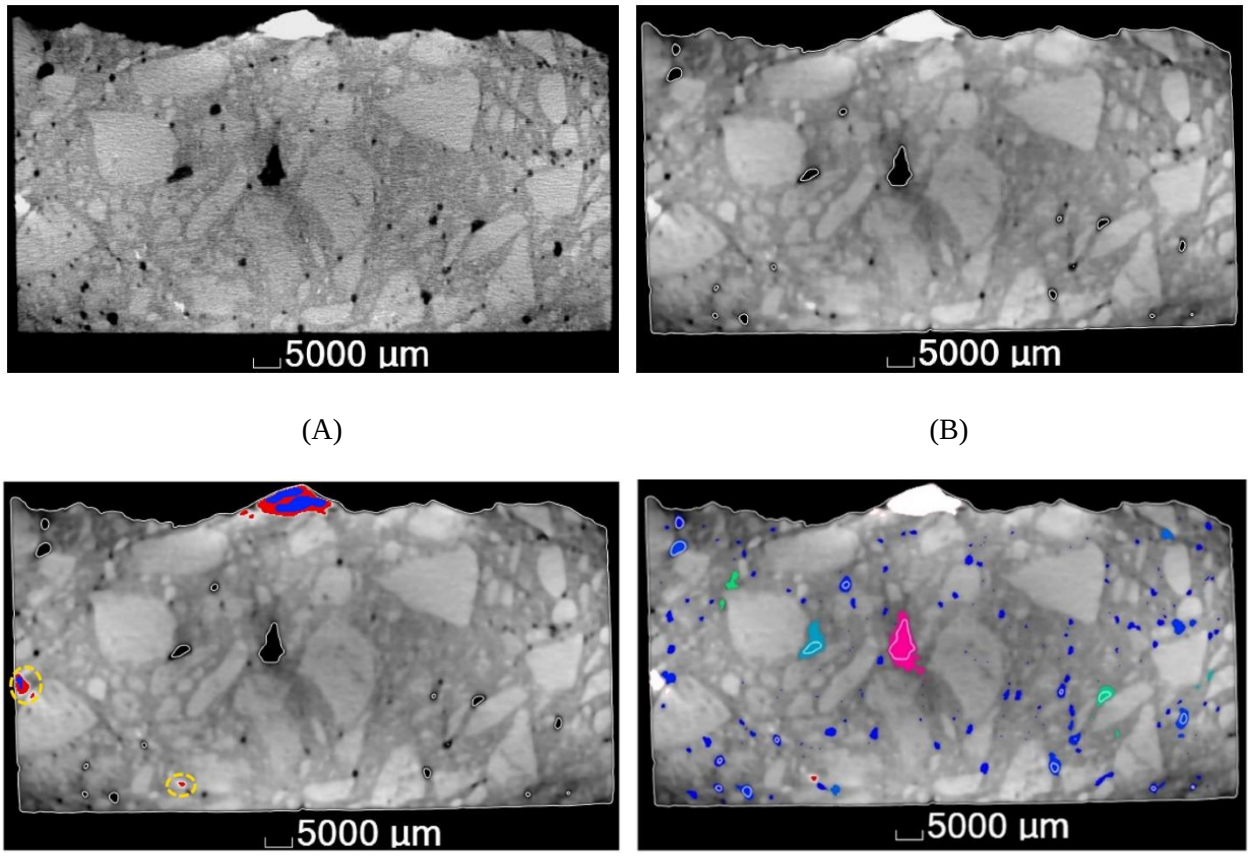

(A) (B)

(C) (D)

Figure 2.3. CT Image of Concrete Element (A) before and after (B) Median Filtration (3×3×3 Pixels), (C) Material Segmentation, and (D) Void Detection

2.2.2. CT Imaging Parameters

The resolution of CT imaging can be affected by several parameters, including the number of collected images, the X-ray exposure time per image, the voxel size (spatial resolution), and the applied tube voltage and current. Applying higher voltage generally produces photons with higher penetrative power, allowing more photons to pass through specimens [86]. However, emitting high-energy photons can sometimes diminish the contrast and reduce the resolution of CT images since blocking a sufficient portion of photons is essential for producing high contrast [87,88].

On the other hand, applying a higher tube current increases the number of emitted photons leading to more extensive data collection [89]. While collecting more CT images can enhance the precision of the generated 3D reconstruction, extending the X-ray exposure time per image can minimize artifacts and improve the overall resolution of CT photos [86]. Also, minimizing the voxel size allows capturing finer details and enhances the quality of the CT images. The resolution of the CT images can also be improved by utilizing thin metallic filters (e.g., copper) through which beam-hardening artifacts are reduced [88]. It is worth stating that overusing any of the aforementioned imaging parameters can overload the CT imaging system and shorten its components' service life. Thereby, the scanning parameters applied in the literature for attaining high-resolution CT images of corrosion and freeze-thaw specimens are listed in Table 2.1.

It can be observed that specimens with a wide range of thicknesses extending from 5 mm to 100 mm were CT scanned. As a result, a broad extent of voxel sizes of 0.1^3–48^3 μm^3 was used. Nevertheless, most researchers tested small specimens with a thickness of 10 mm to minimize the voxel size and enhance the resolution of CT imaging. The applied tube voltage and current were 43–400 kV and 50–300,000 µA, respectively, and the number of captured images per CT scan ranged between 1,000 and 3,141.

Table 2.1. Micro-Computed Tomography (μCT) Imaging Parameters Utilized in the Literature

Corrosion Tests						
Material and Thickness (mm)	**No. of Images**	**Voltage (kV)**	**Current (μA)**	**Exposure Time (s)**	**Voxel Size (μm^3)**	**Ref.**
Cement | 5	1,024	43	NA	0.35	NA	[90]
Concrete | 10	1,000	70	114	NA	15^3	[91]
Cement | 10	1,000	139	62	NA	7.6^3	[92]
Cement | 10	NA	120 – 150	65 – 82	NA	NA	[93]
Mortar | 10	NA	70	114	4	13.5^3	[94]
Mortar | 10	1,000	70	114	NA	15^3	[95,96]
Mortar | 10	1,001	70	100	4	13.5^3	[56]
Mortar | 10	1,000	139	62	NA	15^3	[97]
Mortar | 10	NA	80 – 120	80 – 100	NA	3^3 – 12.1^3	[44]
Mortar | 10	NA	70	62	NA	15^3	[55]
Mortar | 10	1,014	70	100	4	NA	[98]
Mortar | 20	3,141	150	77	1	16.3^3	[99]
Concrete | 20	2,303	150	NA	NA	20^3	[40]
Mortar | 36	2,400	180	140	3	18^3	[100]
Mortar | 40	1,080	159	600	NA	45^3	[101]
Mortar | 40	1,600	220	100	1	20^3	[102]
Concrete | 50	1,080	225	650	NA	48^3	[103]
Freeze-Thaw Tests						
Material and Thickness (mm)	**No. of Images**	**Voltage (kV)**	**Current (μA)**	**Exposure Time (s)**	**Voxel Size (μm^3)**	**Ref.**
Cement | 5	1284	100	50	NA	2.97^3	[104]
Mortar | 9	NA	80	110	NA	3^3	[105]
Mortar | 10	1600	120 – 140	140 – 200	0.99	7.15^3	[106]
Mortar | 10	NA	60	133	NA	15.2^3	[107]
Concrete | 10	1000	80	87	NA	2.57^3	[59]
Mortar | 12	1024	150	100	NA	NA	[108,109]
Cement | 20	1601	60	150	6	1.81^3	[110]
Mortar | 40	NA	100	400	0.3	0.4^3	[38]
Concrete | 50	NA	225	1,700	NA	NA	[58]
Concrete | 50	NA	120	300,000	NA	NA	[111]
Concrete | 50	NA	400	300,000	NA	NA	[112]
Mortar | 51	NA	150	100	NA	NA	[113]
Concrete | 100	NA	120	300,000	0.4	0.1^3	[114]

2.3. CT Imaging of Corrosion

2.3.1. Corrosion Induction Methods

Impressed current and wet-dry are the main methods used for inducing reinforcement corrosion within concrete specimens. The electric circuit of the impressed current method consists of three main components, namely, an anode element (steel reinforcement), a cathode material (e.g., copper), and an electrically conductive electrolyte (salt water) [92]. A current-controlled DC power supply is typically used to promote electron transfer without causing sharp current spikes during the corrosion process [115]. It is important to note that the intensity of the applied impressed current can considerably alter the reinforcement corrosion and specimen cracking mechanisms [12,116–118]; therefore, the corrosion-induction conditions used in the literature were reviewed to provide a basis for further testing. The small specimens, mostly made of mortar, were 5–50 mm thick. Before applying the impressed current, the specimens were immersed in salt water with a sodium chloride content (wt% NaCl) of 3.5–5 wt% for days to allow deep penetration of the electrolyte [103,119]. While some researchers employed titanium and silver as cathode materials attributed to their high electrode potential [120–123], most researchers used copper instead due to its availability and affordability. A wide range of impressed current densities extending from 0.2 $\mu A/mm^2$ to 53.08 $\mu A/mm^2$ was repeatedly applied until considerable cracking was observed. The electrolyte solution was regularly replaced to maintain a consistent corrosion environment [18]. The conditions of the impressed current technique applied in the literature are listed in Table 2.2.

The cyclic wetting-drying method is based on frequent exposure of specimens to salt water to induce reinforcement corrosion. In the wetting step, specimens are immersed in salt water for a period ranging from a few hours to several days. Exposure to oxygen-rich salt water can boost the oxidation process causing faster reinforcement corrosion [124–126]. Each wet-dry cycle is

completed after performing the drying step through which the specimens are dehydrated under either natural or controlled environments. The cyclic wet-dry method can provide a realistic representation of natural reinforcement corrosion due to the lack of artificial corrosion-accelerating conditions [118].

Nevertheless, exposure to elevated temperatures during the dehydration process can cause internal thermal stress within the damaged specimens, leading to further cracking [127–129]. Thereby, the conditions applied in the literature are presented. During each wet-dry cycle, the small specimens with a thickness of 10–40 mm were first immersed in salt water with an average sodium chloride content (wt% NaCl) of 3.8% (±0.9) for 3–48 hours. The specimens were dehydrated for 3–144 hours either under natural environmental conditions or using a heated oven at a temperature of around 50 ^{o}C, which is not high enough to cause considerable cracking. In other words, the interval of each applied wet-dry cycle ranged from 6 hours to a week. More details of the applied conditions are listed in Table 2.2.

Table 2.2. Conditions of Applied Wet-Dry Cycles

Impressed Current Method					
Material and Thickness (mm)	**Mix Ratios (C:W:S:A)**	**Rebar Dia. (mm)**	**Impressed Current Density (μA/mm^2)**	**Electrolyte (% NaCl)**	**Ref.**
Cement | 5	1:0.4:0:0	0.5	50	3.5	[90]
Mortar | 10	1:0.5:2:0	3	0.2 – 6	3.5	[98]
Mortar | 10	1:0.5:2:0	3	3 – 5	3.5	[94]
Mortar | 10	1:0.5:1:0	2	53.08	5	[44]
Cement | 10	1:0.4:0:0	3	4, 42	3.5	[93]
Concrete | 24.75	1:0.5:1.8:2.9	6.5	49	5	[119]
Mortar | 36	1:0.5:2.5:0	6	1	5	[100]
Concrete | 50	1:0.53:2:3	10	3.2	3.5	[103]

* C: Cement, W: Water, S: Sand, A: Aggregates

Table 2.2. (Continued) Conditions of Applied Wet-Dry Cycles

Wet-Dry Method						
Material and Thickness (mm)	**Mix Ratios (C:W:S:A)**	**Rebar Dia. (mm)**	**No. of Cycles**	**Wet/Dry Periods (hrs)**	**Electrolyte (% NaCl)**	**Ref.**
Mortar | 10	1:0.4:1:0	2	48	3/3	3.5	[97]
Mortar | 10	1:0.5:3:0	2.5	12	3/3	3.5	[96]
Mortar | 10	1:0.5:3:0	2.5	12	3/3	3.5	[55]
Mortar | 20	1:0.4:1:0	2.94	NA	4/20	5.8	[99]
Mortar | 30	1:1:4:0	5	12	48/120	3.5	[130]
Mortar | 40	1:0.53:1.5:0	8	24	24/144	3	[101]

* C: Cement, W: Water, S: Sand, A: Aggregates

2.3.2. Corrosion Diffusion

CT imaging provided an in-depth understanding of the process of reinforcement corrosion diffusion within the concrete sample. The corrosion process started after the de-passivation of steel reinforcement, and it was accelerated upon cracking of the cover material due to exposure to more oxygen atoms dissolved within the salt water [131–134]. Therefore, different phases were observed in the course of the corrosion process, as reported by Dong et al. (2018a, b, c), Chen and Mahadevan (2008), Fang et al. (2019), and Hong et al. (2020a) [55,91,95–97,135]. As a result, the corrosion level-time diagram exhibited three linear phases, namely: corrosion initiation, free rust expansion, and cover cracking, as illustrated in Figure 2.4 [55,135]. In the initiation phase, the steel reinforcement can experience de-passivation because of the carbonation of cover material (e.g., concrete) and the penetration of chloride ions, causing reinforcement corrosion as shown in Figure 2.5 (A) [135–137]. During the free expansion phase, the produced rust diffuses into the vacant space within the reinforcement interface [40,88,102]. Hence, interfacial defects (voids) can lead to localized corrosion, also called pitting corrosion, resulting in non-uniform rust distribution as demonstrated in Figure 2.5 (B) [44,138,139]. Once the surrounding space is filled with corrosion

products, further production of rust can induce expansive internal pressure at the reinforcement interface [100,140]. Interfacial cracks can result when the produced tensile stress exceeds the tensile strength of the cover material, as illustrated in Figure 2.5 (C).

Despite its potential in capturing the corrosion distribution within small concrete specimens, accurate detection of corrosion products in large concrete samples using CT imaging is still a challenge. This can be attributed to the high X-ray attenuation of aggregates in addition to the low image resolution caused by scanning larger specimens. However, this challenge can be overcome by using porous aggregates to minimize the X-ray attenuation. Based on the reported literature, the potential of this approach was not tested. Another applicable approach is the use of advanced image-analysis algorithms to separate the captured corrosion products from falsely detected aggregates.

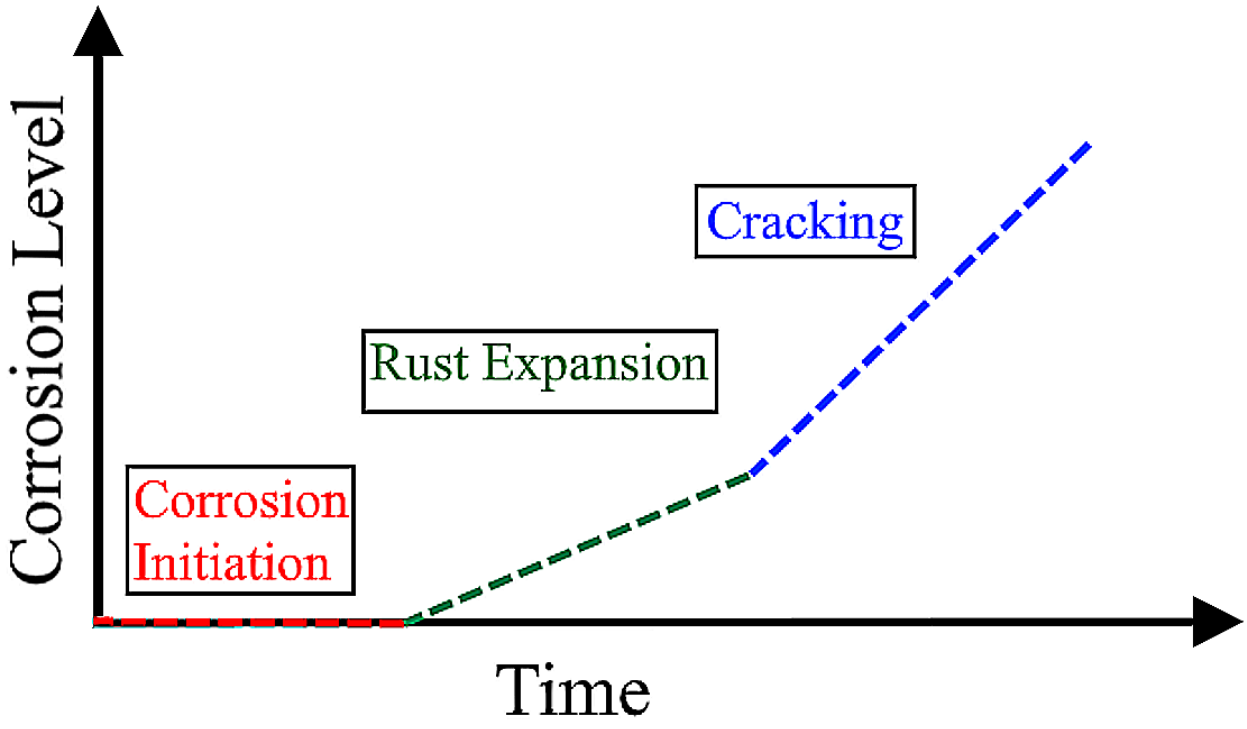

Figure 2.4. Corrosion Level at Different Phases of Corrosion Process. Recreated from Chen and Mahadevan [135] with Permission from Elsevier.

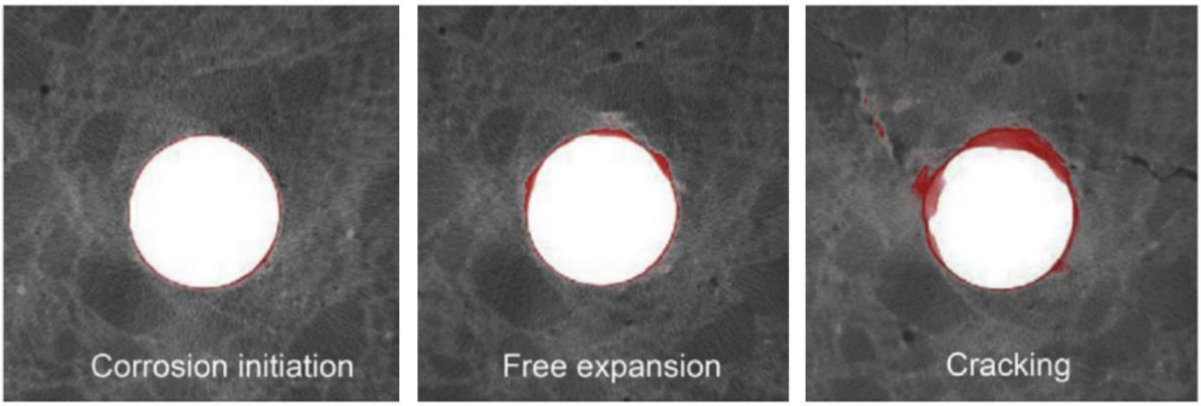

(A) (B) (C)

Figure 2.5. CT Imaging of a 2.5 mm Rebar (White), Rust (Red), and a 10×10×10 mm^3Concrete at Different Phases of Corrosion. Reproduced from Dong et al. [55] with Permission from Elsevier.

2.3.3. Damage Propagation

The corroded portion of steel reinforcement experiences a volumetric expansion resulting in internal tensile stress within structural elements. As reported by Fang et al. (2019) and Zhang et al. (2019), the volumetric expansion of corrosion products varied from 1.19% to 1.92% for mortar specimens and from 2.71% to 3.97%. for concrete samples [44,97]. This variation of volumetric expansion can be attributed to several factors, including the cover material and thickness (confinement), the void distribution, and the surrounding environment [141,142]. Once the produced tensile stress exceeds the tensile strength of the cover material (e.g., mortar), cracks are initiated within structural elements, as demonstrated in Figure 2.6 (A) [90,99]. CT images showed that cracks appeared at the reinforcement interface or the external surface of the cover material depending on the location of the weakest spot within the specimen [93,143]. Also, cracks propagated in a longitudinal, lateral, or diagonal manner along the most fragile path, as shown in Figure 2.6 (B) [44,100]. This can be attributed to the distribution of defects within the specimens since cracks are more likely to extend toward voids due to the reduced confinement [44]. In case

of concrete elements, cracks also tended to propagate along the aggregate interface because of the high strength of aggregates and the relatively low interfacial bond strength, as illustrated in Figure 2.7 [144]. Also, cracks propagated through weak or porous aggregates, as reported by Shi et al. (2018) [103].

It is worth noting that corrosion products were seen to be entrapped nearby narrow cracks causing higher internal pressure [44,145]. As corrosion increases, these cracks may expand linearly or exponentially with corrosion products, as observed by Wang et al. (2020a) and Hong et al. (2020a), respectively [96,143]. Once the crack width reaches a certain threshold, corrosion products can leak through the open crack without causing further internal pressure, limiting the number of cracks and resulting in more severe pitting corrosion of the reinforcement surface near the open crack [90,119].

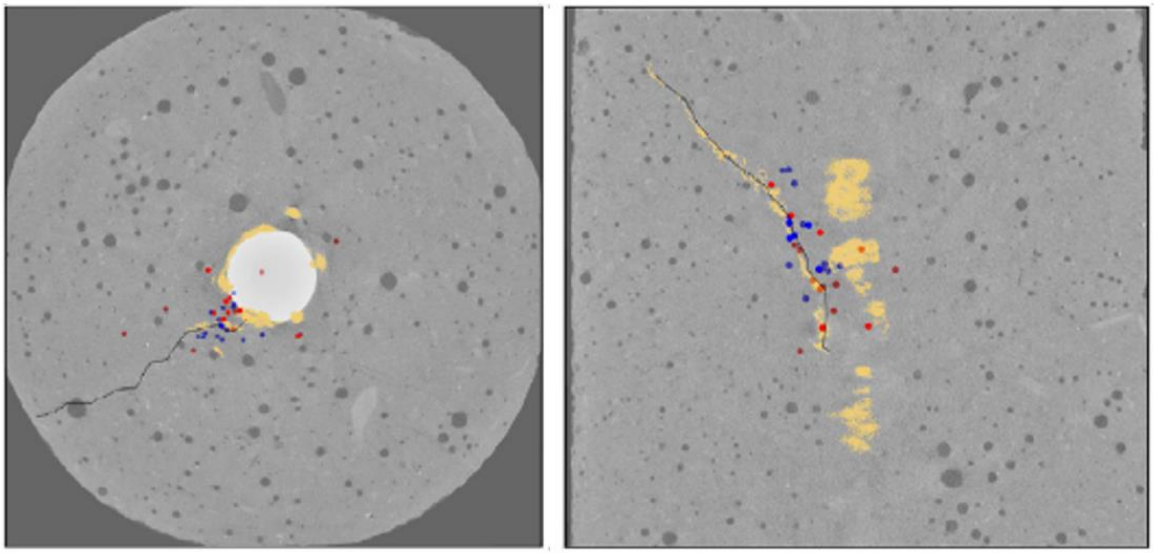

(A) (B)

Figure 2.6. CT Images of Corrosion-Induced Crack of a Mortar Specimen of a 36 mm Diameter Reinforced with a 6 mm Steel Reinforcement: (A) Top View, and (B) Side View. Reproduced from Van Steen et al. [100] with Permission from Elsevier.

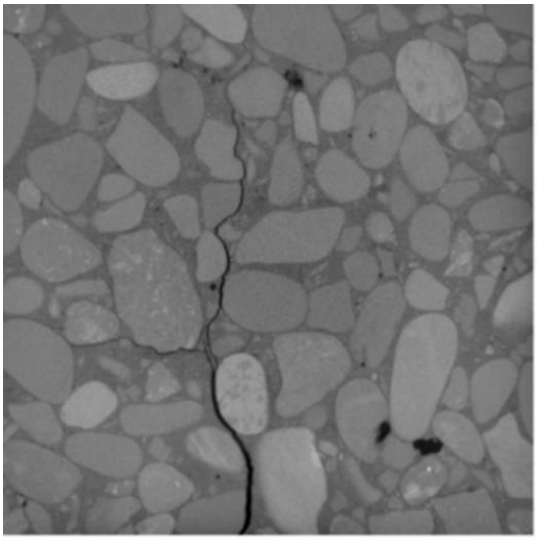

Figure 2.7. CT Image of Preferred Path of Concrete Cracking due to Corrosion of a 12 mm Rebar. Reproduced from Wang et al. [144] with Permission from Elsevier.

2.3.4. Mass Loss

Accurate measurement of steel mass loss is a good indication of the severity of reinforcement deterioration and the induced corrosion level. To examine the accuracy of mass loss measurements collected through CT imaging, researchers compared imaging-based data to experimental and analytical results attained using gravimetric testing and Faraday's law, respectively. Dong et al. (2017) measured the mass loss of a 2 mm steel rebar embedded in a 10 mm cement cylinder using CT imaging and observed generally a good agreement between the recorded data and the results obtained through gravimetric testing and Faraday's law [92]. Although no consistent trend between the results of CT imaging and Faraday's law was noted, gravimetric testing seemed to yield the least mass loss in all tests. On the contrary, Hong et al. (2020d), after measuring the mass loss of a 3 mm steel reinforcement placed within 10 mm mortar, indicated that gravimetric testing produced higher mass loss results compared to those obtained using CT imaging, as shown in Figure 2.8 [94]. Unlike CT imaging and gravimetric testing, Faraday's law with the actual valency of 2 could not accurately estimate the pre-cracking mass loss due to the reduced current efficiency,

which is the percentage of the impressed current contributing to the corrosion reaction. However, the experimental mass loss measurements seemed to approach the theoretical ones as the current efficiency increased due to mortar cracking, as illustrated in Figure 2.8. High accuracy of CT measurement of reinforcement mass loss was also reported by Zhang et al. (2019) and Hong et al. (2020c), both tested 10 mm mortar specimens [44,56].

It is worth mentioning that the accuracy of CT measurements is significantly impacted by the resolution of the collected images, as observed by measuring the mass loss of larger samples of a 6 mm rebar embedded in a 36 mm concrete cylinder [100]. Van Steen et al. (2019) noted that CT imaging substantially underestimated the steel mass loss, possibly due to the resolution (18 µm) of CT images in addition to segmentation error. The aforementioned findings proved that CT imaging could accurately measure steel reinforcement's mass loss, provided that high-resolution CT images are captured.

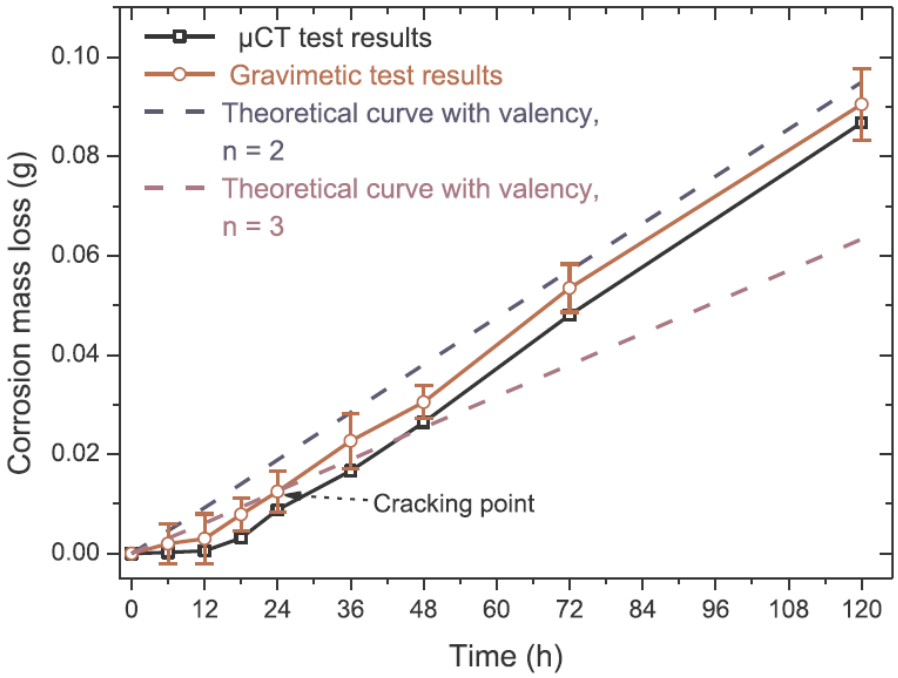

Figure 2.8. Reinforcement Mass Loss Data Attained Using CT Imaging, Gravimetric Test, and Faraday's Law. Reproduced from Hong et al. [94] with Permission from Elsevier.

2.3.5. Effect of Impressed Current Densities

The effect of induced current density on the corrosion and cracking mechanisms is important for accurate corrosion analysis, in addition to selecting a suitable range of current density. Hong et al. (2020b) applied current densities of 20, 75, 150, 300, and 600 $\mu A/cm^2$ to a 3 mm steel rebar embedded within a 10 mm cylindrical mortar specimen [98]. After analyzing the collected CT images, it was observed that decreasing the current density from 600 $\mu A/cm^2$ to 20 $\mu A/cm^2$ extended the exposure time prior to cracking by 30 times. Also, using lower impressed current density produced rust with higher diffusivity and resulted in more mass loss of the steel reinforcement, which was attributed to the longer exposure time before mortar cracking. On the other hand, applying higher current density caused earlier and wider mortar cracks despite creating only minor and uniform rust distributed mainly around the reinforcement interface, as illustrated in Figure 2.9, which is not a good representation of natural corrosion. In other studies, it was demonstrated that applying a current density of 600 $\mu A/cm^2$ produced a uniform mass loss of reinforcement; on the contrary, using a current density of 20 $\mu A/cm^2$ resulted in localized pitting corrosion, as shown in Figure 2.10 [56]. It was also reported that applying a current density of 305 $\mu A/cm^2$ instead of 500 $\mu A/cm^2$ extended the exposure time prior to failure from 72 hours to more than 120 hours, which increased the corrosion products [94].

Sun et al. (2017) studied the effect of the impressed current by applying two current densities of 4 and 42 $\mu A/mm^2$ to a 3 mm steel rebar placed into a 10 mm cement cylinder for 24 hours [93]. It was reported that inducing a low impressed current caused pitting corrosion despite the low corrosion level of only 2%. On the other hand, a higher current density produced a more severe corrosion level of 18%; however, the corrosion distribution was more homogenous. Nevertheless, it was observed that all specimens experienced localized corrosion, which did not match the

reported findings of Hong et al. (2020b, c, d). This disagreement is attributed to the eccentricity of steel reinforcement and the nonuniform distribution of voids within the cement specimens. These factors can cause pitting corrosion, as explained in the following sections. Further research is needed to better understand the effect of the applied impressed density on the corrosion and cracking mechanisms of structural elements.

Since the reported studies focused mainly on the corrosion of smooth rebars and the cracking mechanisms of cement and mortar specimens, investigating the effect of induced current on concrete specimens with aggregates is a potential area of research. Also, the effect of rebar ribs on the corrosion distribution under different levels of induced current can be investigated to provide more realistic representations of the corrosion process and cracking mechanisms of reinforced concrete structures.

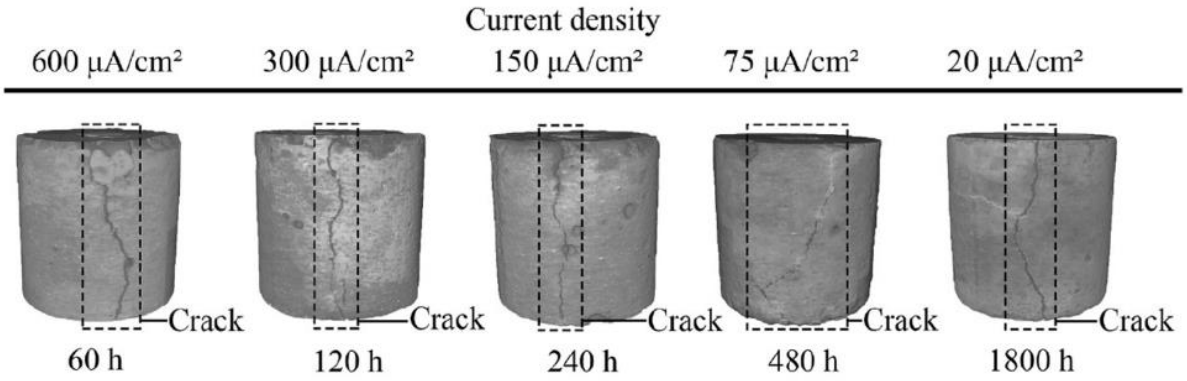

Figure 2.9. Corrosion-Induced Mortar Cracking with Reinforcement Exposed to Different Levels of Impressed Current Density. Reproduced from Hong et al. [98] with Permission from Elsevier.

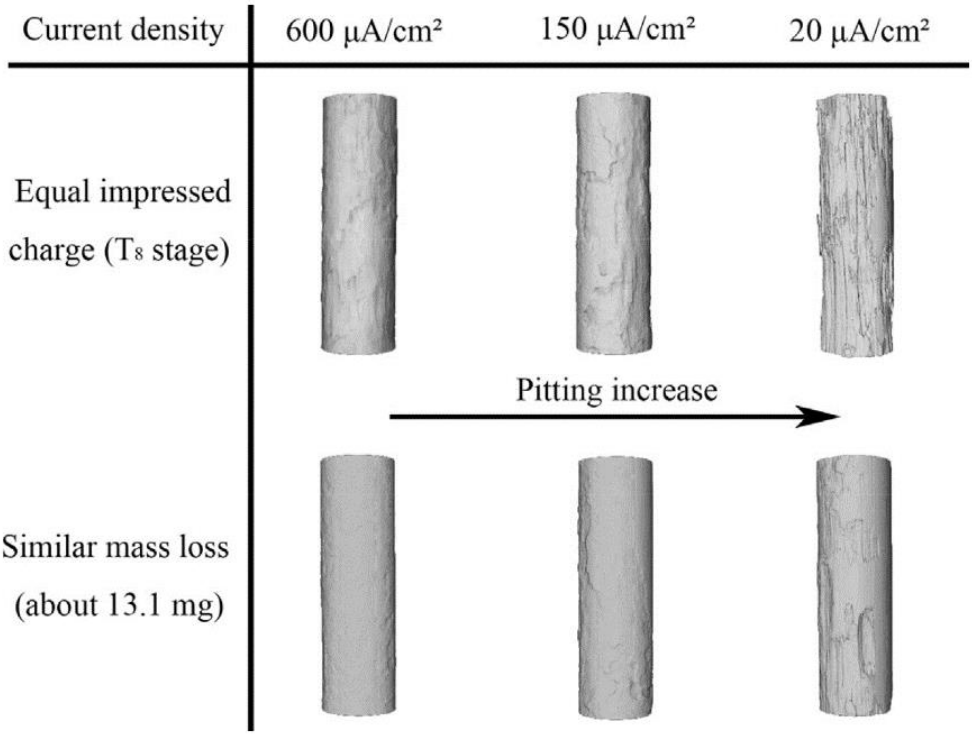

Figure 2.10. Corroded Steel Reinforcement after Exposure to Current Densities of 0.2, 1.5, and 6 $\mu A/mm^2$. Reproduced from Hong et al. [56] with Permission from Elsevier.

2.3.6. Effect of Steel Reinforcement Material

Investigating the effect of steel reinforcement material on the corrosion and cracking mechanisms is critical for anticipating the severity of the resulted concrete damage and identifying the appropriate types of steel reinforcement. Shi et al. (2018) used CT imaging to examine the corrosion behavior of low-alloy and low-carbon steel rebars with a diameter of 10 mm embedded within 50 x 50 mm^2 concrete cover after applying an impressed current density of 3.2 $\mu A/mm^2$ for 10 days [103]. It was reported that corroding the low-alloy steel reinforcement produced compact rust that concentrated mostly around the rebar, as shown in the enlarged rebar images in Figure 2.11 (A). However, the induced corrosion of low-carbon

steel rebar created loose corrosion products with more rust diffusion, as illustrated in Figure 2.11 (B).

Likewise, Itty et al. (2014) used CT imaging to study the corrosion mechanisms of carbon steel and stainless steel wires with a diameter of 0.5 mm inserted into a 5 mm cement cylinder after inducing an impressed current density of 50 $\mu A/mm^2$ for about 3 hours [90]. It was observed that although corrosion initiation was relatively fast in the carbon steel reinforcement due to its inferior corrosion resistance, the corrosion was uniform throughout the process, attributed to its even corrosion resistance across its surface. In contrast, the high corrosion resistance of stainless-steel reinforcement experienced a slow corrosion process; however, once corroded, the stainless steel suffered from localized pitting corrosion that resulted in deeper pits with as much as twice the depth of the deepest pit within carbon steel reinforcement. It was also observed that the homogenous corrosion of carbon steel reinforcement produced uniform internal expansive stress, which produced narrow cracks, as shown in Figure 2.12 (A). On the contrary, the localized corrosion of stainless steel reinforcement caused stress concentration within the cement cover resulting in wider and more severe cracking, as illustrated in Figure 2.12 (B).

While the presented studies examined the corrosion and cracking mechanisms using different grades of steel reinforcement, the effect of the different steel galvanization and coating methods on the corrosion distribution and the resulted concrete cracking can be investigated. This can provide more insight into the reinforcement corrosion for different structural applications using various steel galvanization and coating techniques.

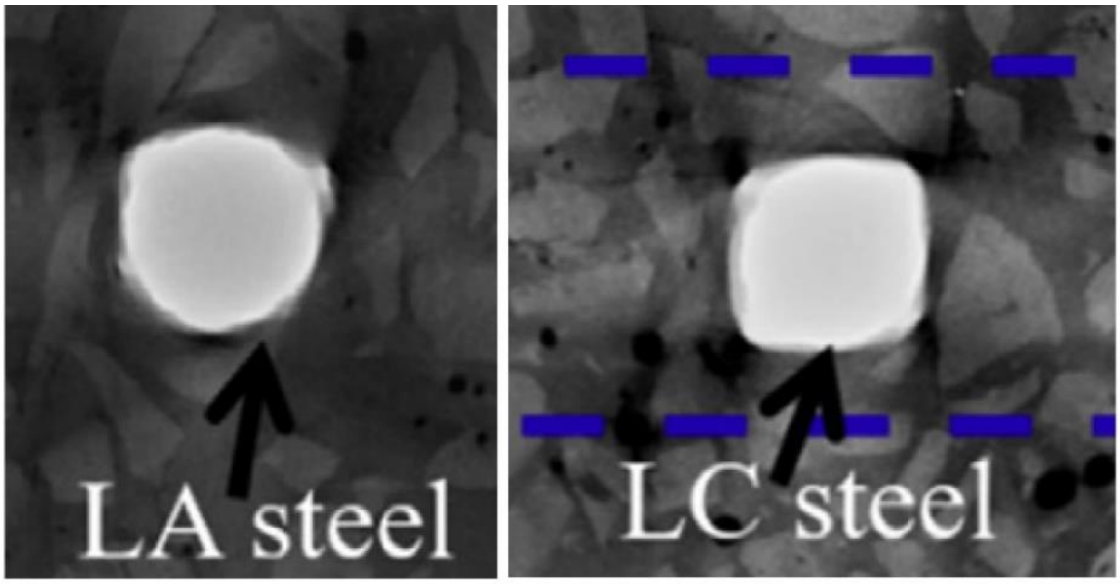

(A) (B)

Figure 2.11. Enlarged Images of Corroded (A) Low Alloy Steel, and (B) Low Carbon Steel Reinforcements with a Diameter of 10 mm. Reproduced from Shi et al. [103] with Permission from Elsevier.

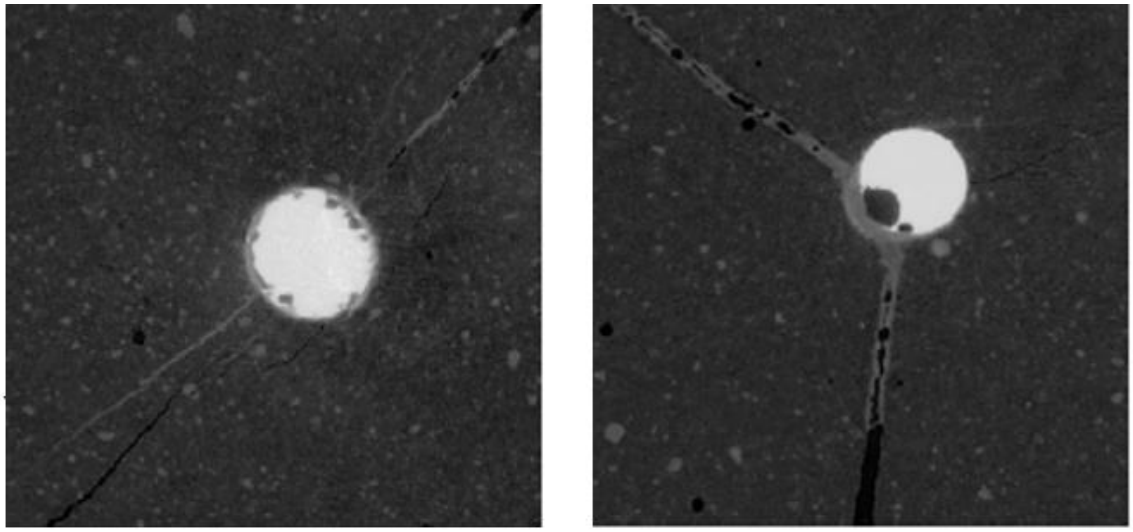

(A) (B)

Figure 2.12. Corrosion-Induced Crack of Mortar (5 mm in Diameter) with embedded (A) Carbon Steel, and (B) Stainless Steel Reinforcements with a Diameter of 0.5 mm. Reproduced from Itty et al. [90] with Permission from Elsevier.

2.3.7. Effect of Voids

Understanding the effect of defects, such as voids, on the corrosion and cracking processes is crucial for assessing the rigorousness of the concrete damage and prioritizing the required repairs accordingly. This can be facilitated using CT imaging to examine the corrosion and cracking mechanisms of structural specimens with defects at different locations, namely: the reinforcement interface, the midsection of the cover material, and the outer surface of the samples. Rossi et al. (2020) induced natural corrosion in 8 mm steel rebars embedded within 20 mm concrete cylinders and examined the effect of the interfacial defect on reinforcement corrosion [40]. It was reported that voids generally accelerated the corrosion of the nearby reinforcement surface. Therefore, uniform interfacial defects resulted in producing homogenous corrosion, as illustrated in Figure 2.13 (A). In contrast, exposure to dispersed voids caused localized pitting corrosion, as shown in Figure 2.13 (B). Once the closed interfacial defects were filled with corrosion products, further production of rust increased the internal tensile stress resulting in concrete cracking, as demonstrated in Figure 2.13 (C). Comparable findings were also reported by Shi and Ming (2017) and Bernachy-Barbe et al. (2020) [101,102].

Similarly, Zhang et al. (2019) employed CT imaging to study the effect of defects located at the reinforcement interface, midsection, and external element surface after applying a current density of 53.08 $\mu A/mm^2$ to a 2 mm steel reinforcement surrounded by a 10 mm cylindrical mortar cover [44]. It was noted that while the interfacial defects caused severe and localized corrosion, the midsection and outer surface defects did not disturb the uniformity of reinforcement corrosion, as illustrated in Figure 2.14. Also, the midsection and outer surface defects produced mild reinforcement corrosion, unlike the interfacial defects. Nevertheless, the midsection and outer surface defects caused denser and more severe mortar cracking at later

corrosion stages attributed to the resulted stress concentration and reduced confinement, as shown in Figure 2.14. In other words, steel reinforcement is more vulnerable to pitting corrosion upon exposure to interfacial defects; on the other hand, reinforced structures with outer surface defects are more likely to experience substantial corrosion-induced cracking. Hence, the findings of these studies suggest that it is imperative to repair surface defects to reduce stress concentration, inhibit concrete cracking, and slow down the corrosion rate by limiting the permeability.

The research articles studied the effect of void location on corrosion distribution and concrete cracking; however, more research is needed to investigate the effects of more void characteristics, including void content, distribution, size, and geometry. Investigating these parameters can present a more comprehensive understanding of the effect of concrete voids on the resulted corrosion distribution and cracks.

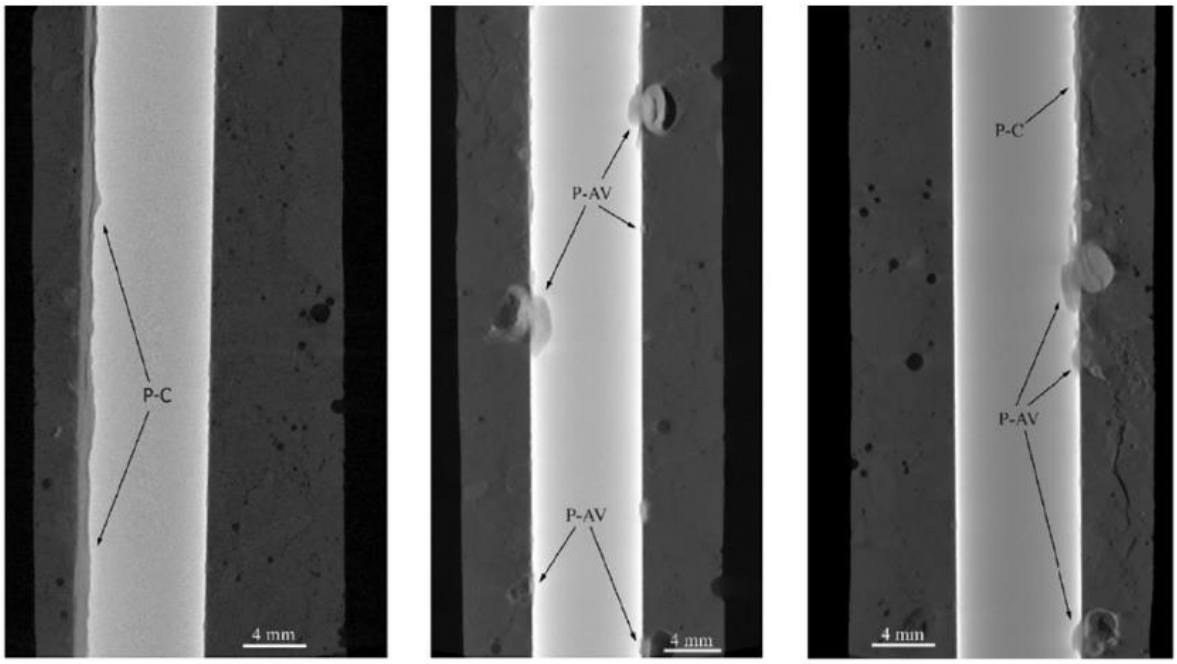

(A) (B) (C)

Figure 2.13. Corrosion of Steel Reinforcement Exposed to Different Interfacial Defects. Reproduced from Rossi et al. [40] with Permission from Elsevier.

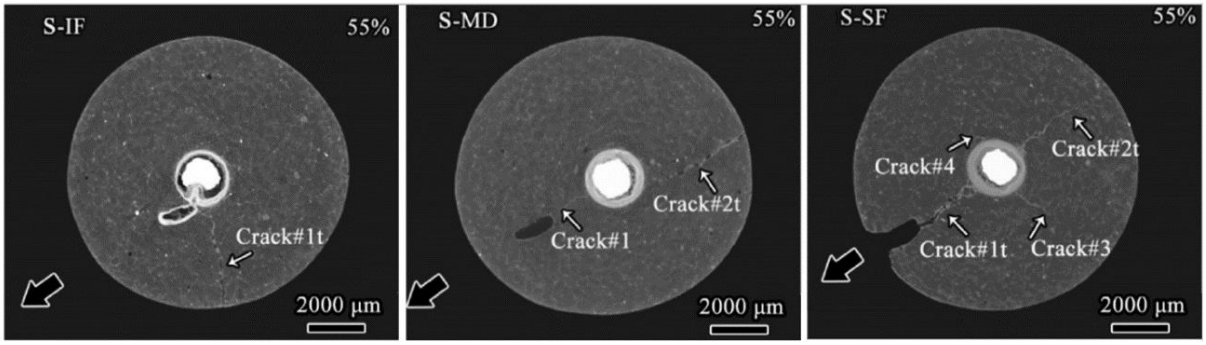

(A) (B) (C)

Figure 2.14. Corrosion Distribution and Cracking of Mortar with (A) Interfacial, (B) Midsection, and (C) External Surface Defects. Reproduced from Zhang et al. [44] with Permission from Elsevier.

2.3.8. Effect of Confinement

The corrosion behavior can significantly differ between the reinforcing steel rebars of a single concrete structure accredited to various underlying causes, including concrete confinement. Applying higher concrete confinement (e.g., concrete cover thickness) can limit cracking and slow down the carbonation and corrosion processes. Thus, a better understanding of the effect of concrete confinement is important for anticipating the corrosion damage in different segments of concrete structures and determining the appropriate reinforcement distribution through which optimal performance is achieved. Zhou et al. (2019) used CT imaging to examine the effect of confinement after applying an impressed current density of 49 $\mu A/mm^2$ to a 6.5 mm steel rebar inserted into a 10 mm concrete cover [119]. The external confinement was provided by surrounding the concrete specimens with layers of fiber-reinforced polymer (FRP) laminates. It was noted that increasing the confinement substantially reduced the number of corrosion-induced cracks by 60%. As a result, applying higher confinement minimized the severity of reinforcement corrosion attributed to the reduced access of salt water through the limited cracks. Also, applying higher confinement constrained the diffusion of rust into the concrete element leading to a more uniform mass loss of steel reinforcement, as shown in Figure 2.15.

On the other hand, Xi and Yang (2019) utilized CT imaging to study the confinement effect by placing the steel reinforcement near the corner of a concrete specimen [99]. While two sides of the 2.94 mm rebar were surrounded by a 4 mm thick concrete cover, the other two sides of the rebar were protected by a concrete cover with a thickness of 13 mm. The specimen was exposed to a cyclic wet-dry corrosion process with 4 hours of wetting and 20 hours of dehydration under a temperature of 48 ^{o}C. It was observed that the well-confined and protected portion of the steel rebar experienced only minor and uniform corrosion, which matched the findings of Zhou et al. (2019). On the contrary, the reinforcement portion under low confinement suffered from harsh and concentrated pitting corrosion. This localized corrosion induced stress concentration within the nearby low-thickness concrete cover and resulted in substantial longitudinal and lateral cracking, as demonstrated in Figure 2.16. Based on the aforementioned observations, increasing the thickness of structural materials or applying higher external confinement can generally limit the number and severity of produced cracks resulting in more controlled and uniform reinforcement corrosion.

The reported articles illustrated that applying higher concrete confinement can minimize corrosion damage. Therefore, finding the appropriate confinement level is a promising area of research. Also, investigating the effect of localized confinement defects (e.g., damaged FRP confinement) on the distribution and severity of reinforcement corrosion can be a good contributing factor to understanding concrete reinforcement corrosion. Thus, further testing can provide a better insight into the confinement effect on the corrosion and cracking mechanisms.

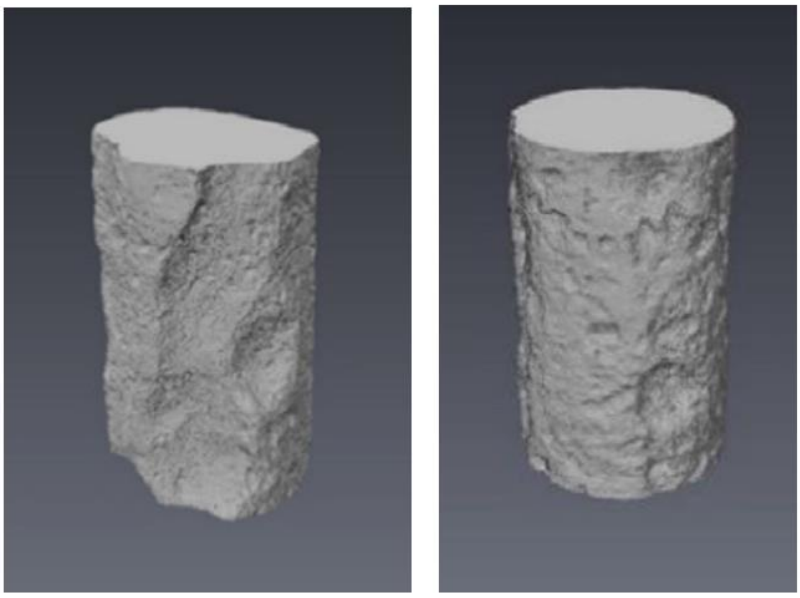

(A) (B)

Figure 2.15. Corroded Steel Reinforcement (A) without FRP Confinement, and (B) with FRP Confinement. Reproduced from Zhou et al. [119] with Permission from Elsevier.

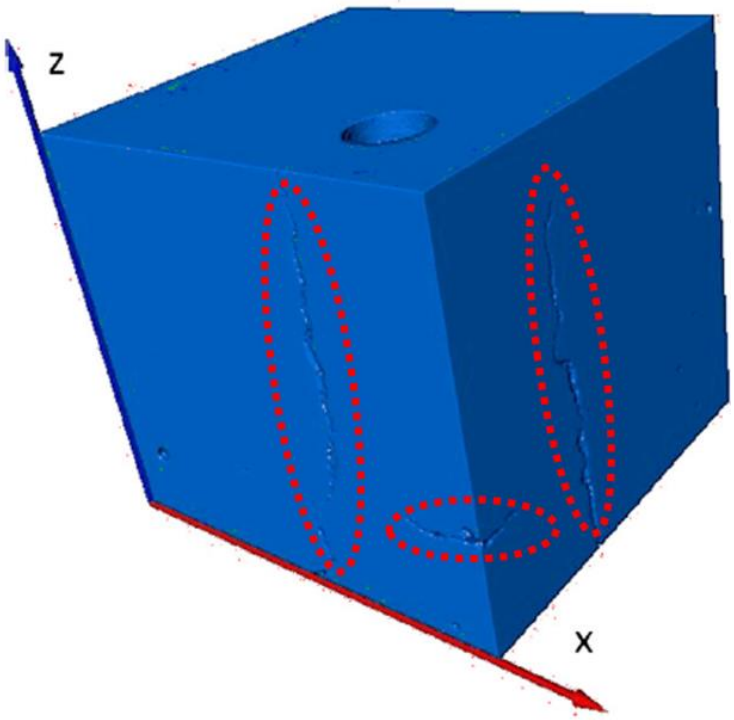

Figure 2.16. Longitudinal and Lateral Corrosion-Induced Cracks within Mortar Cover of Eccentric Reinforcement. Reproduced from Xi and Yang [99] with Permission from Elsevier.

2.4. CT Imaging of Freeze-Thaw Damage

2.4.1. Test Methodologies

The severity of frost damage is affected by various parameters: concrete's pore properties and strength, number and duration of freeze-thaw cycles, frost and defrost temperatures, degree of saturation, and composition of the freezing solution. While decreasing the frost temperature can accelerate the expansion of freezing water, elevating the defrost temperature can induce high thermal stress and inflict concrete cracking [127–129]. Likewise, increasing the number and duration of frost cycles and the saturation level can amplify concrete damage [146–149]. The freeze-thaw conditions reported in the literature are summarized in Table 2.3. Most specimens were made of concrete with a thickness of 5–100 mm. The applied freezing temperature ranged from -165 ^{o}C to -37 ^{o}C, while the defrost temperature was 2–25 ^{o}C. The average number and duration of the applied freeze-thaw cycles are 75 (±84) cycles and 15 (±18) hours.

Table 2.3. Freeze-Thaw Conditions Applied in the Literature

Material and Thickness (mm)	Mix Ratios (C:W:S:A)	Freeze/Thaw Temperature (^{o}C)	Freeze-Thaw Period (hours)	Cycles	Ref.
Cement | 5	1:0.5:0:0	-20/20	6	48	[104]
Mortar | 10	1:0.42:2.33:0	-35/23	43.5	1	[29]
Mortar | 15	1:0.54:3.48:0	-20/20	8	25	[38]
Cement | 16	1:0.42:0:0	-15/16.5	4	30	[150]
Concrete | 25	1:0.42:1.07:1.29	-165/20	NA	NA	[151]
Concrete | 25.4	1:0.42: NA: NA	-37/25	55	NA	[59]
Concrete | 50	1:0.5:1.63:3.03	-18/5	NA	75	[58]
Concrete | 50	1:0.35:1.89:2.83	-18/2	16–18	56	[152]
Concrete | 75	1:0.5:1.73:2.95	-17/8	5	36	[153]
Concrete | 76.2	1:0.16:1.94:3.92	-18/4	4	300	[150]
Concrete | 100	1:0.4:1.83:3.26	-18/5	2–4	100	[114]
Concrete | 100	1:0.5:1:77:3.59	-18/4	3	NA	[53]

* C: Cement, W: Water, S: Sand, A: Aggregates

2.4.2. Damage Propagation

Upon exposure to freezing environments, water retained within concrete freezes and expands, producing expansive internal pressure. Also, the fluctuation between the frost and defrost temperatures can contribute to concrete degradation by producing thermal stress within the interfacial transition zone (ITZ) between the mortar and aggregates, attributed to the mismatching thermal expansion coefficients [26,27,76]. The severity of frost damage is directly impacted by the pore morphology of concrete, including the size and distribution of air pores [38,114]. For example, concrete elements with smaller and more uniformly distributed voids tend to experience lower frost damage due to the fact that the freezing water can expand into the surrounding small pores with little micro-cracking [29,150]. Freeze-thaw damage can initiate when the stress induced by the freezing water exceeds the tensile strength of concrete, which is more likely to occur when the degree of saturation surpasses its critical threshold of 50–90% [29–34]. Hence, concrete structures with lower tensile strength and higher saturation degrees are more susceptible to freeze-thaw degradation [152]. It is worth noting that the critical degree of saturation can vary significantly depending on the concrete's composition, tensile strength, and pore morphology, in addition to the applied freeze-thaw conditions.

The frost damage propagates on a layer-by-layer basis, as shown in Figure 2.17, starting from the exterior surface, due to its direct exposure to the freezing water [58,153,154]. Thus, concrete scaling can occur as surface cracks grow and connect [59,61,72]. Also, cracks tend to appear within the aggregate-mortar interface, as illustrated in Figure 2.17 (F), ascribed to its low bonding strength and rough surface, which can lead to stress concentration [29,57,58]. Moreover, the frost damage rate can accelerate over time since surface cracks increase water ingress and deteriorate the concrete cover, causing exponential growth of mass loss as shown in Figure 2.18 [154].

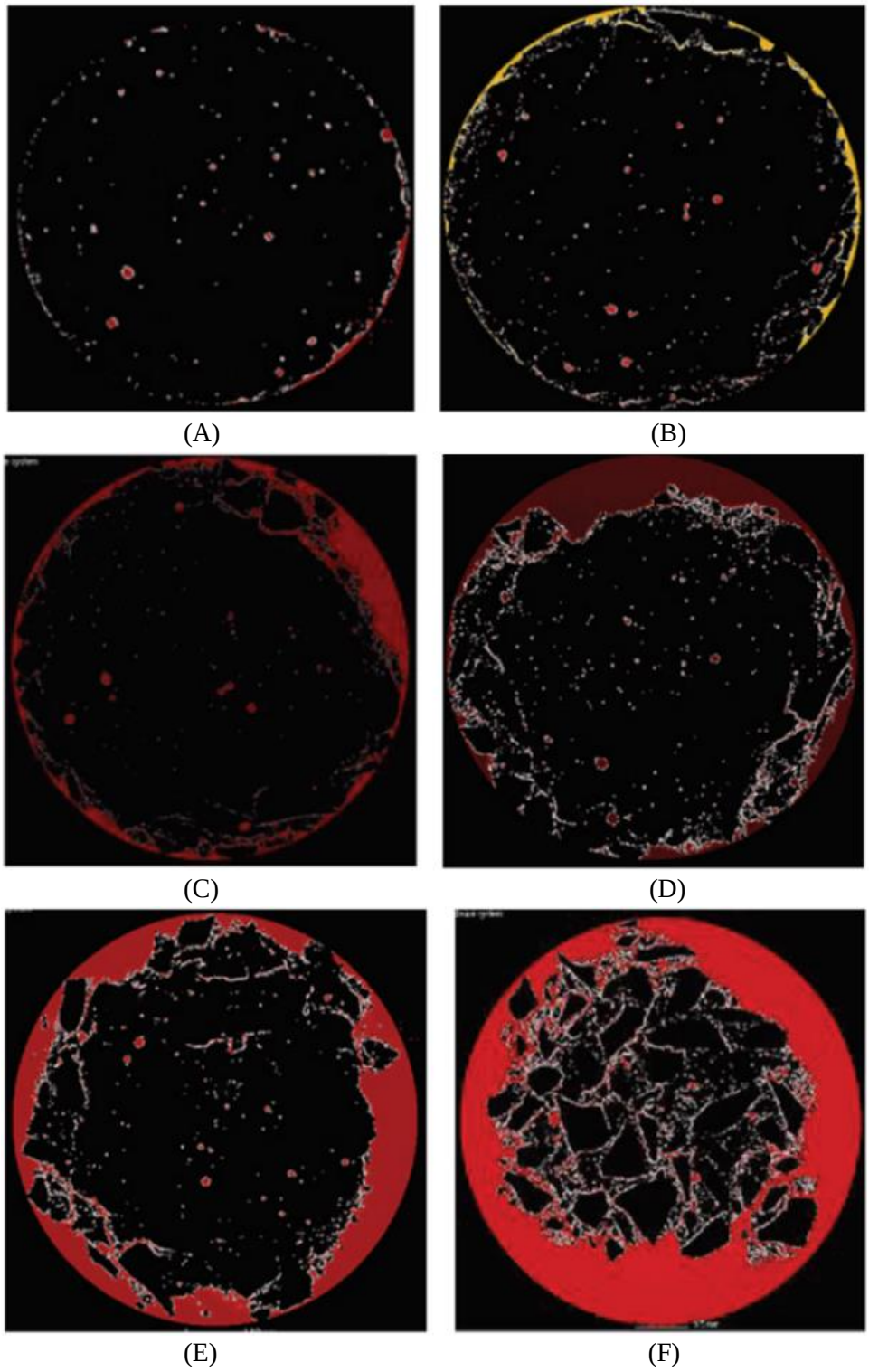

Figure 2.17. Progression of Damage of a Concrete Element with a Diameter of 75 mm Induced by (A) 0, (B) 12, (C) 18, (D) 24, (E) 30, and (F) 36 Freeze-Thaw Cycles. Reproduced from Jie Yuan et al. [153] with Permission from Hindawi

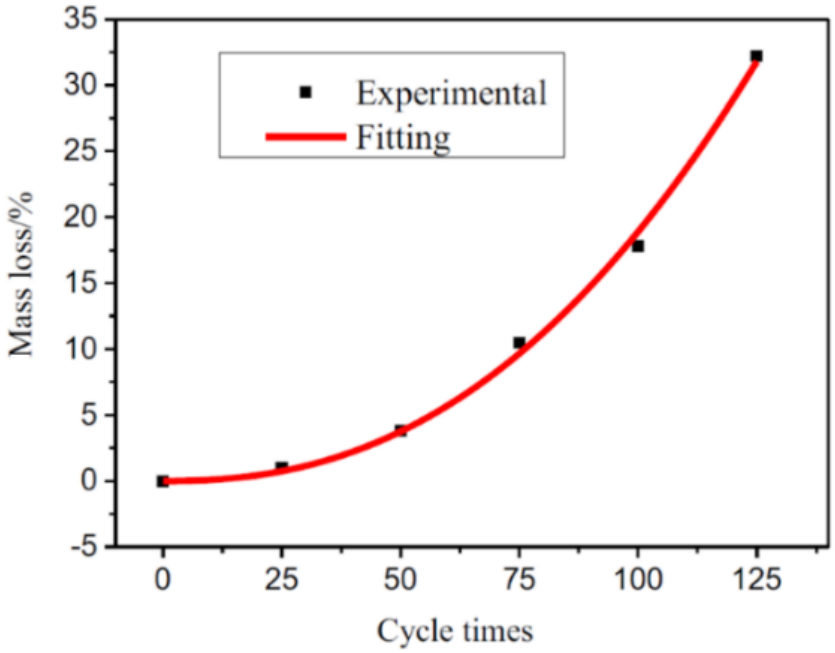

Figure 2.18. Mass Loss Resulted from Exposure to Freeze-Thaw Cycles. Reproduced from Li et al. [154] with Permission from Elsevier.

2.4.3. Effect of Mixture Proportions

The water/cement (W/C) and sand/cement (S/C) ratios have a diverse effect on concrete's mechanical properties and freeze-thaw resistance. Through destructive experimental testing, it was reported that increasing the W/C ratio can degrade the compressive, tensile, and flexural strengths of concrete [155–157]. Also, a higher W/C ratio can increase the concrete's permeability, resulting in a degraded resistance to freeze-thaw damage [158]. On the contrary, increasing the S/C ratio can enhance the compressive, tensile, and flexural strengths of concrete [159], but it deteriorates the freeze-thaw resistance of concrete by increasing its permeability [38].

To investigate the effect of the W/C ratio on the freeze-thaw resistance of 5 mm thick cement elements, Wei et al. (2020) utilized CT imaging to monitor the internal microstructural damage [104]. The specimens were prepared using W/C ratios of 0.3 and 0.5, respectively, and cured at a constant temperature of 23 °C and relative humidity of 50% for a week. The samples were

subjected to 48 air freeze-thaw cycles, six hours each, at temperatures of -20 ^{o}C and 20 ^{o}C. After applying the freeze-thaw cycles, the specimens were cured for additional 21 days before CT imaging. It was observed from the CT data that increasing the W/C ratio from 0.3 to 0.5 doubled the porosity from 9% to 18%. Also, subjecting the cement specimen with a W/C ratio of 0.5 increased its porosity to 27%, whereas the other sample maintained its porosity throughout the applied cycles. In other words, increasing the W/C ratio produced more porous cement elements with lower resistance to freeze-thaw damage.

Despite the substantial impact of W/C and S/C ratios on concrete's freeze-thaw resistance, limited research employed micro-computed tomography to investigate the effects of concrete mixture proportions on its microscale pore characteristics, such as pore size, shape, and distribution, and freeze-thaw damage mechanisms. Therefore, further investigation is needed to better understand the microscale effects of W/C and S/C ratios on concrete's pore morphology and frost damage mechanisms.

2.4.4. Effect of Sulfate Salts

Exposure to sulfate environments has diverse effects on concrete's freeze-thaw resistance [160–162], which are dependent on the type and concentration of the sulfate solution [163–165]. For example, Jiang et al. (2015) and Li et al. (2018) observed that exposure to 5% sodium sulfate solution improved the freeze-thaw resistance of concrete specimens and minimized mass loss, whereas subjecting the concrete to 5% magnesium sulfate solution accelerated the concrete damage [164,165]. On the contrary, Zhao (2020) noted that exposure to 10% magnesium sulfate solution enhanced concrete's freeze-thaw resistance, while exposure to 10% sodium sulfate solution accelerated the frost damage [163].

Liu et al. (2018) utilized CT imaging to investigate the microstructural effect of exposure to a 5% sodium sulfate solution on the freeze-thaw resistance of concrete specimens [57]. The specimens, which were 210 mm in height, and 70.7 mm in width and thickness, were CT scanned before and after being subjected to 450 freeze-thaw cycles. It was observed that applying the freeze-thaw cycles reduced the percentage of small pores (0.01–0.3 mm^2) from 66.5% to 61.2%, attributed to concrete expansion induced by the sodium sulfate solution. Sulfate exposure also decreased the freezing temperature and, hence, minimized the resulted damage. It is undeniable that prolonged exposure to sodium sulfate can degrade the strength of concrete. However, this weakening effect is not clear in this study due to the relatively short testing period and the fact that sulfate erosion decelerates at low temperatures. It was also noted that applying 250 freeze-thaw cycles did not cause any visible cracks; nevertheless, minor interfacial cracks were detected after applying 450 freeze-thaw cycles, as shown in Figure 2.19. Despite that many freeze-thaw cycles are applied, only limited and minor cracks are detected mainly near the exterior surface, which confirmed the improved freeze-thaw resistance of concrete under the applied sodium sulfate environment.

In spite of the importance of understanding the microscale effects of sulfate salt on the severity and mechanisms of freeze-thaw damage, little research investigated the coupled freeze-thaw and sulfate damage of concrete using micro-computed tomography. Thus, further research is needed to study the microstructural freeze-thaw damage mechanisms in distinct sulfate environments, such as magnesium sulfate and potassium sulfate.

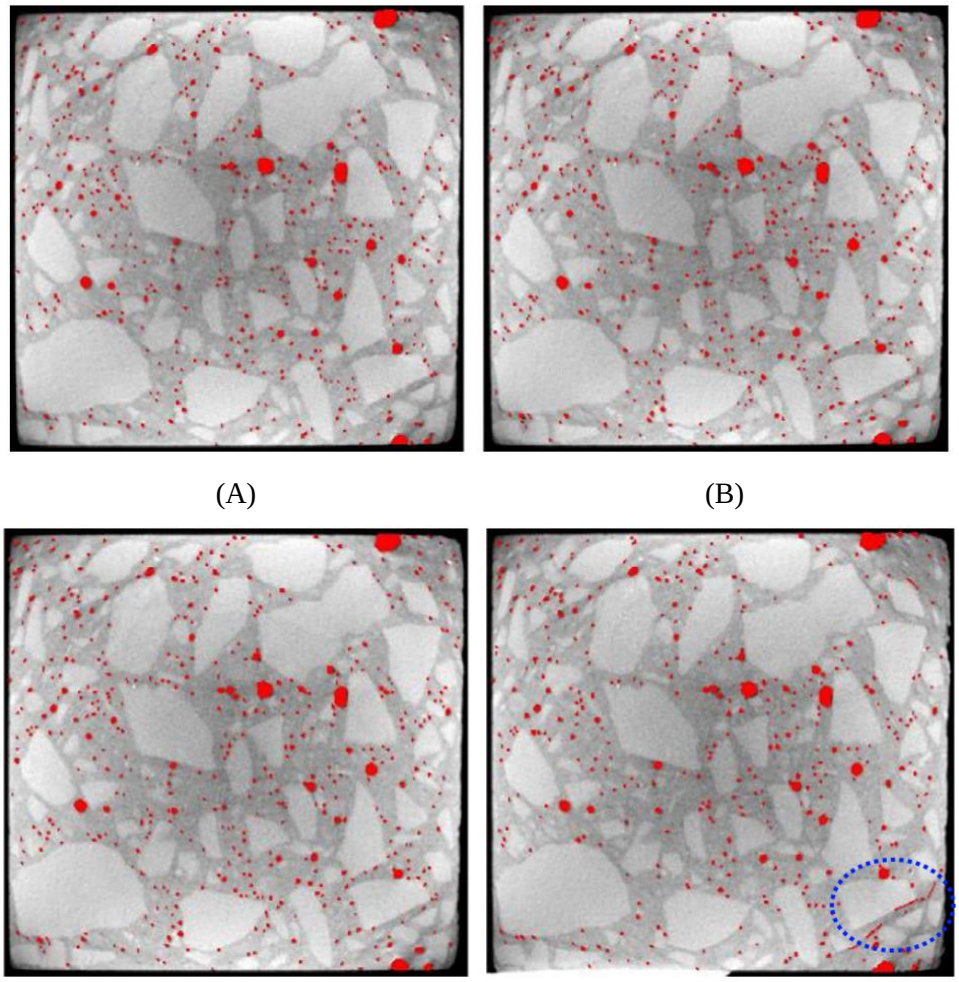

Figure 2.19. CT Imaging of Concrete Voids/Cracks of a 70.7×70.7×210 mm^3 Element after Exposure to (A) 0, (B)75, (C) 250, and (D) 450 Freeze-Thaw Cycles. Reproduced from Liu et al. [57] with Permission from Elsevier.

2.4.5. Effect of Air Entrainment

Applying air-entraining admixtures to the concrete mix can enhance its workability and the uniformity of its pore distribution [166]. Hence, the air entrainment of concrete can increase its freeze-thaw resistance by creating more pores that relieve the internal stress induced by the freezing water [42,45,167–170]. Sokhansefat et al. (2020) used CT imaging to study the effect of air-entrainment of mortar specimens on the pore microstructure and freeze-thaw resistance [29]. Air-entrained (AE) and non-air-entrained (nAE) specimens of 10 mm diameter and 10 mm height

were subjected to a single freeze-thaw cycle with a total period of 43.5 hours at temperatures of -35 ^{o}C and 23 ^{o}C. It was observed that air-entraining the mortar element substantially increased the initial porosity from about 5.5% to 10%. A calcium-rich substance formed during the freeze-thaw cycle was detected more within the nAE specimen despite having less porosity than the AE specimen, as shown in Figure 2.20. This significant difference in pore filling was attributed to the fact that the formed materials were more likely to be entrapped by the smaller voids. On the other hand, the AE specimen experienced only minor void infill despite its high porosity. Nevertheless, only one freeze-thaw cycle was applied, so the study provides little details of the freeze-thaw damage mechanisms.

Likewise, Yuan et al. (2018) employed a CT imaging system to examine air entrainment's effect on the pore properties and freeze-thaw resistance of concrete [45]. Four different amounts of the air-entrainment agent (0, 0.01%, 0.02%, 0.03%) were used for preparing specimens A-D respectively. The 40×40×160 mm concrete specimens were cured for 20 days before being subjected to 25 freeze-thaw cycles, six hours each, at temperatures of -20 ^{o}C and 15 ^{o}C. It was observed that applying higher amounts of the air-entrainment agent produced more porous concrete specimens. While the porosity of the control specimen A was 1.1%, the porosity of specimen D was 9.3%. However, applying more air-entrainment agents seems to improve the quality of concrete's pore structure by increasing the number of micro-voids. Also, applying an air-entrainment agent of 0.02% decreased the pore gap from around 470 µm to 180 µm, which can enhance the freeze-thaw resistance. As a result, the air-entrained elements experienced minor mass losses (e.g., 0.5 kg/m^2), unlike the control specimen, which suffered a mass loss of 1.4 kg/m^2.

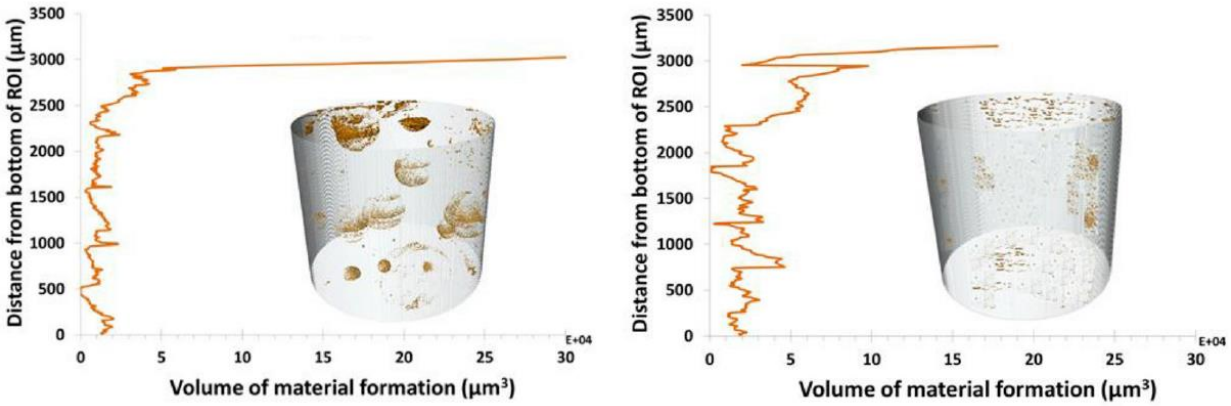

(A) (B)

Figure 2.20. Material Formation within (A) nAE, and (B) AE Mortar Specimens after Freeze-Thaw Testing. Reproduced from Sokhansefat et al. [29] with Permission from Elsevier.

2.4.6. Effect of Nano-Additives

The addition of silica (SiO_2), titania (TiO_2), and nano-kaolinite clay (NKC) nanoparticles (NPs) to the concrete mix has been reported to enhance its strength [171–176]; however, excessive usage of NPs can degrade its mechanical performance [173,175]. Liu et al. (2019) investigated the effect of silica (15 nm or 30 nm) and titania (30 nm) nanoparticles on the pore microstructure and the freeze-thaw resistance of concrete specimens, which were 50 mm in diameter and 90 mm in height [58]. The specimens were prepared using different dosages of NPs ranging from 0.2 wt.% to 2 wt.% and exposed to 75 freeze-thaw cycles at temperatures of -18 ^{o}C and 5 ^{o}C. It was observed that increasing the content of NPs beyond a certain threshold can deteriorate the freeze-thaw resistance. The optimal dosages of the 15 nm and 30 nm silica NPs and the 30 nm titania NPs were 0.6%, 0.4%, and 0.6%, respectively. In general, the silica specimens demonstrated better freeze-thaw performance than the titania specimens. It was also noted that using the 15 nm silica NPs produced the highest freeze-thaw resistance, which indicates that smaller NPs are more effective in enhancing the pore structure and the freeze-thaw resistance of concrete. Thus, while the silica

specimens with 15 nm and 30 nm NPs experienced mass losses of only 3.42% and 3.55%, the titania specimen lost 3.99% of its mass. Nevertheless, this slight difference in mass loss did not appear to affect the mechanisms of freeze-thaw damage. All the samples experienced surface peeling and interfacial cracking near the external surface, as shown in Figure 2.21.

On the other hand, Fan et al. (2015) utilized CT imaging to gain more insight into the effect of nano-kaolinite clay (NKC) on the freeze-thaw resistance of concrete specimens (NC0, NC1, NC3, and NC5) after applying NKC dosages of 0, 1, 3, and 5 wt.%, respectively [53]. The concrete specimens, which were 100 mm in width and thickness and 400 mm in height, were subjected to 125 freeze-thaw cycles (375 hours in total) at temperatures of -18 ^{o}C and 4 ^{o}C. It was noted that the control specimen (NC0) and sample NC1 suffered from early surface scaling and severe freeze-thaw cracking, indicating that the addition of 1 wt.% of nano-kaolinite clay did not considerably affect the freeze-thaw resistance. Nevertheless, it was observed that specimens NC3 and NC5 did not suffer any detectable cracks. Hence, the addition of at least 3 wt.% of nano-kaolinite clay substantially improved the freeze-thaw resistance and inhibited concrete cracking. It is worth noting that the imaging resolution (e.g., voxel size) used in this study is 100 μm^3, which is insufficient for detecting small air pores.

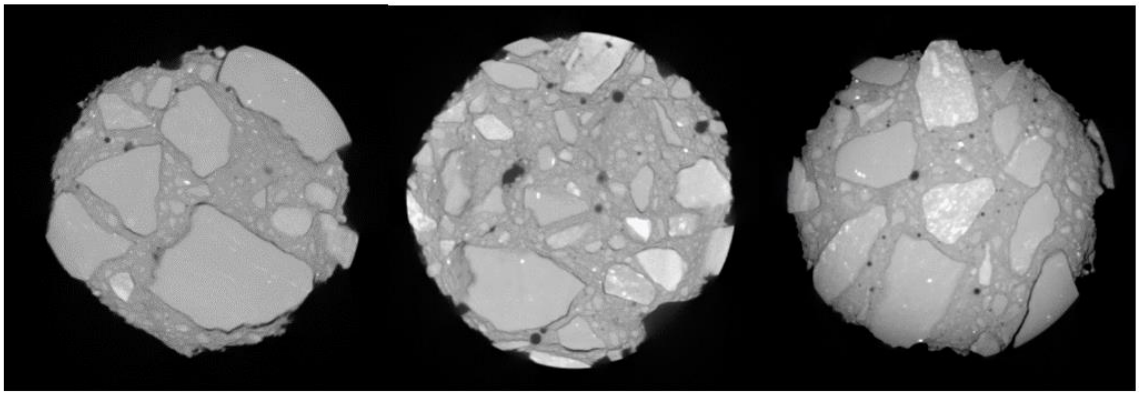

(A) (B) (C)

Figure 2.21. Post-Test CT Images of Concrete Specimens with (A) 0.6% 15 nm SiO_2 NPs, (B) 0.4% 30 nm SiO_2 NPs, and (C) 0.6% 30 nm TiO_2 NPs. Reproduced from Liu et al. [58] with Permission from MDPI.

2.4.7. Effect of Saturation Level

Increasing the degree of saturation is reported to intensify the severity of freeze-thaw damage [29–31,59]. Sokhansefat et al. (2020) used CT imaging to investigate the microstructural frost damage within concrete specimens, which are 10 mm in diameter and height, after applying a single freeze-thaw cycle at temperatures of -35 ^{o}C and 23 ^{o}C (43.5 hours) under different saturation levels of 93% and 100% [29]. The 93% saturation level is attained by dehydrating a fully saturated specimen for a specific period before sealing and freeze-thaw testing. It was observed that concrete subjected to freeze-thaw cycles under a saturation level of 93% experienced pore filling with calcium-rich products. On the other hand, the fully saturated concrete element experienced pore expansion and cracking, as shown in Figure 2.22. This demonstrates that increasing the degree of water saturation can amplify the freeze-thaw damage. It is imperative to note that the concrete specimens tested in this study are composed of low-quality aggregates with pre-existing cracks. Thus, it was observed that the fully saturated concrete specimen suffered major aggregate cracking, as illustrated in Figure 2.22.

Similarly, Shields et al. (2018) employed CT imaging to study the effect of the degree of saturation on the freeze-thaw damage within concrete specimens, which are 10 mm in diameter and 20 mm in height [59]. A single 55-hour freeze-thaw cycle is applied at temperatures of about -35 ^{o}C and 25 ^{o}C under various saturation levels of 75, 90, 95, and 100%. It was observed that increasing the saturation level generally resulted in more severe cracking, as illustrated in Figure 2.23. Thus, while the 75% saturation specimen experienced only minor interfacial cracks, the 95% saturation sample suffered both interfacial and aggregate cracking. Increasing the saturation level to 100% caused more severe cracking throughout the specimen, as shown in Figure 2.23 (D). By normalizing the correlation between the crack volume ratio and the water saturation level, it was determined that the critical saturation level, which if exceeded noticeable cracking can occur, is 86.7%. However, this critical degree of saturation depends on different parameters, including the specimen's composition, tensile strength, pore morphology, and freeze-thaw conditions; hence, further research is needed.

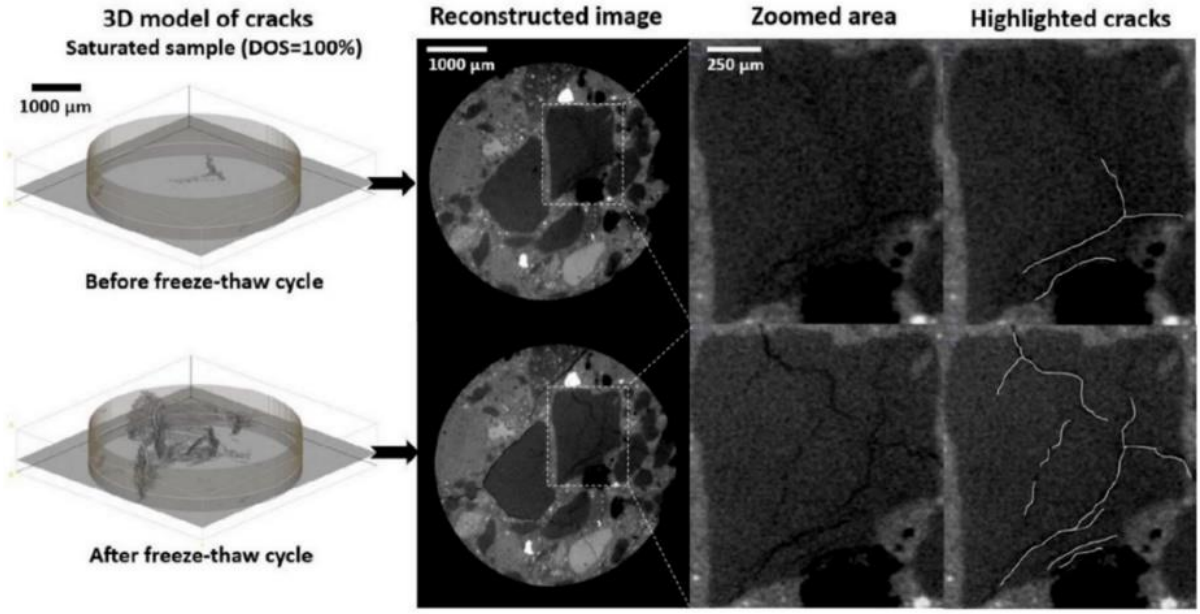

Figure 2.22. Freeze-Thaw Damage within Mortar Specimen under 100% Water Saturation. Reproduced from Sokhansefat et al. [29] with Permission from Elsevier.

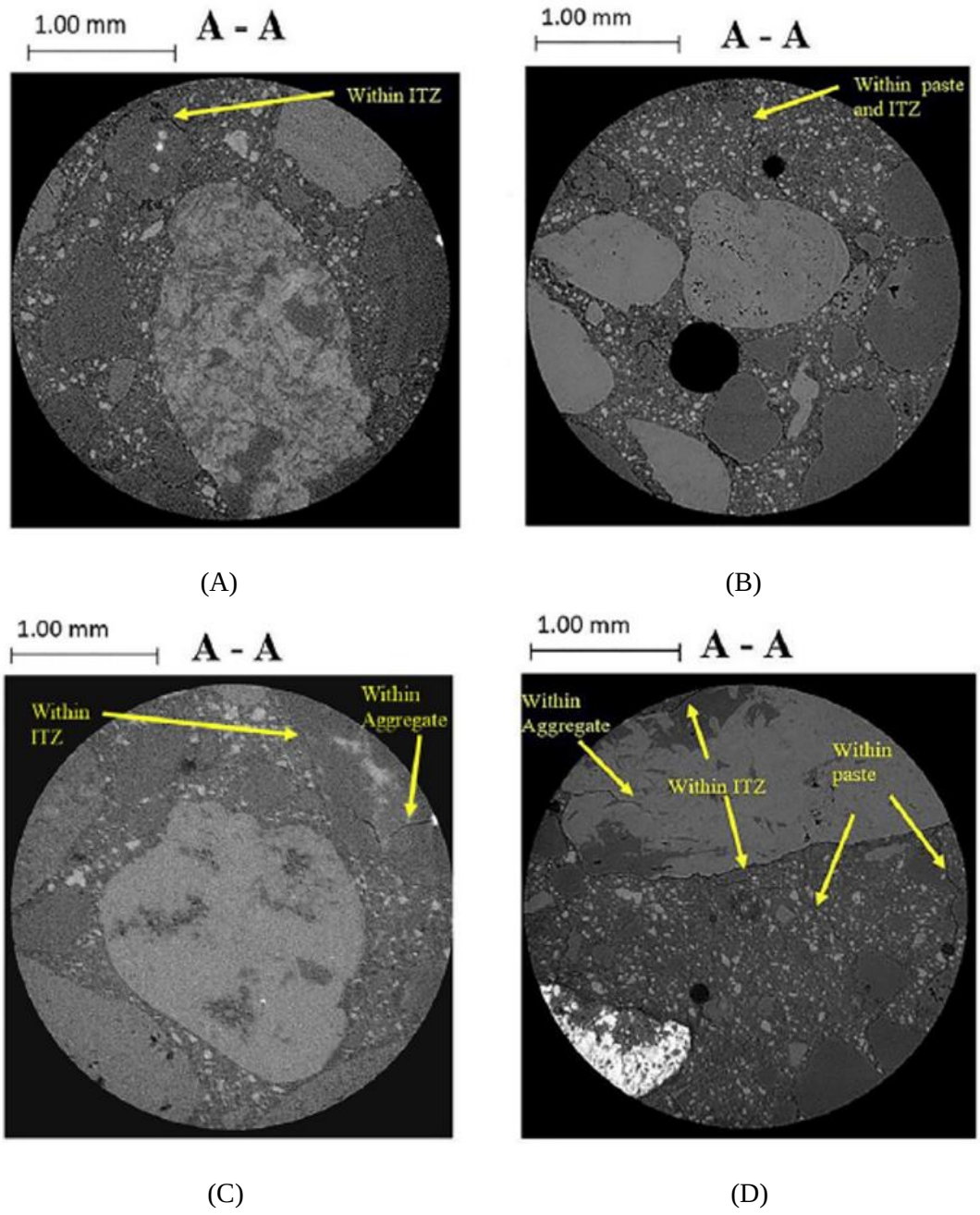

Figure 2.23. Freeze-Thaw Damage within Concrete Specimens of (A) 75%, (B) 90%, (C) 95%, and (D) 100% Saturation levels. Reproduced from Shields et al. [59] with Permission from Elsevier.

2.5. Conclusions and Research Gaps

This chapter reviewed the processes of CT imaging, corrosion progression, and freeze-thaw testing presented in the literature and discussed the reported findings, based on which the following conclusions are made:

- CT imaging is a good tool for detecting and tracking corrosion and freeze-thaw damage in a non-destructive manner.
- Inducing reinforcement corrosion using impressed current density can accelerate the corrosion process but can considerably alter the corrosion diffusion and damage mechanisms. On the contrary, subjecting concrete to wet-dry cycles will produce natural corrosion but at a slower rate. Thus, this research will investigate the mechanisms of natural corrosion by exposing concrete elements to wet-dry cycles in salt water.
- The pore morphology of concrete has a significant impact on its damage resistance and mechanisms. Thereby, this research will monitor concrete's pore characteristics (e.g., porosity and pore size) throughout the testing process.
- The water/cement (W/C) and sand/cement (S/C) ratios of concrete substantially affect its pore morphology and damage resistance, yet little research studied the microscale effects of concrete mixture proportions on the severity and mechanisms of microstructural corrosion and freeze-thaw damage. Hence, this research will fill the research gap in Chapter 3.
- The potential of using CT imaging to detect corrosion products within large concrete elements has yet to be determined. Therefore, this research will utilize CT imaging to detect the natural corrosion within a large 50-year-old concrete sample in Chapter 4

- Limited research investigated the microscale freeze-thaw damage of concrete in distinct sulfate environments using CT imaging. Thus, this research will address the research gap by examining the severity and mechanisms of microstructural frost damage of concrete in magnesium sulfate and potassium sulfate environments with different concentrations in Chapter 5.
- Image-based microstructural finite element models of corrosion and freeze-thaw damage of concrete have yet to be developed. Thereby, in this research, microstructural FE models of corrosion and frost damage will be developed using actual concrete specimens, and the FE results will be compared to experimental data in Chapter 6.

Chapter 3: 3D CT Imaging of Corrosion and Freeze-Thaw Damage of Concrete of Different Mixing Proportions

3.1. Introduction

In the early stages of reinforcement corrosion, the corrosion products occupy the interfacial voids without inducing any considerable internal stress [55], as demonstrated in Figure 3.1 (B). After filling the surrounding pores, further corrosion products start to generate expansive internal pressure that eventually results in concrete cracking and spalling [140,177]. The concrete cracking mostly occurs at the external surface of the concrete [144] and regions of stress concentration, such as the steel-concrete interface [178]. The cracks propagate along the weakest path, which includes midsection pores and interfacial transmission zones between the aggregates and the mortar, as shown in Figure 3.1 (C). Although the interfacial pores adjacent to steel can provide temporary stress relief, they accelerate the corrosion of the exposed areas of steel reinforcement, resulting in localized pitting corrosion [40]. Unlike uniform corrosion, pitting corrosion can induce stress concentration within the concrete element [90], leading to substantial cracking of the surrounding concrete cover [135].

On the other hand, freeze-thaw damage normally initiates within the concrete surface because of its direct exposure to the freezing environment, and the interfacial transmission zones between its aggregates and cement mortar due to its complex morphology, low strength, and porous nature [26,27]. The frost damage propagates inward on a layer-by-layer basis, causing scaling and interfacial cracking [26,59], as shown in Figure 3.2. The crack path is determined by the nature and distribution of internal pores and aggregates [38], as demonstrated in Figure 3.2 (B). Cracks tend to propagate along the surface of aggregates, as indicated by the red dashed lines [29]. Also,

open pores, which are accessible to concrete's external surface, allow further penetration of freezing water and deeper crack propagation, making concrete more vulnerable to losing large intact volumes. Similarly, large internal pores retain more water resulting in higher accumulative expansive pressure upon freezing. Also, the complex morphology of large pores makes them more prone to stress concentration, unlike the small spherical pores. Thus, cracks tend to propagate toward large pores, possibly scaling large pieces of concrete as shown in Figure 3.2 (C) [58,153].

The severity and mechanisms of corrosion and freeze-thaw damage are directly impacted by the concrete's strength and pore properties. Hence, extensive research has been conducted to investigate the effects of concrete composition and mixing proportions on its strength, pore characteristics [179], and corrosion [180] and freeze-thaw damage [38,181]. The resistance of concrete to corrosion and frost damage can be improved by using the appropriate water/cement (W/C) and sand/cement (S/C) ratios besides the addition of concrete admixtures, such as silica fume and fly ash [164,182–188]. Increasing the W/C ratio produces weaker concrete with higher porosity and permeability, reducing the concrete resistance to reinforcement corrosion and cracking [104,157,188–190]. In contrast, using a higher S/C ratio with an appropriate W/C of 0.5 enhances the concrete strength [191], but it also increases its porosity and permeability [159,179,192], degrading its resistance to corrosion and freeze-thaw damage [38].

At the microscale level, little research using 3D CT imaging has been conducted to investigate the effects of concrete mixture proportions on the microstructural mechanisms of corrosion and frost damage with detailed pore properties (e.g., size, morphology, and distribution). Thus, the main objective of this chapter is to examine the effects of W/C and S/C ratios on the pore morphology and the microscale damage mechanisms of concrete subjected to corrosion and freeze-thaw using non-destructive micro-computed tomography (μCT) imaging.

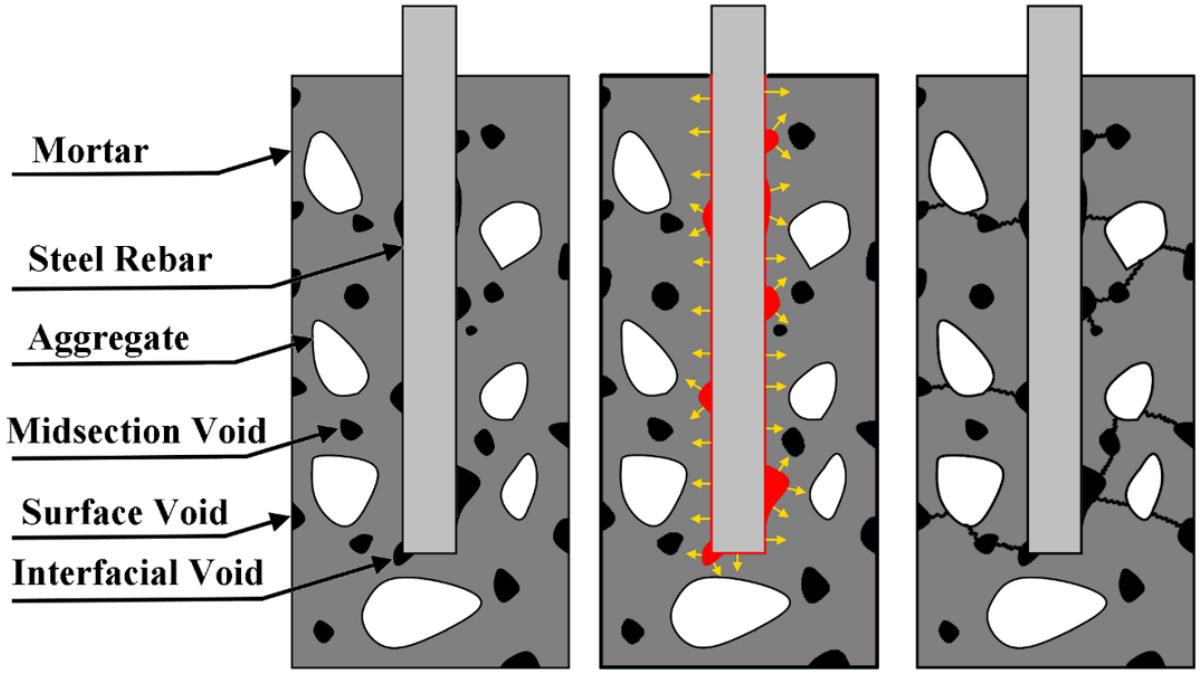

Figure 3.1. Concrete Element (A) before Reinforcement Corrosion, (B) after Filling Interfacial Voids with Corrosion Products (Red), and (C) after Cracking by the Expansive Internal Pressure

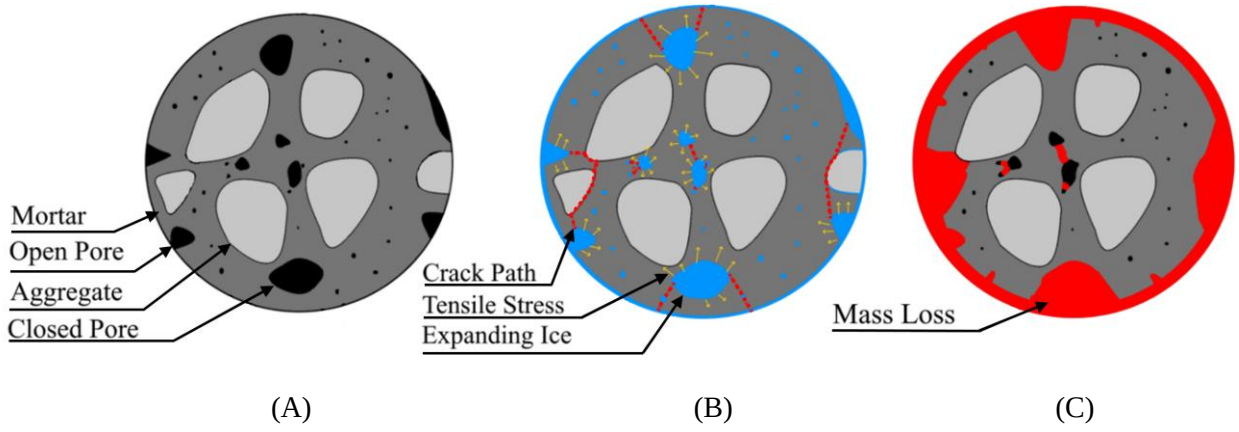

Figure 3.2. Concrete (A) before Freezing, (B) while Freezing, and (C) after Freeze-Thaw Damage

3.2. Materials and Methodologies

3.2.1. Specimen Preparation

Seventeen concrete specimens were cast using different water-to-cement (W/C) and sand-to-cement (S/C) ratios with a fixed aggregate-to-cement ratio of 1.5 to investigate the effects of the mixture proportion on pore morphology and the severity and mechanisms of corrosion and freeze-thaw damage.

The corrosion damage was examined using eight concrete specimens, each of which consisted of a 3 mm diameter low-carbon steel rod embedded at the center, whereas the remaining nine concrete specimens were used to study the freeze-thaw damage. Five corrosion specimens (CW4, CW5/CS10, CW6, CW7, and CW8) were cast using W/C ratios of 0.4−0.8 and an S/C ratio of 1, and three corrosion samples (CS5, CS20, and CS30) were prepared with a W/C ratio of 0.5 and S/C ratios of 0.5−3. Similarly, six freeze-thaw samples (FW4, FW5/FS10, FW6, FW7, FW8, and FW9) were made using W/C ratios of 0.4−0.9 and an S/C ratio of 1, while three specimens (FS5, FS20, and FS30) were cast with a W/C ratio of 0.5 and S/C ratios of 0.5−3, as listed in Table 3.1. The naming convention of the specimens is shown below.

Corrosion ← CW4 → W/C = 0.4

Freeze-Thaw ← FS10 → S/C = 1

The corrosion and freeze-thaw concrete specimens, shown in Figure 3.3, are about 40 mm long and 14 mm in diameter. One day after casting, the casting molds were removed, and the samples were water cured for 28 days and dried for at least three days before the μCT imaging, followed by exposure to either wet-dry cycles for corrosion testing or freeze-thaw cycles for investigating the frost damage. It is worth noting that the non-uniform bottom surfaces of the concrete specimens were caused by the area variation at the bottom section of the utilized plastic molds.

Table 3.1. Composition of Concrete Specimens

Corrosion Specimen	Freeze-Thaw Specimen	Water/Cement	Sand/Cement	Aggregate/Cement
CW4	FW4	0.4	1	1.5
CW5 || CS10	FW5 || FS10	0.5	1	1.5
CW6	FW6	0.6	1	1.5
CW7	FW7	0.7	1	1.5
CW8	FW8	0.8	1	1.5
—	FW9	0.9	1	1.5
CS5	FS5	0.5	0.5	1.5
CS20	FS20	0.5	2	1.5
CS30	FS30	0.5	3	1.5

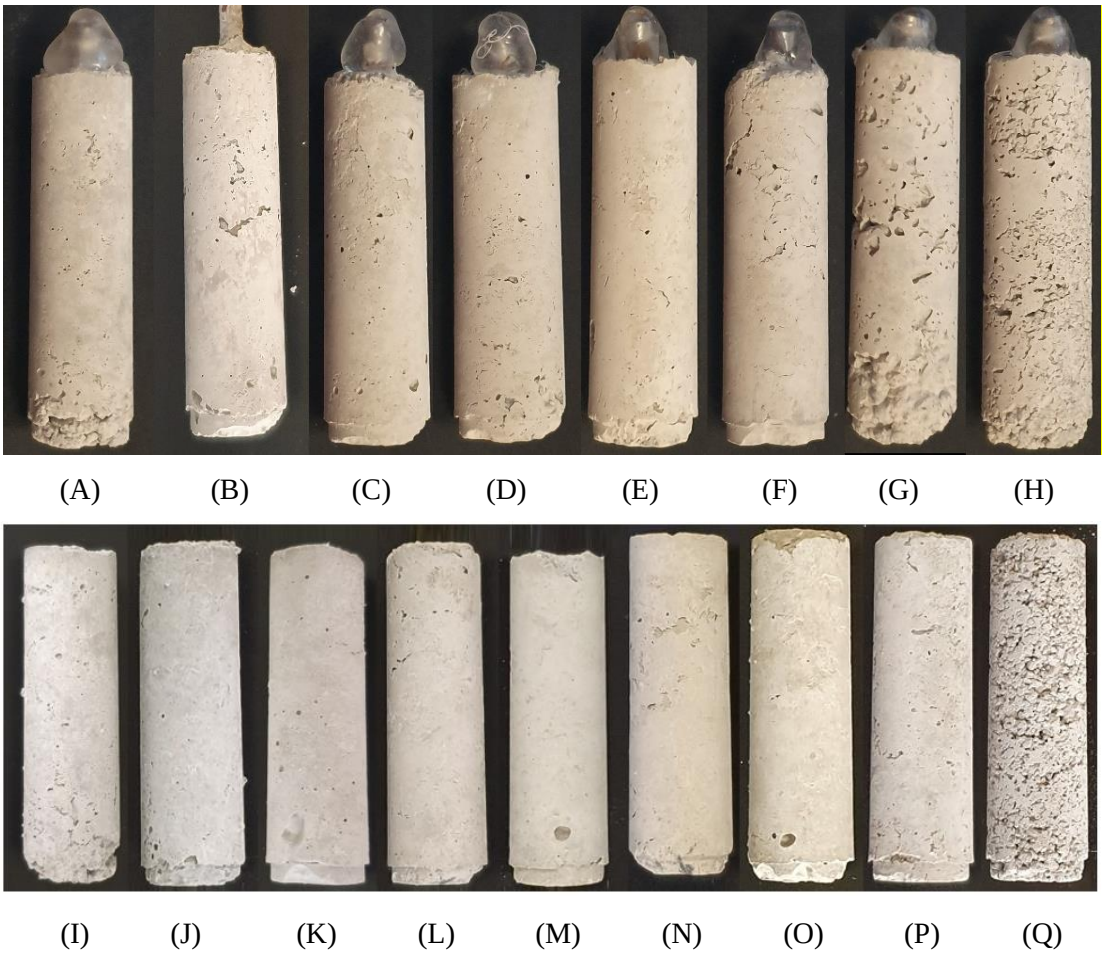

(A) (B) (C) (D) (E) (F) (G) (H)

(I) (J) (K) (L) (M) (N) (O) (P) (Q)

Figure 3.3. Concrete Specimens (A) CW4, (B) CW5/CS10, (C) CW6, (D) CW7, (E) CW8, (F) CS5, (G) CS20, (H) CS30, (I) FW4, (J) FW5/FS10, (K) FW6, (L) FW7, (M) FW8, (N) FW9, (O) FS5, (P) FS20, and (Q) FS30 before Testing

3.2.2. CT Imaging

An industrial micro-computed tomography (μCT), shown in Figure 3.4 (A), was employed to examine the internal microstructure of the concrete specimens before and after exposure to 40 freeze-thaw cycles. The CT scans were conducted using voltage and current of 100 kV and 80 μA, respectively. A total of 1,000 images were collected using a voxel size of 49.1 μm and an exposure time of 0.333 seconds per image. Using VGStudio Max 2.2, image analysis was performed only on the 36 mm middle segment of the sample height, illustrated in Figure 3.4 (B), to minimize the inconsistencies caused by the nonuniform top and bottom surfaces. At the image analysis stage, several post-imaging processes, including median filtration (3×3×3 pixels) and segmentation, were applied to reduce artifacts and improve the accuracy of pore analysis. Finally, three-dimensional reconstructions of the detected air pores, shown in Figure 3.4 (C), were produced and analyzed to determine the characteristics of individual pores, including the accessibility, size, shape, and distribution. The pore accessibility is defined as the ratio of the combined volume of open pores to the total pore volume, representing the open pore ratio. On the other hand, the pore size was represented by the large-pore ratio, which is the ratio of the accumulative volume of pores with a size of $\geq 1.18\times10^{6}$ μm^3 to the total pore volume. Similarly, the pore shape was represented by the pore sphericity, which is the ratio between the surface of a volumetrically equivalent spherical pore and its actual surface [193]. Also, the pore distribution was determined by the pore gap, which is the distance between a single void and its closest neighboring pore.

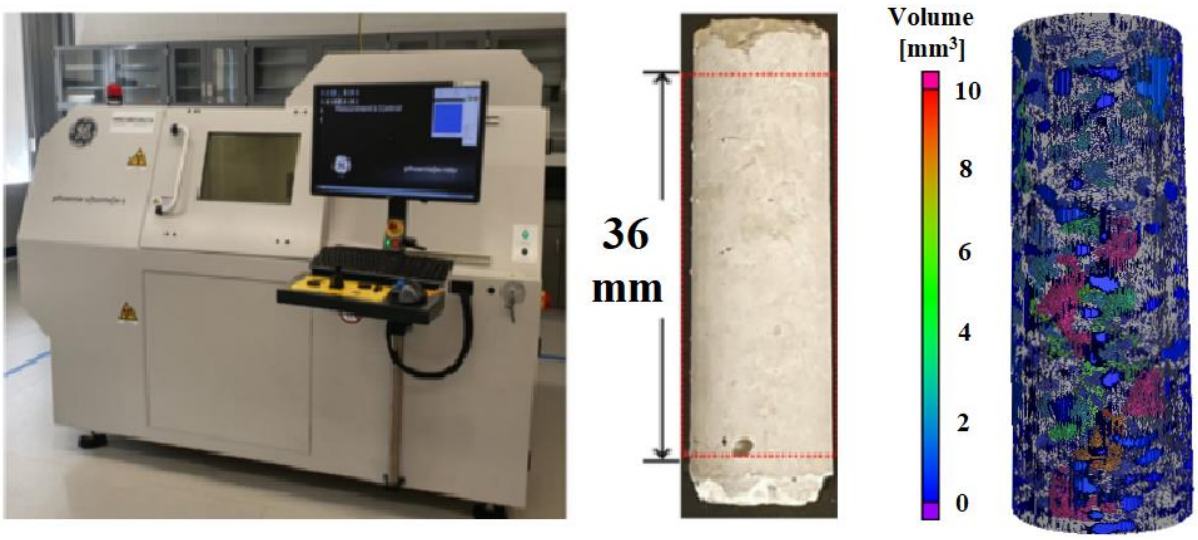

(A) (B) (C)

Figure 3.4. (A) μCT Imaging System, (B) Specimen's Region of Interest, and (C) Three-Dimensional Reconstruction of Detected Air Pores

3.2.3. Wet-Dry Cycles

Before subjecting the corrosion specimens to wet-dry cycles, the exposed area of the low-carbon steel reinforcement was isolated from the corrosion environment using clear glue, as illustrated in Figure 3.3. The corrosion concrete specimens were then subjected to a total of 120 wet-dry cycles (480 hours). Each cycle consisted of 3 hours of immersion in salt water with a sodium chloride concentration (wt.% NaCl) of 3.5% and 1 hour of accelerated dehydration at a temperature of only 45 ^{o}C to avoid causing thermal damage. After every 40 wet-dry cycles, the specimens were fully dehydrated by being subjected to a temperature of 45 ^{o}C for at least an hour followed by 3 days of exposure to room temperature before conducting weight measurements. The specimens were imaged before and after applying 120 cycles. Also, the salt water was replaced at least once during every 40 cycles to maintain the concentration of sodium chloride.

3.2.4. Freeze-Thaw Cycles

The freeze-thaw specimens were immersed in tap water for at least 6 hours before freeze-thaw testing to allow full saturation. The samples were subjected to 40 freeze-thaw cycles at temperatures ranging from -25 ^{o}C to 11 ^{o}C using an automated freezing chamber. Each freeze-thaw cycle lasted one day: 12.5 hours of freezing and 11.5 hours of melting. The temperature at each freeze-thaw cycle was lowered from about 11 ^{o}C at the start of the cycle to -25 ^{o}C using an average cooling rate of -13.5 ^{o}C/hour. The temperature was maintained between -18 ^{o}C and -25 ^{o}C for 7.2 hours, then increased gradually at a slow rate with an average of 1.9 ^{o}C/hour to minimize thermal damage. Notably, the applied freeze-thaw temperatures and periods were selected to mimic actual conditions of cold environments. The applied environment temperature throughout each freeze-thaw cycle is shown in Figure 3.5.

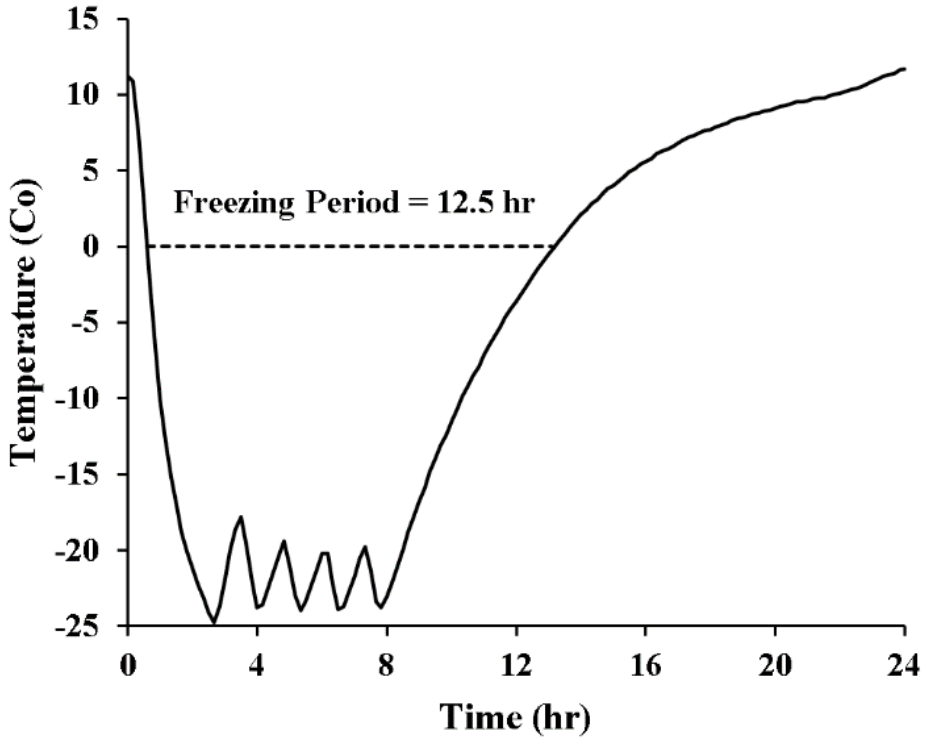

Figure 3.5. Temperature of Controlled Environment throughout Each Freeze-Thaw Cycle

3.3. Results and Discussion

3.3.1. Corrosion Damage

3.3.1.1. General

After subjecting the concrete elements to a total of 120 wet-dry cycles to investigate corrosion, mass measurement, porosity, and corrosion detection analyses were conducted to investigate the effects of W/C and S/C ratios on the progression of corrosion. It was observed that exposure to the wet-dry cycles resulted in a mass gain in all specimens and a minor change of porosity, indicating the absence of severe concrete damage. It was noted that increasing the W/C and S/C ratios resulted in a higher mass gain, mostly by chloride reaction with steel reinforcement and corrosion, salt saturation, and concrete hydration. Hence, specimens CW4 and CW5 (CS10) had the lowest mass gain. The porosity analysis produced similar findings. It was observed that the concrete porosity decreased in most specimens, mostly due to pore filling with corrosion products. However, the porosity of samples CW6 and CS5 increased, indicating that pore expansion is more dominant than pore filling. On the other hand, specimen CW5, which had a low mass gain, experienced the least change of porosity, illustrating its resistance to reinforcement corrosion. In terms of the corrosion mechanisms, it was noted from the 2D and 3D reconstructions that only specimens CW5 (S10), CW6, and CS5 experienced mostly uniform corrosion. All the other specimens suffered harsh pitting corrosion. The effects of W/C and S/C ratios on the severity and mechanisms of reinforcement corrosion are discussed further in the following sections.

3.3.1.2. Porosity of Corrosion Specimens

Porosity is defined as the ratio of the volume of the pores to the overall volume of concrete. It is one of the widely used characteristics of concrete material internal structures as it is crucial for investigating the severity of reinforcement corrosion and concrete damage (e.g., pore expansion).

The corrosion of steel within concrete induced by frequent wet-dry cycles decreases the porosity caused by pore filling with corrosion products and saturated salt. This is a more dominant behavior before the corrosion damage occurs due to pore expansion. This expansion is caused by the corrosion product that results in the disintegration of the concrete element when the expansion stress exceeds the strength of the concrete.

The concrete porosity was analyzed before and after subjecting the specimens to 120 wet-dry cycles, as shown in Figure 3.6. It was observed that using moderate W/C ratios produced concrete with the least porosity, as demonstrated in Figure 3.6 (A). Thus, while specimens CW5 and CW6 had initial porosities of 2.72% and 3.32%, the porosities of samples CW4, CW7, and CW8 were 4.38%, 3.79%, and 4.79%, respectively. After applying 120 wet-dry cycles, the porosities of specimens CW4, CW7, and CW8 decreased to 3.58%, 3.64%, and 4.33%, respectively, indicating a dominant pore filling with corrosion products. In contrast, the corrosion damage of sample CW6 surpassed the pore filling, resulting in a higher porosity of 4.01%. Specimen CW5 almost maintained its porosity.

Regarding the effects of the S/C ratio, it was noted that increasing the S/C ratio produced concrete with higher initial porosity, as demonstrated in Figure 3.6 (B) where the porosities increased from 2.24% to 3.76% for specimens CS5 and CS30, respectively. It is interesting to note that the sample with the lowest porosity (CS5) experienced the highest pore expansion after being subjected to 120 wet-dry cycles, increasing its porosity from 2.24% to 2.95%. Similarly, the porosities of specimens CS20 and CS30 increased from 3.5% to 4.05% and from 3.76% to 4.13%, respectively. On the other hand, sample CS10 experienced the least change in porosity. Based on the above observations, it can be concluded that using a W/C ratio of 0.5 and an S/C ratio of 1 produced concrete with the highest resistance to porosity change and likely reinforcement corrosion.

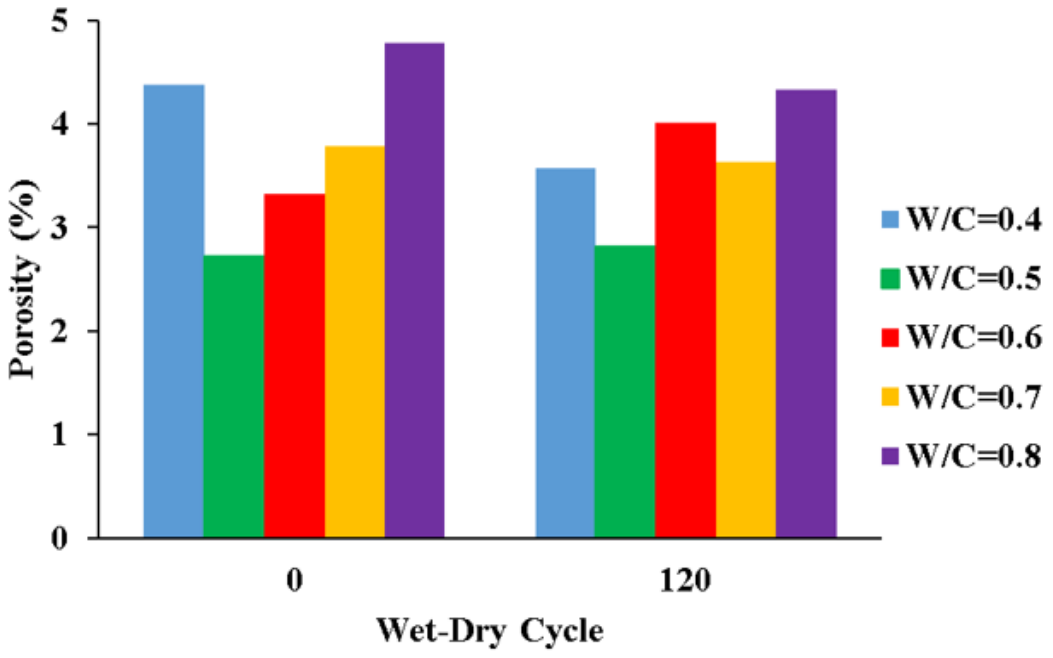

(A)

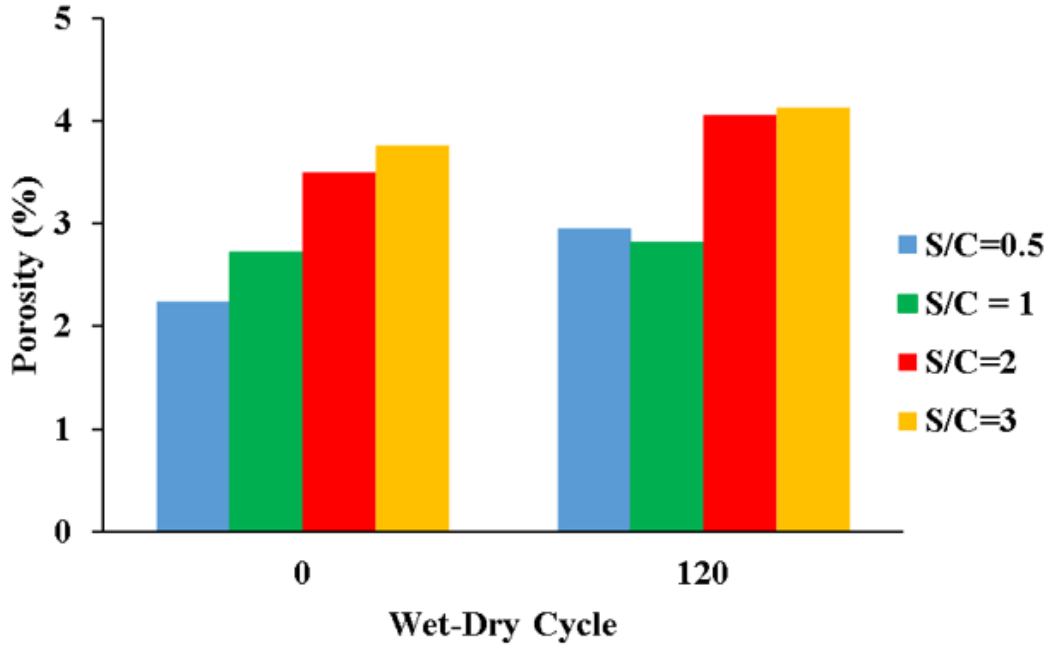

(B)

Figure 3.6. Porosity (%) of (A) W/C, and (B) S/C Concrete Specimens after Applying 120 Wet-Dry Cycles

3.3.1.3. Weight Measurement of Corrosion Specimens

The mass of the concrete specimens can change due to multiple factors, including reinforcement corrosion, salt saturation, residual moisture, and concrete hydration. However, since all specimens were subjected to the same salt water and experienced only minor cracking, it is possible to investigate the effects of W/C and S/C ratios on the corrosion rate by analyzing the overall trends of mass gain data. Also, the mass measurements can provide useful information when synthesized with the data of other analyses, such as the porosity measurement. Thus, the weight change of the concrete specimens was investigated before and after applying 40, 80, and 120 wet-dry cycles, as demonstrated in Figure 3.7. It was observed that concrete made of higher W/C ratios potentially experienced more corrosion while attaining considerably higher weight gain, as shown in Figure 3.7 (A). As a result, subjecting the concrete elements to 120 wet-dry cycles increased the mass of specimens CW6, CW7, and CW8 (e.g., W/C = 0.6, 0.7, and 0.8) by 4.7%, 4.2%, and 5%, respectively, whereas the mass gain of samples CW4 and CW5 (e.g., W/C = 0.4 and 0.5) was only 2.2% and 2.4%, respectively. Hence, increasing the W/C ratio seems to make concrete more susceptible to mass change and, potentially, reinforcement corrosion.

In terms of the effect of the S/C ratio, it was noted that specimen CS10 (e.g., S/C = 1) had the least mass gain of 2.4%, as illustrated in Figure 3.7 (B). On the other hand, the mass of samples CS5, CS20, and CS30 (e.g., S/C = 0.5, 2, and 3) increased by 5.1%, 3.6%, and 3.5%, respectively. Thereby, using a moderate S/C ratio of 1 produced concrete with the highest mass stability and likely the highest resistance to reinforcement corrosion, as discussed in the following sections.

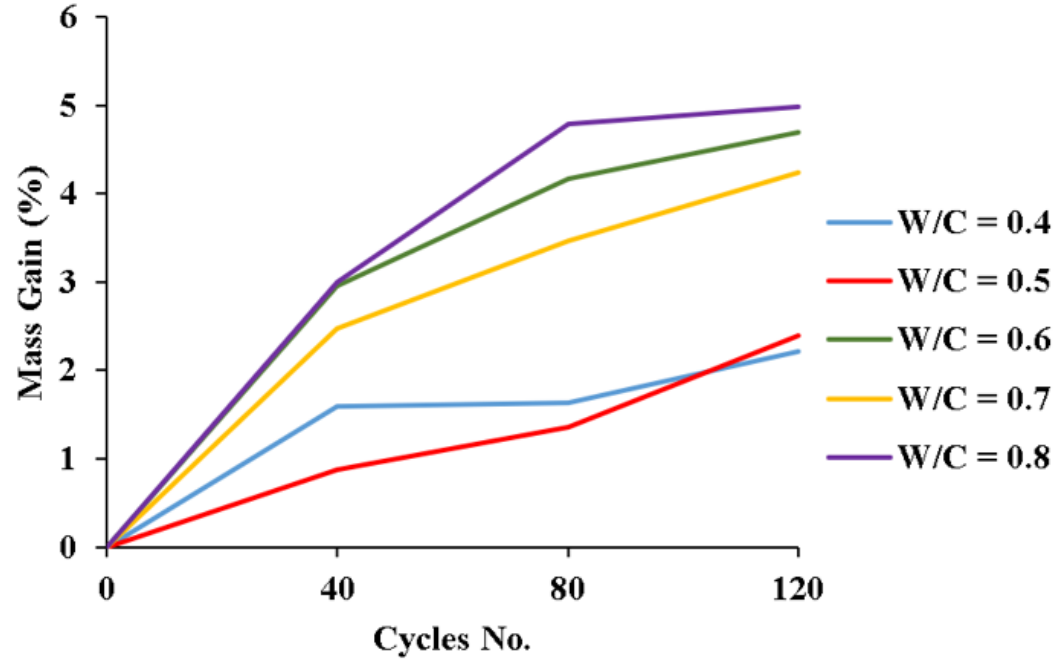

(A)

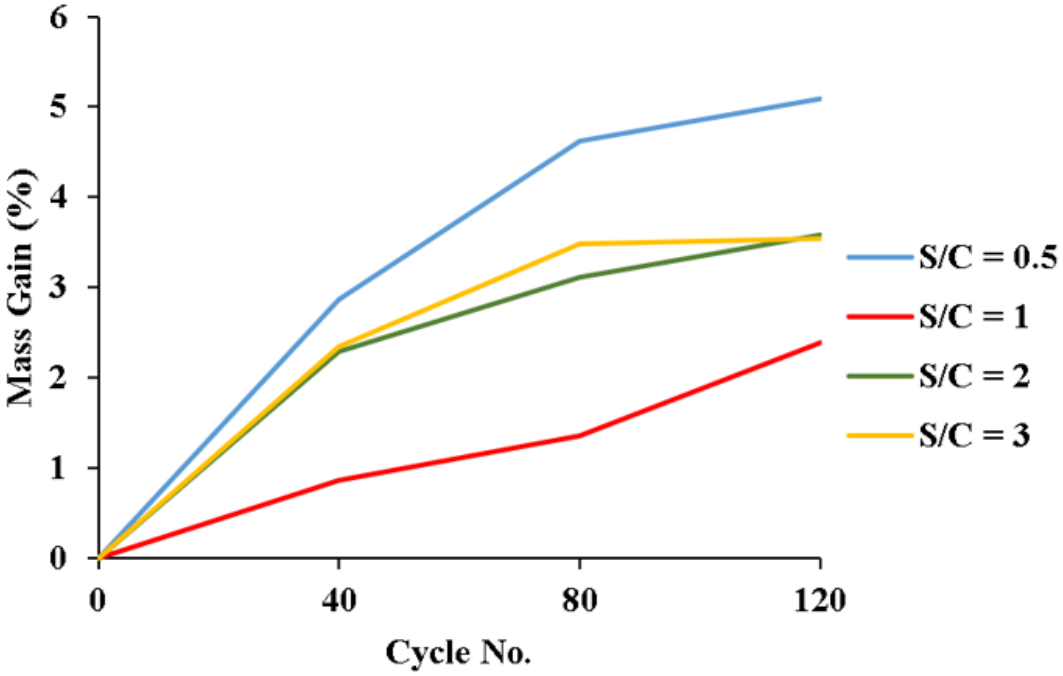

(B)

Figure 3.7. Mass Gain (%) of (A) W/C, and (B) S/C Concrete Specimens after Applying Wet-Dry Cycles

3.3.1.4. Corrosion Mechanisms

The effects of W/C and S/C ratios on the mechanisms of reinforcement corrosion were investigated by highlighting the corrosion products and monitoring the filling of the surrounding pores. The uniform portion of reinforcement corrosion was red-colored, while the localized pitting corrosion products were highlighted with yellow ellipses, as illustrated in Figure 3.8 and later verified in Figure 3.9. It was observed that increasing the W/C ratio resulted in more non-uniform corrosion, as indicated by the yellow highlights. Thus, while the corrosion of samples CW4, CW5, and CW6 seems to be mostly uniform, specimens CW7 and CW8 experienced severe pitting corrosion. Similarly, higher S/C ratios produced more pitting corrosion in specimens CS20 and CS30 than in samples CS5 and CS10 which experienced more uniform corrosion. It is worth mentioning that although the 2D illustrations of the corrosion products are important for locating the areas of pitting corrosion, they provide little detail about the severity of reinforcement corrosion. Therefore, the severity of pitting corrosion was investigated by monitoring the corrosion-induced filling of the surrounding voids using 3D reconstructions of the concrete pore structures generated before and after applying 120 wet-dry cycles, as demonstrated in Figure 3.9. It was noted that although sample CW4 had only a few areas of non-uniform corrosion, it suffered harsh pitting corrosion at these spots, as indicated by the large pore filling in Figure 3.9 (A). On the other hand, the corrosion of specimens CW5 (CS10), CW6, and CS5 was mostly uniform, as illustrated in Figure 3.9 (B and C). All the other samples endured severe pitting corrosion. It is worth noting that samples CW6 and CS5 experienced considerable pore expansion despite the uniform reinforcement corrosion. Thereby, specimen CW5 (CS10) not only experienced uniform reinforcement corrosion but also endured the least corrosion damage (e.g., pore expansion). Hence, it can be concluded that using a W/C ratio of 0.5 and an S/C ratio of 1 produced concrete with the highest corrosion resistance.

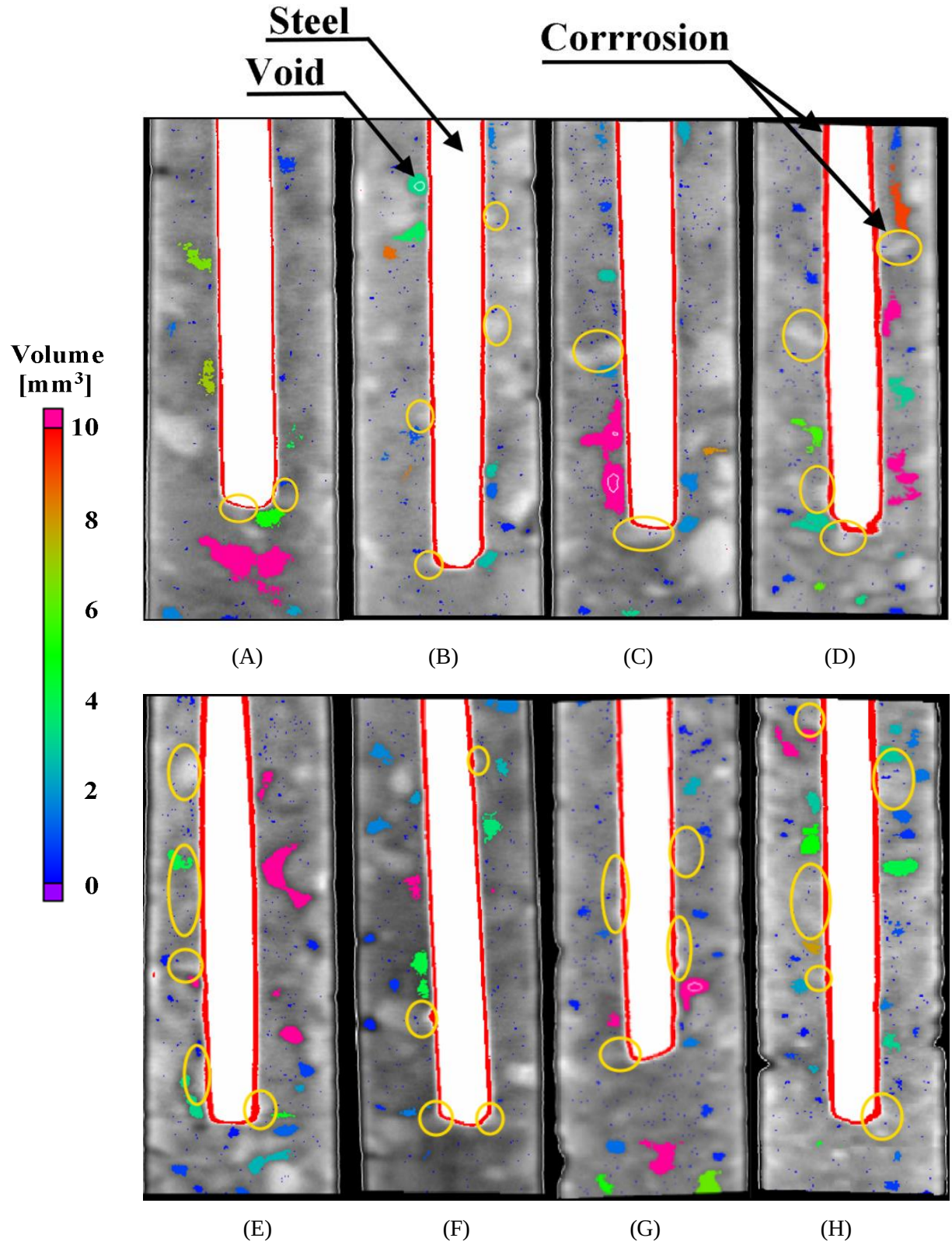

Figure 3.8. Detected Corrosion Products (Red and Yellow Highlights) within the 36 mm Midsection of Specimens (A) CW4, (B) CW5/CS10, (C) CW6, (D) CW7, (E) CW8, (F) CS5, (G) CS20, and (H) CS30

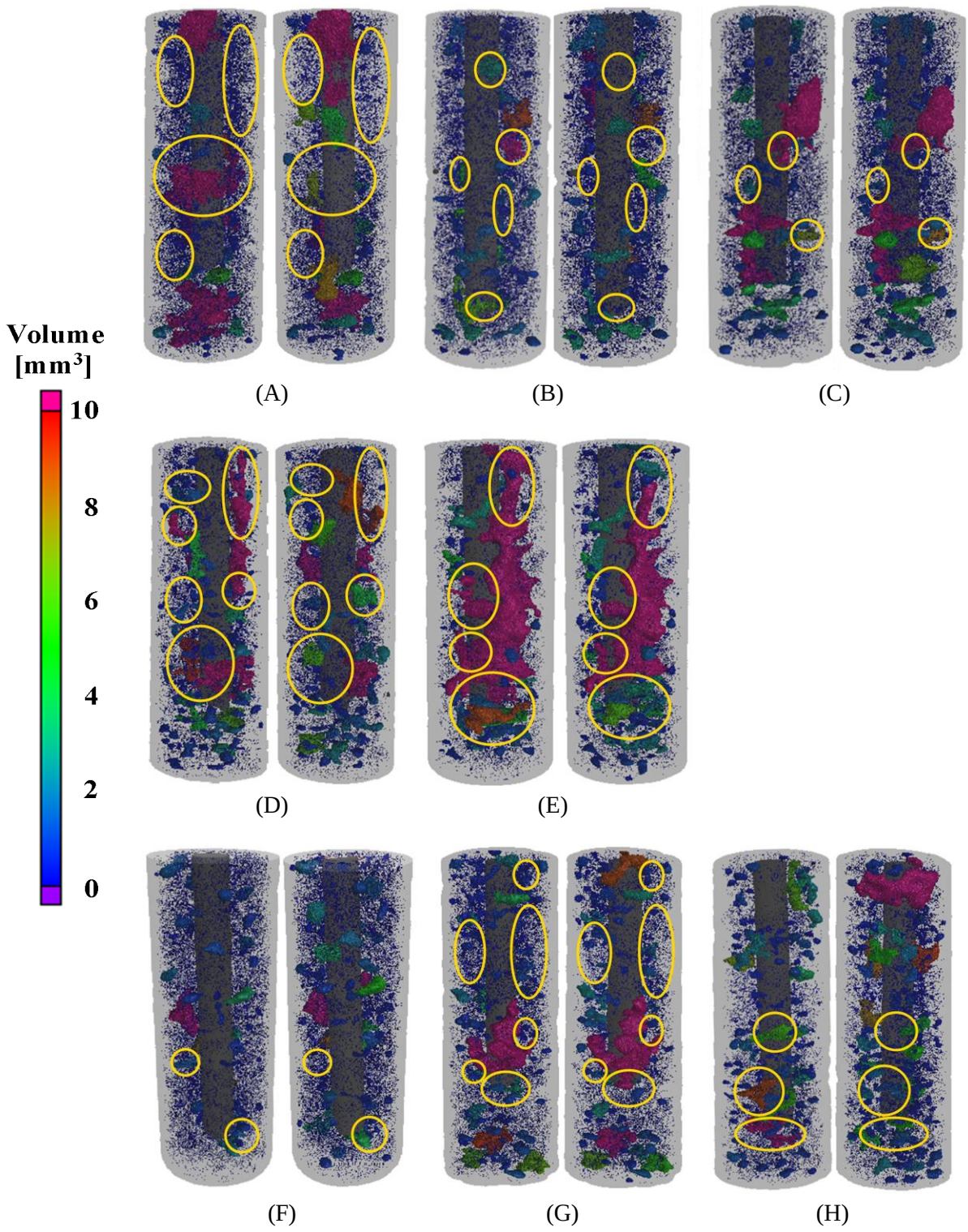

Figure 3.9. 3D Reconstructions of Pore Structures of Specimens (A) CW4, (B) CW5/CS10, (C) CW6, (D) CW7, (E) CW8, (F) CS5, (G) CS20, and (H) CS30 before (Left) and after (Right) 120 Wet-Dry Cycles

3.3.2. Freeze-Thaw Damage

3.3.2.1. General

The effects of the water-to-cement (W/C) and sand-to-cement (S/C) ratios on the pore properties, freeze-thaw resistance, and frost damage mechanisms were investigated using six W/C ratios (0.4 to 0.9) and four S/C ratios (0.5 to 3). The specimens were imaged using µCT before and after applying 40 freeze-thaw cycles, and the detected concrete voids were analyzed. From the pre-test µCT data of the concrete pores, plotted in Figure 3.10, it was observed that increasing the W/C and S/C ratios beyond 0.6 and 1, respectively, slightly increased the concrete porosity and reduced the volume occupied by smaller voids, resulting in lower frost resistance. For example, increasing the W/C ratio from 0.6 to 0.8 increased the porosity from 3.26% to 4.44% and decreased the cumulative porosity of small voids (<0.012 mm^3) from 0.74% to 0.55%. It is worth noting that the small indetectable pores could slightly reduce the porosity readings; however, this has little impact on the observed trends of concrete's pore characteristics.

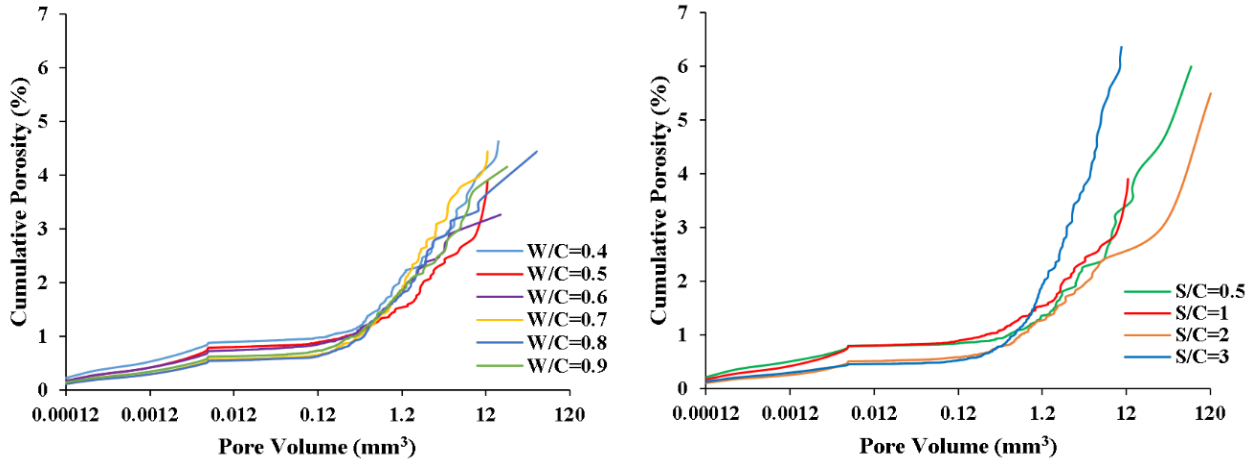

(A) (B)

Figure 3.10. Cumulative Porosity vs. Pore Size for Concrete Specimens with different (A) W/C and (B) S/C Ratios before Freeze-Thaw Exposure

Three-dimensional (3D) reconstructions of pore structures, shown in Figure 3.11, were generated and analyzed to investigate the effects of the W/C and S/C ratios on different pore properties: pore accessibility, size, shape, and distribution. A closer look at the illustrated pores revealed that increasing the W/C or S/C ratio produced more open, increasing water ingress. More quantitative analyses are presented in the following sections to investigate the effects of concrete mixing proportion on the other pore properties, such as internal pore size and shape, as they are hard to deduce visually.

After the freeze-thaw cycles, it was observed through 3D imaging that using high W/C ratios (>0.6) degraded the quality of the concrete pore structure significantly. This was demonstrated by the increased open-pore ratio, large-pore ratio, and non-uniformity of pore distribution, resulting in more severe frost damage and mass loss. For example, specimens FW8 and FW9 (W/C=0.8 and 0.9) had the highest open-pore ratios and pore gaps and were fully disintegrated by the 40 freeze-thaw cycles, as shown in Figure 3.12. Despite having almost the same porosity as specimens FW8 and FW9, specimen FW7 (W/C=0.7) suffered a mass loss of about 19.7%, illustrating the positive effect of the reduced open-pore ratio and pore gap. Likewise, specimen FW4 (W/C=0.4) had a comparable porosity but the lowest open-pore ratio, which resulted in the least mass loss of 4%. On the other hand, specimen FW6 (W/C = 0.6), which had the lowest porosity, large-pore ratio, and pore gap, suffered a considerable mass loss of 15.5%, attributed to its high open-pore ratio. Based on the aforementioned observations, the open-pore ratio seems to have the most dominant impact on the resulted frost damage due to the associated increase of permeability that allowed easy access of more water to concrete. Thus, investigating the open-pore ratio is essential for determining the freeze-thaw resistance of concrete. Also, it was observed that exposure to freeze-

thaw cycles could considerably alter some pore properties of concrete; thereby, analyzing more pore characteristics is vital for a reliable evaluation of freeze-thaw resistance.

In terms of the sand content, it was noted that using high S/C ratios created specimens with high porosity, open-pore ratio, and pore gap, which deteriorated the freeze-thaw resistance of concrete. For example, specimen FS10 (S/C=1) experienced a mass loss of only 4.3%, compared with 7.2% observed in specimen FS30 (S/C=3). Similarly, applying a low S/C ratio of 0.5 weakened the freeze-thaw resistance of specimen FS5 despite decreasing its open-pore ratio and pore gap, leading to a mass loss of 5.6%. It is critical to note that the open-pore ratio of specimen FS5 exceeded that of specimen FS10 after freeze-thaw exposure, which shows that determining the freeze-thaw resistance may require more than one pore property.

Based on these results, it can be concluded that the highest frost resistance was attained using the W/C and S/C ratios of 0.4−0.5 and 1, respectively, which is in good agreement with the reported values available in the literature. Also, the impact of the W/C ratio on the concrete pores was similar to the S/C ratio but to a greater extent. The detailed effects of W/C and S/C ratios on the pore morphology and damage mechanisms are discussed in the following sections.

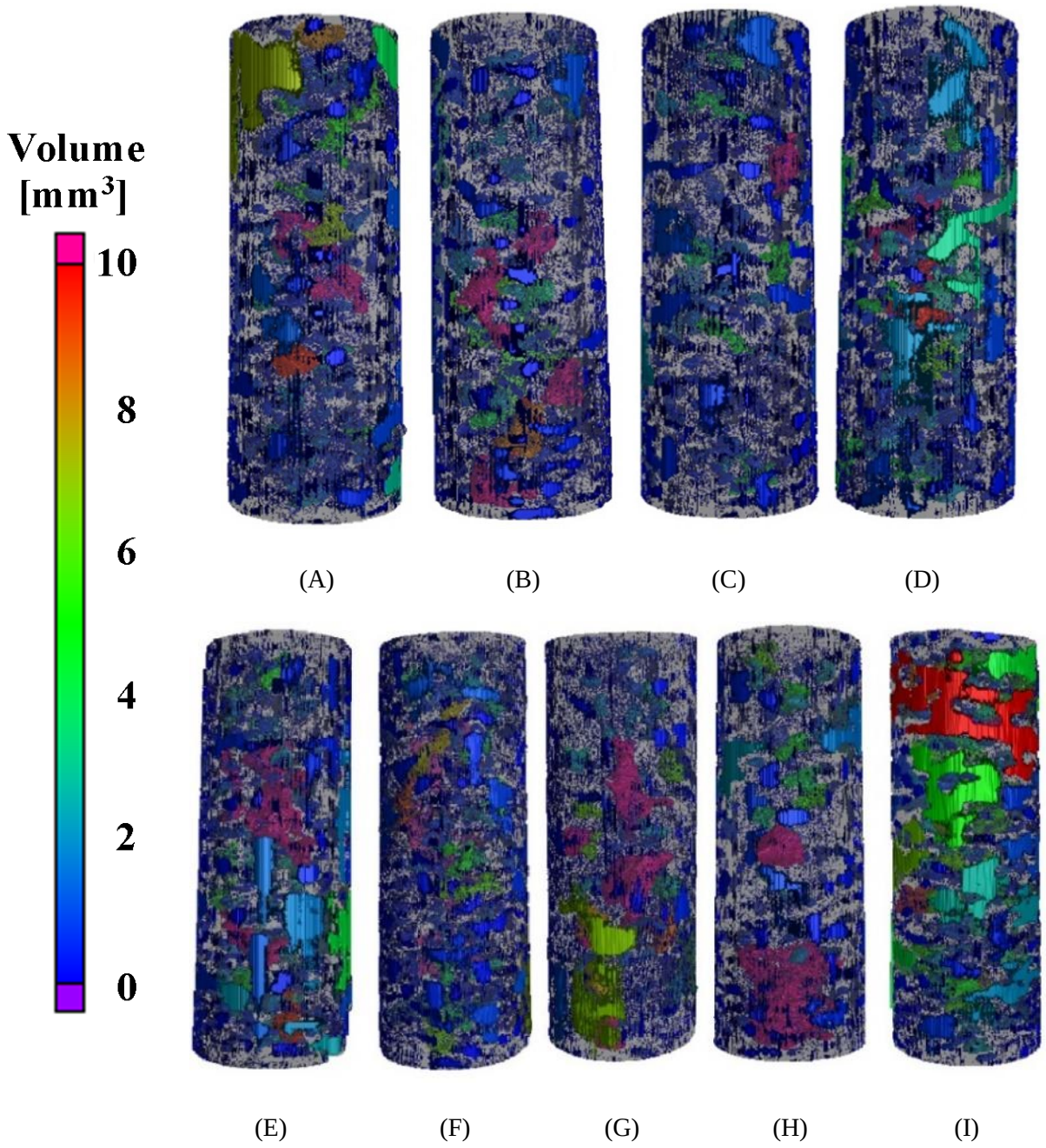

Figure 3.11. 3D Reconstructions of Pore Structures of Specimens (A) FW4, (B) FW5/FS10, (C) FW6, (D) FW7, (E) FW8, (F) FW9, (G) FS5, (H) FS20, and (I) FS30 before Freeze-Thaw Test.

(A) (B)

Figure 3.12. Damaged Concrete Specimens (A) FW8, and (B) FW9 after 40 Freeze-Thaw Cycles

3.3.2.2. Porosity of Freeze-Thaw Specimens

The effects of W/C and S/C ratios on the porosity were analyzed before and after applying 40 freeze-thaw cycles, as shown in Figure 3.13. Based on the applied resolution, it was observed that increasing the W/C ratio from 0.4 to 0.6 decreased the porosity from 4.6% to 3.3%, attributed to the improved workability that facilitated the casting of the small concrete specimens. However, using higher W/C ratios (>0.6) produced specimens with almost the same porosity as specimen FW6 of about 4.3% due to substantial concrete bleeding, pushing excess water out of the specimens.

After exposure to 40 freeze-thaw cycles, specimens FW8 and FW9 were destroyed; hence, their post-test porosities were not measured. The porosity of specimen FW7 increased considerably from 4.4% to 10.8%. Similarly, specimen FW6, despite having the least initial porosity of 3.3%, experienced a porosity expansion to 4.55%. On the contrary, specimen FW4, which had the highest initial porosity of 4.6%, maintained its porosity throughout the freeze-thaw process. Likewise, the

porosity of specimen FW5 slightly increased from 3.9% to 4.22%. As demonstrated by the results shown in Figure 3.13 (A), determining the initial porosity of concrete that has been conventionally used in literature is inadequate for evaluating its freeze-thaw resistance, illustrating the importance of the other pore properties.

The concrete porosity of different S/C ratios before and after freeze-thaw exposure was demonstrated in Figure 3.13 (B). Utilizing an S/C ratio of 1 enhanced the workability of concrete, making specimen FS10 with the least porosity of 3.9%. While using a high S/C ratio of 3 degraded the concrete workability, applying a low S/C ratio of 0.5 created a concrete mix with high water content, producing higher porosity by causing more concrete shrinkage. As a result, specimens FS5 and FS30 had the highest initial porosities of 6% and 6.4%, respectively. After subjecting the specimens to 40 freeze-thaw cycles, the porosity of specimens FS5 and FS30 increased to 7.1% and 7.2%, respectively. Specimen FS20 had moderate porosity and freeze-thaw resistance; on the other hand, specimen FS10 experienced the lowest porosity expansion by freeze-thaw exposure. Hence, using an S/C ratio of 1 can produce concrete with the highest freeze-thaw resistance. It can also be concluded from the above results that the W/C ratio's effect on the post-test porosity increment is more significant than that of the S/C ratio.

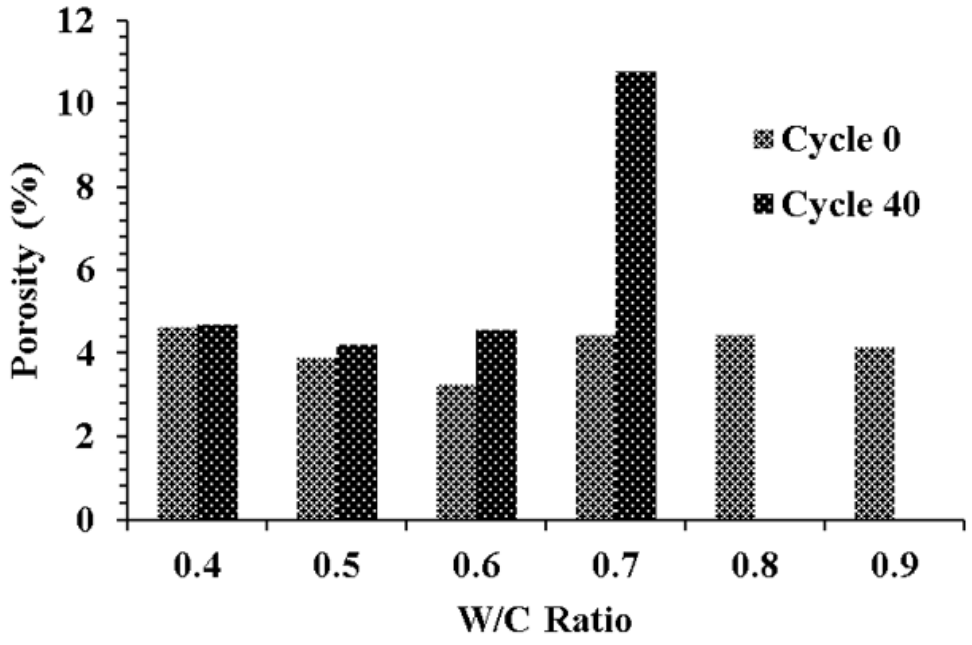

(A)

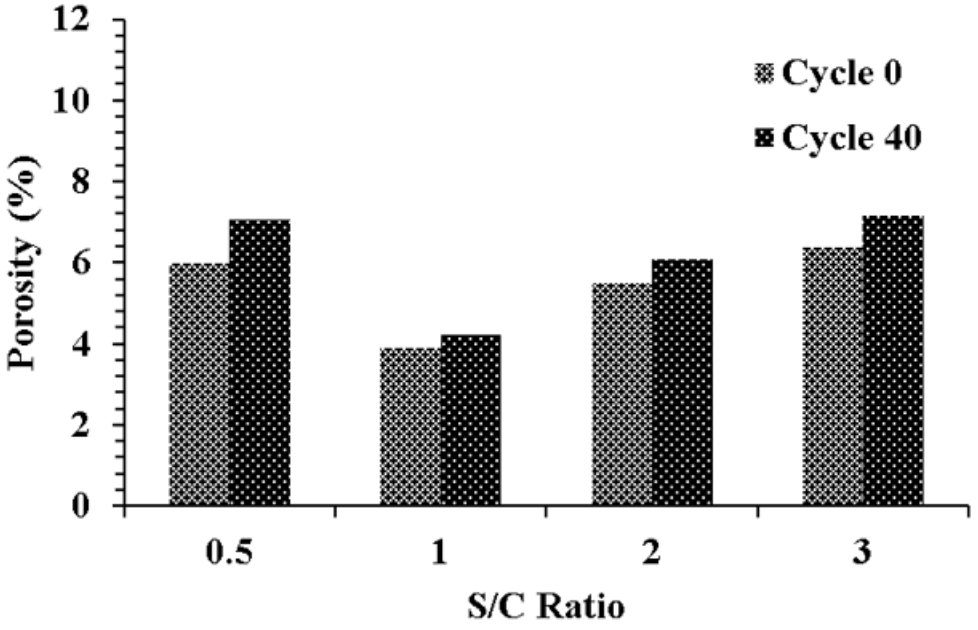

(B)

Figure 3.13. Porosity of Concrete Specimens with Different (A) W/C, and (B) S/C Ratios before and after Freeze-Thaw Cycles

3.3.2.3. Pore Accessibility of Freeze-Thaw Specimens

Pore accessibility can significantly affect the freeze-thaw resistance of concrete. This impact stems from the fact that open pores reduce the concrete confinement, making it more susceptible to cracking, and increase its permeability, leading to higher ingress of chloride and CO_2 [194–197]. On the other hand, inaccessible subsurface (closed) pores can provide space for freezing water and minimize frost damage [21,198,199]. Thus, increasing the open-pore ratio can deteriorate the freeze-thaw resistance of concrete.

The impact of W/C and S/C ratios on concrete's open-pore content before and after freeze-thaw exposure was investigated. It was observed that applying higher W/C ratios increased the volume ratio of open pores, as shown in Figure 3.14 (A), which is predictable since open pores are more susceptible to expansion by excessive concrete drying shrinkage than the well-confined closed (internal) pores. While specimens FW4 and FW5 had open-pore ratios of 23% and 24%, the open-pore ratios of specimens FW8 and FW9 were 28.6% and 38.2%, which contributed to substantial freeze-thaw damage. After 40 freeze-thaw cycles, the open-pore ratios of specimens FW4 and FW5 were almost maintained throughout the process, demonstrating their superior freeze-thaw resistance. The open-pore ratios of specimens FW6 and FW7 increased considerably to 54.3% and 77.7% despite having comparable initial open-pore ratios of 27.7% and 27%, respectively. An exponential correlation between the open-pore and W/C ratios became apparent after applying 40 freeze-thaw cycles.

The effect of the S/C ratio on the open-pore ratio of concrete before and after freeze-thaw testing is demonstrated in Figure 3.14 (B). While specimens FS5 and FS20 had the least open-pore ratio of 10.9% and 14.2%, the open-pore ratios of specimens FS10 and FS30 were 24% and 45.3%, respectively. After subjecting the specimens to 40 freeze-thaw cycles, the open-pore ratio of

specimen FS10, which was the second highest before freeze-thaw exposure, was maintained throughout the testing process. On the other hand, the open-pore ratio of specimens FS5, FS20, and FS30 increased considerably to 44.3%, 28.3%, and 58.5%, respectively. Therefore, using an S/C ratio of 1 seems to improve the freeze-thaw performance of concrete. It is worth mentioning that specimen FS5 had the least open-pore ratio, but it experienced the highest increase in open-pore ratio after freeze-thaw exposure. Therefore, determining the freeze-thaw resistance of concrete requires more pore analysis beyond the open-pore ratio. Also, increasing the size of the specimens can decrease the open-pore ratio by decreasing the surface/volume ratio of concrete.

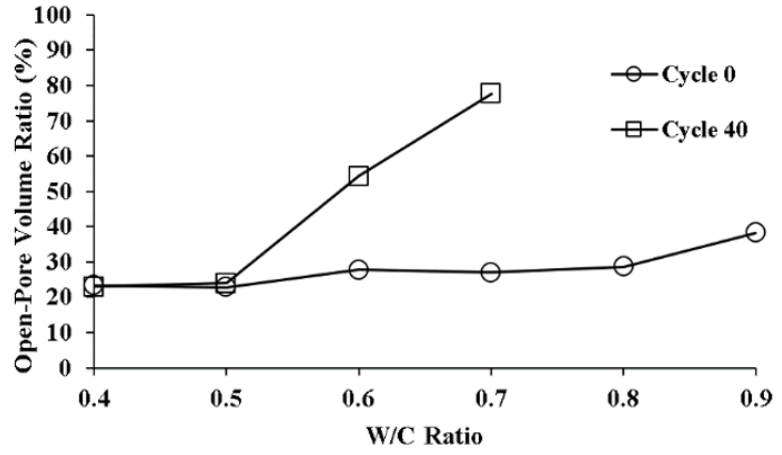

(A)

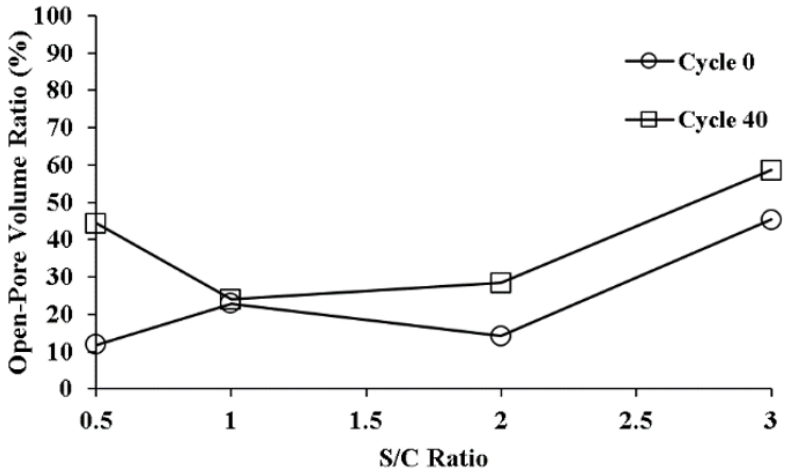

(B)

Figure 3.14. Open-Pore Ratio (%) of Concrete Specimens with Different (A) W/C, and (B) S/C Ratios before and after Testing

3.3.2.4. Pore Size of Freeze-Thaw Specimens

The pore size is another crucial parameter for determining the freeze-thaw resistance of concrete. Small pores can relieve the pressure induced by the expanding ice by allowing it to flow in after creating minor microcracks, mitigating severe freeze-thaw damage, in a manner similar to that reported in air-entrained concrete [200]. On the other hand, large pores retain more water, which upon freezing, produces higher accumulative expansive pressure and larger concrete cracks [23,194,201,202]. Hence, increasing the large-pore ratio can deteriorate the freeze-thaw resistance of concrete. In addition to demonstrating the percentage of large voids, the rate of change of the large-pore ratio throughout the freeze-thaw cycles can be used in conjunction with the porosity data to obtain useful information about the damage mechanisms. For example, a rapid increase of the large-pore ratio with a little increase in the porosity can indicate a considerable pore interconnection (cracking).

As Zhang et al. reported, pores with a size of more than 200 nm can degrade the freeze-thaw resistance of concrete [203]. However, capturing such small pores is beyond the detection capability of the μCT imaging system. Thus, in this study, pores with a volume of more than 1.18×10^{6} μm^3, which is 10 times the volume of the smallest detected void, are treated as large pores. It is worth mentioning that the general trends of the attained results are not sensitive to the utilized volume threshold. For example, changing the volume threshold from 1.18×10^{6} μm^3 to about 1.00×10^{10} μm^3 had little effect on the reported observations.

The large-pore ratio was analyzed to investigate the effects of W/C and S/C ratios on the large-pore content before and after applying 40 freeze-thaw cycles, and the recorded volume ratios of large pores are illustrated in Figure 3.15. As shown, specimen FW6 had the lowest initial large-pore ratio of 87.6%. Increasing the W/C ratio beyond 0.6 produced a concrete mix with high water

content, causing considerable concrete shrinkage and creating more large voids. Likewise, reducing the W/C ratio to 0.4 decreased the concrete workability, producing a higher large-pore ratio of about 89.1%. Notably, subjecting the specimens to 40 freeze-thaw cycles considerably changed the large-pore ratios, resulting in an exponential correlation between the W/C and large-pore ratios, as shown in Figure 3.15 (A). Although the initial large-pore ratios of specimens FW4 and FW5 were relatively high, they were mostly maintained throughout the freeze-thaw process. In contrast, the large-pore ratios of specimens FW6 and FW7 increased substantially from 87.6% and 93.5% to 91.6% and 98.4%, respectively. Thus, increasing the W/C ratio beyond 0.5 significantly increased the concrete large-pore ratio after the freeze-thaw cycles, making it more vulnerable to frost damage.

In terms of the S/C ratio's effect, it was observed that specimen FS10 had the least large-pore ratio of 89.7%, as illustrated in Figure 3.15 (B). Decreasing the sand content (e.g., S/C=0.5) created a concrete mixture with high water content, leading to a higher large-pore ratio of 91.7%. In contrast, using high S/C ratios degraded the workability of concrete, producing specimens FS20 and FS30 with a large-pore ratio of 95.5%. Exposure to freeze-thaw cycles had distinct effects on the specimens due to the varying small- and large-pore expansion rates. Although the large-pore ratios of specimens FS5 and FS30 increased to 94.6% and 96.7%, more small-pore expansion occurred in FS20, resulting in a lower large-pore ratio of 93%, as illustrated in Figure 3.15 (B). On the other hand, specimen FS10 almost maintained its large-pore ratio, indicating that the expansion rates of its small and large pores are comparable. Based on the results, concrete with the least large-pore ratio before and after freeze-thaw exposure can be attained using an S/C ratio of 1. Also, the effect of the W/C ratio on concrete's large-pore ratio is clearly more substantial than that of the S/C ratio.

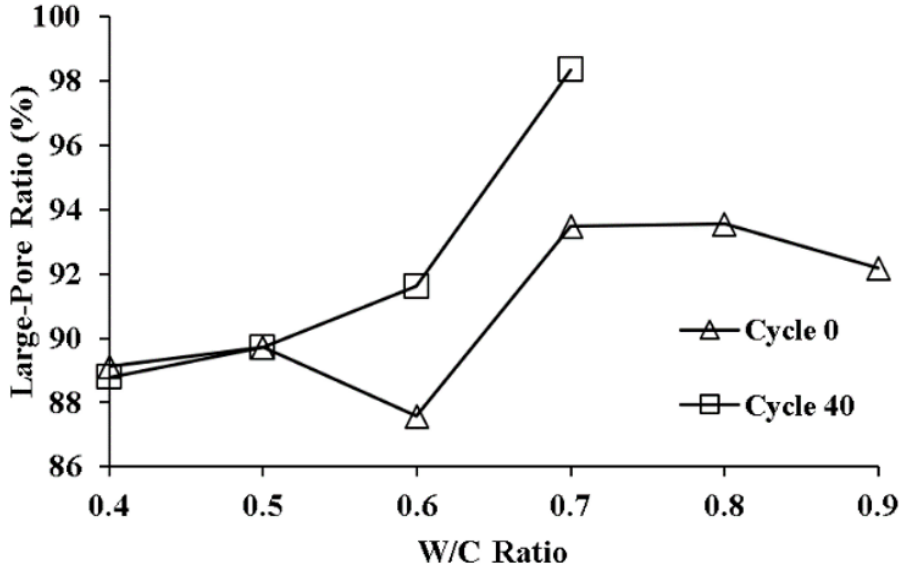

(A)

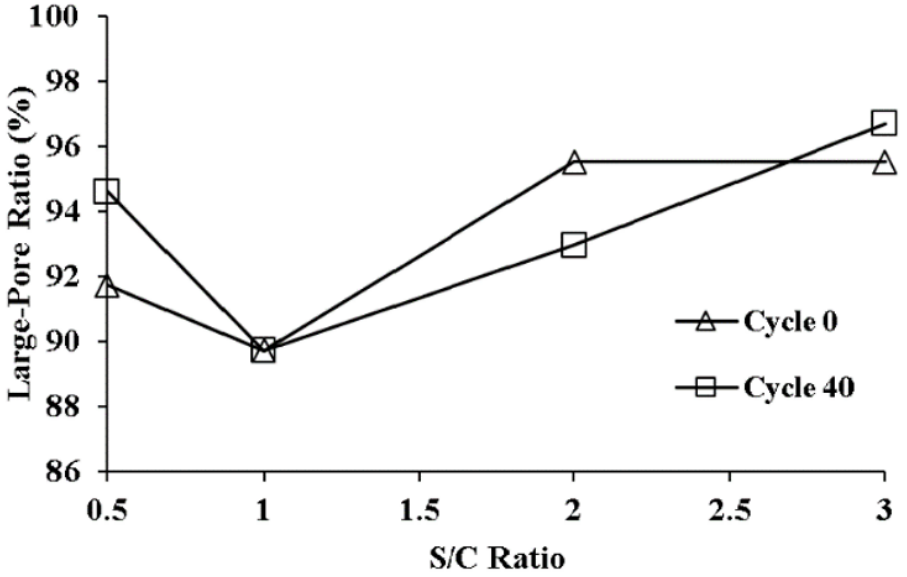

(B)

Figure 3.15. Large-Pore (>1.18×10^6 μm^3) Ratio (%) of Concrete Specimens with Different (A) W/C, and (B) S/C Ratios before and after Testing

3.3.2.5. Pore Shape of Freeze-Thaw Specimens

The cracking resistance of an expanding pore is dependent on its shape. The uniform surface of spherical voids, for example, makes them more resilient to cracking when subjected to expansive internal pressure due to the role of the spherical shape in making stress distribution more uniform

[204], hence, mitigating stress concentration. Thus, the freeze-thaw resistance of concrete can be enhanced by increasing its pores' sphericity [205,206]. Hence, the effects of W/C and S/C ratios on concrete's average pore sphericity have been investigated before and after freeze-thaw exposure.

Concrete pores were categorized into high-sphericity (>0.5) and low-sphericity (≤0.5) pores, as shown in Figure 3.16. It was observed that increasing the W/C ratio from 0.4 to 0.6 improved the average sphericity of concrete pores. For example, while specimens FW4 and FW5 had comparable high-sphericity ratios of 13% and 14.5%, respectively, the high-sphericity ratio of sample FW6 was 18.6%. However, applying a W/C ratio beyond 0.6 considerably reduced the high-sphericity ratio due to high concrete shrinkage and large pore size. Thus, the high-sphericity ratio of specimens FW7, FW8, and FW9 were 11.7%, 9.4%, and 10.9%, respectively. Notably, exposure to 40 freeze-thaw cycles increased the high-sphericity ratios of specimens FW4 and FW5 to 14.6% and 15.8%; on the contrary, specimens FW6 and FW7 experienced sphericity reduction to 11.9% and 3.7%, respectively. Therefore, using the W/C ratios of 0.4 and 0.5 enhanced the average pore sphericity throughout the freeze-thaw process.

The average sphericity of concrete's pore structure was also analyzed using various S/C ratios, as illustrated in Figure 3.16 (B). It was noted that increasing the S/C ratio decreased the sphericity, ascribed to concrete's reduced workability. As a result, while specimen FS5 had a high-sphericity ratio of 16.6%, the high-sphericity ratio of specimen FS30 was 9.1%. Furthermore, applying 40 freeze-thaw cycles increased the high-sphericity ratios of specimens FS10 and FS20 from 14.5% and 6.2% to 15.8% and 11.6%, respectively. On the other hand, the high-sphericity ratios of specimens FS5 and FS30 decreased to 13.7% and 8.5%. Thereby, concrete prepared using an S/C ratio of 1 maintained relatively high sphericity before and after freeze-thaw exposure. The results

also demonstrated that determining the initial pore sphericity is insufficient for anticipating the freeze-thaw resistance of concrete since it can change during freeze-thaw exposure. Thus, the pore sphericity must be used in conjunction with other pore properties.

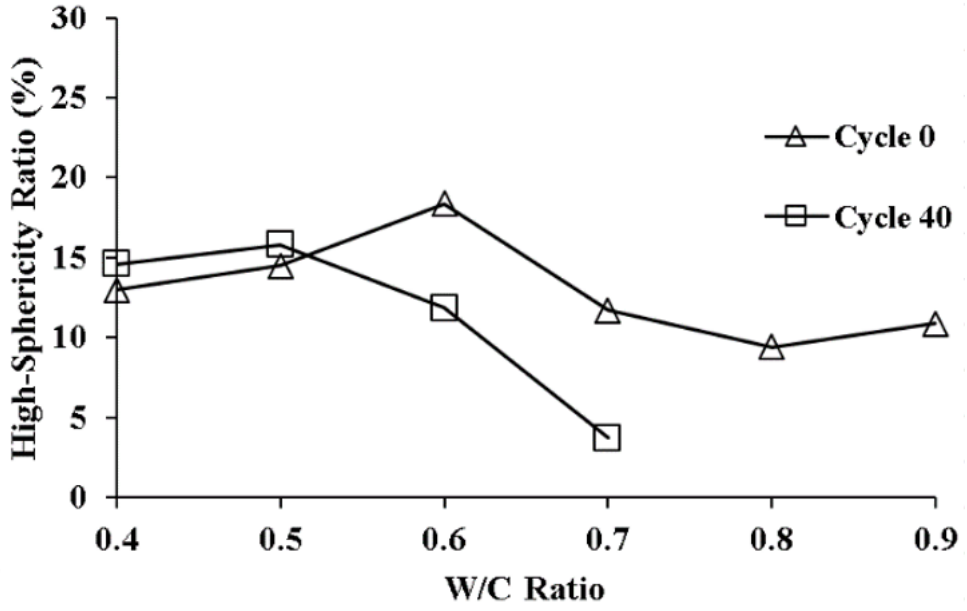

(A)

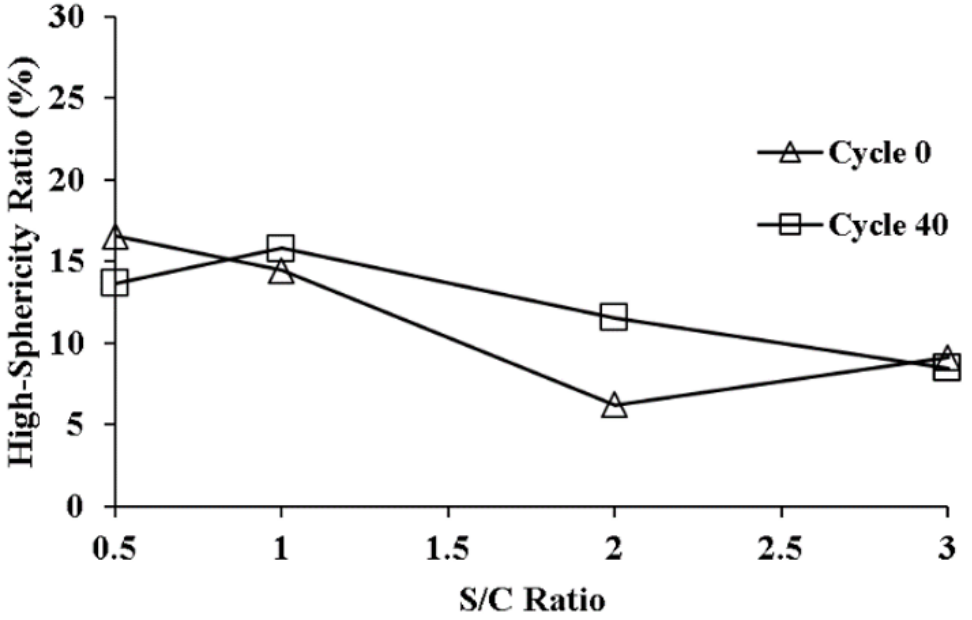

(B)

Figure 3.16. High-Sphericity (>0.5) Ratio (%) of Concrete Specimens with Different (A) W/C, and (B) S/C Ratios before and after Testing

3.3.2.6. Pore Distribution of Freeze-Thaw Specimens

The uniform distribution of pores can enhance the freeze-thaw resistance of concrete by minimizing the likelihood of void cluster formation, which can weaken the concrete strength and increase its permeability. Highly uniform microscale pore distribution decreases the average pore gap, which is the distance between a single void and its closest neighboring pore. Minimizing the pore gaps makes it easier for ice to expand into the surrounding pores by creating microcracks, preventing pressure accumulation and extensive concrete cracking [207,208]. Thus, decreasing the pore gaps through the uniform distribution of micropores can considerably enhance the freeze-thaw resistance of concrete [22,24].

The average pore gap of concrete specimens of different W/C and S/C ratios were examined. It was observed that using a W/C ratio beyond 0.6 increased the average pore gap on an exponential basis, contributing to the severe frost damage of specimens FW7, FW8, and FW9. For example, although specimen FW6 had an average pore gap of only 0.57 (±0.75) mm, the average pore gap of specimen FW9 was 2.28 (±2.65) mm. Subjecting the specimens to freeze-thaw cycles made the exponential correlation between the W/C ratio and the average pore gap more apparent, as shown in Figure 3.17 (A). While the average pore gaps of specimens FW4 and FW5 decreased to 0.74 (±0.92) mm and 0.68 (±0.81) mm due to the development of more small pores, the average pore gaps of specimens FW6 and FW7 increased considerably to 1.57 (±1.57) mm and 8.74 (±5.07) mm, respectively. Hence, applying W/C ratios of 0.4 and 0.5 produced concrete with more uniformly distributed pores and improved freeze-thaw resistance.

The effect of the S/C ratio on the average pore gap, illustrated in Figure 3.17 (B), was limited compared to the W/C ratio. It was noted that applying moderate S/C ratios of 1 and 2 produced specimens with the least average pore gaps of 0.92 (±1.22) mm and 0.55 (±0.84) mm, whereas

specimens FS5 and FS30 had average pore gaps of 0.73 (±0.95) mm and 1.52 (±1.44) mm, respectively. Exposure to 40 freeze-thaw cycles slightly increased the average pore gaps of the specimens, which indicates that no specimen experienced severed freeze-thaw damage. Nonetheless, only specimen FS10 experienced a pore gap reduction to 0.68 (±0.81) mm, illustrating its superior freeze-thaw performance.

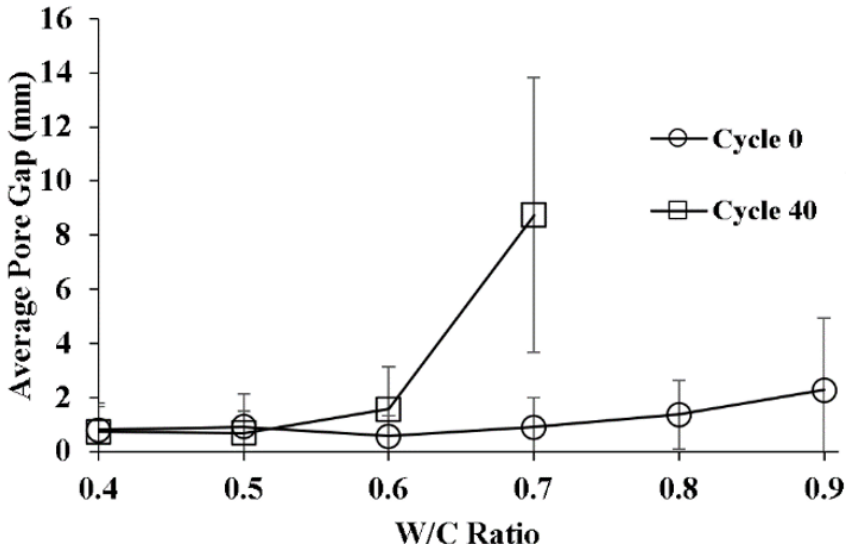

(A)

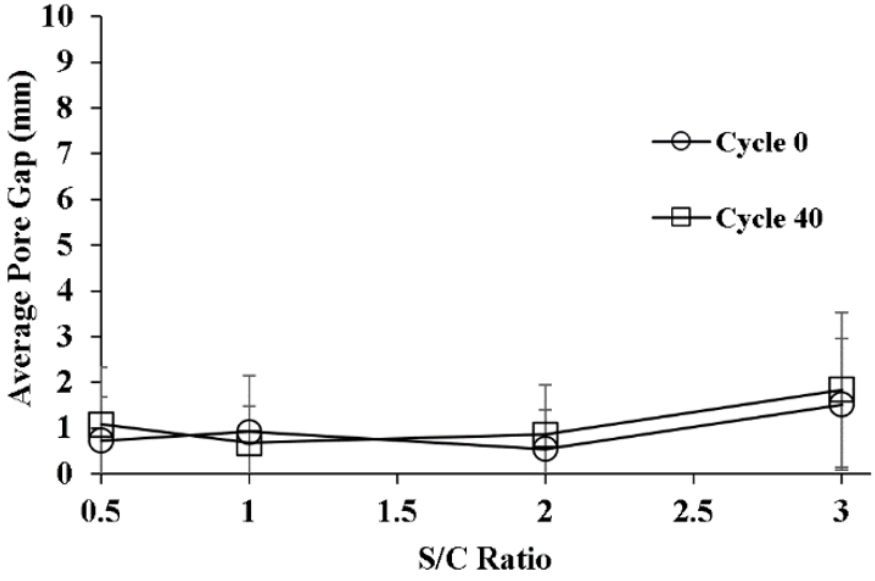

(B)

Figure 3.17. Average Pore Gap of Concrete Specimens with Different (A) W/C, and (B) S/C Ratios before and after Testing

3.3.2.7. Severity and Mechanisms of Freeze-Thaw Damage

The effects of W/C and S/C ratios on the freeze-thaw resistance of concrete were evaluated by measuring the specimens' mass losses due to freeze-thaw exposure, as demonstrated in Figure 3.18. It was noted that applying higher W/C ratios increased the resulted mass loss on an exponential basis. While specimen FW4 lost 4% of its mass, a mass loss of 19.7% was experienced by specimen FW7. Specimens FW8 and FW9 were destroyed, so they were not considered in the analysis.

The frost damage mechanisms of the specimens are illustrated in Figure 3.19. As shown, specimens FW4 and FW5 experienced only minor internal pore expansion with minimal scaling. Also, numerous small pores were detected in the two specimens after the expansion of previously indetectable caused by freeze-thaw exposure, which decreased the average pore gap as previously noted. In contrast, specimens FW6 and FW7 suffered considerable scaling, which increased the concrete permeability and degraded its confinement and freeze-thaw resistance. The presented 2D section of specimen FW7 started with smaller open pores than specimen FW6, yet it experienced more severe scaling, possibly due to the lack of small pores. This shows that the frost vulnerability caused by one pore property can be mitigated by the other ones, proving the importance of assessing the freeze-thaw resistance using multiple pore characteristics.

Unlike the W/C ratio, the S/C ratio had a limited effect on the frost damage of concrete, as demonstrated in Figure 3.18 (B). Increasing the S/C ratios from 1 to 3 degraded concrete's freeze-thaw resistance, resulting in mass losses of 4.35% and 7.17%, respectively. Applying an S/C ratio of 1 produced concrete with the highest freeze-thaw performance. Also, as illustrated in Figure 3.19, while exposure to freeze-thaw cycles created many small pores in specimens FS10 and FS20, it caused noticeable large-pore expansion in specimens FS5 and FS30, making them more

susceptible to freeze-thaw damage. It is worth noting that the large pores of specimens FS5 (green) and FS20 (pink) propagated inward despite being close to the surface, demonstrating the positive effect of the small pore gap between the voids. On the other hand, the small pores of specimen FS30 with a larger pore gap between them expanded outward toward the surface, which can harshly detriment the frost resistance by increasing the permeability and reducing the confinement of concrete. Based on the aforementioned results, the mixing proportion of concrete can considerably alter the severity and mechanisms of frost damage. Also, the highest freeze-thaw resistance of concrete was attained using a low W/C ratio of 0.4−0.5 and an S/C ratio of 1.

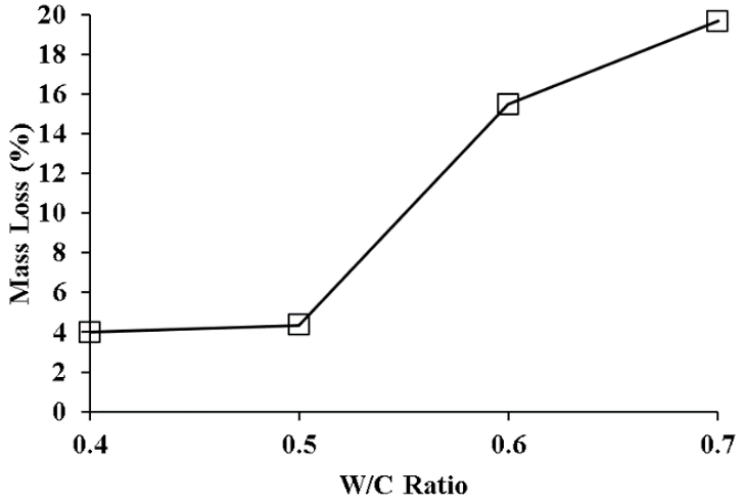

(A)

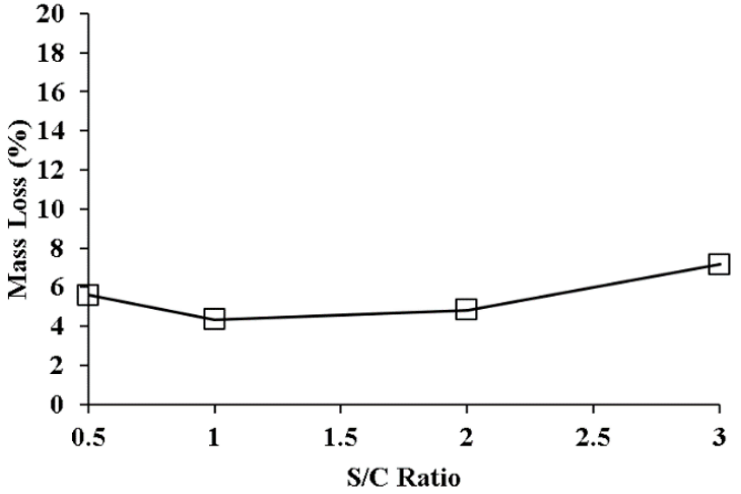

(B)

Figure 3.18. Mass Loss of Concrete Specimens of Different (A) W/C, and (B) S/C Ratios

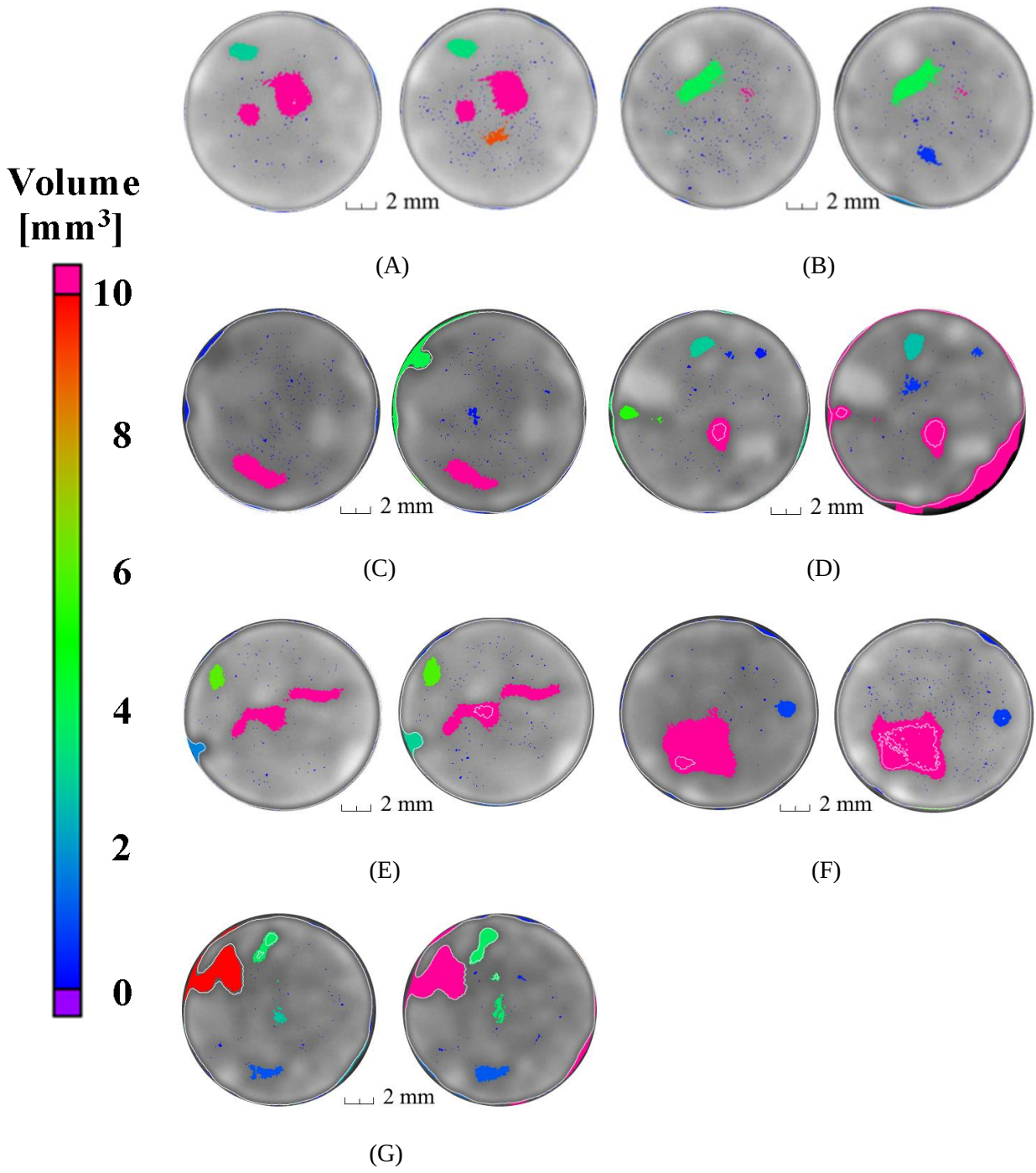

Figure 3.19. 2D Section of Specimens (A) FW4, (B) FW5/FS10. (C) FW6, (D) FW7, (E) FS5, (F) FS20, and (G) FS30 before (Left) and after (Right) Exposure to 40 Freeze-Thaw Cycles

3.4. Conclusions

The effects of W/C and S/C ratios on concrete's pore morphology and corrosion and freeze-thaw damage mechanisms were investigated using 3D µCT images. The pore structures of the specimens were monitored, analyzed, and correlated to the resulted corrosion and freeze-thaw damage, and the following points were concluded.

- Micro-computed tomography (µCT) imaging is an excellent non-destructive tool for investigating the pore characteristics, including the accessibility, size, shape, and distribution of air voids, in addition to the mechanisms of microstructural concrete damage.

- Increasing the W/C and S/C ratios degraded the quality of the concrete's pore structure, making it more susceptible to reinforcement corrosion and freeze-thaw damage.
- The severity and mechanisms of reinforcement corrosion and freeze-thaw seem correlated with the pore structure's quality. For example, while specimen CW5 experienced minor and uniform corrosion, sample CW8 suffered severe pitting corrosion. Similarly, specimens FW4 and FW5 (FS10), which were produced using the appropriate W/C ratios of 0.4−0.5 and S/C ratio of 1, experienced a minor yet almost uniform expansion of both open and internal (closed) pores. On the other hand, the other concrete samples suffered more dominant expansion within the open pores, leading to accelerated and more severe scaling damage.

- Using a W/C ratio of 0.5 and an S/C ratio of 1 produced concrete with the highest resistance to reinforcement corrosion and freeze-thaw damage.

- Air voids surrounding the steel reinforcement greatly impacted its corrosion mechanisms, making it more prone to pitting corrosion.
- Assessing the freeze-thaw resistance using multiple pore properties is recommended because using one property (e.g., pore sphericity) can be considerably impacted by frost-induced pore expansion and scaling damage.
- The open-pore ratio and pore gap substantially impact the confinement, pore distribution, and freeze-thaw resistance of concrete. Thereby, analyzing these two parameters is critical for assessing the freeze-thaw resistance.

Chapter 4: CT Imaging of Large Naturally Corroded Reinforced Concrete Element

This chapter investigates the accuracy of three-dimensional detection of reinforcement corrosion within large concrete elements using an industrial micro-computed (μCT) imaging system.

4.1. Introduction

Reinforcement corrosion is one of the leading causes of concrete damage [8,209]. Thus, extensive research has been conducted during the last decades to thoroughly understand the mechanisms of reinforcement corrosion using different techniques such as energy dispersive X-ray spectrometry (EDS) and acoustic emission testing (AET) [88,210]. These methods, however, provide limited details of corrosion distribution and damage mechanisms. Hence, researchers started using an innovative non-destructive micro-computed tomography (μCT) to track and measure corrosion of reinforced structural elements [55,90,92,93,100]. However, most research has focused on small-diameter steel wires and bars, which are 0.5–3 mm in diameter [90,93,98].

Sun et al. (2017) investigated the corrosion of a 3 mm steel wire embedded in a 10 mm cement cylinder. The sample was CT scanned using tube voltage and current of 135 kV and 73.5 μA, respectively [93]. It was noted that the corrosion process was accelerated by the neighboring cracks exposing the steel wire to surrounding fluids. On the other hand, Itty et al. (2014) compared the corrosion and cracking mechanisms of 0.46 mm carbon steel and 0.37 mm stainless steel wires, each of which was inserted into a 5 mm cement cylinder [90]. After CT imaging the samples using a photon energy of 43 keV, it was observed that while corrosion was homogenous within the carbon steel wire, it was localized in the stainless-steel wire leading to a higher depth of pitting

corrosion. Corrosion products of the stainless-steel wire also resulted in larger cracks within the cement paste than the corroded carbon steel wire.

Dong et al. (2017) measured the corrosion content of a 2 mm carbon steel rod inserted into a 10 mm cement cylinder using computed tomography with a photon energy of 139 keV and a current of 62 μA [92]. The CT results were reported to correlate well with the mass-loss data attained using sample weighing and computed using Faraday's law. Similarly, Van Steen et al. (2019) measured the corrosion content using CT imaging by applying a voltage of 180 kV and a current of 140 μA and compared its results to the mass-loss data determined by sample weighing and Faraday's law [100]. However, it was found that the CT results were in disagreement with the other techniques because of the inadequate resolution of the μCT images. On the other hand, Dong et al. (2018) studied the time dependence of reinforcement corrosion and the associated crack initiation and propagation [55]. The corrosion of a 2.5 mm steel rebar embedded into a 1,000 mm^3 concrete cube was examined using CT imaging by applying a voltage of 70 kV and a current of 62 μA. Different phases of the corrosion process were identified, namely, corrosion initiation, rust expansion, and concrete cracking.

Limited research examined the potential of utilizing CT imaging to detect corrosion products within large naturally corroded concrete specimens. Hence, the main objective of this chapter is to investigate the distribution of corrosion products and the damage mechanisms of a large naturally corroded 50-year-old concrete element using CT imaging.

4.2. Materials and Methodologies

4.2.1. Specimen

A large reinforced concrete block with excessive natural corrosion, shown in Figure 4.1 (A), was obtained from a 50-year-old building. The specimen was cut into a 12×6×17 cm^3 (width × depth × height) sample, shown in Figure 4.1 (B), to remove the unaffected concrete mass and to improve imaging quality by reducing beam hardening artifacts. Through visual inspection, it was observed that corrosion did not affect the internal depth of the concrete (i.e., the negative Z direction shown in the figure opposite to the concrete cover). Most of the corrosion damage occurred on the surface of the steel reinforcement facing the external concrete cover resulting in substantial concrete cracking. Also, corrosion appeared to propagate into the sides (X direction) of the 10M steel rebar. The corrosion products seen at the bottom left of Figure 4.1 (B) were caused by another corroded steel rebar orthogonal to the rebar under consideration.

(A) (B)

Figure 4.1. Naturally Corroded Reinforced Concrete before Cutting (A), and after Cutting (B)

4.2.2. CT Imaging

An industrial micro-computed tomography (μCT) was utilized to scan the concrete sample using high-energy imaging parameters to enhance the quality of CT images. Using a tube voltage of 200 kV and a current of 100 μA was sufficient to scan the large concrete element without overloading the imaging system. Also, a copper filter with a thickness of 0.5 mm was used to block low-energy photons and minimize imaging artifacts. One thousand images were collected as the specimen was spinning 360^{o} using an acquisition time of 333 milliseconds per image. High-quality CT images were captured using a spatial resolution (voxel size) of 142 μm. The corroded concrete specimen was scanned in its standing position, previously shown in Figure 4.1 (B), to improve the quality of CT images by minimizing the beam-hardening and metal artifacts. It is worth noting that applying a higher tube voltage can degrade the contrast of the CT images, whereas increasing the current and the image-acquisition time can damage the X-ray detector.

4.2.3. Post-Processing of CT Images

The captured CT images were post-processed using Volume Graphics software (VGStudio). The images were stacked, as shown in Figure 4.2 (A), to create a three-dimensional (3D) reconstruction of the concrete element, as illustrated in Figure 4.2 (B). Three-dimensional image filtration (3×3×3 pixels), such as a median filter, was applied to improve the detection accuracy of corrosion products and air pores by minimizing the scanning artifacts (i.e., beam-hardening and metal artifacts), as shown in Figure 4.3. Also, material thresholding was used to segment the intact steel reinforcement (blue highlight) and the corrosion products (red highlight) from the concrete. Similarly, a built-in void detection algorithm was applied to highlight the air pores within the concrete element, as illustrated in Figure 4.3. The detected corrosion products and the air voids in

the concrete section were analyzed separately to demonstrate the corrosion distribution and damage mechanisms, as discussed in the following sections.

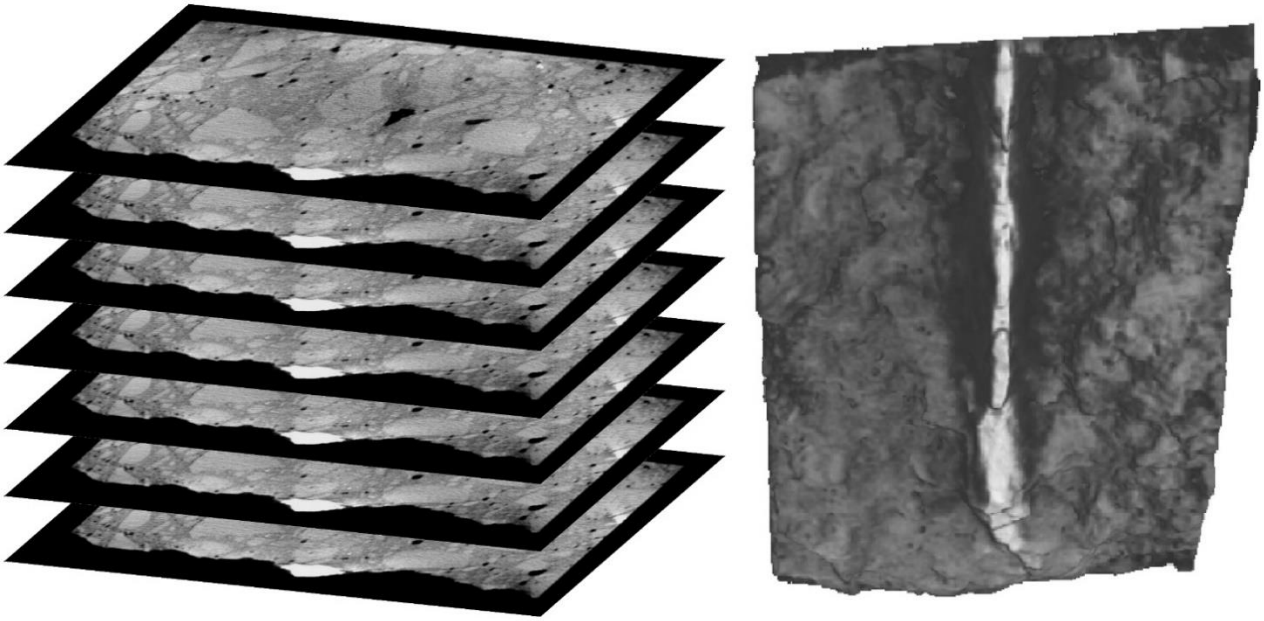

(A) (B)

Figure 4.2. Three-dimensional (A) Image Stacking, and (B) Reconstruction of the Concrete Specimen

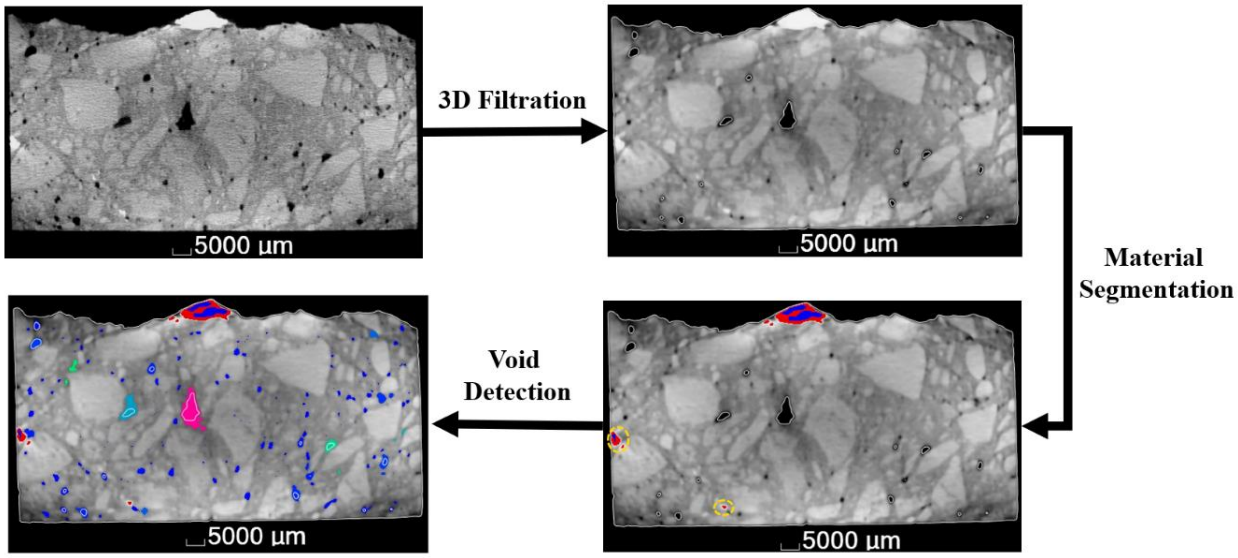

Figure 4.3. Steps of Post-Processing the CT Images

4.3. Results and Discussion

4.3.1. General

A large 50-year-old naturally corroded concrete specimen was scanned using a high-energy CT imaging system. The CT images were processed and reconstructed into the 3D model shown in Figure 4.4 (A). Material segmentation was applied to separate the intact steel reinforcement and the corrosion products from the concrete part, as illustrated in Figure 4.4 (B and C). The corrosion damage within the steel reinforcement and concrete element was investigated. It was observed that the steel reinforcement experienced severe corrosion, mostly within its exposed surface facing the already delaminated concrete cover. The other side of the steel reinforcement was protected by the surrounding concrete; hence, it experienced minor corrosion damage. By measuring the volume of the intact steel reinforcement, it was determined that the corrosion damage disintegrated two-thirds of the volume of the steel reinforcement. On the other hand, the damage mechanisms of the concrete element were investigated by analyzing the distribution of air pores to track the path of concrete cracking. It was observed that the volume of air pores surrounding the steel reinforcement was low, indicating the absence of cracks toward the core of the concrete element. Thereby, the corrosion-induced cracking propagated mostly along the delaminated surface of the concrete element.

The distribution of corrosion products was also investigated, and it was observed that the corrosion products dispersed mostly around the exposed area of the steel reinforcement and the delaminated surface of the concrete specimen. Also, it was noted that the corrosion products and staining did not spread to the inner core of the concrete element, which confirms that the corrosion-induced cracks occurred mostly within the delaminated concrete surface. Additionally, the accuracy of corrosion detection using CT imaging was examined by visually comparing the detected corrosion

products with the actual corrosion of the concrete specimen. It was found that CT imaging is capable of accurately capturing most of the corrosion products of the large concrete element. Also, it was observed that mere corrosion stains were not detectable, attributed to the low X-ray attenuation of corrosion stains. Also, it was observed that small parts of some aggregates were falsely detected as corrosion products, possibly due to the minerals within these aggregates in addition to the beam-hardening and metal imaging artifacts. It is possible to improve the accuracy of corrosion detection by ignoring the falsely detected corrosion products that are a certain distance away from the steel reinforcement, as discussed in the following sections.

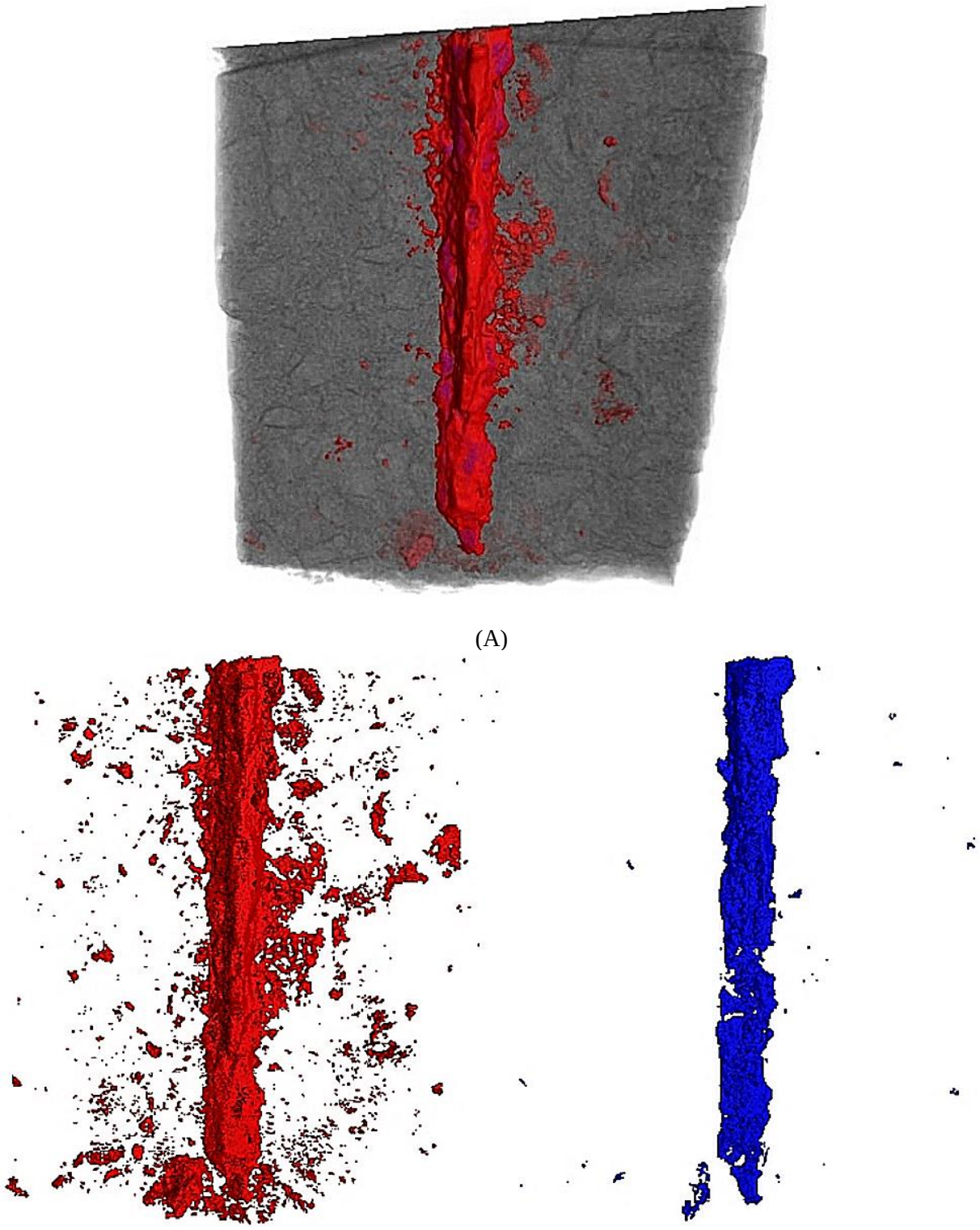

(A)

(B) (C)

Figure 4.4. 3D Reconstructions of (A) Corroded Concrete Specimen, (B) Detected Rust, and (C) Exposed Surface of Steel Reinforcement

4.3.2. Corrosion Damage

The severity of corrosion-induced degradation of concrete structures can be determined by analyzing the damage within the steel reinforcement and the surrounding concrete. The corrosion level of the steel reinforcement was estimated by measuring the volumetric ratio of intact steel to the rebar's original volume. It was observed that the volume of the uncorroded segment of the 10M steel rebar is 4195.4 mm^3, and its original volume was around 12,750 mm^3, which was calculated using the rebar's length and original cross-sectional area. Therefore, only one-third of the steel rebar remained intact. Also, it was noted that while the exposed surface of steel reinforcement experienced severe corrosion, as shown in Figure 4.5 (A), the other side of the steel rebar surrounded by the concrete was fully intact and experienced only minor corrosion. The absence of significant corrosion within the protected segment of the steel reinforcement was proven by its clearly visible clamps, as illustrated in Figure 4.5 (B).

On the other hand, it is hard to determine the severity of corrosion-induced concrete damage since the specimen is part of a concrete structure that was subjected to different loads and environments for 50 years. However, CT imaging made it possible to investigate the distribution of air pores within the concrete element, which can provide an indication of the concrete damage mechanisms. Thus, the air pores of the concrete element were detected and analyzed, and three-dimensional reconstructions of the pore structure and the intact steel reinforcement (blue colored) were demonstrated in Figure 4.6. As illustrated, the concrete element had mostly small pores (red colored) and some large voids dispersed throughout the specimen. It is worth noting that no cracks were detected within the concrete element, which indicates that the concrete cracks propagated mostly within the delaminated concrete surface. To better analyze the air pore distribution, the accumulated pore volumes along the concrete width (analysis direction shown in Figure 4.6) were

computed and plotted in Figure 4.7. It was observed that the accumulative volume of air pores was nearly uniform along the concrete width. Also, it was noted that the pore volume across the location of steel reinforcement (black dashed line) was only slightly higher than the average accumulative pore volume (red dashed line), indicating the absence of corrosion-induced pore expansion and cracking. Based on the results, the concrete element only experienced cracking within the delaminated surface.

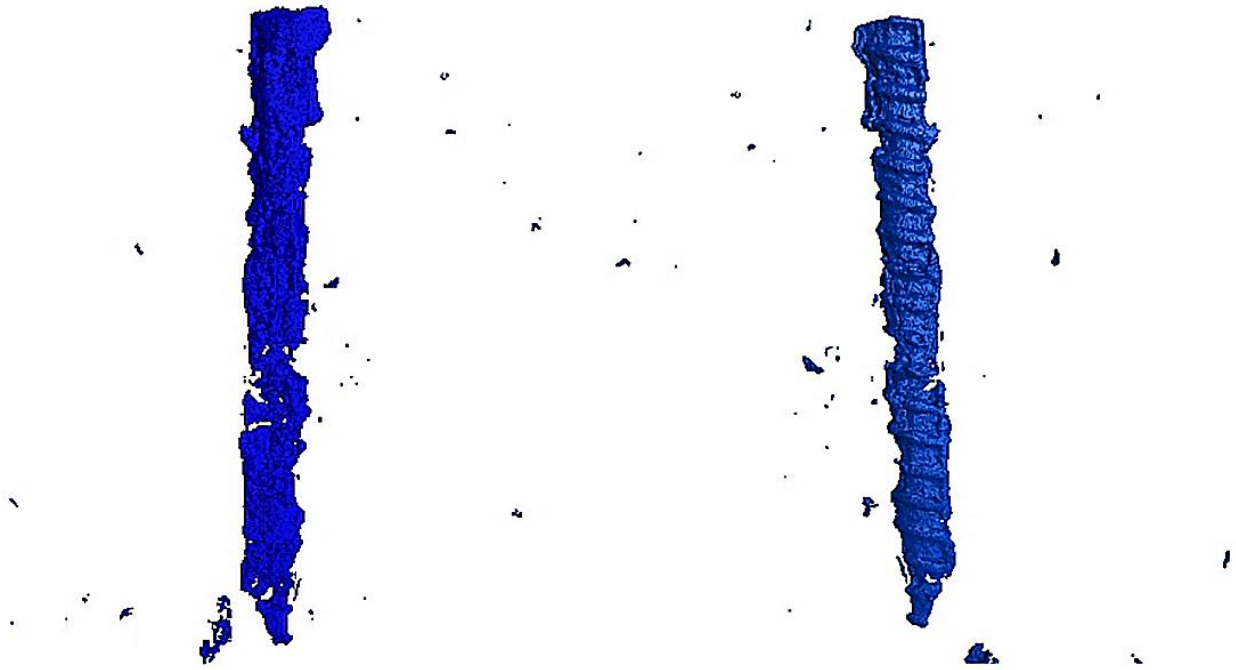

(A) (B)

Figure 4.5. 3D Reconstructions of (A) the Exposed Side of Steel Reinforcement, and (B) the Covered Side of Steel Reinforcement

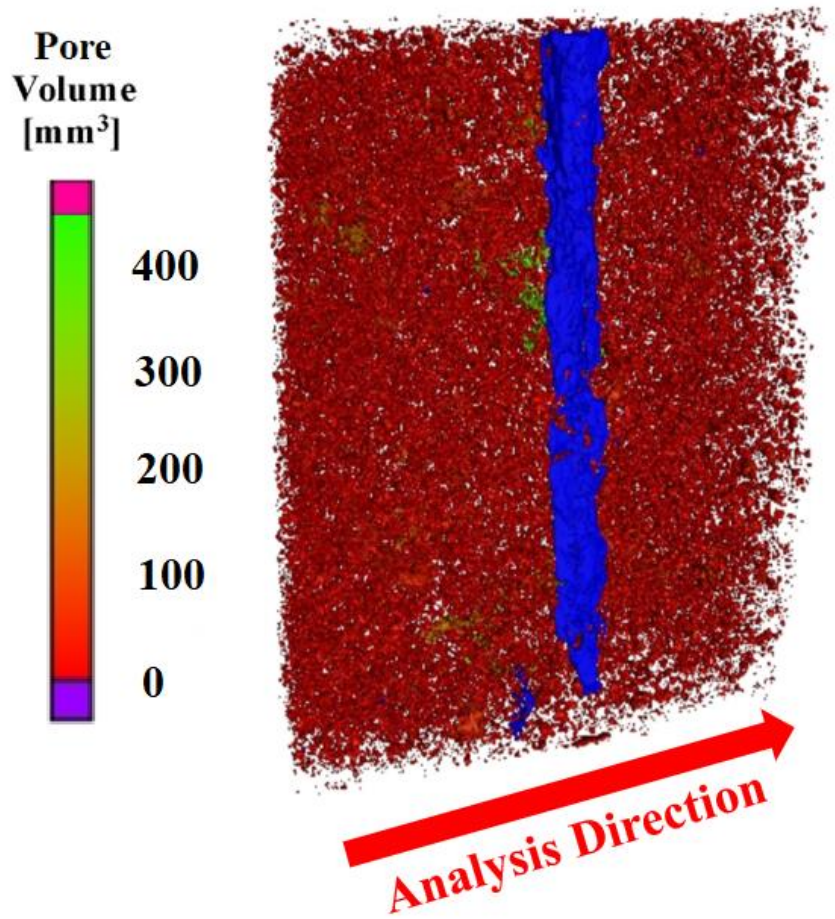

Figure 4.6. Detected Air Pores and the Analysis Direction of Accumulated Pore Volume

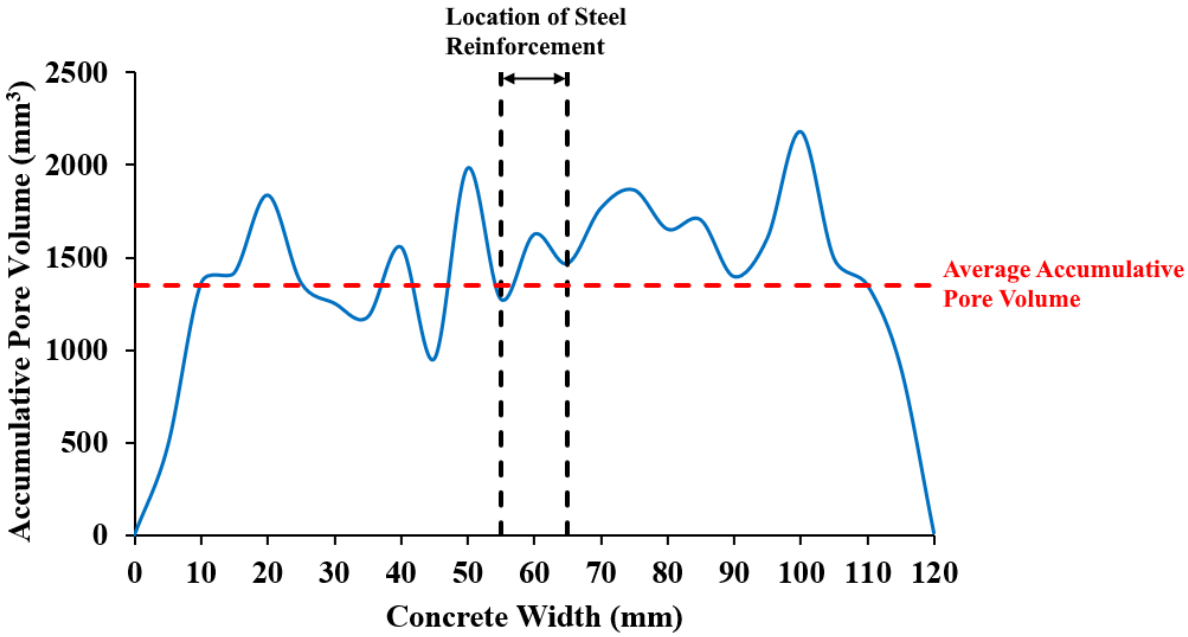

Figure 4.7. Accumulative Pore Volume along the Concrete Width

4.3.3. Corrosion Distribution and Detection Accuracy

The distribution of detected corrosion products was investigated. It was observed that the exposed surface of steel reinforcement experienced severe corrosion that resulted in a dispersed distribution of corrosion products, as illustrated in Figure 4.8 (A). It was observed that small parts of some aggregates were falsely detected as corrosion products, as highlighted in Figure 4.9. It is, however, visually possible to distinguish the actual corrosion products from the falsely detected ones. Thus, it is feasible to enhance the accuracy of corrosion detection by removing the falsely detected aggregates manually or through automated algorithms. One simple method for improving the detection accuracy is removing the corrosion products that are a specific distance away from the steel reinforcement, which can be determined from the CT images. By applying this method, most falsely detected aggregates were disregarded, leaving only the actual corrosion products demonstrated in Figure 4.8 (B).

To examine the accuracy of corrosion detection, some of the detected corrosion products were visually compared to the corroded concrete specimen, and a clear correlation was observed, as shown in Figure 4.10. The micro-computed tomography successfully captured most of the visible corrosion products despite the large size of the concrete sample. It is worth noting that some minor corrosion stains were not detectable because the mere color contents of these stains are insufficient for creating contrast within the CT images. Thereby, it can be concluded that the CT imaging system can capture vital corrosion products within large concrete elements in a non-destructive and timely manner.

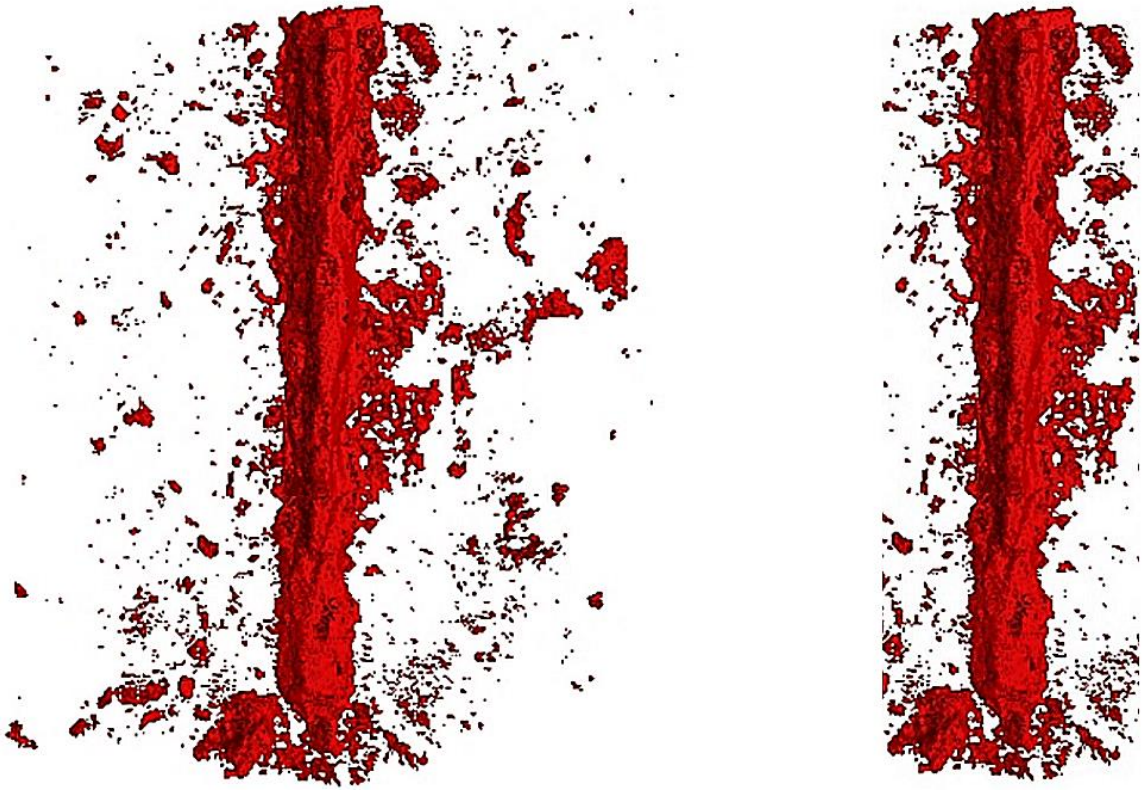

(A) (B)

Figure 4.8. Detected Corrosion Products

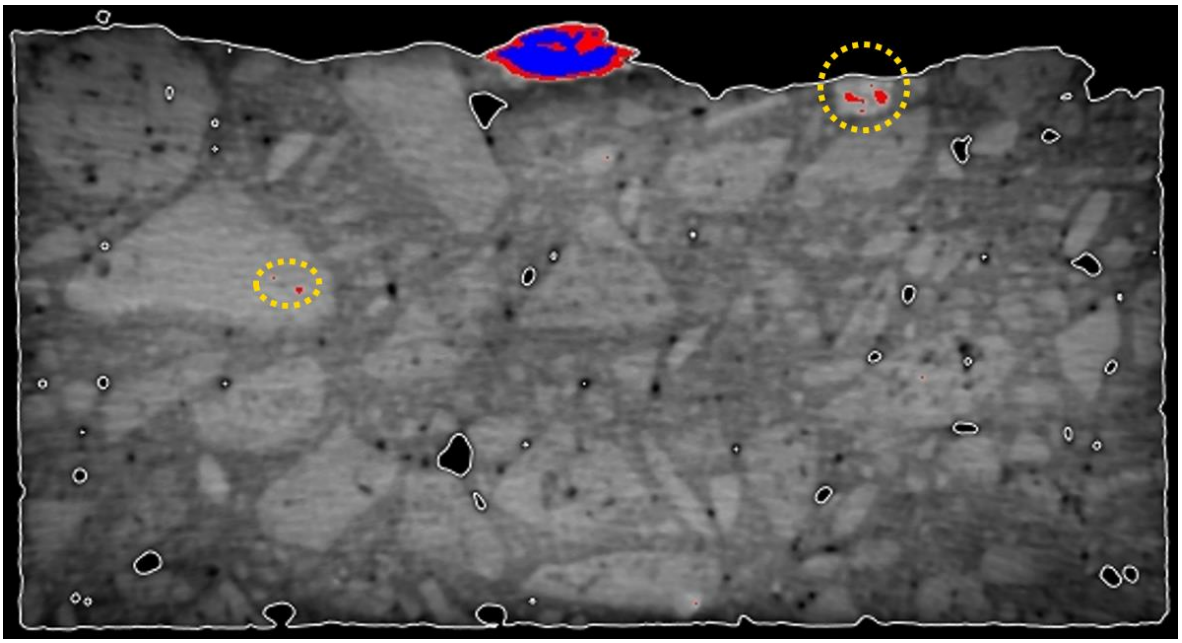

Figure 4.9. Top-View Section of the Specimen Showing the Uncorroded Rebar (Blue), Corrosion Products (Red), and Falsely Detected Aggregates (Highlighted)

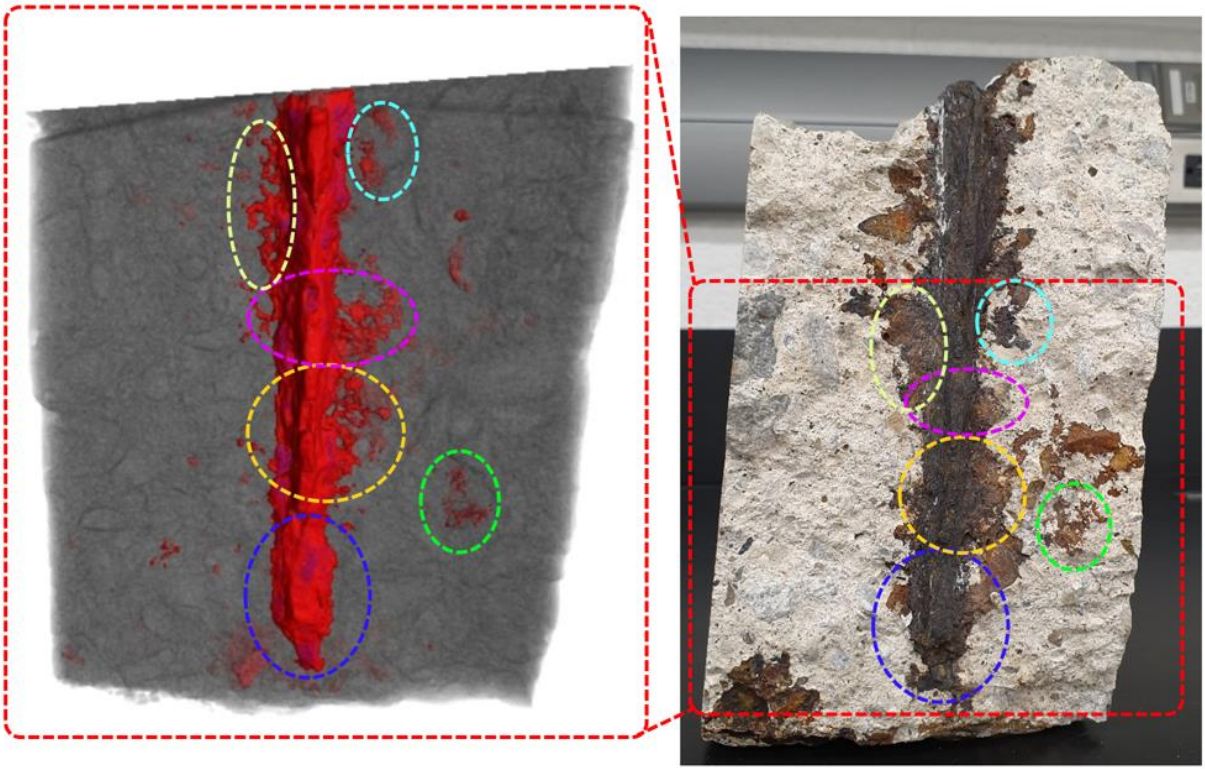

(A) (B)

Figure 4.10. Comparison between (A) Detected Corrosion Products, and (B) Actual Rust

4.4. Conclusions

The natural reinforcement corrosion of a large 50-year-old concrete specimen was investigated using high-resolution micro-computed tomography (µCT), and the following points were concluded.

- CT imaging enabled the detection of corrosion products within large concrete elements.
- The steel reinforcement experienced severe corrosion that disintegrated two-thirds of its volume. Also, while the exposed surface of the steel bar was considerably damaged, the reinforcement surface surrounded by the concrete material was well protected, as indicated by the intact rebar ribs.

- The detected corrosion products were mostly surrounding the exposed surface of steel reinforcement, and no cracks were detected toward the core of the concrete element, indicating that cracks propagated mostly within its delaminated surface.
- Small parts of some aggregates were falsely detected as corrosion products due to imaging artifacts and the minerals within the aggregates. Thus, the accuracy of corrosion detection can be improved by enhancing the imaging resolution and disregarding the falsely detected aggregates that are a certain distance away from the steel reinforcement.

Chapter 5: CT Imaging of Concrete Damage under Coupled Freeze-Thaw and Sulfate Attack Conditions

This chapter investigates the severity and mechanisms of freeze-thaw damage of concrete in potassium sulfate and magnesium sulfate environments with different concentrations using a high-resolution micro-computed tomography (μCT) imaging system.

5.1. Introduction

It is well known that prolonged exposure of concrete material to detrimental environments, such as freeze-thaw and sulfate environments, can accelerate its degradation, which eventually results in more extensive rehabilitation work requirements [211–214]. Thus, a deeper understanding of concrete's freeze-thaw and sulfate damage is vital for taking preventive measures. Frequent exposure to sub-zero temperatures can induce expansive internal pressure within the concrete by freezing the water retained within its capillaries, leading to severe layer-by-layer scaling damage normally initiating at the external surface and propagating inward [59,61,72–74,153,215,216]. Also, the recurrent fluctuation between freezing (e.g., -20 ^{o}C) and mild (e.g., 10 ^{o}C) environments can cause cracking within the mortar-aggregate interfacial transmission zone (ITZ) due to the mismatching thermal expansion coefficients of these two materials [28]. The severity of the freeze-thaw damage is directly impacted by the concrete's strength and pore morphology. As observed by Alhusain and Al-Mayah (2022), concrete with large surface pores is quite vulnerable to frost damage [217].

On the other hand, prolonged exposure to sulfate salts, such as magnesium sulfate ($MgSO_4$) and potassium sulfate (K_2SO_4), weakens the concrete strength by chemically reacting with the calcium hydroxide of its cement paste, producing expansive materials such as gypsum, thaumasite, and

ettringite [218–224]. These expansive by-products precipitate within the concrete capillaries, causing expansive internal pressure and spalling damage [225–228]. Also, concrete exposure to sulfate environments can accelerate the de-passivation of its steel reinforcement, causing earlier and more severe corrosion damage [229]. The severity of sulfate damage is affected by multiple parameters, including the type and concentration of the sulfate salt. It is well-documented that magnesium sulfate is the most detrimental sulfate salt, attributed to its high solubility and reactivity [228,230,231]. Also, increasing the concentration of sulfate salt can accelerate concrete damage. As reported by Cheng et al. (2021), increasing the concentration of sodium sulfate from 3% to 10% increased the mass loss from about 0.9% to 2.3% after 150 days of sulfate exposure [232].

In addition to degrading the concrete strength, both freeze-thaw and sulfate damage increase the concrete permeability, making it more vulnerable to different forms of environmental damage, including reinforcement corrosion, carbonation, and chemical attack [104,154,180,217]. Hence, extensive research has been conducted to investigate the severity and mechanisms of concrete damage under coupled freeze-thaw and sulfate environments. The mesoscale concrete damage under coupled action of sulfate and freeze-thaw was investigated mostly in sodium sulfate solutions. Xiao et al. (2019) examined the freeze-thaw damage of concrete in sodium sulfate solution with a concentration of 5%. It was observed that subjecting concrete to 300 freeze-thaw cycles (2-4 hours each) resulted in a mass loss of 1.7% and a compressive strength reduction of 29.5% [233]. Similarly, Ren and Lai (2021) analyzed the concrete damage after applying 300 freeze-thaw cycles (1,200 hours in total) in Na_2SO_4 solution with a concentration of 5%. The reported concrete mass loss and compressive strength reduction were 0.72% and 56.3%, respectively [207].

Little effort has been dedicated to investigating the microscale damage mechanisms of concrete under coupled action of sulfate and freeze-thaw conditions. Therefore, the main objective of the paper is to study the microstructural freeze-thaw damage of concrete in magnesium sulfate and potassium sulfate environments with 5% and 10% concentrations using high-resolution micro-computed tomography (μCT) imaging. The specimens were scanned using μCT before and after exposure to 40 and 80 freeze-thaw cycles. The effects of the sulfate environments on the severity and mechanisms of frost damage were studied by analyzing mass loss data and the variation of distinct pore properties, including the pore content, size, and accessibility. The damage mechanisms of the concrete were discussed using 2D and 3D images of internal microstructures.

5.2. Materials and Methodologies

5.2.1. Specimens

Five concrete specimens of the same mixture proportions were prepared using small aggregates (<5 mm), fine sand, and ordinary Portland cement, which has the chemical composition listed in Table 5.1. The utilized concrete mixture had water-to-cement, sand-to-cement, and aggregate-to-cement ratios of 0.5, 1, and 1.5, respectively. The samples, shown in Figure 5.1, were 40 mm long and 15 mm in diameter. The specimens were de-molded 24 hours after casting and water cured for 28 days at a temperature of 20 ^{o}C before μCT imaging and frost testing. The specimens were labeled based on the freeze-thaw environment. For example, specimens PS-10% and MS-10% were subjected to frost cycles in potassium sulfate and magnesium sulfate solutions, respectively, with a concentration of 10%. As discussed in the following sections, the specimens have similar pore properties, mitigating the need for duplicate samples.

Table 5.1. Chemical Composition of Portland Cement [234]

Chemical Composition (wt. %)								
CaO	SiO_2	Al_2O_3	Fe_2O_3	SO_3	MgO	CO_2	K_2O	Na_2O
62.9	20.6	4.4	3.3	3.2	2.2	1.5	0.5	0.19

(A) (B) (C) (D) (E)

Figure 5.1. (A) Control, (B) PS-5%, (C) PS-10%, (D) MS-5%, and (E) MS-10% Concrete Specimens

5.2.2. Cyclic Freeze-Thaw Exposure

The concrete specimens were tested under different freeze-thaw environments: water (control), magnesium sulfate (MS-5% and MS-10%), and potassium sulfate (PS-5% and PS-10%) at concentrations of 5% and 10%, as listed in Table 5.2. The concentrations of sulfate salts were selected in order to compare the CT results with the existing values reported in the literature. Before testing, the samples were immersed into the associated solutions for at least 6 hours to ensure full saturation, after which the specimens were subjected to 80 freeze-thaw cycles. Each

cycle consisted of 12.5 hours of freezing and 11.5 hours of melting to mimic actual freezing environments. Each cycle started at a temperature of about 11 ^{o}C and then cooled down to a temperature of -25 ^{o}C with an average cooling rate of -13.5 ^{o}C/hour. The temperature was allowed to fluctuate between -18 ^{o}C and -25 ^{o}C for 7.2 hours to fully freeze the specimens. Afterward, the temperature was gradually increased with an average warming rate of 1.9 ^{o}C/hour. The applied environment temperature throughout each freeze-thaw cycle is demonstrated in Figure 5.2.

Table 5.2. Composition of Freeze-Thaw Solution

Specimen	Solution
Control	Tap water
PS-5%	Tap water + 5 wt.% of K_2SO_4
PS-10%	Tap water + 10 wt.% of K_2SO_4
MS-5%	Tap water + 5 wt.% of $MgSO_4$
MS-10%	Tap water + 10 wt.% of $MgSO_4$

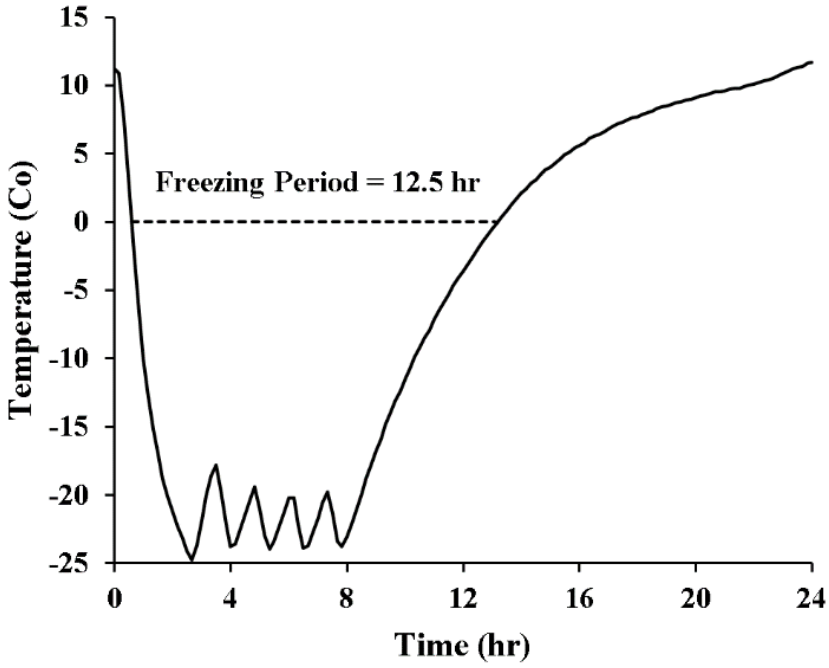

Figure 5.2. Temperature of Controlled Environment throughout Each Freeze-Thaw Cycle [217]

5.2.3. µCT Imaging

Three-dimensional images of the concrete specimens were collected before and after every 40 freeze-thaw cycles using industrial micro-computed tomography (µCT). One thousand images were captured using the tube voltage and current of 100 kV and 80 µA, respectively. The scanning resolution (voxel size) is 49.1 µm and the X-ray exposure period per image is 0.33 seconds. The 3D images were segmented and analyzed using thresholding and median filtration (3×3×3 pixels) available in the VGStudio MAX 2.2 software to minimize scanning artifacts. Microstructural pore analysis was conducted on the 36 mm long mid-segment of the specimens to reduce inconsistencies that may be caused during casting near the bottom and top ends.

5.3. Results and Discussion

5.3.1. General

Before subjecting the concrete specimens to the freeze-thaw cycles in different sulfate environments, the pore microstructures of the specimens were investigated using µCT imaging to confirm that they have comparable pore properties, which is essential for attaining reliable results. It was found that the average porosity, large-pore ratio, and open-pore ratio of the specimens were 3.92% (±0.52%), 88.5% (±2.27%), and 26.6% (±3.18%), respectively. Thus, the samples have similar pore characteristics, as indicated by the low standard deviations.

After 40 freeze-thaw cycles, it was observed that exposure to potassium sulfate accelerated the frost damage of specimens PS-5% and PS-10%, as illustrated in Figure 5.3 (D and E). The damage within the other specimens was not visually clear; thus, another 40 cycles (80 cycles in total) were applied. While the control sample experienced severe scaling damage, specimens PS-5% and PS-10% were completely disintegrated, as shown in Figure 5.4 (A, D,

and E). On the other hand, specimens MS-5% and MS-10% experienced minimal damage, as demonstrated in Figure 5.4 (B and C). Thereby, exposure to magnesium sulfate considerably improved the freeze-thaw resistance of concrete.

The frost damage mechanisms were investigated using μCT imaging. It was found that exposure to potassium sulfate accelerated the freeze-thaw damage without affecting its typical mechanisms, where the damage initiates at the surface and propagates inward, as illustrated by the large pink void highlighted in Figure 5.5 (A). For example, specimens PS-5% and PS-10% experienced a considerable increase in porosities, large-pore ratios, and open-pore ratios. In contrast, exposure to magnesium sulfate minimized the frost damage and altered its mechanisms. It was observed that the expansion of the internal pores of specimens MS-5% and MS-10% was more dominant than the surface voids. In other words, the frost damage initiated from within, as demonstrated in Figure 5.5 (B), unlike the typical freeze-thaw damage that occurs at the external surface and propagates inward on a layer-by-layer basis. In addition, the freeze-thaw resistance of specimen MS-5% was enhanced after being subjected to 40 cycles, attributed to the filling of the surface voids by the precipitated sulfate salt and its chemical by-products, which was verified by applying another 40 cycles. Also, it was observed that increasing the concentration of magnesium sulfate decreased its positive effect on frost resistance. Thereby, sample MS-10% experienced relatively more scaling damage than specimen MS-5%. It is worth noting that specimen MS-10% experienced less severe and more uniform frost damage than the control sample, indicating the beneficial effect of magnesium sulfate even at high concentrations.

(A) (B) (C) (D) (E)

Figure 5.3. (A) Control, (B) MS-5%, (C) MS-10%, (D) PS-5%, and (E) PS-10% Concrete Specimens after 40 Freeze-Thaw Cycles

(A) (B) (C)

(D) (E)

Figure 5.4. (A) Control, (B) MS-5%, (C) MS-10%, (D) PS-5%, and (E) PS-10% Concrete Specimens after 80 Freeze-Thaw Cycles

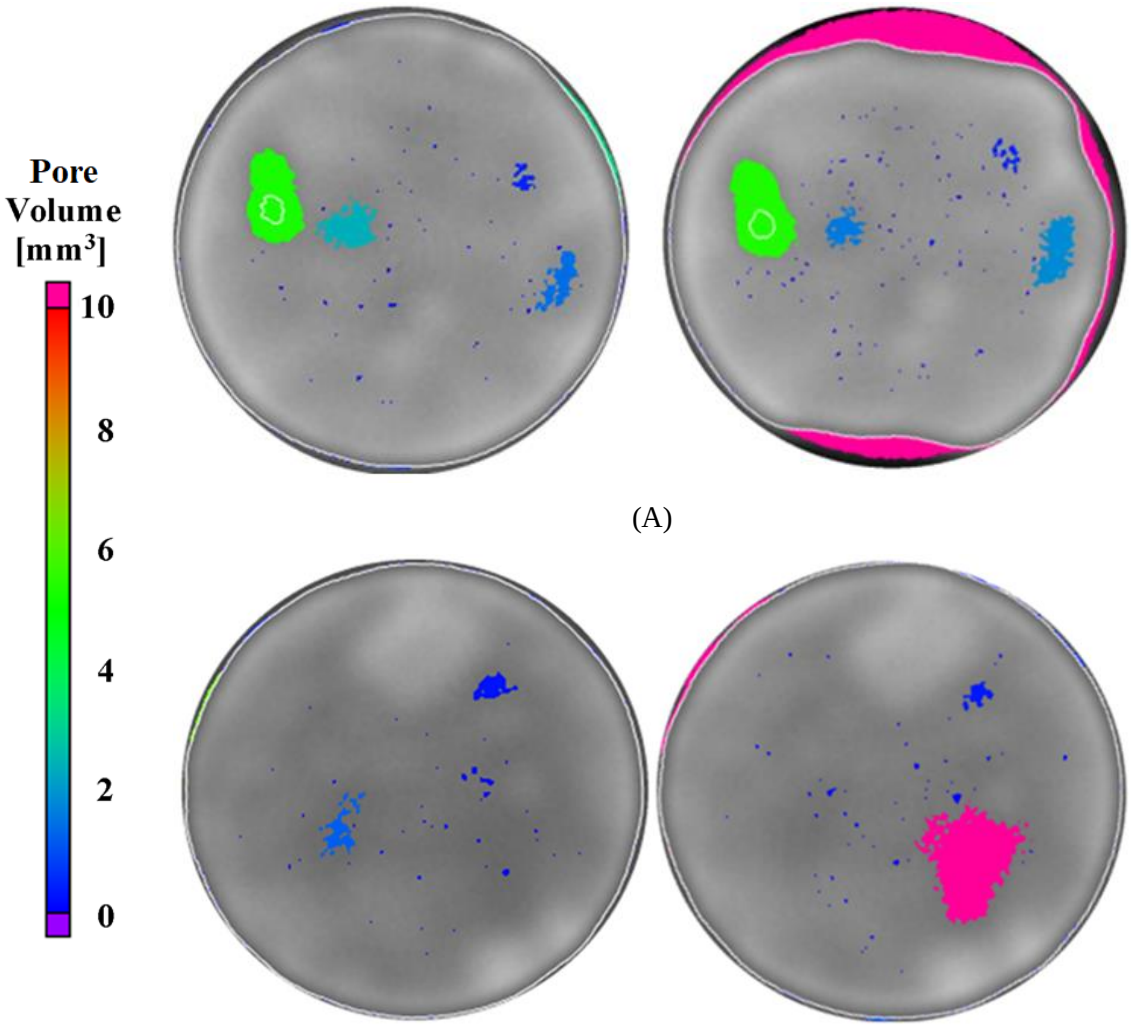

Figure 5.5. 2D CT Images of Specimens (A) PS-10%, and (B) MS-10% before (Left) and after 40 (Right) Freeze-Thaw Cycles

5.3.2. Mass Loss

Mass loss analysis was conducted using a sensitive scale (± 0.01 g) before and after every 40 freeze-thaw cycles, as demonstrated in Figure 5.6. After applying 40 cycles, it was observed that the specimens Control, PS-5%, and PS-10% endured comparable mass losses of 4.35%, 5.06%, and 3.56%, respectively. On the other hand, the mass losses of specimens MS-5% and MS-10% were 0.78% and 0.95%, which are significantly lower than the control sample. Another 40 freeze-thaw cycles (80 in total) were applied to illustrate the effects of

the sulfate environments on the frost damage more clearly. It was noted that the control sample suffered a mass loss of 19.57%, while specimens PS-5% and PS-10% were fully disintegrated. Thus, exposure to potassium sulfate clearly accelerated the frost damage of concrete. In contrast, specimens MS-5% and MS-10% experienced minor mass losses of 1.08% and 1.67%. Evidently, exposure to magnesium sulfate with a concentration of 5% enhanced the freeze-thaw resistance of concrete due to the filling of surface pores by the precipitated sulfate by-products, as illustrated in Figure 5.7 and discussed in the following sections. Also, increasing the concentration of magnesium sulfate resulted in higher mass loss, possibly because increasing the concentration of the sulfate salt accelerated the sulfate damage [232].

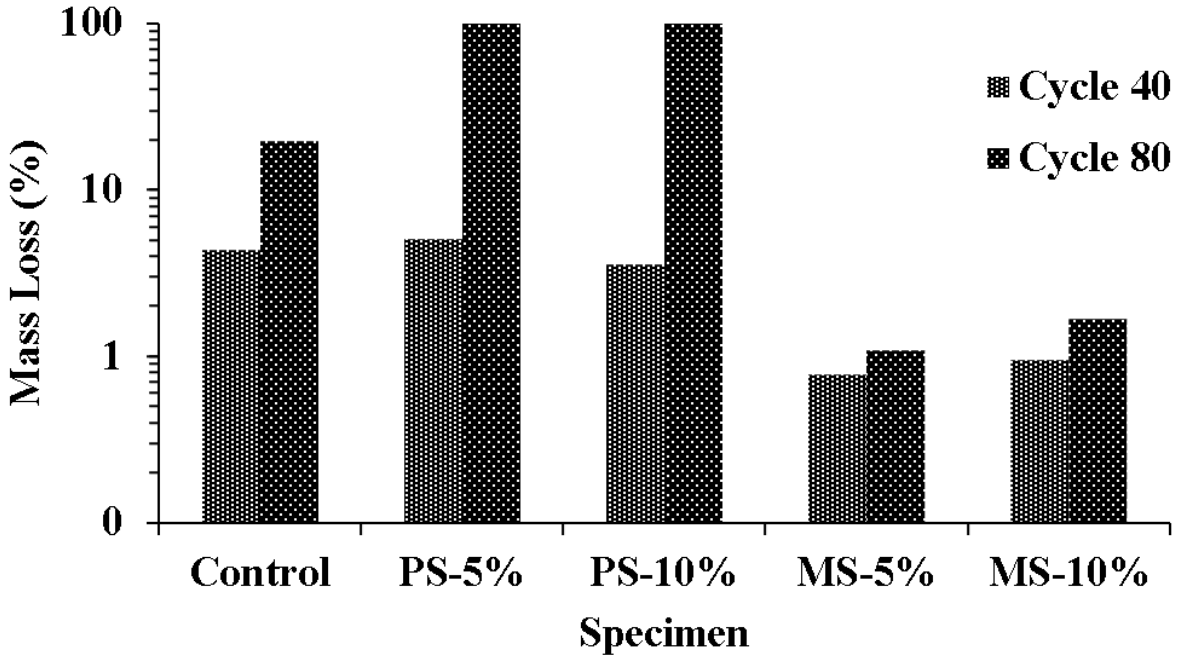

Figure 5.6. Frost-Induced Mass Loss (%) of Concrete Specimens

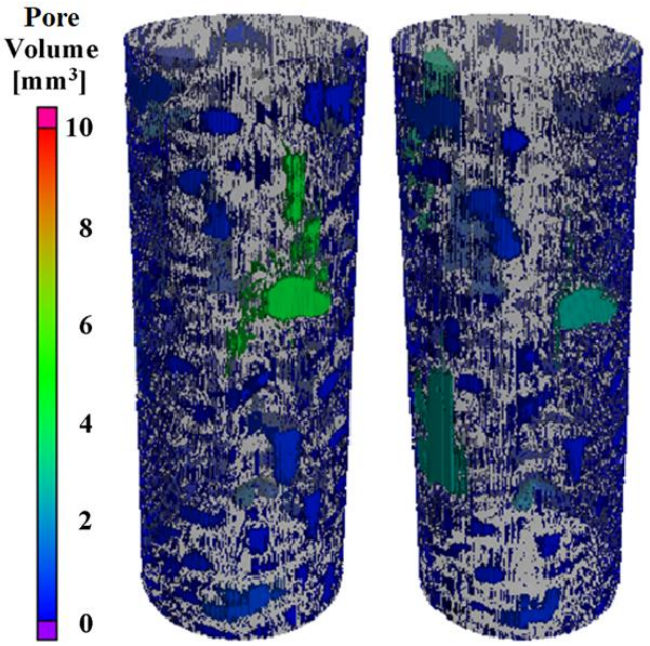

(A) (B)

Figure 5.7. Surface Pores of Specimen MS-5% (A) before, and (B) after 40 Freeze-Thaw Cycles

5.3.3. Frost Damage Characterization Using Pore Properties

5.3.3.1. Porosity

Porosity is the ratio of the total pore volume to the total volume of the specimen. The porosity variation during the freeze-thaw cycles can provide an indication of the rate of pore expansion, illustrating the severity of concrete damage. The porosity of the concrete specimens was analyzed before and after 40 and 80 cycles, as demonstrated in Figure 5.8. It was observed that the samples had comparable initial porosities ranging from 3.22% to 4.59%, with an average porosity of 3.92% (±0.52%). Applying 40 freeze-thaw cycles considerably increased the porosity of samples PS-5% and PS-10% to 5.29% (+0.89%) and 6.07% (+1.48%), demonstrating the detrimental effect of potassium sulfate exposure. On the other hand, specimens Control and MS-5% experienced minor porosity expansion to 4.22% (+0.32%) and 3.86% (+0.37%), respectively. As previously noted, increasing the concentration of magnesium sulfate to 10% resulted in greater freeze-thaw damage

and higher porosity of 3.99% (+0.77%), attributed to the fact that increasing the concentration of $MgSO_4$ accelerated the sulfate damage.

After applying another 40 freeze-thaw cycles (80 cycles in total), it was noted that specimens PS-5% and PS-10% were completely disintegrated, indicating a significant reduction of the freeze-thaw resistance. Similarly, the control specimen's frost damage rate accelerated significantly as it was subjected to more cycles, increasing its porosity to 13.89% (+9.67%). On the contrary, the porosity of specimens MS-5% and MS-10% expanded slightly to 4.24% (+0.38%) and 7.13% (+3.14%). Thus, exposure to magnesium sulfate enhanced the freeze-thaw resistance of concrete, unlike potassium sulfate, which accelerated the frost damage. Although specimen MS-10% initially experienced more pore expansion than the control sample, it endured less damage as more cycles were applied. In other words, prolonged exposure to magnesium sulfate slowed the rate of freeze-thaw damage, attributed to the fact that the sulfate by-products were filling the surface pores and potentially reducing the permeability as more time passed, as discussed further in the following sections.

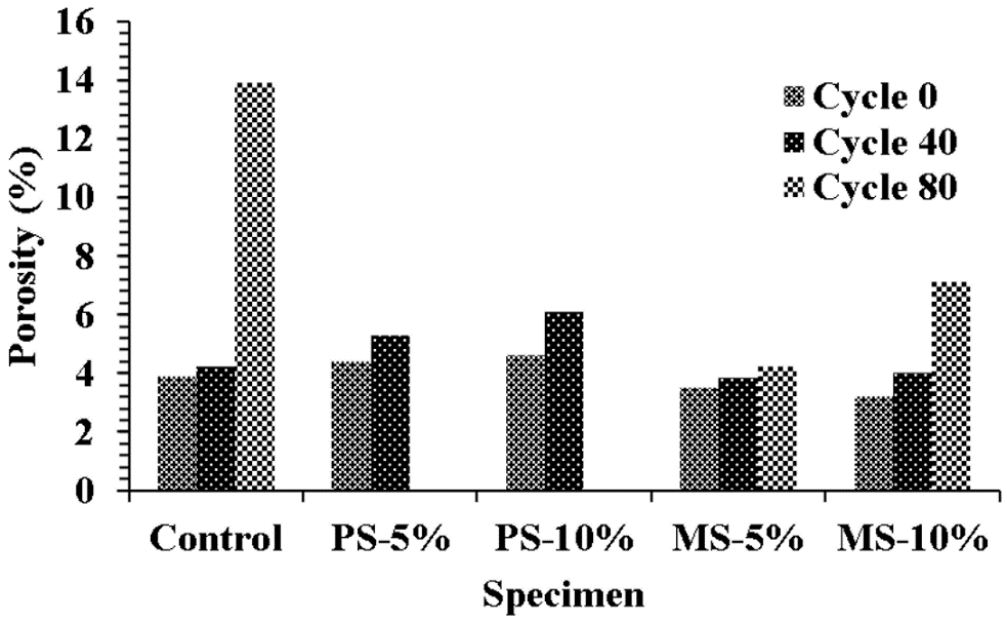

Figure 5.8. Porosity (%) of Concrete Specimens before and after the Freeze-Thaw Cycles

5.3.3.2. Pore Size

The size of voids can significantly impact concrete's freeze-thaw resistance. In general, the larger the pores are, the more water they can retain, resulting in higher expansive stress upon freezing and more concrete damage [217]. Thus, increasing the large-pore ratio, which is the total volume of large voids divided by the total pore volume, can degrade the frost resistance of concrete. In this study, pores with a volume of more than 1.18×10^{6} μm^3, which is 10 times the volume of the smallest detected void, were considered large pores. It was observed that the general trends of the reported results were not sensitive to the applied volume threshold. Increasing the volume threshold from 1.18×10^{6} μm^3 to about 1.00×10^{10} μm^3 had little effect on the discussed observations [217]. In addition to representing the pore size, the variation of the large-pore ratio can demonstrate the expansion dominance of large voids compared to small ones. For example, an increase in the large-pore ratio means that the expansion of the large pores is higher than the small voids. Also, a rapid increase in the large-pore ratio can indicate pore interconnection and cracking of concrete.

The large-pore ratio of the concrete specimens was computed before and after applying 40 and 80 freeze-thaw cycles, as demonstrated in Figure 5.9. The initial large-pore ratios of the samples ranged from 84.7% to 90.6%, with an average of 88.5% (±2.27%). Applying 40 freeze-thaw cycles had a negligible effect on the large-pore ratio of the control specimen, despite experiencing minor porosity expansion, as observed in the previous section. This indicates that the relative growth of small and large pores was comparable, as illustrated by the 3D reconstruction of large voids shown in Figure 5.10 (A). The large-pore ratios of specimens PS-5%, PS-10%, MS-5%, and MS-10% increased to 91.8% (+1.19%), 92.7% (+2.04%), 88.1% (+0.82%), and 87.9% (+3.18%), respectively. As shown in Figure 5.10, the considerable growth of the large-pore ratios of

specimens PS-5%, PS-10%, and MS-10% was caused by significant pore expansions and interconnection, resulting in surface scaling.

Subjecting the specimens to 80 freeze-thaw cycles destroyed specimens PS-5% and PS-10% and significantly increased the large-pore ratios of samples Control and MS-10% to 98.1% (+8.71%) and 94.1% (+6.2%), respectively. However, while the large voids of specimen MS-10% interconnected mostly at the surface, causing uniform scaling as shown in Figure 5.10 (E), the large pores of the control sample interconnected throughout its surface and across its core, disintegrating its 5 mm high bottom segment as demonstrated in Figure 5.10 (A). In contrast, specimen MS-5% experienced the least growth of large-pore ratio to 89.5% (+1.42%), as illustrated in Figure 5.10 (C). Thus, subjecting concrete to potassium sulfate generally accelerated the growth of large voids, leading to harsher frost damage, whereas exposure to magnesium sulfate decreased the rate of large-pore expansion, slowing the freeze-thaw damage. Also, it was observed that increasing the potassium sulfate or magnesium sulfate concentration accelerated the expansion of large voids.

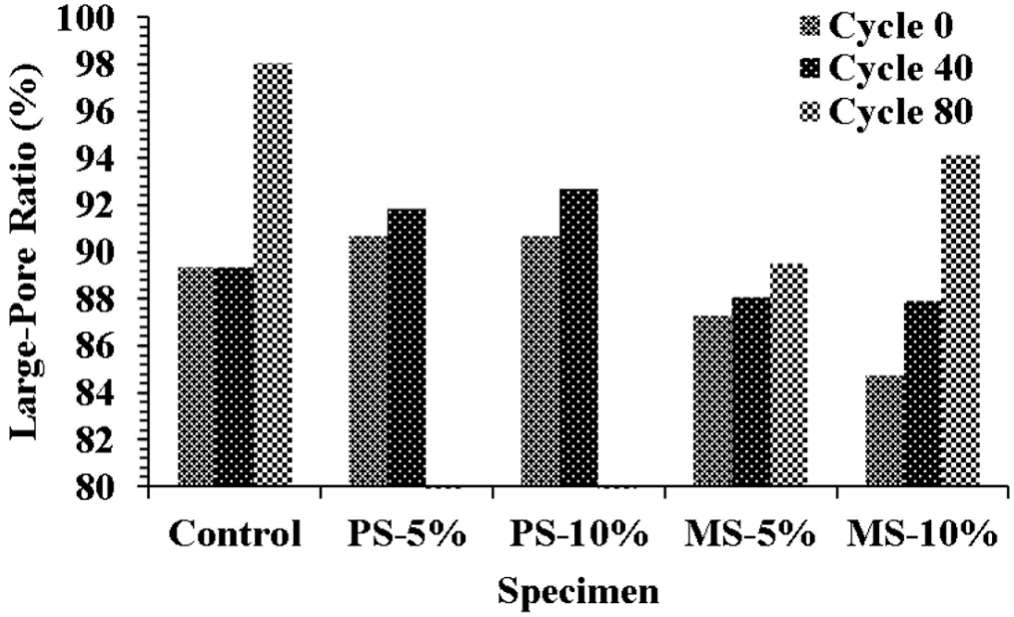

Figure 5.9. Large-Pore Ratio (%) of Concrete Specimens before and after the Frost Cycles

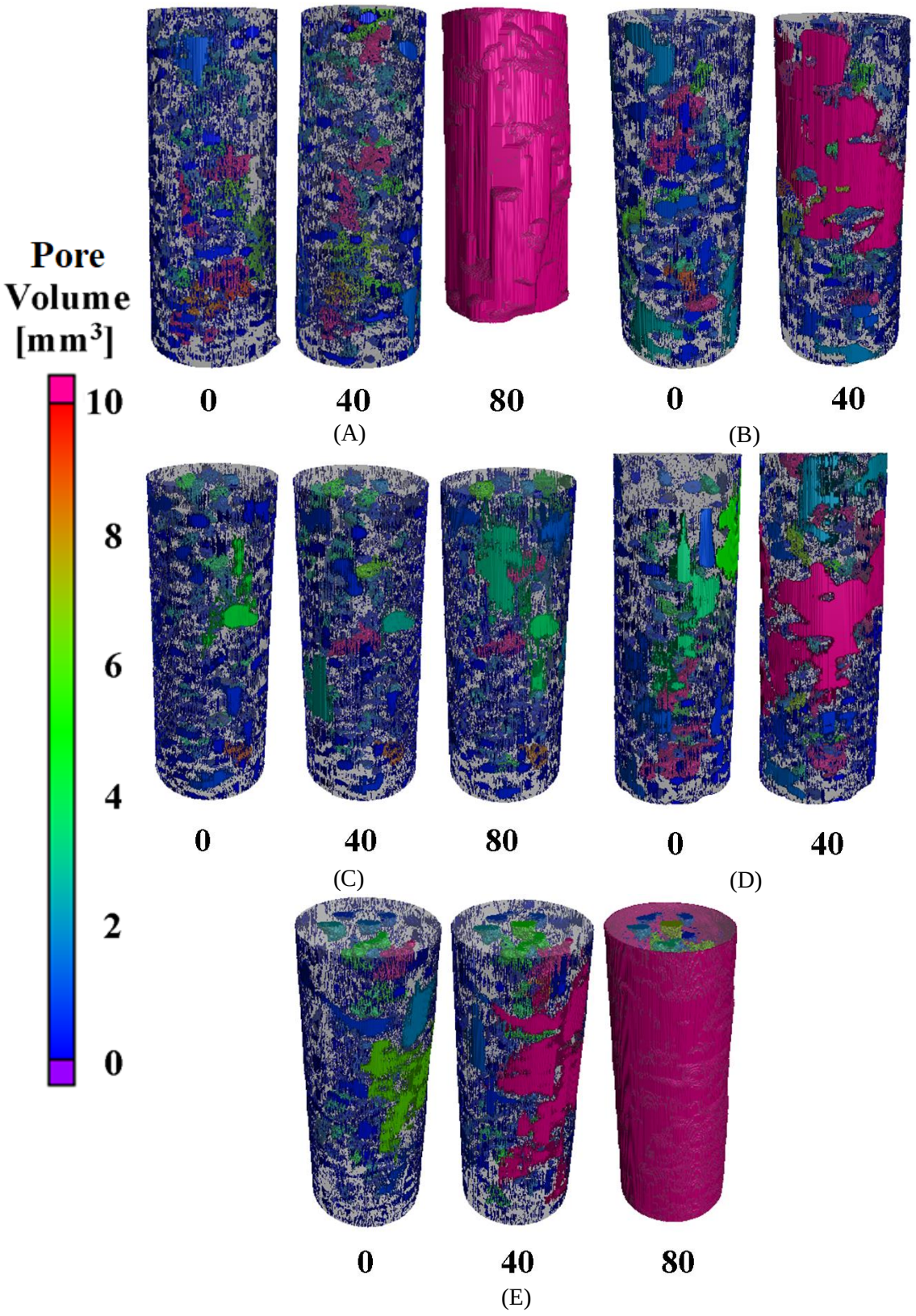

Figure 5.10. Large Pores of Specimens (A) Control, (B) PS-5%, (C) MS-5%, (D) PS-10%, and (E) MS-10% before (Left) and after 40 (Middle) and 80 (Right) Freeze-Thaw Cycles

5.3.3.3. Surface Pore

Higher open (surface) pores content can be an indication of higher permeability of concrete, resulting in higher water ingress and, consequently, more severe sulfate and frost damage [41,42]. Analyzing the open-pore ratio, which is the volumetric ratio of surface pores to the total pore volume, is crucial for investigating concrete resistance to environmental damage. Also, the variation of the open-pore ratio throughout the applied freeze-thaw cycles can indicate the expansion dominance of surface pores compared to internal voids. For example, while a rapid increase in the open-pore ratio signifies concrete scaling, a reduced open-pore ratio can indicate the filling of surface pores by the precipitated sulfate by-products. Hence, the open-pore ratio was analyzed before and after applying 40 and 80 freeze-thaw cycles, as shown in Figure 5.11, to investigate the severity and mechanisms of frost damage.

It was observed that the concrete samples initially had comparable open-pore ratios with an average of 26.6% (±3.2%), as demonstrated by the 3D reconstructions of open voids shown in Figure 5.12. After applying 40 freeze-thaw cycles, the open-pore ratio of the control sample increased slightly to 24% (+1.1%). On the other hand, specimens PS-5% and PS-10% suffered considerable expansion of open-pore ratio to 52.3% (+27.7%) and 38% (+12.7%), respectively. Thus, subjecting concrete to potassium sulfate weakened its frost resistance and resulted in considerable scaling, as illustrated in Figure 5.12 (B and D). On the contrary, the open-pore ratios of samples MS-5% and MS-10% decreased to 25.4% (-3.4%) and 26.6% (-5.1%), despite starting with the highest open-pore ratios. The volume of specimens' open voids increased, as demonstrated in Figure 5.12 (C and E), yet their open-pore ratios decreased. This indicates that the expansion of internal pores was more dominant than surface voids.

The concrete specimens were subjected to another 40 freeze-thaw cycles (80 cycles in total), and it was observed that specimens PS-5% and PS-10% were destroyed, demonstrating the detrimental effect of potassium sulfate exposure. The control specimen experienced severe and localized scaling, increasing its open-pore ratio to 87.4% (+63.4%). In contrast, the open-pore ratios of specimens MS-5% and MS-10% increased to 28.1% (+2.7%) and 66% (+39.4%), respectively. It is worth noting that exposure to magnesium sulfate not only minimized the frost damage but also improved its geometry and distribution uniformity. Thus, while the control sample endured localized damage, destroying its bottom 5 mm high segment, as shown in Figure 5.12 (A), specimen MS-10 experienced uniform surface scaling even though it initially had localized surface pores, as illustrated in Figure 5.12 (E).

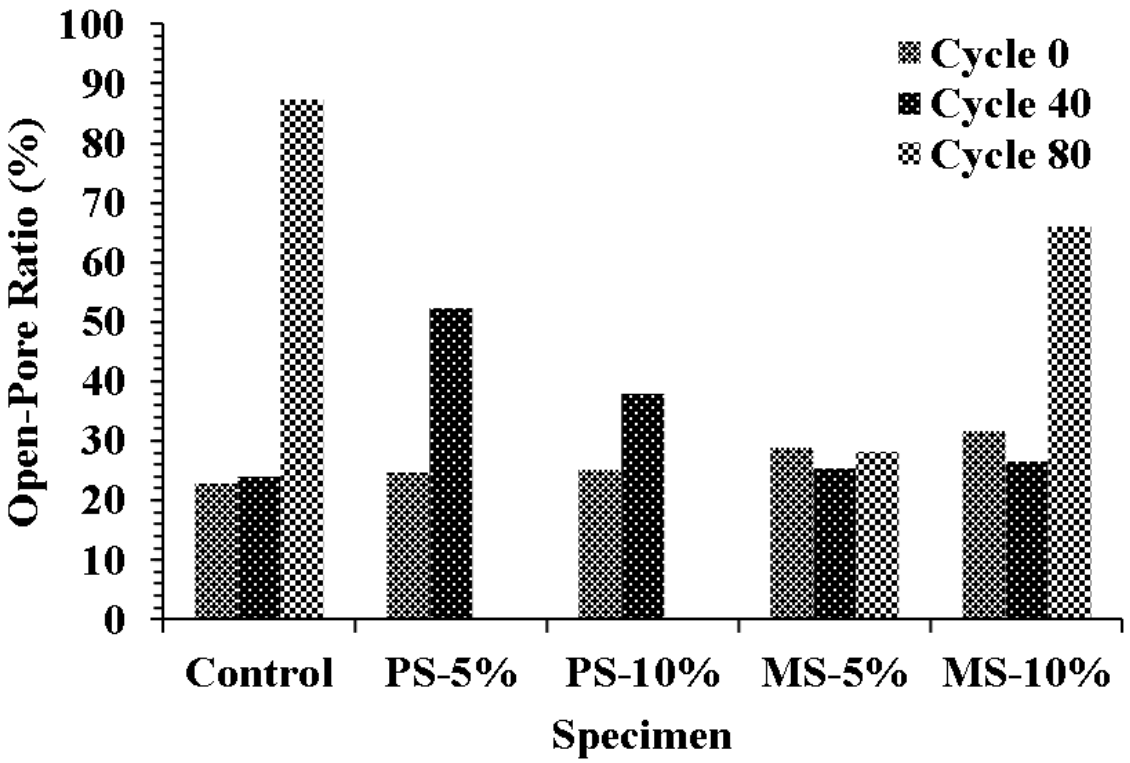

Figure 5.11. Open-Pore Ratio (%) of Concrete Specimens before and after the Freeze-Thaw Cycles

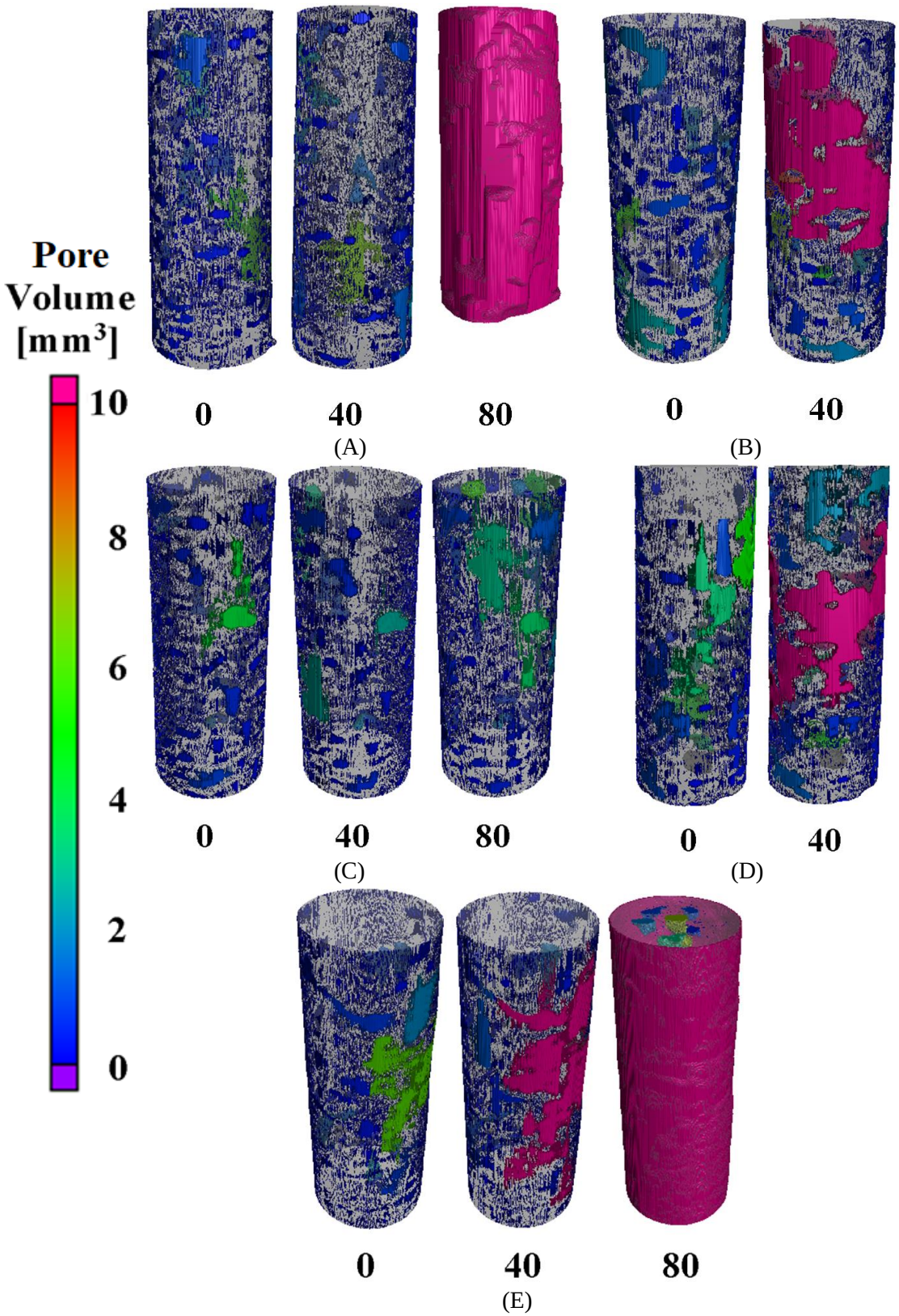

Figure 5.12. Surface (Open) Pores of Specimens (A) Control, (B) PS-5%, (C) MS-5%, (D) PS-10%, and (E) MS-10% before (Left) and after 40 (Middle) and 80 (Right) Freeze-Thaw Cycles

5.3.4. Frost Damage Mechanisms

This section discusses the concrete damage mechanisms by synthesizing the previously reported data and the 2D and 3D representations of concrete pore microstructures, shown in Figure 5.13 and Figure 5.14. It was observed that subjecting the control specimen to 40 freeze-thaw cycles expanded its small ($\leq 1.18\times10^{-3}$ mm^3) and large ($>1.18\times10^{-3}$ mm^3) voids almost evenly, resulting in an unchanged large-pore ratio. Minor scaling damage occurred, as illustrated in Figure 5.13 (A), causing little increase in the open-pore ratio. Applying another 40 cycles produced the typical freeze-thaw damage mechanism, through which mass loss is initiated mostly at the external surface and propagated inward on a layer-by-layer basis. The control specimen suffered localized scaling and disintegrated its 5 mm high bottom segment, as demonstrated in Figure 5.14 (A).

Exposure to potassium sulfate generally accelerated the freeze-thaw damage without altering its mechanisms. As a result, subjecting specimens PS-5% and PS-10% to 40 frost cycles caused extensive scaling damage even though the internal pores were shrinking due to the precipitation of sulfate salt and its chemical by-products, as shown in Figure 5.13 (B and C) and Figure 5.14 (B and D). Thus, both samples experienced a substantial expansion of large and surface voids. Further exposure to freeze-thaw cycles in potassium sulfate completely disintegrated both specimens, indicating the significant degradation of the frost resistance.

On the contrary, subjecting concrete to magnesium sulfate minimized its frost damage and altered its mechanisms. It was observed that subjecting specimens MS-5% and MS-10% to 40 freeze-thaw cycles resulted in considerable expansion of the internal pores, contradicting typical frost damage mechanisms. It is believed that the internal pore expansion was caused by the sulfate damage, as observed in an earlier publication [235]. As illustrated in Figure 5.13 (D) and Figure 5.14 (C), the internal voids of sample MS-5% clearly expanded and interconnected into larger pores, despite

enduring minimal surface damage, which explains the reduction of the open-pore ratio. It is worth noting that the reduced open-pore ratio of specimen MS-5% improved its freeze-thaw resistance; hence, applying another 40 cycles expanded its pores only slightly. On the other hand, sample MS-10% experienced both internal and external pore expansion after being subjected to 40 freeze-thaw cycles, as shown in Figure 5.13 (E) and Figure 5.14 (E). Therefore, increasing the concentration of magnesium sulfate decreased its positive effect on freeze-thaw resistance. This was verified by applying another 40 cycles, which caused uniform scaling damage. Also, exposure to 80 freeze-thaw cycles in magnesium sulfate with a concentration of 10% produced uniform surface damage despite starting with localized surface pores, unlike the control sample, which had uniformly distributed surface voids but ended up with severely localized scaling damage. In other words, exposure to magnesium sulfate accelerated internal pore expansion and slowed the growth of surface voids, mitigating the freeze-thaw damage and improving its uniformity.

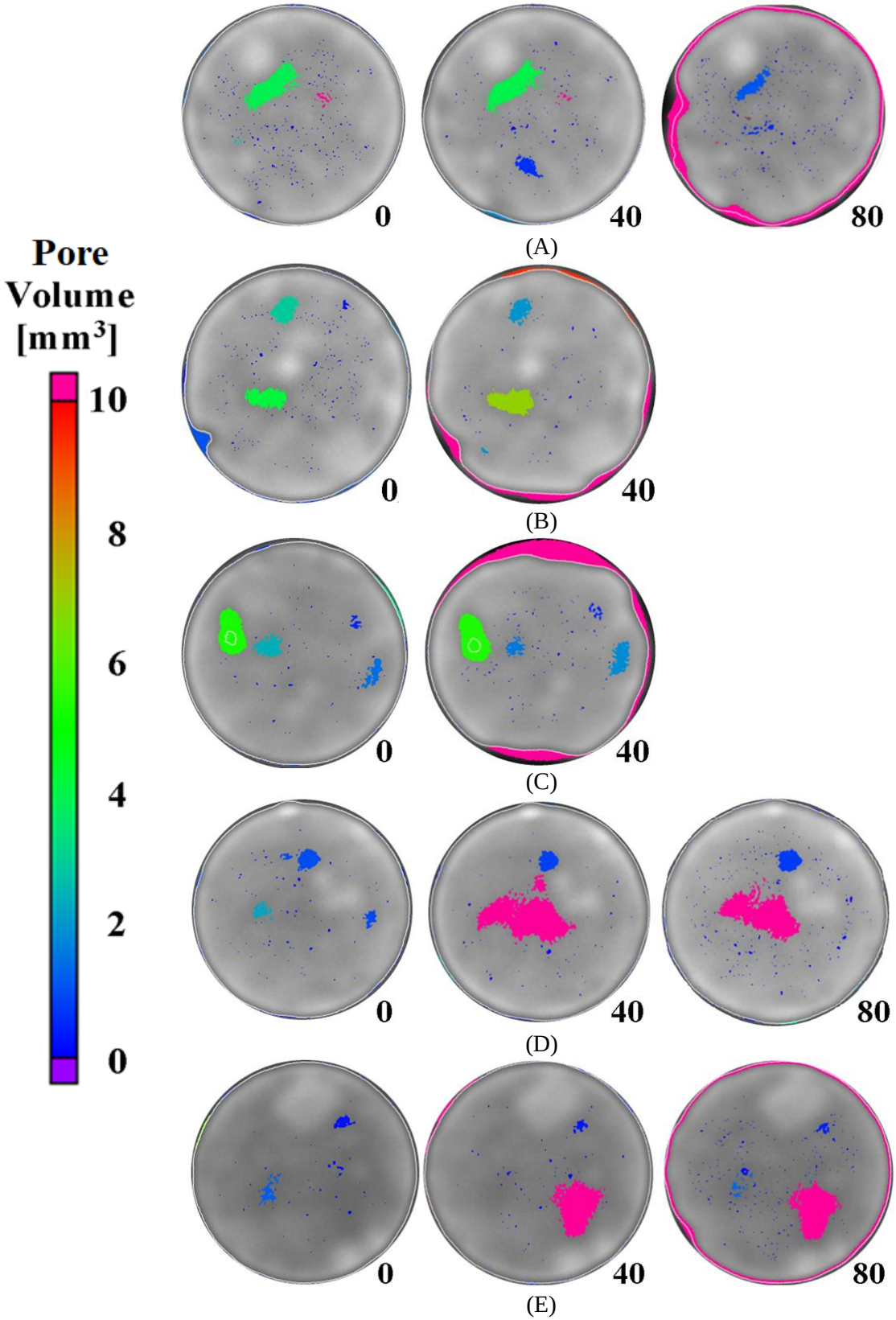

Figure 5.13. 2D Sections of Specimens (A) Control, (B) PS-5%, (C) PS-10%, (D) MS-5%, and (E) MS-10% before (Left) and after 40 (Middle) and 80 (Right) Freeze-Thaw Cycles

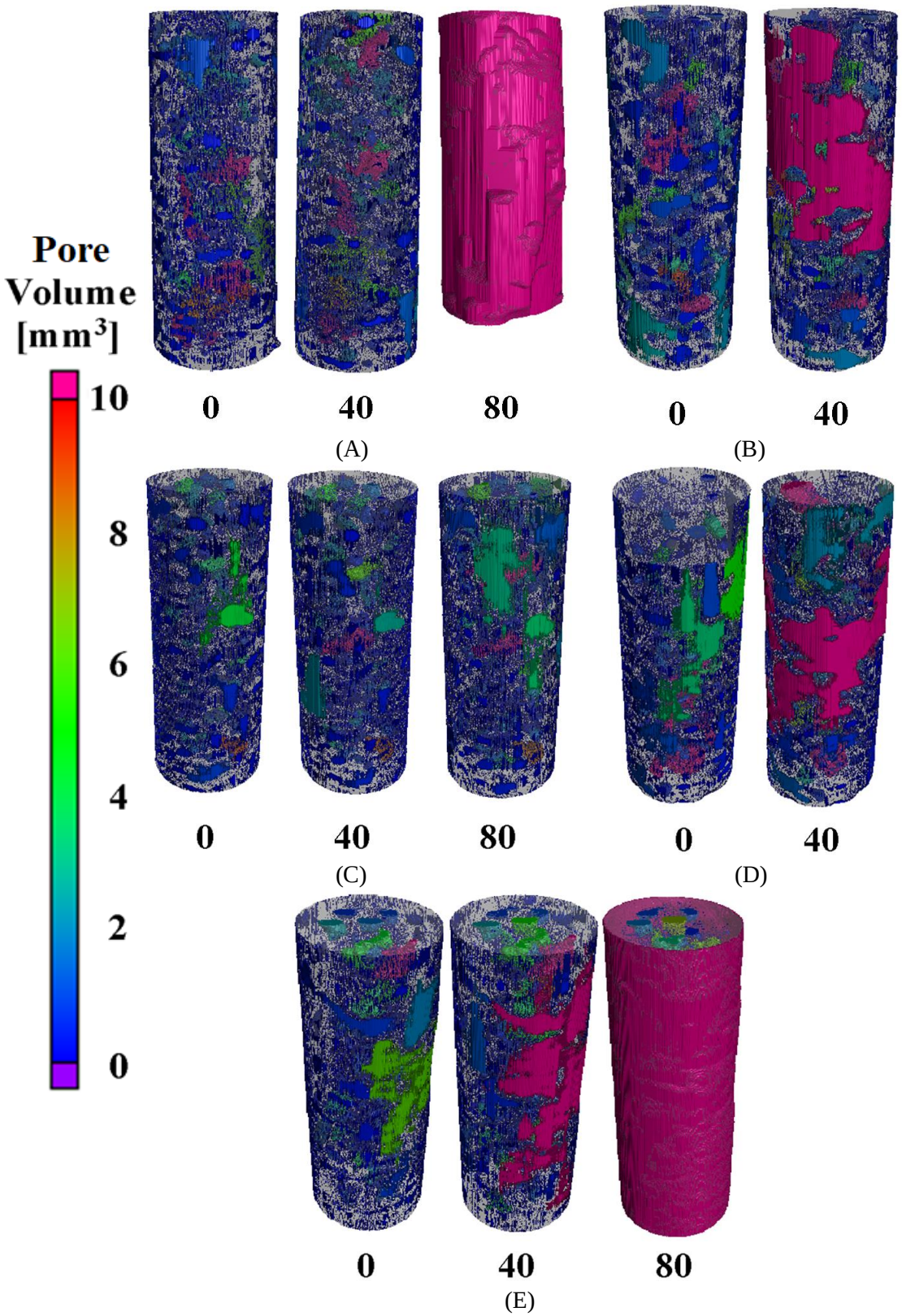

Figure 5.14. 3D Pore Structure of Specimens (A) Control, (B) PS-5%, (C) MS-5%, (D) PS-10%, and (E) MS-10% before (Left) and after 40 (Middle) and 80 (Right) Freeze-Thaw Cycles

5.4. Conclusions

The concrete damage mechanisms under a coupled action sulfate and freeze-thaw exposure were examined in potassium sulfate and magnesium sulfate environments with different concentrations and analyzed using μCT imaging, and the following points were concluded.

- Microstructural pore analysis using μCT imaging is a promising approach for investigating the damage mechanisms of concrete through its capability to quantify and visualize the morphology progression of air pores throughout the applied freeze-thaw cycles.
- Subjecting concrete to potassium sulfate accelerated the expansion of large and surface voids, causing severe frost damage.
- Exposure to magnesium sulfate accelerated the growth of internal pores while slowing the expansion of surface voids, mitigating the scaling damage and improving its uniformity.
- Increasing the concentration of potassium sulfate or magnesium sulfate resulted in faster and more severe freeze-thaw damage.

Chapter 6: Image-Based Microstructural Finite Element (FE) Modelling of Corrosion and Freeze-Thaw Damage

This chapter presents the development and preliminary verification of image-based microstructural finite element (FE) models that simulate the damage mechanisms of real concrete specimens under corrosion and freeze-thaw condition.

6.1. Introduction

Extensive research has investigated the corrosion and frost damage modes of concrete through experimental testing and finite element (FE) modeling. Experimental testing of the corrosion damage and freeze-thaw damage is crucial for examining the severity and mechanisms of concrete damage; however, it is time-consuming and provides no details on the stress distribution within concrete. Hence, different types of FE models were developed, including solid macroscale [236–238], mesostructured [201,239–241], and microstructured models [242–244]. Solid macroscale FE models treat concrete as a single homogenous material, ignoring the mechanical interaction between its cement mortar and aggregates. In contrast, mesostructured and microstructured FE models treat concrete as a composite material by modeling its mortar and aggregates as individual elements fully attached to each other (i.e., no interfacial contact is considered). The prime difference between mesostructured and microstructure FE models is the process of constructing the 3D models of the aggregates, air voids, and cement mortar. The three-dimensional elements of mesostructured FE models are generated mathematically, whereas the image-based elements of microstructure FE models are created by stacking 2D images of an actual concrete, normally captured using micro-computed tomography (μCT). Thus, a microstructure FE model provide the most realistic representation of concrete damage, making it an excellent tool for investigating the microscale corrosion and freeze-thaw damage of actual concrete elements in a timely and efficient

manner by minimizing the need for applying lengthy wet-dry or freeze-thaw cycles and expensive CT scans.

The chapter's prime objective is to develop two realistic microstructural finite element models to simulate the corrosion and frost damage within actual concrete specimens. The corrosion FE model was constructed by CT imaging an actual reinforced concrete specimen. Likewise, the freeze-thaw FE model was sample-specific that was based on 3D images of concrete specimens. The severity and mechanisms of the corrosion damage were investigated by analyzing the stress distribution and crack propagation. Similarly, the severity of freeze-thaw damage was investigated using the concrete's volume loss data. The damage progression was monitored throughout the applied frost cycles and compared to the experimental results to examine the accuracy of the FE model.

6.2. Finite Element (FE) Model

6.2.1. General

The first step of developing the microstructural image-based corrosion and freeze-thaw FE models was collecting three-dimensional imaging of actual concrete specimens using an industrial μCT imaging system. The concrete elements (about 14 mm in diameter and 40 mm in height) were made using water/cement, sand/cement, and aggregate/cement ratios of 0.5, 1, and 1.5, respectively. One day after casting, the casting molds were removed, and the specimens were water cured for 28 days before μCT imaging and testing. The corrosion FE model was constructed using the CT images of a concrete sample reinforced with a 3.175 mm diameter steel bar, as shown in Figure 6.1 (A). On the other hand, the freeze-thaw FE model was based on the images of the two concrete elements demonstrated in Figure 6.1 (B).

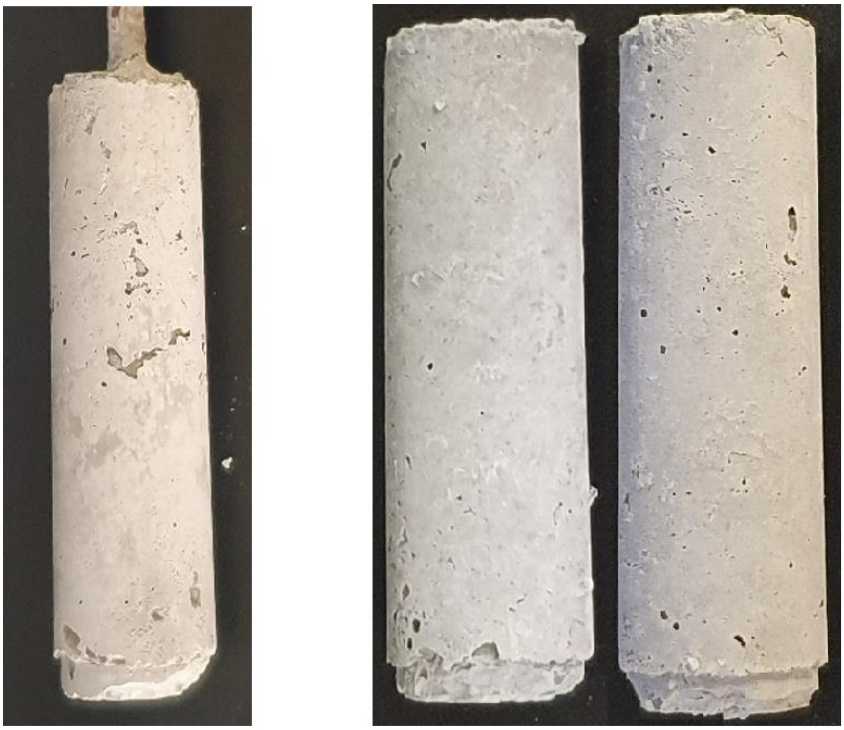

(A) (B)

Figure 6.1. (A) Corrosion Specimen, and (B) Freeze-Thaw Specimens 1 (Left) and 2 (Right)

A high-resolution micro-computed tomography (μCT) imaging system with a 240 kV tube was employed to scan the concrete specimens using tube voltage and current of 100 kV and 80 μA, respectively. One thousand images with a resolution (voxel size) of 49.1 μm were captured in each scan using an X-ray exposure period of 0.333 seconds per image. It is worth noting that only the 36 mm midsection was analyzed and modeled to minimize inconsistencies caused by the non-uniform top and bottom surfaces. The collected CT images were median filtered (3×3×3 pixels) to reduce scanning artifacts and stacked into 3D elements, after which the images were segmented using thresholding to separate the different concrete components (i.e., aggregates and cement mortar), in addition to micro-scale air voids.

Three-dimensional mesh elements of the aggregates, voids, and mortar were generated, cleaned, and converted into solid 3D models. Different software packages were used to create the 3D configuration of the FE models, namely, Image J, Geomagic Design X, and Autodesk Fusion 360. The 3D reconstructions of the corrosion FE model's elements, including the steel reinforcement, are illustrated in Figure 6.2. In terms of the freeze-thaw FE model, the detected air pores were filled with ice since concrete is fully saturated throughout the freeze-thaw cycles. The 3D reconstructions of the two concrete specimens of the freeze-thaw FE model are demonstrated in Figure 6.3. Due to the complex configurations of the 3D components, tetrahedral mesh elements (C3D4) were used. The mesh sizes of ice (e.g., 0.46 – 4.6 μm), aggregates (e.g., 0.58 – 5.8 μm), and cement mortar (e.g., 9.2 – 92 μm) were automatically selected by ABAQUS (Dassault Systems version 2019), resulting a total number of mesh elements of over 4.3 million elements. The mechanical properties, surface-contact conditions, applied corrosion expansion for the corrosion FE model, and applied frost cycles for the freeze-thaw FE model are discussed in the following sections. It is important to note the morphology of the modeled components can be enhanced by using higher-resolution CT images.

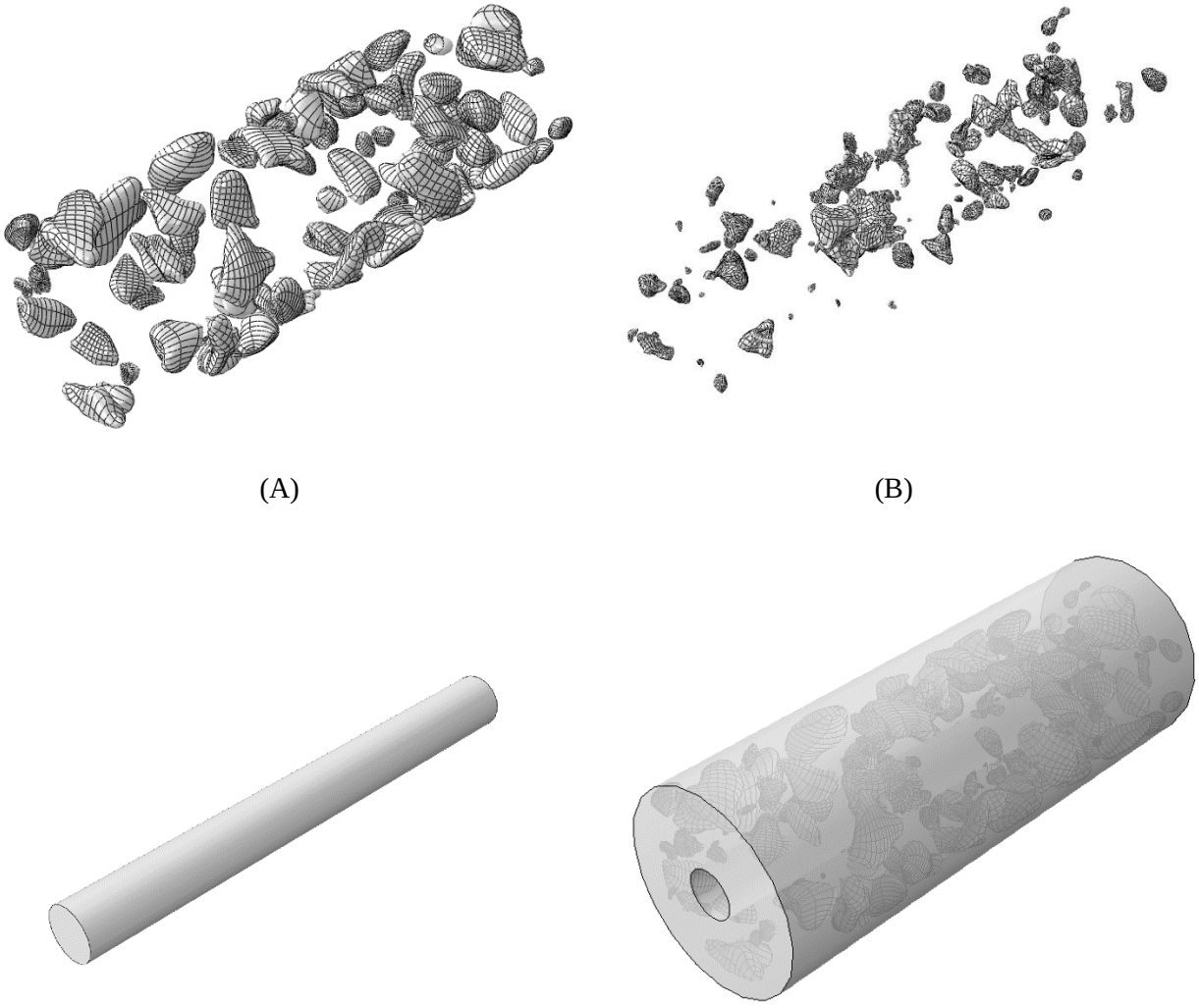

Figure 6.2. 3D Models of (A) Aggregates, (B) Air Voids, (C) Steel Reinforcement, and (D) Cement Mortar

(A)

(B)

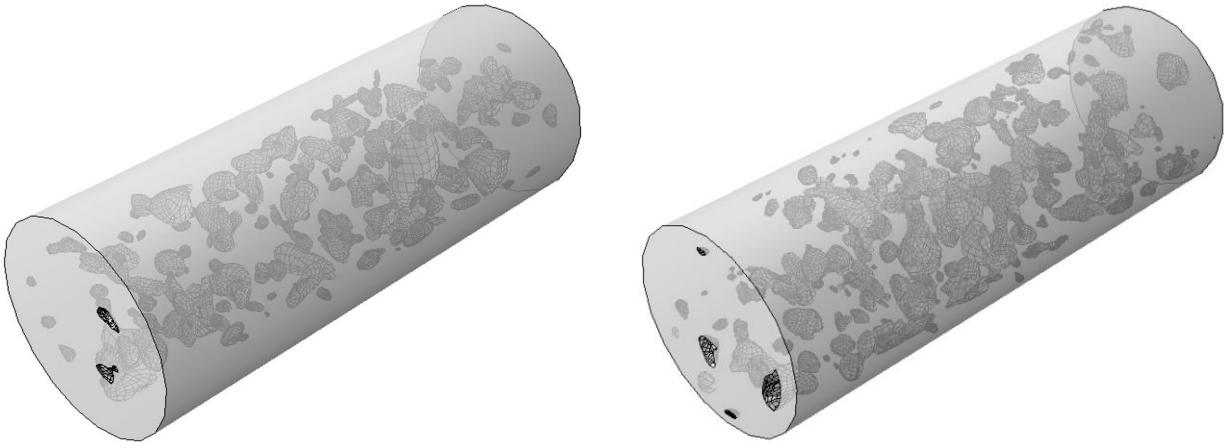

(C)

Figure 6.3. 3D Models of (A) Aggregates, (B) Ice (Voids), and (C) Cement Mortar of Specimens 1 (Left) and 2 (Right)

6.2.2. Mechanical Properties

The mechanical properties of the cement mortar, aggregates, and steel reinforcement are listed in Table 6.1. It is anticipated that the concrete damage will occur mainly within the cement mortar and the aggregate interface due to the high strength of aggregates. Therefore, the aggregates and the steel reinforcement were modeled as elastic elements. The aggregates have a modulus of elasticity, a density, and a Poisson's ratio of 47,00 MPa, 2,680 Kg/m^3, and 0.2, respectively. Also, the elastic modulus, density, and Poisson's ratio of the steel bar are 200,000 MPa, 7,850 Kg/m^3, and 0.3, respectively. On the other hand, the cement mortar's compressive strength, tensile strength, density, and Poisson's ratio are 25.28 MPa, 3.2 MPa, 2,022 Kg/m^3, and 0.3, respectively. Also, the modulus of elasticity and shear strength of the mortar element were computed in accordance with ACI 318 (2014) using the equations below.

$$E = 57{,}000\sqrt{f_c} \text{ (in psi)} \tag{6.1}$$

$$V = 4\lambda\sqrt{f_c} \text{ (in psi)} \tag{6.2}$$

Where E: Modulus of Elasticity, V: Shear Strength, f_c: Compressive Strength, λ =1

Table 6.1. Mechanical Properties of Cement Mortar, Aggregates, and Steel Reinforcement

Property	**Cement Mortar** [245–247]	**Aggregates** [248,249]	**Steel** [250,251]
Compressive Strength (MPa)	25.28	–––	–––
Tensile Strength (MPa)	3.2	–––	–––
Shear Strength (MPa)	0.553	–––	–––
Modulus of Elasticity (MPa)	23797.1	47,200	200,000
Density (Kg/m^3)	2,022	2,680	7,850
Poisson's Ratio	0.3	0.2	0.3

To model the volume increase of water in voids during the freeze-thaw cycles, the temperature-dependent mechanical properties of ice were utilized. The modulus of elasticity, thermal expansion coefficient, density, and Poisson's ratio of the ice are plotted in Figure 6.4.

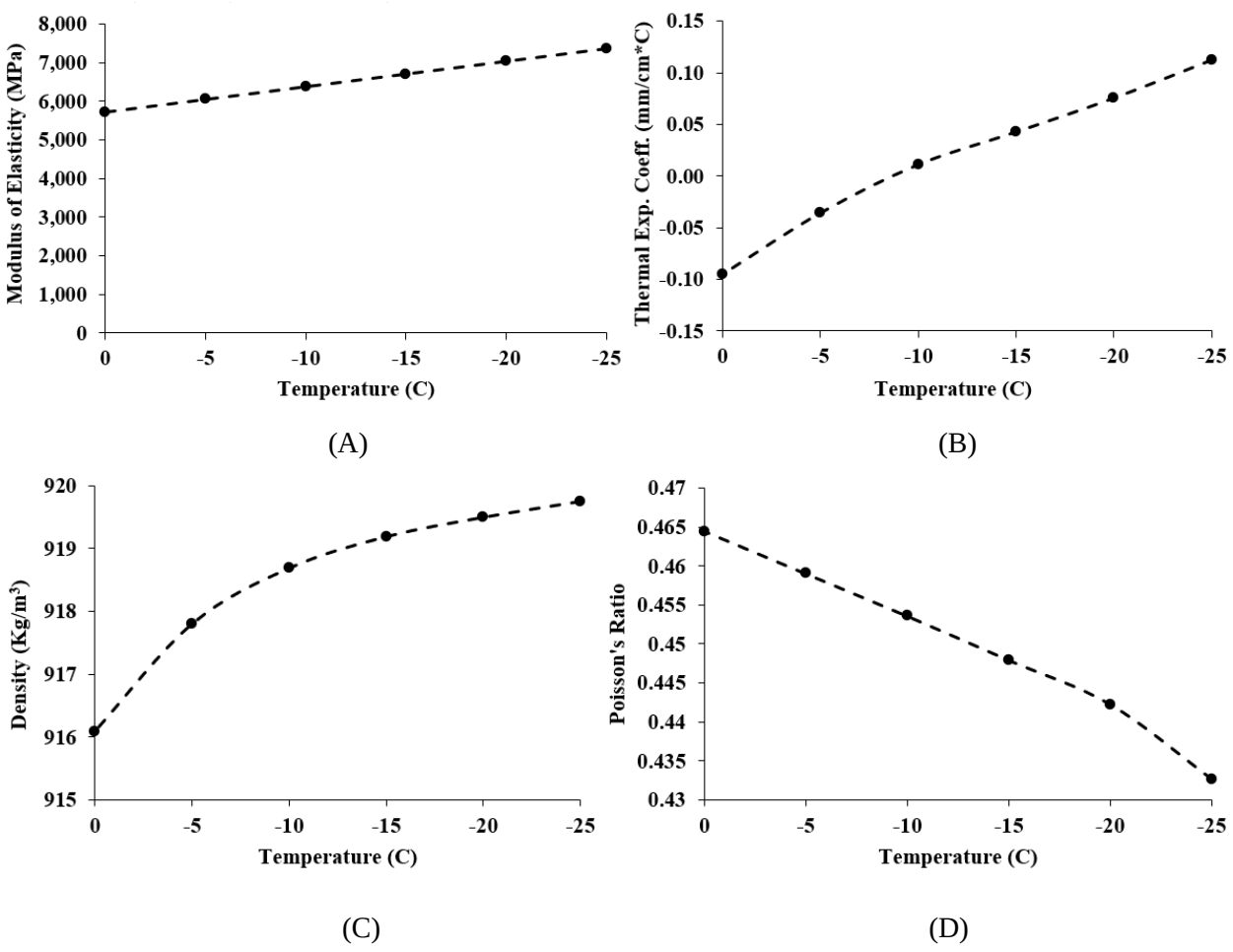

Figure 6.4. (A) Modulus of Elasticity, (B) Thermal Expansion Coefficient, (C) Density, and (D) Poisson's Ratio of Ice at Different Freezing Temperatures. Recreated from [252–255]

The corrosion damage and freeze-thaw damage within the mortar were investigated via the Concrete Damage Plasticity (CDP) model using the default parameters listed in Table 6.2. Also, the CDP model was based on the mortar's compressive and tensile stress-strain curves, shown in Figure 6.5, which were attained using the equations of Saenz [256] and Desay & Krishnan [257], respectively.

Table 6.2. Parameters of Concrete Damage Plasticity Model

Dilation Angle	Eccentricity	Stress Ratio	Shape Factor	Viscosity Parameter
40[1] 45[2]	0.1	1.16	0.667	0.0005

[1] Corrosion FE Model

[2] Freeze-Thaw FE Model

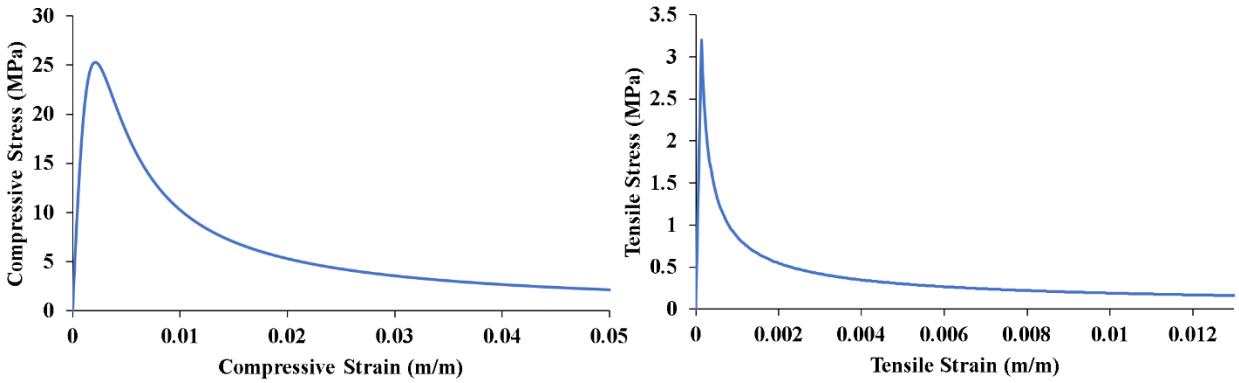

(A) (B)

Figure 6.5. (A) Compressive and (B) Tensile Stress-Strain Curves of Cement Mortar

6.2.3. Contact Characteristics

Different interfaces were applied in each model of corrosion and freeze-thaw investigation. In the corrosion model, there were three contact surfaces: mortar-aggregate, mortar-steel, and aggregate-steel interfaces. On the other hand, the freeze-thaw models include mortar-aggregate, aggregate-ice, and mortar-ice interfaces. The contact conditions of the aforementioned interfaces are summarized in Table 6.3.

At the mortar-aggregate and steel-mortar adhesive interfaces, tensile strength and shear strength are controlled by the weakest contacting materials (i.e., the mortar). Therefore, it was assumed that the tensile and shear strengths of the adhesive contact were the same as the cement mortar, which are 3.2 MPa and 0.554 MPa, respectively. Although the mortar-aggregate and mortar-steel interfaces have the same adhesive conditions, they have different friction-based slide conditions.

The friction coefficients of the mortar-aggregate and mortar-steel interfaces are 0.6 and 0.55, respectively. On the other hand, only a friction-based contact condition was applied in the aggregate-steel interface with a friction coefficient of 0.65. Also, due to the nature of ice related to its very low friction resistance during sliding, a frictionless slide condition was applied in the mortar-ice and aggregate-ice interfaces.

Table 6.3. Contact Conditions of the Mortar-Aggregate, Mortar-Steel, Aggregate-Steel, Mortar-Ice, and Aggregate-Ice Interfaces

Interface	**Adhesive Condition** [246]	**Friction Condition** [258–260]
Mortar-Aggregate	Tensile Strength = 3.2 MPa Shear Strength = 0.554 MPa	Friction Coef. = 0.6
Mortar-Steel[1]	Tensile Strength = 3.2 MPa Shear Strength = 0.554 MPa	Friction Coef. = 0.55
Aggregate-Steel[1]	–––	Friction Coef. = 0.65
Mortar-Ice[2]	–––	Frictionless
Aggregate-Ice[2]	–––	Frictionless

[1] Corrosion FE Model

[2] Freeze-Thaw FE Mod

6.2.4. Reinforcement Corrosion

To investigate the impact of uniform reinforcement corrosion on concrete, the size increase of corrosion products was simulated by applying volumetric expansion. Although different corrosion levels can be applied, in this model, the thickness of the uniform rust layer surrounding steel reinforcement was about 0.1 mm based on observation reported by Robuschi et al. (2021) [261]. Thus, an equivalent uniform steel expansion of 6% was applied in the FE model, corresponding to an increase in diameter from 3.175 mm to 3.375 mm.

6.2.5. Freeze-Thaw Cycles

Two actual concrete specimens were subjected to 40 freeze-thaw cycles, each of which had a controlled environment temperature ranging from 11 ^{o}C to -25 ^{o}C, as shown in Figure 3.5. The lowest temperature fluctuated around an average of -22 ^{o}C, which is considered the lowest ice temperature. Also, since the frost damage is caused mostly by ice expansion, it is possible to simulate the freeze-thaw damage by modeling only the freezing period of the cycles, significantly decreasing the required computational time. Thus, the temperature of the simulated cycles of the freeze-thaw FE model fluctuated between 0 ^{o}C and -22 ^{o}C, as illustrated in Figure 6.7.

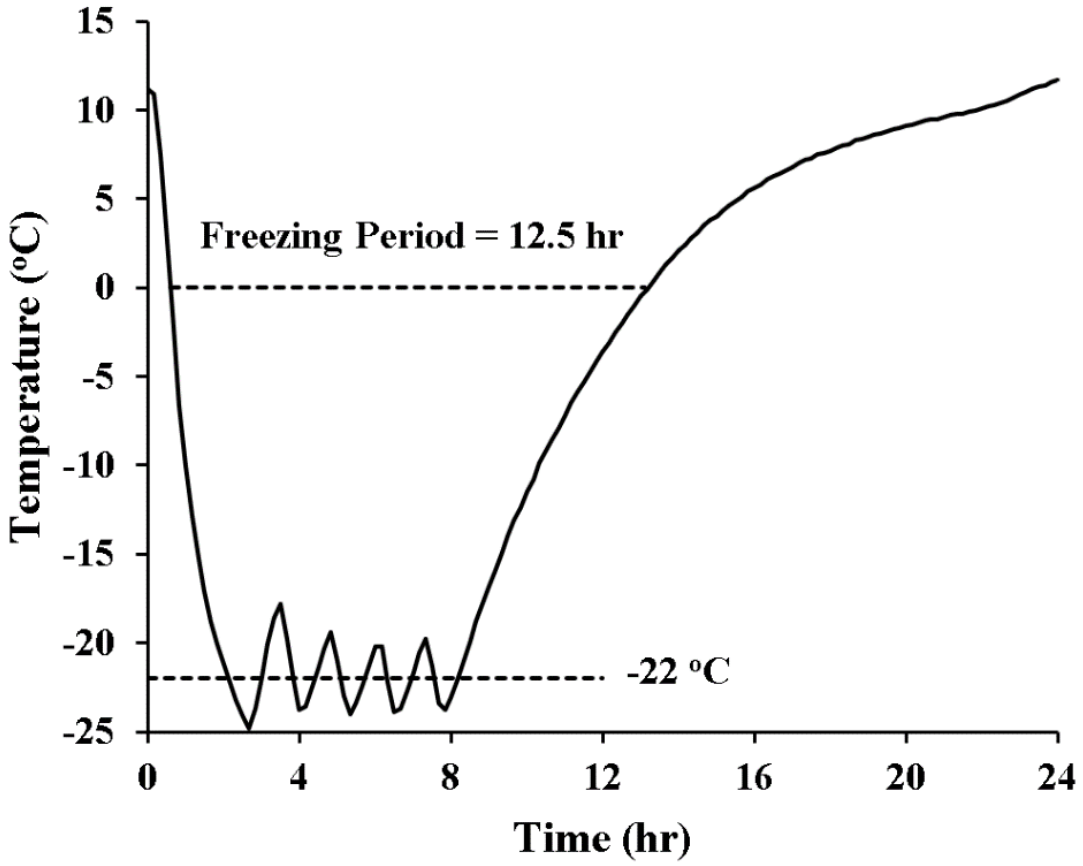

Figure 6.6. The Controlled Environment Temperature of a Single Freeze-Thaw Cycle [217]

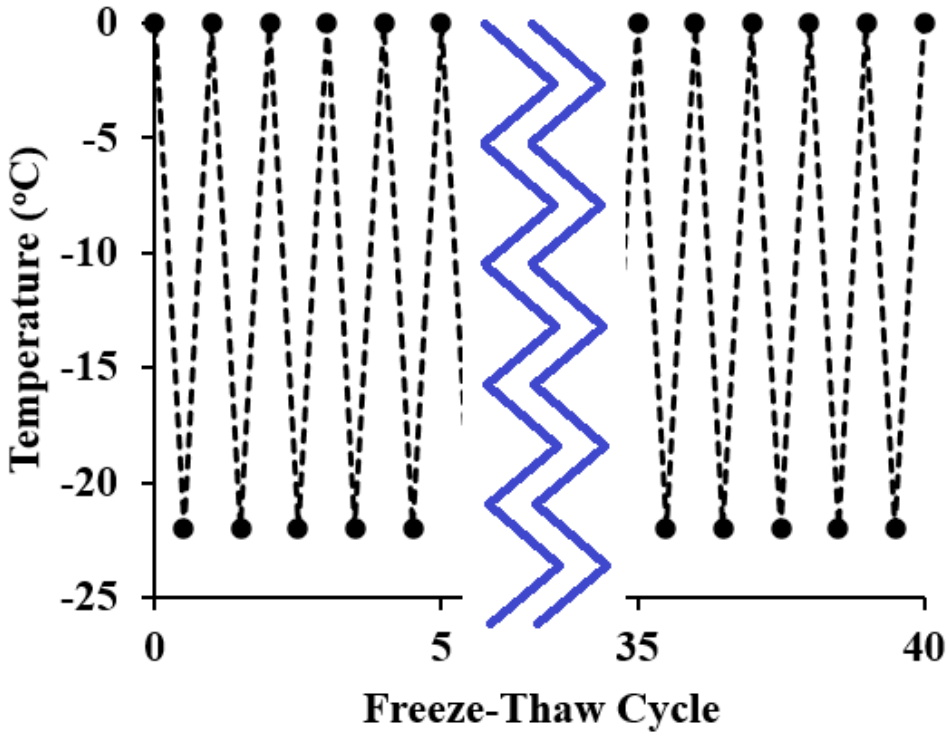

Figure 6.7. Temperature of the Applied Freeze-Thaw Cycles

6.3. Results and Discussion

6.3.1. Corrosion Damage

6.3.1.1. General

A preliminary microscale finite element model of a reinforced concrete element was developed and tested. The internal stress distribution was studied at different stages of reinforcement corrosion. The corrosion damage mechanisms were thoroughly investigated, and preliminary accuracy analysis of the concrete damage was conducted. It was noted that at the pre-crack state, stress concentration occurred in the concrete weakest regions: around air pores and mortar-aggregate interface, resulting in early cracking. As the number of cracks increased, the confinement of the surrounding concrete diminished, making concrete more susceptible to cracking in the reinforcement interface. Further discussion is provided in the following sections.

6.3.1.2. Stress Distribution of Corrosion FE Model

Although concrete stress is normally analyzed using the principal stresses, it was observed that von Mises stress yielded the clearest stress distribution, which is the focus of this section. Hence, the von Mises stress distribution within the mortar element at 0.6%, 3%, and 6% of reinforcement expansion was analyzed, as illustrated in Figure 6.8. It is clear from Figure 6.8 (A) that even in the case of uniform corrosion (e.g., uniform expansion), the resulted internal stress is substantially uneven, attributed to the fact that stress concentration occurs at the air pores and the mortar-aggregate interfacial zone. Notably, the porous segments and the mortar-aggregate interface also have low strength. In other words, stress concentration occurs in the weakest spots of the concrete, leading to early cracking. As demonstrated in Figure 6.8 (B), cracks initiated in the areas containing the air voids (red highlight) and the interfacial transmission zone between the mortar and the aggregates. It is worth noting that cracks can considerably alter the stress distribution by relieving the stress at the cracked region, shifting the locations of the highest stress, and altering the damage mechanisms. The confinement of the surrounding concrete diminished upon further cracking, making its reinforcement interfacial zone more susceptible to cracking. As a result, the steel-concrete interface suffered more cracks (green highlight) in the later stages of reinforcement corrosion, as shown in Figure 6.8 (C).

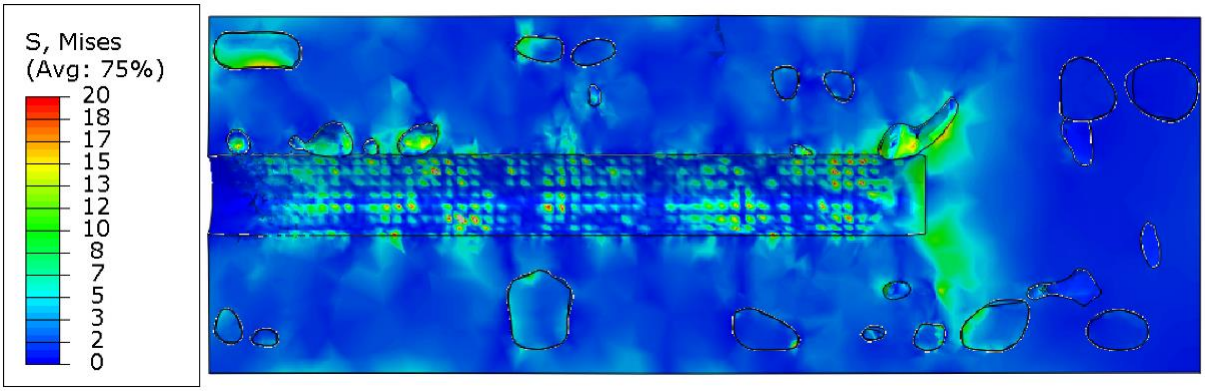

(A)

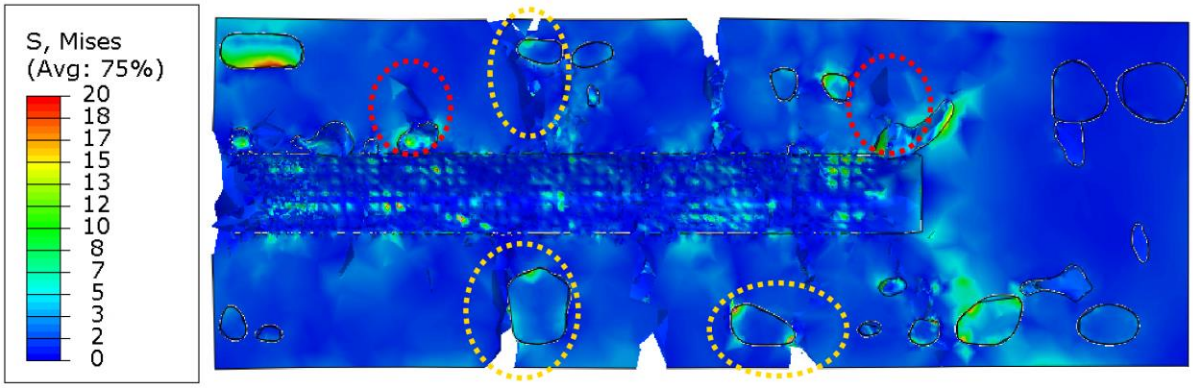

(B)

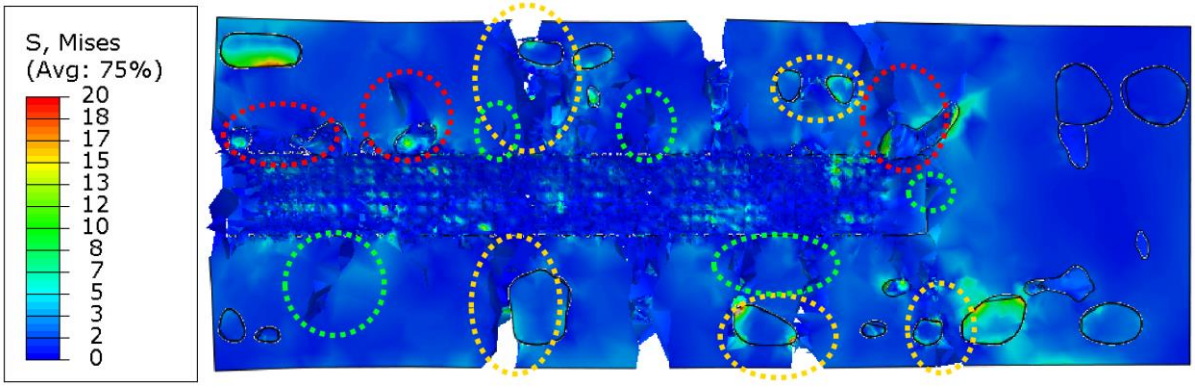

(C)

Figure 6.8. von Mises Stress (MPa) Distribution within the Cement Mortar at (A) 0.6%, (B) 3%, and (C) 6% of the Reinforcement Expansion

6.3.1.3. Corrosion Damage Mechanisms

Corrosion-induced concrete cracks normally initiate at the steel-concrete interface [20,262,263] or the external surface of concrete [263–265] and propagate across the surrounding concrete. To investigate the concrete damage mechanisms, a two-dimensional slice of the concrete specimen was monitored throughout the reinforcement expansion process to track the progress and mechanics of reinforcement corrosion-induced damage, as shown in Figure 6.9. It was observed that the corrosion-induced cracks initiated at different areas, including the reinforcement interface (green highlight), the mortar-aggregate interface (yellow highlight), and the external surface of the concrete element (red highlight). To demonstrate the dominant locations of concrete cracks during the different levels of reinforcement expansion, only the newly created cracks per expansion level are highlighted. As illustrated, during the early stages of corrosion damage, cracks dominantly occurred in the external surface of concrete and the surface of the nearby aggregates, attributed to the fact that the reinforcement interface is initially well confined by the surrounding concrete. As the external surface of the mortar cracks, the confinement of the steel reinforcement degrades considerably, making the concrete specimen more susceptible to internal cracking in the reinforcement interface, as clearly demonstrated in Figure 6.9. In other words, the level of the corrosion damage can impact the mechanisms of further concrete damage. Also, it was noted that cracks propagate across the air voids and along with the mortar-aggregate interfacial zone. It is worth noting that similar damage mechanisms have been reported in the literature, where concrete experienced visible surface cracking followed by internal cracking within the steel-concrete interface [264].

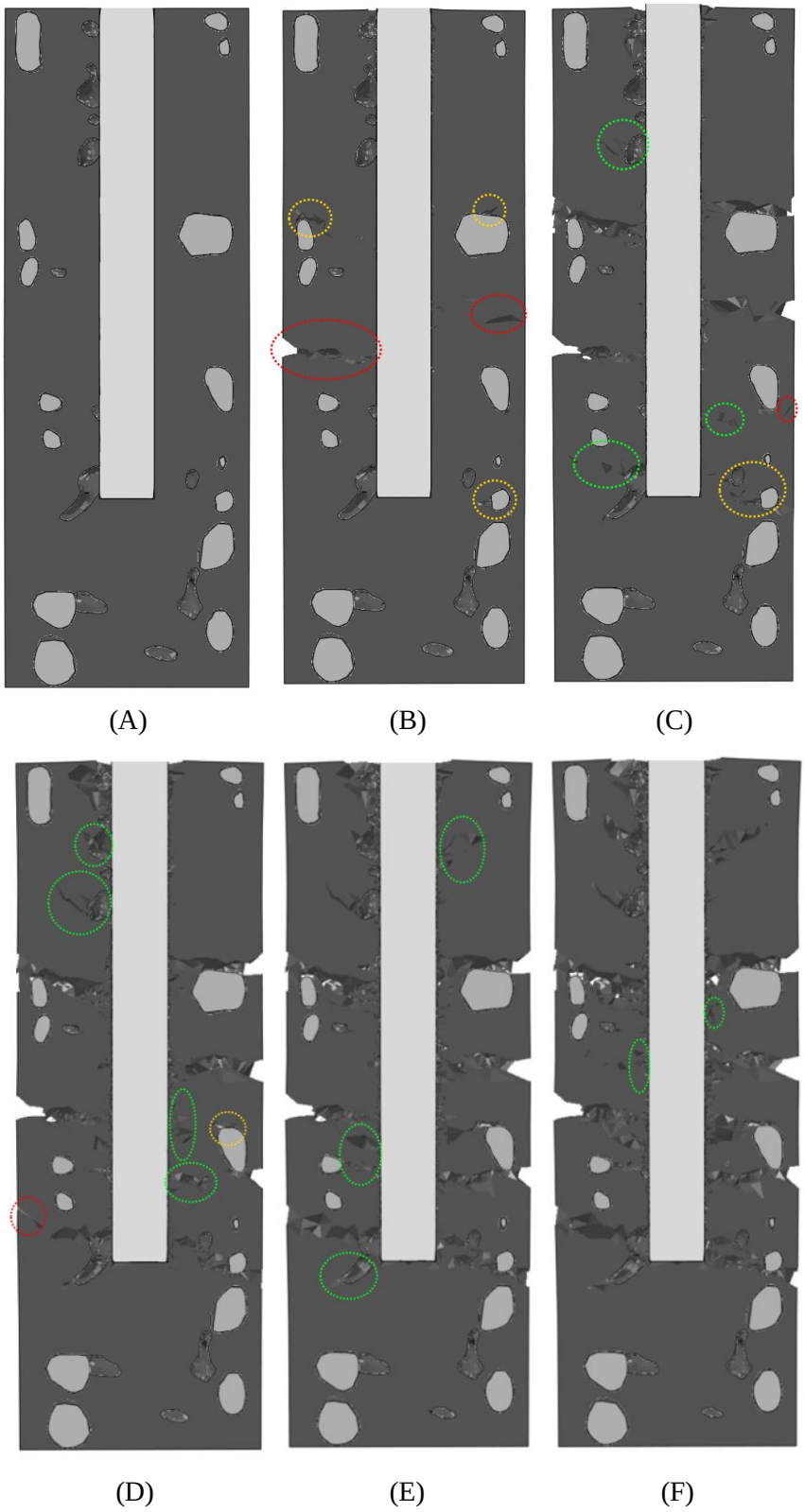

Figure 6.9. 2D Propagation of Concrete Damage (A) before, and after (B) 1.2%, (C) 2.4%, (D) 3.6%, (E) 4.8%, and (F) 6% of Reinforcement Expansion

6.3.1.4. Preliminary Accuracy Analysis of Corrosion FE Model

A preliminary comparison between the damage mechanisms of the FE model and the actual concrete specimen was conducted. Natural and uniform reinforcement corrosion was produced by subjecting the concrete element, shown in Figure 6.10 (A), to 160 wet-dry cycles in salt water with a sodium chloride concentration of 3.5%. Each wet-dry cycle consisted of 3 hours of immersion and 1 hour of accelerated dehydration at a temperature of 45 ^{o}C. As demonstrated in Figure 6.10, the FE model successfully anticipated the location of the largest crack of the concrete specimen, illustrating the potential of the developed microstructural FE model. Nonetheless, further investigation of the model's accuracy is necessary.

(A) (B)

Figure 6.10. Comparison between (A) the Actual Concrete Damage and (B) the Simulated Concrete Damage at 1.5% of Reinforcement Expansion

6.3.2. Freeze-Thaw Damage

6.3.2.1. General

The stress distribution induced by the expansion of freezing water inside voids within concrete was investigated. It was observed that the stress was concentrated mostly around the expanding ice and within the mortar-aggregate interface. As more cycles were applied, minor cracking occurred around the expanding ice, locally relieving the stress and altering the stress distribution within the concrete element. Also, the severity of frost damage was investigated by analyzing the volume loss of concrete. A good agreement was observed between the volume loss of the FE model and the experimental CT imaging data. In terms of the damage progression, it was noted that the concrete specimens experienced only minor frost damage that was hard to analyze through visual inspection, as shown in Figure 6.11. Thus, the damage progression of the FE model was compared with the frost-induced damage detected using CT imaging, and the observed agreement was discussed.

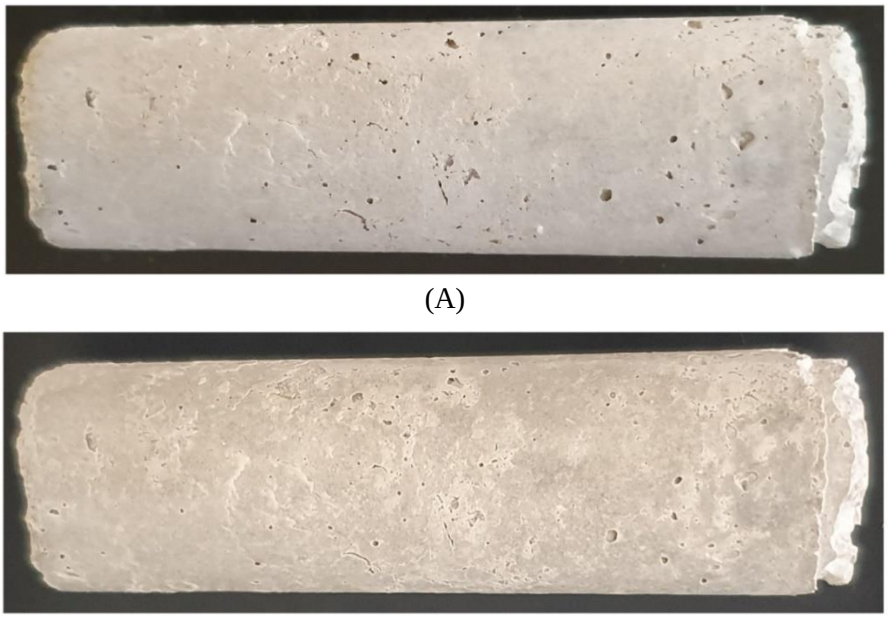

(A)

(B)

Figure 6.11. Concrete Specimen #1 (A) before and (B) after 40 Freeze-Thaw Cycles

6.3.2.2. Stress Distribution of Freeze-Thaw FE Model

The distribution of the von Mises stress within the concrete specimen #1 was analyzed after applying 5, 20, and 40 freeze-thaw cycles, as illustrated in Figure 6.12. It was observed after applying 5 cycles that the stress around the expanding ice was mostly uniform. After applying 20 cycles, the concrete element experienced minor local cracking nearby the ice, partially relieving the surrounding high stress. It is worth noting that the frost-induced cracks at cycle 20 relieved the high stress at the top and bottom surfaces of the concrete, shifting the stress to its side surface, as shown in Figure 6.12 (C). Also, it was noted that subjecting concrete to 20 cycles propagated the stress toward the nearby aggregates, increasing the likelihood of stress concentration within the mortar-aggregate interfacial zone. Exposure to 40 freeze-thaw cycles produced more cracks within the cement mortar, making the stress distribution more localized, as demonstrated in Figure 6.12 (D).

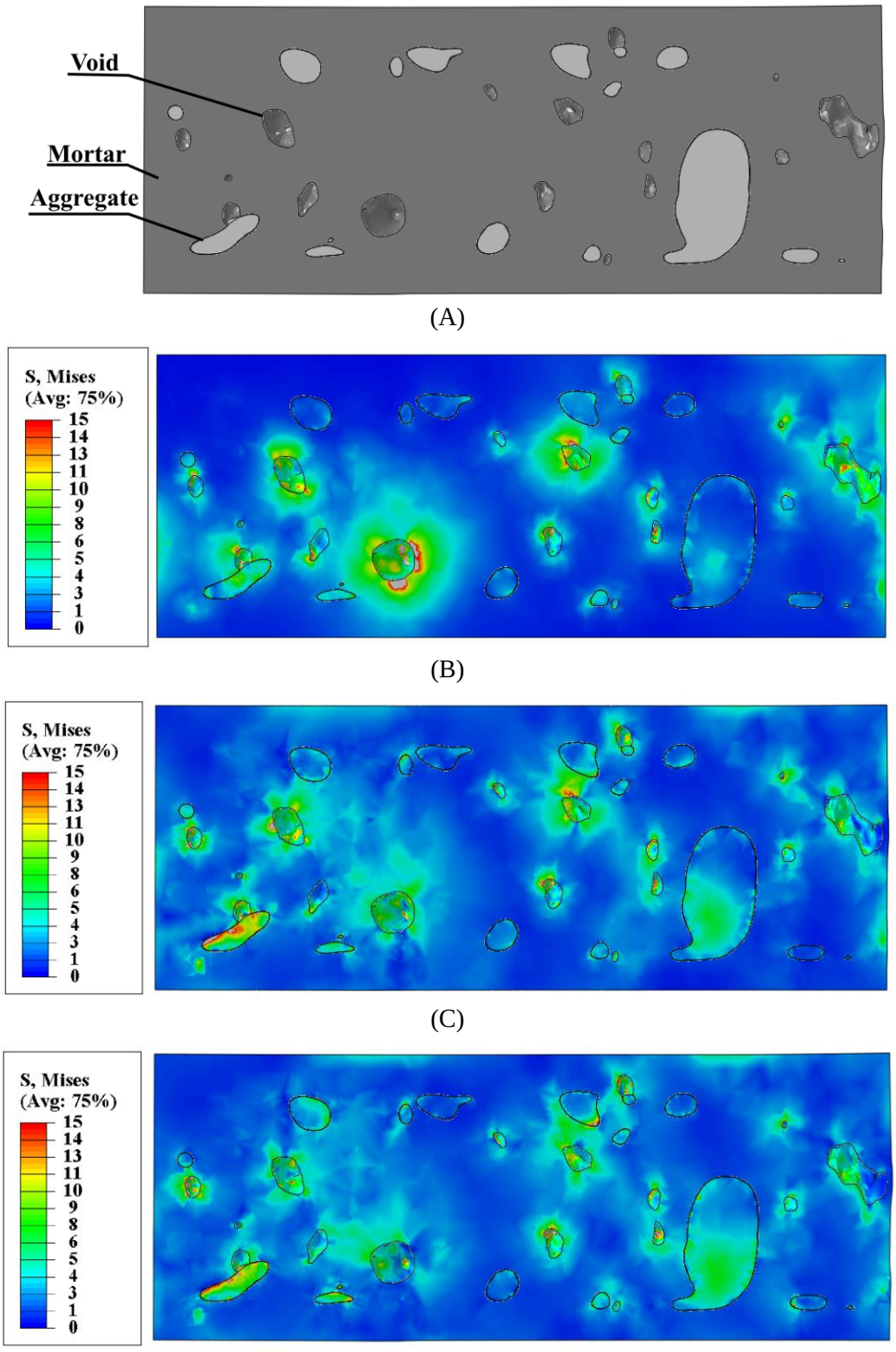

Figure 6.12. von Mises Stress Distribution within the Concrete Specimen #1 (A) before and after (B) 5, (C) 20, and (D) 40 Freeze-Thaw Cycles

6.3.2.3. Severity of Freeze-Thaw Damage

The severity of the simulated frost damage of specimens 1 and 2 was investigated by computing the volume loss of concrete, which represents the volume of the damaged elements determined using the Concrete Damage Plasticity (CDP) model, as demonstrated in Figure 6.13. Also, the actual volume loss of the two samples at cycle 40 was measured using the experimental CT imaging data, which was plotted as a polynomial curve. It was observed that the actual volume losses of samples 1 and 2 after 40 freeze-thaw cycles were 5.70 mm^3 and 12.99 mm^3, respectively, whereas the simulated volume losses of the two specimens were 5.93 mm^3 and 12.06 mm^3, corresponding to percent errors of 3.96% and 7.21%, respectively. It is worth noting that although the two specimens were made of the same mixture proportions, the frost-induced volume loss of specimen 2 was over twice that of specimen 1, attributed to the different pore structures. Despite that, the developed FE model accurately predicted the frost damage of the two samples by taking into consideration the pore structure of each specimen, proving its potential. Also, the simulated volume loss grew exponentially, matching the observations reported by Li et al. (2018). In conclusion, the microstructural FE model successfully utilized the micro-scale configurations of the aggregates and ice (voids) to assess the concrete's frost damage accurately, illustrating its potential for investigating the freeze-thaw damage of concrete.

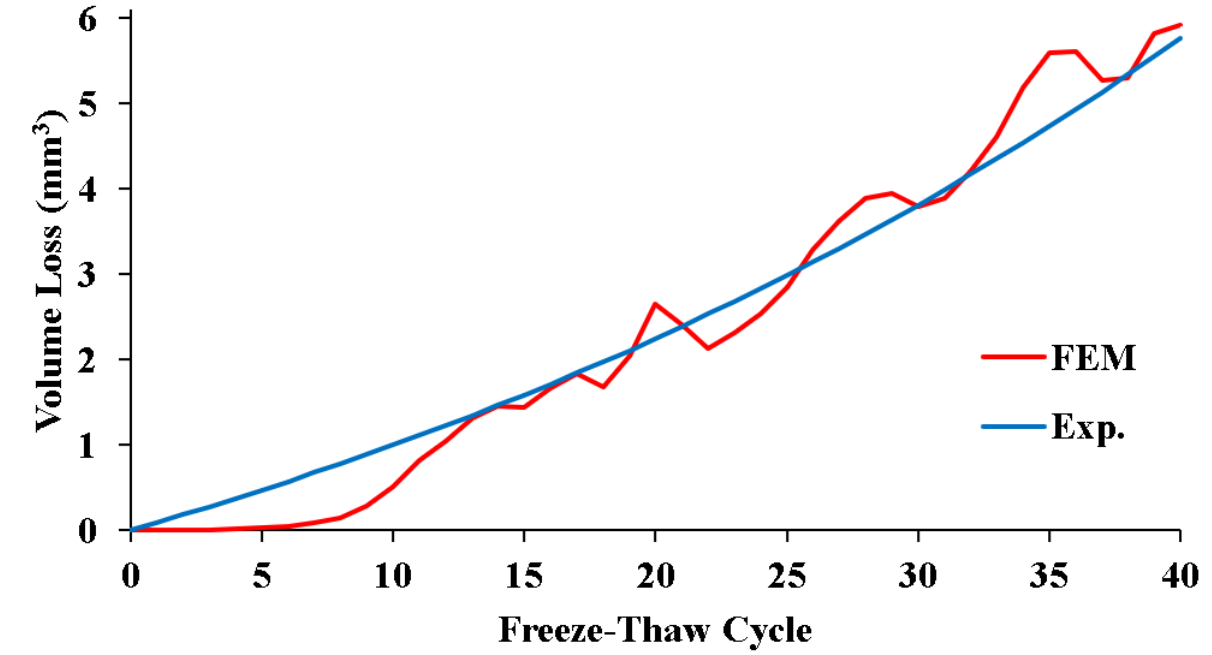

(A)

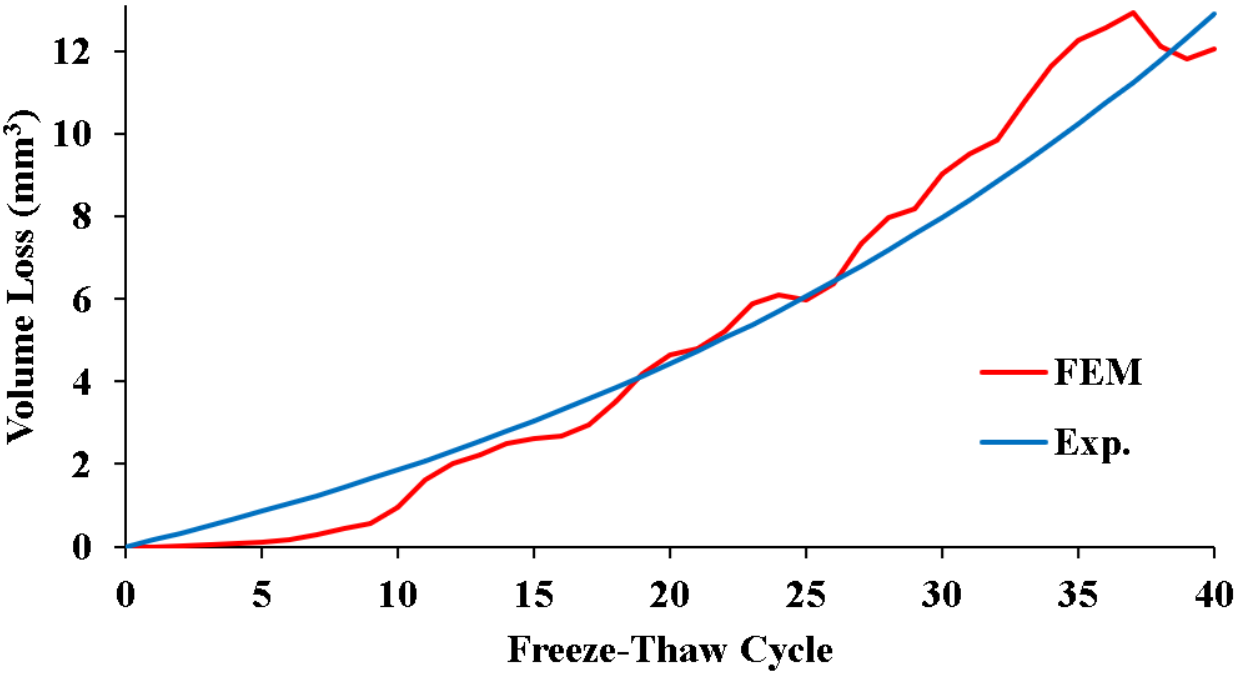

(B)

Figure 6.13. Volume Loss of (A) Specimen #1, and (B) Specimen #2 after 40 Freeze-Thaw Cycles

6.3.2.4. Freeze-Thaw Damage Progression

The progression of the simulated frost damage of specimen #1 was studied after applying 5, 20, and 40 cycles, as illustrated in Figure 6.14. It was noted that cracks initiated in the top and bottom surfaces of the concrete, which relieved the stress within these surfaces, as discussed in the previous section. As more freeze-thaw cycles were applied, the concrete damage propagated from the top and bottom surfaces to the center of the concrete element.

The accuracy of the simulated frost damage was examined by comparing the concrete damage of the FE model to the expansion of the concrete's internal pore structures, shown in Figure 6.15 (A and B). It was observed that exposure to 40 freeze-thaw cycles produced mostly internal pore expansion, which seems similar to the FE model's frost damage, as indicated by the red and yellow highlights. Based on these results, it appears that the microstructure FE model accurately anticipated the locations of frost damage within the concrete element. However, further investigation is required to determine the accuracy of the simulated mechanisms of frost damage.

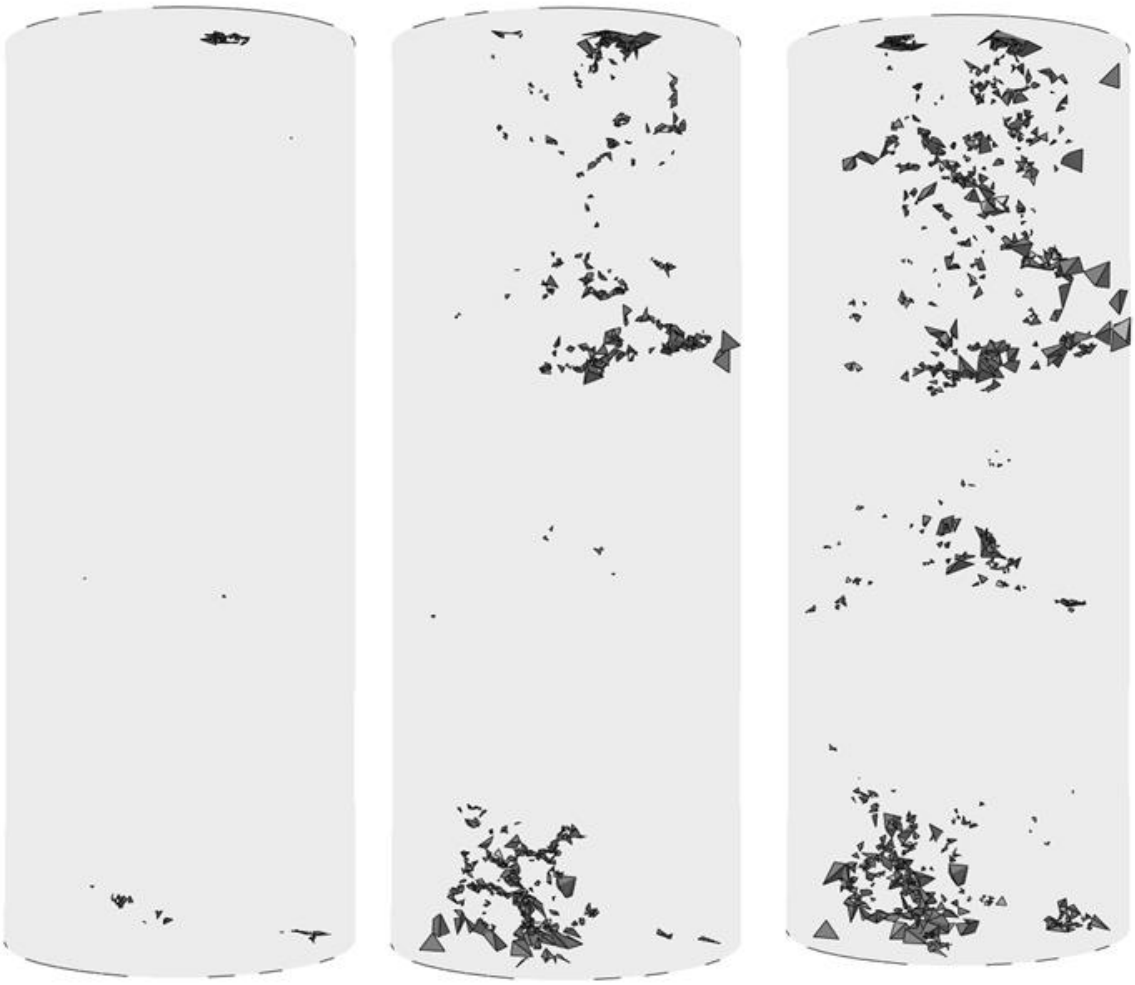

(A) (B) (C)

Figure 6.14. Freeze-Thaw Damage of the Modeled Concrete after (A) 5, (B) 20, and (C) 40 Freeze-Thaw Cycles

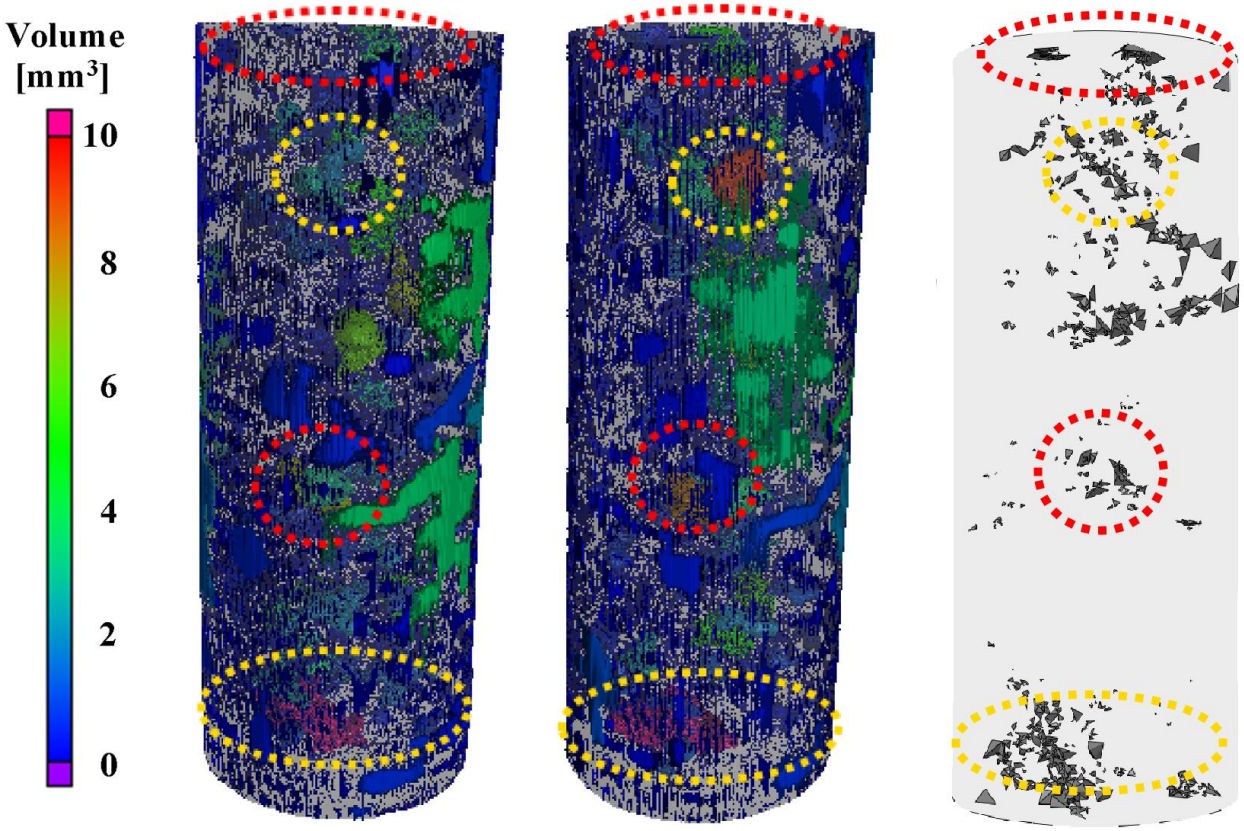

(A) (B) (C)

Figure 6.15. Internal Pore Structures of Specimen #1 (A) before and (B) after 40 Freeze-Thaw Cycles, and (C) the Frost Damage of the FE Model

6.4. Conclusions

Two image-based microstructural finite element models of corrosion damage and freeze-thaw damage were developed and utilized to investigate the internal stress distribution within the concrete element and the severity and mechanisms of concrete damage throughout the applied test conditions. The damage mechanisms of the FE models were compared to the actual concrete specimens, and an agreement was observed. Based on the aforementioned analysis, the following points were concluded.

- Constructing image-based 3D elements for FE modeling using micro-computed tomography is an interesting approach with excellent potential for investigating the internal micro-scale stress distribution and damage mechanisms of concrete.
- The corrosion FE model successfully predicted the actual path of crack propagation during the early stages of corrosion damage.
- The level of corrosion damage considerably impacts the corrosion damage mechanisms. During the early stage of reinforcement corrosion, cracks occur mostly within the concrete's external surface and the mortar-aggregate interface since the steel interfacial zone is well confined by the surrounding concrete. However, the concrete confinement diminishes as the concrete surface cracks, resulting in a sudden increase of cracks in the reinforcement interfacial zone.
- The freeze-thaw FE model accurately anticipated the severity of the frost damage of two actual concrete specimens, as indicated by the volume loss data.
- In the early stages of freeze-thaw damage, the frost-induced stress within concrete was uniformly surrounding the expanding ice. However, further exposure to frost cycles produced minor cracks, which locally relieved the high stress and altered the stress distribution.
- The stress within the mortar-aggregate interfacial zone increased as more corrosion expansion or freeze-thaw cycles were applied, potentially leading to more severe stress concentration and interfacial cracking.

Chapter 7: Conclusions and Recommendations

7.1. General

The presented work provides a deeper understanding of concrete's corrosion and freeze-thaw damage by thoroughly investigating the pore morphology and microstructural damage mechanisms using a non-destructive micro-computed tomography (μCT) imaging system. The research gaps were identified by conducting a comprehensive literature review of CT imaging of concrete damage under corrosion and frost conditions. Although CT imaging has excellent potential for three-dimensional characterization of concrete internal pore structure, limited work has been done to investigate the microstructural corrosion and freeze-thaw damage mechanisms using different mixture proportions. Also, most corrosion research was conducted on small specimens, paying little attention to the potential of using CT imaging to detect the corrosion products within large concrete specimens. In addition, limited research studied the severity and mechanisms of freeze-thaw damage in detrimental environments, such as sulfate environments. Furthermore, despite the potential of using CT imaging to capture high-resolution 3D images, realistic 3D microstructural finite element (FE) models of corrosion and freeze-thaw damage with the appropriate contact conditions have yet to be developed. Thus, the aforementioned research gaps were addressed.

7.2. Corrosion and Freeze-Thaw Damage of Concrete of Different Mixing Proportions

The effects of water/cement (W/C) and sand/cement (S/C) ratios on the concrete damage under corrosion and freeze-thaw conditions were investigated using concrete specimens made of W/C ratios of 0.4–0.9 and S/C ratios of 0.5–3. One day after casting, the concrete elements were water

cured for 28 days, after which the corrosion specimens were subjected to 120 wet-dry cycles (4 hours each) in salt water, whereas the frost specimens were exposed to 40 freeze-thaw cycles (1 day each). Weight measurements and CT imaging were performed before and after applying the wet-dry and freeze-thaw cycles. Using the CT images, the pore properties, including the pore size, shape, and distribution, and the concrete damage mechanisms were investigated.

It was observed that increasing the W/C and S/C ratios beyond the appropriate level produced concrete with higher porosity with larger and more clustered air pores, making concrete more vulnerable to reinforcement corrosion and freeze-thaw damage. Also, it was noted that the pore morphology greatly impacted the concrete damage mechanisms. For example, increasing the W/C ratio produced more interfacial voids at the steel-concrete interface that locally accelerated the reinforcement corrosion, leading to pitting corrosion. Likewise, concrete made of a high W/C ratio had more open pores that accelerated water ingress and reduced the concrete confinement, making concrete more susceptible to frost-induced scaling damage. In general, the effects of increasing the W/C ratio were similar but more detrimental than the S/C ratio. Also, it was observed that using a W/C ratio of 1 and an S/C ratio of 0.5 produced concrete with the highest resistance to reinforcement corrosion and freeze-thaw damage.

The presented results proved the potential of CT imaging to study the effects of concrete composition on its durability and damage mechanisms. However, the tested specimens are small; hence, the impact of W/C and S/C ratios can be investigated further using larger concrete samples. Also, using higher-resolution images, the effects of the mixture proportions on the concrete capillaries can be investigated. Further research can be conducted to examine the effects of concrete additives such as silica fume and fly ash on its pore structure and resistance to environmental damage.

7.3. Naturally Corroded Reinforced Concrete Element

The potential of using CT imaging to detect the corrosion products within large concrete elements was investigated using a large naturally corroded 50-year-old concrete specimen, which is 120 mm wide, 60 mm thick, and 170 mm high. The concrete element was CT scanned using high-imaging parameters of 200 kV and 100 µA to attain high-resolution images. It was observed that steel reinforcement experienced severe pitting corrosion mostly within its exposed surface, causing the disintegration of two-thirds of the reinforcement volume. On the other hand, the internal reinforcement surface surrounded by the concrete (i.e., opposite to the concrete cover) experienced minor corrosion damage, as indicated by the intact rebar threads. Also, it was noted that while the concrete surrounding the exposed steel surface was fully delaminated, no cracks were detected within the concrete surrounding the intact steel surface. It was also observed that the majority of detected corrosion products were mostly dispersed around the exposed surface of steel reinforcement. Thus, the corrosion-induced cracks propagated mostly within its delaminated surface.

The accuracy of corrosion detection was examined by comparing the captured corrosion products with the actual rust on the concrete surface. It was observed that most corrosion products were detected except for small and minor corrosion strains due to the low X-ray attenuation. Also, it was noted that small parts of some aggregates were falsely detected as corrosion products because of imaging artifacts and the metal contents of some aggregates. However, the falsely detected aggregates that are far from the steel reinforcement can be ignored since most corrosion products surround the steel rebar.

Based on the results, CT imaging is an excellent tool for 3D detection of corrosion products within large concrete elements paving the way for more advanced applications. For example, more

research can be conducted to gain a deeper understanding of the microstructural mechanisms of the progression of corrosion damage. Also, high-resolution CT images should be used to mitigate void detection errors, such as the interconnection of nearby air pores. In addition, further research can be performed to quantify the corrosion detection accuracy by comparing the CT results with other technologies, such as energy dispersive spectroscopy. Furthermore, efficient automated algorithms can be developed to improve corrosion detection accuracy by removing the falsely detected aggregates.

7.4. Concrete Damage under Coupled Freeze-Thaw and Sulfate Attack Conditions

The effects of sulfate environments on the severity and mechanisms of freeze-thaw damage were investigated. Concrete specimens with a W/C ratio of 0.5 and an S/C ratio of 1 were water cured for 28 days before being subjected to 80 freeze-thaw cycles in different sulfate solutions with various concentrations, namely, magnesium sulfate and potassium sulfate with concentrations of 5% and 10%. Weight measurement and CT imaging were performed before and after every 40 cycles to determine the mass loss and the expansion of porosity, large pores, and open pores. The substantial impact of the sulfate environments on the severity and mechanisms of frost damage was illustrated using 3D reconstructions of the concrete pore structures.

It was observed that exposing concrete to potassium sulfate accelerated the expansion of its large open pores and, consequently, frost-induced scaling damage. On the contrary, subjecting concrete to magnesium sulfate accelerated the expansion of internal voids while slowing the growth of open pores, resulting in minor and more uniform freeze-thaw damage. Thus, while the concrete elements exposed to potassium sulfate were completely disintegrated by the applied freeze-thaw cycles, the concrete specimens subjected to

magnesium sulfate experienced mild scaling damage. It was also noted that increasing the concentration of the magnesium sulfate salt accelerated the process of concrete damage. Hence, the type and concentration of the sulfate environment can significantly impact the severity and mechanisms of freeze-thaw damage.

More research is needed to examine the effects of different concentrations of magnesium sulfate, potassium sulfate, and calcium sulfate on the severity and mechanism of freeze-thaw damage, particularly since most research was focused on studying frost damage in a sodium sulfate solution. It is also important to investigate how the sulfate type and concentration impacted the freezing temperature of the water. Also, further investigation should be conducted using large concrete specimens to gain a better understanding of the concrete damage mechanisms under coupled freeze-thaw and sulfate environments.

7.5. Image-Based Microstructural Finite Element (FE) Modeling of Corrosion and Freeze-Thaw Damage

Two image-based microstructural finite element models for corrosion and freeze-thaw damage of concrete were developed using the CT images of actual specimens. The captured CT images were post-processed and stacked to create 3D reconstructions of the cement mortar, aggregates, and air pores. The corrosion FE model also consisted of cylindrical steel reinforcement, whereas the air pores of the freeze-thaw model were filled with freezing water to simulate freeze-thaw cycles under a full saturation condition. Also, while the corrosion-induced reinforcement expansion of the corrosion FE model was based on the literature, the freeze-thaw FE model was simulated by subjecting concrete to 40 cycles. The stress distribution and concrete damage mechanisms of the two FE models were analyzed, and the accuracy of each model was investigated by comparing the FE results to experimental data.

After analyzing the stress distribution, it was observed from the FE model of corrosion that the internal stress concentrated mainly within the steel-concrete and mortar-aggregate interfaces. Also, it was noted that during the early stages of reinforcement corrosion, concrete experienced cracking mostly within the external surface of concrete and the mortar-aggregate interface since the steel interfacial zone was well confined by the surrounding concrete. However, as surface cracks propagated toward the concrete core, the concrete confinement diminished considerably, causing considerable cracking within the reinforcement interfacial zone. Through visual inspection, it was deduced that the corrosion FE model anticipated the corrosion-induced crack path of the actual concrete specimen with acceptable accuracy.

In terms of the freeze-thaw FE model, it was noted that the maximum internal expansive stress occurred around the large pores full of freezing water. The larger the volume of freezing water, the higher the internal stress. Also, it was observed that the expanding ice induced uniform internal stress on the surrounding concrete. However, as more freeze-thaw cycles were applied, minor cracking occurred, locally relieving some regions of high stress and altering the internal stress distribution. The accuracy of the freeze-thaw FE model was examined by comparing the volume loss data of two specimens to the respective experimental measurements. It was noted that the FE model successfully determined the volume loss of the concrete specimens with an average error of only 5.59% (±1.63%). The accuracy of the FE model was also verified by comparing the simulated concrete damage with the 3D CT images, from which a good agreement was observed.

While the developed FE models provided an excellent presentation of the potential of using CT imaging to construct realistic microstructural FE models, the models can be improved further by using higher-resolution CT images and performing mesh independency analysis.

Also, the configurational accuracy of the FE elements can be investigated by comparing the volume of the modeled air pores and aggregates with the total pore volume attained using CT imaging and the actual volume of aggregates before casting, assuming that all aggregates are used in the imaged concrete specimen. In terms of the corrosion FE model, more research can be conducted to simulate concrete damage under nonuniform reinforcement corrosion. On the other hand, more cycles should be applied in the freeze-thaw FE model to investigate the damage mechanisms at the late stages. Also, both FE models can be used on larger concrete specimens under different forms of external loading.

References

[1] Cabrera JG. Deterioration of concrete due to reinforcement steel corrosion. Cem Concr Compos 1996;18:47–59. https://doi.org/10.1016/0958-9465(95)00043-7.

[2] Page CL. Mechanism of corrosion protection in reinforced concrete marine structures. Nature 1975;258:514–5. https://doi.org/10.1038/258514a0.

[3] Aldea C-M, Shah SP. Effect of Cracking on Water and Chloride Permeability of Concrete. J Mater Civ Eng 1999;11:181. https://doi.org/10.1061/(ASCE)0899-1561(1999)11:3(181).

[4] Ahmad S. Reinforcement corrosion in concrete structures, its monitoring and service life prediction—a review. Cem Concr Compos 2003;25:459–71. https://doi.org/10.1016/S0958-9465(02)00086-0.

[5] Chira S. Mianus Bridge Collapse Scrutuinzed at Hearings. N Y Times 1983.

[6] Leech Thomas G., McHugh Jonathan D., Dicarlantonio George. Lessons from the Kinzua. Civ Eng Mag Arch 2005;75:56–61. https://doi.org/10.1061/ciegag.0000043.

[7] Winfield N. Designer of Genoa bridge warned of corrosion risk 39 years before deadly collapse. The Independent 2018. https://www.independent.co.uk/news/world/europe/genoa-bridge-collapse-engineer-riccardo-morandi-warning-corrosion-rust-concrete-a8498716.html (accessed December 23, 2019).

[8] Petrović ZC. Catastrophes caused by corrosion. Vojnoteh Glas 2016;64:1048–64.

[9] Corrosion Costs and Preventive Strategies In the United States. NACE International; n.d.

[10] Lu C, Jin W, Liu R. Reinforcement corrosion-induced cover cracking and its time prediction for reinforced concrete structures. Corros Sci 2011;53:1337–47. https://doi.org/10.1016/j.corsci.2010.12.026.

[11] Suda K, Misra S, Motohashi K. Corrosion products of reinforcing bars embedded in concrete. Corros Sci 1993;35:1543–9. https://doi.org/10.1016/0010-938X(93)90382-Q.

[12] Chen J, Fu C, Ye H, Jin X. Corrosion of steel embedded in mortar and concrete under different electrolytic accelerated corrosion methods. Constr Build Mater 2020;241:117971. https://doi.org/10.1016/j.conbuildmat.2019.117971.

[13] Capozucca R. Damage to reinforced concrete due to reinforcement corrosion. Constr Build Mater 1995;9:295–303. https://doi.org/10.1016/0950-0618(95)00033-C.

[14] Siamphukdee K, Zou R, Collins F, Shayan A. Modeling Steel-Concrete Bond Strength Depletion during Corrosion. ACI Mater J 2018;115:267–77. https://doi.org/10.14359/51701921.

[15] Lin H, Zhao Y, Ožbolt J, Reinhardt H-W. Bond strength evaluation of corroded steel bars via the surface crack width induced by reinforcement corrosion. Eng Struct 2017;152:506–22. https://doi.org/10.1016/j.engstruct.2017.08.051.

[16] Said ME, Hussein AA. Effect of bandwidth reinforcement corrosion on the response of two way slabs. Constr Build Mater 2019;216:137–48. https://doi.org/10.1016/j.conbuildmat.2019.04.034.

[17] Alhawat M, Ashour A. Bond strength between corroded steel reinforcement and recycled aggregate concrete. Structures 2019;19:369–85. https://doi.org/10.1016/j.istruc.2019.02.001.

[18] Chen Z, Yang E-H. Microstructural investigation of steel corrosion in strain hardening cementitious composite (SHCC). Constr Build Mater 2019;211:185–98. https://doi.org/10.1016/j.conbuildmat.2019.03.247.

[19] Hay R, Ostertag CP. Influence of transverse cracks and interfacial damage on corrosion of steel in concrete with and without fiber hybridization. Corros Sci 2019;153:213–24. https://doi.org/10.1016/j.corsci.2019.03.020.

[20] Cheng X, Su Q, Ma F, Liu X, Liang X. Investigation on crack propagation of concrete cover induced by non-uniform corrosion of multiple rebars. Eng Fract Mech 2018;201:366–84. https://doi.org/10.1016/j.engfracmech.2018.07.037.

[21] Wang B, Wang F, Wang Q. Damage constitutive models of concrete under the coupling action of freeze–thaw cycles and load based on Lemaitre assumption. Constr Build Mater 2018;173:332–41. https://doi.org/10.1016/j.conbuildmat.2018.04.054.

[22] Eriksson D, Wahlbom D, Malm R, Fridh K. Hygro-thermo-mechanical modeling of partially saturated air-entrained concrete containing dissolved salt and exposed to freeze-thaw cycles. Cem Concr Res 2021;141:106314. https://doi.org/10.1016/j.cemconres.2020.106314.

[23] Zou D, Wang Z, Shen M, Liu T, Zhou A. Improvement in freeze-thaw durability of recycled aggregate permeable concrete with silane modification. Constr Build Mater 2020:121097. https://doi.org/10.1016/j.conbuildmat.2020.121097.

[24] Deng X, Gao X, Wang R, Gao M, Yan X, Cao W, et al. Investigation of microstructural damage in air-entrained recycled concrete under a freeze–thaw environment. Constr Build Mater 2021;268:121219. https://doi.org/10.1016/j.conbuildmat.2020.121219.

[25] Liu Z, Hansen W, Wang F. Pumping effect to accelerate liquid uptake in concrete and its implications on salt frost durability. Constr Build Mater 2018;158:181–8. https://doi.org/10.1016/j.conbuildmat.2017.09.154.

[26] Lei B, Li W, Tang Z, Tam VWY, Sun Z. Durability of recycled aggregate concrete under coupling mechanical loading and freeze-thaw cycle in salt-solution. Constr Build Mater 2018;163:840–9. https://doi.org/10.1016/j.conbuildmat.2017.12.194.

[27] Qin X, Meng S, Cao D, Tu Y, Sabourova N, Grip N, et al. Evaluation of freeze-thaw damage on concrete material and prestressed concrete specimens. Constr Build Mater 2016;125:892–904. https://doi.org/10.1016/j.conbuildmat.2016.08.098.

[28] Zheng X, Wang Y, Zhang S, Xu F, Zhu X, Jiang X, et al. Research progress of the thermophysical and mechanical properties of concrete subjected to freeze-thaw cycles. Constr Build Mater 2022;330:127254. https://doi.org/10.1016/j.conbuildmat.2022.127254.

[29] Sokhansefat G, Moradian M, Finnell M, Behravan A, Ley MT, Lucero C, et al. Using X-ray computed tomography to investigate mortar subjected to freeze-thaw cycles. Cem Concr Compos 2020;108:103520. https://doi.org/10.1016/j.cemconcomp.2020.103520.

[30] Farnam Y, Todak H, Spragg R, Weiss J. Electrical response of mortar with different degrees of saturation and deicing salt solutions during freezing and thawing. Cem Concr Compos 2015;59:49–59. https://doi.org/10.1016/j.cemconcomp.2015.03.003.

[31] Li W, Jiang Z, Yang Z, Jiang J, Sun W, Deng Z. Interactive Effect of Mechanical Fatigue Load and the Fatigue Effect of Freeze-Thaw on Combined Damage of Concrete. J Mater Civ Eng 2015;27:04014230. https://doi.org/10.1061/(ASCE)MT.1943-5533.0001176.

[32] Fagerlund G. The international cooperative test of the critical degree of saturation method of assessing the freeze/thaw resistance of concrete. Matér Constr 1977;10:231–53.

[33] Li W, Pour-Ghaz M, Castro J, Weiss J. Water Absorption and Critical Degree of Saturation Relating to Freeze-Thaw Damage in Concrete Pavement Joints. J Mater Civ Eng 2012;24:299–307. https://doi.org/10.1061/(ASCE)MT.1943-5533.0000383.

[34] Fagerlund G. Significance of critical degrees of saturation at freezing of porous and brittle materials. Lund Institute of Technology, Division of Building materials; 1973.

[35] AL-Ameeri AS, Rafiq MI, Tsioulou O. Combined impact of carbonation and crack width on the Chloride Penetration and Corrosion Resistance of Concrete Structures. Cem Concr Compos 2021;115:103819. https://doi.org/10.1016/j.cemconcomp.2020.103819.

[36] Sai Chand VV, Kameswara Rao B, Hanumantha Rao Ch. Investigation on chloride penetration in concrete mixes of different cement replacement percentages with fly ash and silica fume. Mater Today Proc 2020;33:820–7. https://doi.org/10.1016/j.matpr.2020.06.270.

[37] Alonso MC, Luna FJ, Criado M. Corrosion behavior of duplex stainless steel reinforcement in ternary binder concrete exposed to natural chloride penetration. Constr Build Mater 2019;199:385–95. https://doi.org/10.1016/j.conbuildmat.2018.12.036.

[38] Grubesa IN, Markovic B, Vracevic M, Tunkiewicz M, Szenti I, Kukovecz A. Pore Structure as a Response to the Freeze/Thaw Resistance of Mortars. MATERIALS 2019;12. https://doi.org/10.3390/ma12193196.

[39] Algin Z, Gerginci S. Freeze-thaw resistance and water permeability properties of roller compacted concrete produced with macro synthetic fibre. Constr Build Mater 2020;234:117382. https://doi.org/10.1016/j.conbuildmat.2019.117382.

[40] Rossi E, Polder R, Copuroglu O, Nijland T, Šavija B. The influence of defects at the steel/concrete interface for chloride-induced pitting corrosion of naturally-deteriorated 20-years-old specimens studied through X-ray Computed Tomography. Constr Build Mater 2020;235:117474. https://doi.org/10.1016/j.conbuildmat.2019.117474.

[41] Zhang D, Shao Y. Surface scaling of CO2-cured concrete exposed to freeze-thaw cycles. J CO2 Util 2018;27:137–44. https://doi.org/10.1016/j.jcou.2018.07.012.

[42] Shon C-S, Abdigaliyev A, Bagitova S, Chung C-W, Kim D. Determination of air-void system and modified frost resistance number for freeze-thaw resistance evaluation of ternary blended concrete made of ordinary Portland cement/silica fume/class F fly ash. Cold Reg Sci Technol 2018;155:127–36. https://doi.org/10.1016/j.coldregions.2018.08.003.

[43] Liang C, Ma H, Pan Y, Ma Z, Duan Z, He Z. Chloride permeability and the caused steel corrosion in the concrete with carbonated recycled aggregate. Constr Build Mater 2019;218:506–18. https://doi.org/10.1016/j.conbuildmat.2019.05.136.

[44] Zhang X, Zuo G, Memon SA, Xing F, Sun H. Effects of initial defects within mortar cover on corrosion of steel and cracking of cover using X-ray computed tomography. Constr Build Mater 2019;223:265–77. https://doi.org/10.1016/j.conbuildmat.2019.06.172.

[45] Yuan J, Wu Y, Zhang J. Characterization of air voids and frost resistance of concrete based on industrial computerized tomographical technology. Constr Build Mater 2018;168:975–83. https://doi.org/10.1016/j.conbuildmat.2018.01.117.

[46] Wang Y, Han JQ, Li CH. Acoustic emission and CT investigation on fracture evolution of granite containing two flaws subjected to freeze–thaw and cyclic uniaxial increasing-amplitude loading conditions. Constr Build Mater 2020;260:119769. https://doi.org/10.1016/j.conbuildmat.2020.119769.

[47] Choi W-C, Yun H-D. Acoustic emission activity of CFRP-strengthened reinforced concrete beams after freeze–thaw cycling. Cold Reg Sci Technol 2015;110:47–58. https://doi.org/10.1016/j.coldregions.2014.11.004.

[48] Suzuki T, Ohtsu M. Damage estimation of concrete canal due to earthquake effects by acoustic emission method. Constr Build Mater 2014;67:186–91. https://doi.org/10.1016/j.conbuildmat.2014.05.016.

[49] Zeng W, Ding Y, Zhang Y, Dehn F. Effect of steel fiber on the crack permeability evolution and crack surface topography of concrete subjected to freeze-thaw damage. Cem Concr Res 2020;138:106230. https://doi.org/10.1016/j.cemconres.2020.106230.

[50] Wang W, Wang S, Yao D, Wang X, Yu X, Zhang Y. Fabrication of all-dimensional superhydrophobic mortar with enhanced waterproof ability and freeze-thaw resistance. Constr Build Mater 2020;238:117626. https://doi.org/10.1016/j.conbuildmat.2019.117626.

[51] El Mir A, Nehme SG, Assaad JJ. Durability of self-consolidating concrete containing natural waste perlite powders. Heliyon 2020;6:e03165. https://doi.org/10.1016/j.heliyon.2020.e03165.

[52] Cao J, Chung DDL. Damage evolution during freeze–thaw cycling of cement mortar, studied by electrical resistivity measurement. Cem Concr Res 2002;32:1657–61. https://doi.org/10.1016/S0008-8846(02)00856-6.

[53] Fan Y, Zhang S, Wang Q, Shah SP. Effects of nano-kaolinite clay on the freeze–thaw resistance of concrete. Cem Concr Compos 2015;62:1–12. https://doi.org/10.1016/j.cemconcomp.2015.05.001.

[54] Wang Z, Zeng Q, Wang L, Yao Y, Li K. Characterizing blended cement pastes under cyclic freeze–thaw actions by electrical resistivity. Constr Build Mater 2013;44:477–86. https://doi.org/10.1016/j.conbuildmat.2013.02.042.

[55] Dong B, Shi G, Dong P, Ding W, Teng X, Qin S, et al. Visualized tracing of rebar corrosion evolution in concrete with x-ray micro-computed tomography method. Cem Concr Compos 2018;92:102–9. https://doi.org/10.1016/j.cemconcomp.2018.06.003.

[56] Hong S, Zheng F, Shi G, Dong B, Liu M, Tang L, et al. Determining influence of impressed current density on current efficiency with X-ray micro-computed tomography. Constr Build Mater 2020;246:118505. https://doi.org/10.1016/j.conbuildmat.2020.118505.

[57] Liu F, You Z, Yang X, Wang H. Macro-micro degradation process of fly ash concrete under alternation of freeze-thaw cycles subjected to sulfate and carbonation. Constr Build Mater 2018;181:369–80. https://doi.org/10.1016/j.conbuildmat.2018.06.037.

[58] Liu F, Zhang T, Luo T, Zhou M, Ma W, Zhang K. The Effects of Nano-SiO2 and Nano-TiO2 Addition on the Durability and Deterioration of Concrete Subject to Freezing and Thawing Cycles. Mater 1996-1944 2019;12:3608.

[59] Shields Y, Garboczi E, Weiss J, Farnam Y. Freeze-thaw crack determination in cementitious materials using 3D X-ray computed tomography and acoustic emission. Cem Concr Compos 2018;89:120–9. https://doi.org/10.1016/j.cemconcomp.2018.03.004.

[60] ASCE Infrastructure Report Card. American Society of Civil Engineers (ASCE); 2017.

[61] Lu C, Zhou Q, Wang W, Wei S, Wang C. Freeze-thaw resistance of recycled aggregate concrete damaged by simulated acid rain. J Clean Prod 2021;280:124396. https://doi.org/10.1016/j.jclepro.2020.124396.

[62] Sola E, Ožbolt J, Balabanić G, Mir ZM. Experimental and numerical study of accelerated corrosion of steel reinforcement in concrete: Transport of corrosion products. Cem Concr Res 2019;120:119–31. https://doi.org/10.1016/j.cemconres.2019.03.018.

[63] Parthiban T, Ravi R, Parthiban GT, Srinivasan S, Ramakrishnan KR, Raghavan M. Neural network analysis for corrosion of steel in concrete. Corros Sci 2005;47:1625–42. https://doi.org/10.1016/j.corsci.2004.08.011.

[64] Delatte NJ. Failure, Distress and Repair of Concrete Structures. Cambridge, UK: Woodhead Publishing; 2009.

[65] Wu B, Yang Y, Zhang L, Wang Y, Li H. Meso-scale numerical study on the non-uniform corrosion-induced cracking of confined concrete. Constr Build Mater 2020;260:120463. https://doi.org/10.1016/j.conbuildmat.2020.120463.

[66] Cao S, Liu D, Ding H, Wang J, Lu H, Gui J. Task-specific ionic liquids as corrosion inhibitors on carbon steel in 0.5 M HCl solution: An experimental and theoretical study. Corros Sci 2019;153:301–13. https://doi.org/10.1016/j.corsci.2019.03.035.

[67] Page CL, Treadaway KWJ. Aspects of the electrochemistry of steel in concrete. Nature 1982;297:109–15. https://doi.org/10.1038/297109a0.

[68] Williamson J, Isgor OB. The effect of simulated concrete pore solution composition and chlorides on the electronic properties of passive films on carbon steel rebar. Corros Sci 2016;106:82–95. https://doi.org/10.1016/j.corsci.2016.01.027.

[69] Ozˇbolt J, Balabanic G, Kušter M. 3D Numerical modelling of steel corrosion in concrete structures. Corros Sci 2011:12.

[70] Zhang Y, Su RKL. Experimental investigation of the process of corrosion-caused cover cracking. Constr Build Mater 2020;253:119166. https://doi.org/10.1016/j.conbuildmat.2020.119166.

[71] Abosrra L, Ashour AF, Youseffi M. Corrosion of steel reinforcement in concrete of different compressive strengths. Constr Build Mater 2011;25:3915–25. https://doi.org/10.1016/j.conbuildmat.2011.04.023.

[72] Teng F, Qiu W-L, Pan S-S, Hu H. Experimental study on seismic performance of precast segmental concrete columns after seawater freeze-thaw cycles. Constr Build Mater 2020;260:120482. https://doi.org/10.1016/j.conbuildmat.2020.120482.

[73] Zeng Q, Li K, Fen-Chong T, Dangla P. Effect of porosity on thermal expansion coefficient of cement pastes and mortars. Constr Build Mater 2012;28:468–75. https://doi.org/10.1016/j.conbuildmat.2011.09.010.

[74] Maruyama I, Teramoto A. Impact of time-dependant thermal expansion coefficient on the early-age volume changes in cement pastes. Cem Concr Res 2011;41:380–91. https://doi.org/10.1016/j.cemconres.2011.01.003.

[75] Zhang Z, Shakoorioskooie M, Griffa M, Lura P, Angst U. A laboratory investigation of cutting damage to the steel-concrete interface. Cem Concr Res 2020;138:106229. https://doi.org/10.1016/j.cemconres.2020.106229.

[76] Li W, Sun W, Jiang J. Damage of concrete experiencing flexural fatigue load and closed freeze/thaw cycles simultaneously. Constr Build Mater 2011;25:2604–10. https://doi.org/10.1016/j.conbuildmat.2010.12.007.

[77] Otieno M, Beushausen H, Alexander M. Chloride-induced corrosion of steel in cracked concrete – Part I: Experimental studies under accelerated and natural marine environments. Cem Concr Res 2016;79:373–85. https://doi.org/10.1016/j.cemconres.2015.08.009.

[78] Kondratova IL, Montes P, Bremner TW. Natural marine exposure results for reinforced concrete slabs with corrosion inhibitors. Cem Concr Compos 2003;25:483–90. https://doi.org/10.1016/S0958-9465(02)00088-4.

[79] Li Z, Jin Z, Xu X, Zhao T, Wang P, Li Z. Combined application of novel electromagnetic sensors and acoustic emission apparatus to monitor corrosion process of reinforced bars in concrete. Constr Build Mater 2020;245:118472. https://doi.org/10.1016/j.conbuildmat.2020.118472.

[80] Yu A-P, Naqvi MW, Hu L-B, Zhao Y-L. An experimental study of corrosion damage distribution of steel bars in reinforced concrete using acoustic emission technique. Constr Build Mater 2020;254:119256. https://doi.org/10.1016/j.conbuildmat.2020.119256.

[81] Goldaran R, Turer A. Application of acoustic emission for damage classification and assessment of corrosion in pre-stressed concrete pipes. Measurement 2020;160:107855. https://doi.org/10.1016/j.measurement.2020.107855.

[82] Liu Y, Ding W, Zhao P, Qin L, Shiotani T. Research on in-situ corrosion process monitoring and evaluation of reinforced concrete via ultrasonic guided waves. Constr Build Mater 2022;321:126317. https://doi.org/10.1016/j.conbuildmat.2022.126317.

[83] Miró M, Eiras JN, Poveda P, Climent MÁ, Ramis J. Detecting cracks due to steel corrosion in reinforced cement mortar using intermodulation generation of ultrasonic waves. Constr Build Mater 2021;286:122915. https://doi.org/10.1016/j.conbuildmat.2021.122915.

[84] Vásárhelyi L, Kónya Z, Kukovecz Á, Vajtai R. Microcomputed tomography–based characterization of advanced materials: a review. Mater Today Adv 2020;8:100084. https://doi.org/10.1016/j.mtadv.2020.100084.

[85] du Plessis A, Boshoff WP. A review of X-ray computed tomography of concrete and asphalt construction materials. Constr Build Mater 2019;199:637–51. https://doi.org/10.1016/j.conbuildmat.2018.12.049.

[86] du Plessis A, Tshibalanganda M, le Roux SG. Not all scans are equal: X-ray tomography image quality evaluation. Mater Today Commun 2020;22:100792. https://doi.org/10.1016/j.mtcomm.2019.100792.

[87] Booij R, Budde RPJ, Dijkshoorn ML, van Straten M. Technological developments of X-ray computed tomography over half a century: User's influence on protocol optimization. Eur J Radiol 2020;131:109261. https://doi.org/10.1016/j.ejrad.2020.109261.

[88] Šavija B, Luković M, Hosseini S, Pacheco J, Schlangen E. Corrosion induced cover cracking studied by X-ray computed tomography, nanoindentation, and energy dispersive X-ray spectrometry (EDS). Mater Struct 2015;48:2043–62. https://doi.org/10.1617/s11527-014-0292-9.

[89] Villarraga-Gómez H, Herazo EL, Smith ST. X-ray computed tomography: from medical imaging to dimensional metrology. Precis Eng 2019;60:544–69. https://doi.org/10.1016/j.precisioneng.2019.06.007.

[90] Itty P-A, Serdar M, Meral C, Parkinson D, Macdowell AA, Bjegović D, et al. In situ 3D monitoring of corrosion on carbon steel and ferritic stainless steel embedded in cement paste. Corros Sci 2014;83:409–18. https://doi.org/10.1016/j.corsci.2014.03.010.

[91] Dong B, Ding W, Qin S, Fang G, Liu Y, Dong P, et al. 3D visualized tracing of rebar corrosion-inhibiting features in concrete with a novel chemical self-healing system. Constr Build Mater 2018;168:11–20. https://doi.org/10.1016/j.conbuildmat.2018.02.094.

[92] Dong B, Fang G, Liu Y, Dong P, Zhang J, Xing F, et al. Monitoring reinforcement corrosion and corrosion-induced cracking by X-ray microcomputed tomography method. Cem Concr Res 2017;100:311–21. https://doi.org/10.1016/j.cemconres.2017.07.009.

[93] Sun H, Zhao D, Gu Y, Memon SA, Ren Z, Liu B, et al. Three-dimensional characterization of steel corrosion embedded in cement paste. Constr Build Mater 2017;143:24–32. https://doi.org/10.1016/j.conbuildmat.2017.03.106.

[94] Hong S, Zheng F, Shi G, Li J, Luo X, Xing F, et al. Determination of impressed current efficiency during accelerated corrosion of reinforcement. Cem Concr Compos 2020;108:103536. https://doi.org/10.1016/j.cemconcomp.2020.103536.

[95] Dong B, Ding W, Qin S, Han N, Fang G, Liu Y, et al. Chemical self-healing system with novel microcapsules for corrosion inhibition of rebar in concrete. Cem Concr Compos 2018;85:83–91. https://doi.org/10.1016/j.cemconcomp.2017.09.012.

[96] Hong S, Qin S, Dong P, Li G, Zhang Y, Xing F, et al. Quantification of rust penetration profile in reinforced concrete deduced by inverse modeling. Cem Concr Compos 2020;111:103622. https://doi.org/10.1016/j.cemconcomp.2020.103622.

[97] Fang G, Ding W, Liu Y, Zhang J, Xing F, Dong B. Identification of corrosion products and 3D distribution in reinforced concrete using X-ray micro computed tomography. Constr Build Mater 2019;207:304–15. https://doi.org/10.1016/j.conbuildmat.2019.02.133.

[98] Hong S, Shi G, Zheng F, Liu M, Hou D, Dong B. Characterization of the corrosion profiles of reinforcement with different impressed current densities by X-ray micro-computed tomography. Cem Concr Compos 2020;109:103583. https://doi.org/10.1016/j.cemconcomp.2020.103583.

[99] Xi X, Yang S. Investigating the spatial development of corrosion of corner-located steel bar in concrete by X-ray computed tomography. Constr Build Mater 2019;221:177–89. https://doi.org/10.1016/j.conbuildmat.2019.06.023.

[100] Van Steen C, Pahlavan L, Wevers M, Verstrynge E. Localisation and characterisation of corrosion damage in reinforced concrete by means of acoustic emission and X-ray computed tomography. Constr Build Mater 2019;197:21–9. https://doi.org/10.1016/j.conbuildmat.2018.11.159.

[101] Shi J, Ming J. Influence of defects at the steel-mortar interface on the corrosion behavior of steel. Constr Build Mater 2017;136:118–25. https://doi.org/10.1016/j.conbuildmat.2017.01.007.

[102] Bernachy-Barbe F, Sayari T, Dewynter-Marty V, L'Hostis V. Using X-ray microtomography to study the initiation of chloride-induced reinforcement corrosion in cracked concrete. Constr Build Mater 2020;259:119574. https://doi.org/10.1016/j.conbuildmat.2020.119574.

[103] Shi J, Ming J, Zhang Y, Jiang J. Corrosion products and corrosion-induced cracks of low-alloy steel and low-carbon steel in concrete. Cem Concr Compos 2018;88:121–9. https://doi.org/10.1016/j.cemconcomp.2018.02.002.

[104] Wei Y, Guo W, Wu Z, Gao X. Computed permeability for cement paste subject to freeze-thaw cycles at early ages. Constr Build Mater 2020;244:118298. https://doi.org/10.1016/j.conbuildmat.2020.118298.

[105] Konstantopoulos G, Koumoulos E, Karatza A, Charitidis C. Pore and phase identification through nanoindentation mapping and micro-computed tomography in nanoenhanced cement. Cem Concr Compos 2020;114:103741. https://doi.org/10.1016/j.cemconcomp.2020.103741.

[106] Koenig A. Analysis of air voids in cementitious materials using micro X-ray computed tomography (μXCT). Constr Build Mater 2020;244:118313. https://doi.org/10.1016/j.conbuildmat.2020.118313.

[107] Wang Y-S, Dai J-G. X-ray computed tomography for pore-related characterization and simulation of cement mortar matrix. NDT E Int 2017;86:28–35. https://doi.org/10.1016/j.ndteint.2016.11.005.

[108] Yun TS, Kim KY, Choo J, Kang DH. Quantifying the distribution of paste-void spacing of hardened cement paste using X-ray computed tomography. Mater Charact 2012;73:137–43. https://doi.org/10.1016/j.matchar.2012.08.008.

[109] Kim KY, Yun TS, Choo J, Kang DH, Shin HS. Determination of air-void parameters of hardened cement-based materials using X-ray computed tomography. Constr Build Mater 2012;37:93–101. https://doi.org/10.1016/j.conbuildmat.2012.07.012.

[110] Bossa N, Chaurand P, Vicente J, Borschneck D, Levard C, Aguerre-Chariol O, et al. Micro- and nano-X-ray computed-tomography: A step forward in the characterization of the pore network of a leached cement paste. Cem Concr Res 2015;67:138–47. https://doi.org/10.1016/j.cemconres.2014.08.007.

[111] Suzuki T, Shiotani T, Ohtsu M. Evaluation of cracking damage in freeze-thawed concrete using acoustic emission and X-ray CT image. Constr Build Mater 2017;136:619–26. https://doi.org/10.1016/j.conbuildmat.2016.09.013.

[112] Suzuki T, Ogata H, Takada R, Aoki M, Ohtsu M. Use of acoustic emission and X-ray computed tomography for damage evaluation of freeze-thawed concrete. Constr Build Mater 2010;24:2347–52. https://doi.org/10.1016/j.conbuildmat.2010.05.005.

[113] Kim KY, Yun TS, Park KP. Evaluation of pore structures and cracking in cement paste exposed to elevated temperatures by X-ray computed tomography. Cem Concr Res 2013;50:34–40. https://doi.org/10.1016/j.cemconres.2013.03.020.

[114] Tian W, Han N. Pore characteristics (>0.1 mm) of non-air entrained concrete destroyed by freeze-thaw cycles based on CT scanning and 3D printing. Cold Reg Sci Technol 2018;151:314–22. https://doi.org/10.1016/j.coldregions.2018.03.027.

[115] Boulay C, Dal Pont S, Belin P. Real-time evolution of electrical resistance in cracking concrete. Cem Concr Res 2009;39:825–31. https://doi.org/10.1016/j.cemconres.2009.06.003.

[116] Caré S, Raharinaivo A. Influence of impressed current on the initiation of damage in reinforced mortar due to corrosion of embedded steel. Cem Concr Res 2007;37:1598–612. https://doi.org/10.1016/j.cemconres.2007.08.022.

[117] Hay R, Ostertag CP. Acidification at rebar-concrete interface induced by accelerated corrosion test in aggressive chloride environment. Cem Concr Compos 2020;110:103573. https://doi.org/10.1016/j.cemconcomp.2020.103573.

[118] Wang X, Song X, Zhang M, Du X. Experimental comparison of corrosion unevenness and expansive cracking between accelerated corrosion methods used in laboratory research. Constr Build Mater 2017;153:36–43. https://doi.org/10.1016/j.conbuildmat.2017.07.084.

[119] Zhou Y, Zheng B, Sui L, Xing F, Li P, Sun H. Effects of external confinement on steel reinforcement corrosion products monitored by X-ray microcomputer tomography. Constr Build Mater 2019;222:531–43. https://doi.org/10.1016/j.conbuildmat.2019.06.119.

[120] Lang X, Wang D, Tang S, Zhu J, Guo C. Study on titanium foil coated with partial reduction titanium dioxide as bipolar lead-acid battery's substrate. J Power Sources 2014;271:354–9. https://doi.org/10.1016/j.jpowsour.2014.08.012.

[121] Chen X, Xu Z, Zhu D, Fang Z, Zhu D. Experimental research on electrochemical machining of titanium alloy Ti60 for a blisk. Chin J Aeronaut 2016;29:274–82. https://doi.org/10.1016/j.cja.2015.09.010.

[122] Mao Y, Zhang S, Wang W, Yu D. Electroless silver plated flexible graphite felt prepared by dopamine functionalization and applied for electromagnetic interference shielding. Colloids Surf Physicochem Eng Asp 2018;558:538–47. https://doi.org/10.1016/j.colsurfa.2018.09.028.

[123] Tang B, Yu G, Fang J, Shi T. Recovery of high-purity silver directly from dilute effluents by an emulsion liquid membrane-crystallization process. J Hazard Mater 2010;177:377–83. https://doi.org/10.1016/j.jhazmat.2009.12.042.

[124] Gong K, Wu M, Xie F, Liu G. Effect of dissolved oxygen concentration on stress corrosion cracking behavior of pre-corroded X100 steel base metal and the welded joint in wet–dry cycle conditions. J Nat Gas Sci Eng 2020;77:103264. https://doi.org/10.1016/j.jngse.2020.103264.

[125] Stefanoni M, Angst U, Elsener B. The mechanism controlling corrosion of steel in carbonated cementitious materials in wetting and drying exposure. Cem Concr Compos 2020;113:103717. https://doi.org/10.1016/j.cemconcomp.2020.103717.

[126] Sandra N, Kawaai K, Ujike I. Influence of copper slag on corrosion behavior of horizontal steel bars in reinforced concrete column specimen due to chloride-induced corrosion. Constr Build Mater 2020;255:119265. https://doi.org/10.1016/j.conbuildmat.2020.119265.

[127] Andrushia AD, Anand N, Prince Arulraj G. Evaluation of thermal cracks on fire exposed concrete structures using Ripplet transform. Math Comput Simul 2021;180:93–113. https://doi.org/10.1016/j.matcom.2020.07.024.

[128] Akca AH, Özyurt N. Post-fire mechanical behavior and recovery of structural reinforced concrete beams. Constr Build Mater 2020;253:119188. https://doi.org/10.1016/j.conbuildmat.2020.119188.

[129] Wang Y, Liu Z, Fu K, Li Q, Wang Y. Experimental studies on the chloride ion permeability of concrete considering the effect of freeze–thaw damage. Constr Build Mater 2020;236:117556. https://doi.org/10.1016/j.conbuildmat.2019.117556.

[130] Česen A, Kosec T, Legat A. Characterization of steel corrosion in mortar by various electrochemical and physical techniques. Corros Sci 2013;75:47–57. https://doi.org/10.1016/j.corsci.2013.05.015.

[131] Xu F, Xiao Y, Wang S, Li W, Liu W, Du D. Numerical model for corrosion rate of steel reinforcement in cracked reinforced concrete structure. Constr Build Mater 2018;180:55–67. https://doi.org/10.1016/j.conbuildmat.2018.05.215.

[132] de Vera G, Antón C, López MP, Climent MA. Depassivation time estimation in reinforced concrete structures exposed to chloride ingress: A probabilistic approach. Cem Concr Compos 2017;79:21–33. https://doi.org/10.1016/j.cemconcomp.2016.12.012.

[133] Geng C, Xu Y, Weng D, Wu X. A time-saving method to determine the chloride threshold level for depassivation of steel in concrete. Constr Build Mater 2010;24:903–9. https://doi.org/10.1016/j.conbuildmat.2009.12.002.

[134] Jiang J, Yuan Y. Development and prediction strategy of steel corrosion rate in concrete under natural climate. Constr Build Mater 2013;44:287–92. https://doi.org/10.1016/j.conbuildmat.2013.03.033.

[135] Chen D, Mahadevan S. Chloride-induced reinforcement corrosion and concrete cracking simulation. Cem Concr Compos 2008;30:227–38. https://doi.org/10.1016/j.cemconcomp.2006.10.007.

[136] Zhu X, Zi G, Cao Z, Cheng X. Combined effect of carbonation and chloride ingress in concrete. Constr Build Mater 2016;110:369–80. https://doi.org/10.1016/j.conbuildmat.2016.02.034.

[137] Liu J, Qiu Q, Chen X, Xing F, Han N, He Y, et al. Understanding the interacted mechanism between carbonation and chloride aerosol attack in ordinary Portland cement concrete. Cem Concr Res 2017;95:217–25. https://doi.org/10.1016/j.cemconres.2017.02.032.

[138] Ebell G, Burkert A, Fischer J, Lehmann J, Müller T, Meinel D, et al. Investigation of chloride-induced pitting corrosion of steel in concrete with innovative methods. Mater Corros 2016;67:583–90. https://doi.org/10.1002/maco.201608969.

[139] Hong S, Qin S, Dong B, Xing F. Corrosion Features of the Reinforcing Bar in Concrete with Intelligent OH− Regulation of Microcapsules. Mater 1996-1944 2019;12:3966.

[140] Yu L, François R, Gagné R. Influence of steel–concrete interface defects induced by top-casting on development of chloride-induced corrosion in RC beams under sustained loading. Mater Struct 2016;49:5169–81. https://doi.org/10.1617/s11527-016-0852-2.

[141] Liu Q, Su RKL, Li C-Q, Shih K, Liao C. In-situ deformation modulus of rust in concrete under different levels of confinement and rates of corrosion. Constr Build Mater 2020;255:119369. https://doi.org/10.1016/j.conbuildmat.2020.119369.

[142] Zhao Y, Ren H, Dai H, Jin W. Composition and expansion coefficient of rust based on X-ray diffraction and thermal analysis. Corros Sci 2011;53:1646–58. https://doi.org/10.1016/j.corsci.2011.01.007.

[143] Wang P, Qiao H, Zhang Y, Li Y, Chen K, Feng Q. Three-dimensional characteristics of steel corrosion and corrosion-induced cracks in magnesium oxychloride cement concrete monitored by X-ray computed tomography. Constr Build Mater 2020;246:118504. https://doi.org/10.1016/j.conbuildmat.2020.118504.

[144] Wang P, Qiao H, Zhang Y, Li Y, Feng Q, Chen K. Meso-damage evolution analysis of magnesium oxychloride cement concrete based on X-CT and grey-level co-occurrence matrix. Constr Build Mater 2020;255:119373. https://doi.org/10.1016/j.conbuildmat.2020.119373.

[145] Ghantous RM, Poyet S, L'Hostis V, Tran N-C, François R. Effect of crack openings on carbonation-induced corrosion. Cem Concr Res 2017;95:257–69. https://doi.org/10.1016/j.cemconres.2017.02.014.

[146] Luan H, Wu J, Pan J. Saline water absorption behavior and critical saturation degree of recycled aggregate concrete during freeze-thaw cycles. Constr Build Mater 2020;258:119640. https://doi.org/10.1016/j.conbuildmat.2020.119640.

[147] Li Z, Liu L, Yan S, Zhang M, Xia J, Xie Y. Effect of freeze-thaw cycles on mechanical and porosity properties of recycled construction waste mixtures. Constr Build Mater 2019;210:347–63. https://doi.org/10.1016/j.conbuildmat.2019.03.184.

[148] Pilehvar S, Szczotok AM, Rodríguez JF, Valentini L, Lanzón M, Pamies R, et al. Effect of freeze-thaw cycles on the mechanical behavior of geopolymer concrete and Portland cement concrete containing micro-encapsulated phase change materials. Constr Build Mater 2019;200:94–103. https://doi.org/10.1016/j.conbuildmat.2018.12.057.

[149] Li W, Ling C, Jiang Z, Yu Q. Evaluation of the potential use of form-stable phase change materials to improve the freeze-thaw resistance of concrete. Constr Build Mater 2019;203:621–32. https://doi.org/10.1016/j.conbuildmat.2019.01.098.

[150] Frazier SD, Matar MG, Osio-Norgaard J, Aday AN, Delesky EA, Srubar WV. Inhibiting Freeze-Thaw Damage in Cement Paste and Concrete by Mimicking Nature's Antifreeze. Cell Rep Phys Sci 2020;1:100060. https://doi.org/10.1016/j.xcrp.2020.100060.

[151] Kogbara RB, Iyengar SR, Grasley ZC, Rahman S, Masad EA, Zollinger DG. Relating damage evolution of concrete cooled to cryogenic temperatures to permeability. Cryogenics 2014;64:21–8. https://doi.org/10.1016/j.cryogenics.2014.09.001.

[152] Balázs György L., Lublóy Éva, Földes Tamás. Evaluation of Concrete Elements with X-Ray Computed Tomography. J Mater Civ Eng 2018;30:06018010. https://doi.org/10.1061/(ASCE)MT.1943-5533.0002389.

[153] Jie Yuan, Yang Liu, Hongxia Li, Baokun Zhang. Experimental Investigation of the Variation of Concrete Pores under the Action of Freeze-Thaw Cycles by Using X-Ray CT. Adv Mater Sci Eng 2014:1–11. https://doi.org/10.1155/2014/571357.

[154] Li Y, Li Y, Guan Z, Ding Q. Elastic modulus damage model of cement mortar under salt freezing circumstance based on X-ray CT scanning. Constr Build Mater 2018;191:1201–9. https://doi.org/10.1016/j.conbuildmat.2018.10.097.

[155] Lotfi-Omran O, Sadrmomtazi A, Nikbin IM. A comprehensive study on the effect of water to cement ratio on the mechanical and radiation shielding properties of heavyweight concrete. Constr Build Mater 2019;229:116905. https://doi.org/10.1016/j.conbuildmat.2019.116905.

[156] Nikbin IM, Beygi MHA, Kazemi MT, Vaseghi Amiri J, Rabbanifar S, Rahmani E, et al. A comprehensive investigation into the effect of water to cement ratio and powder content on mechanical properties of self-compacting concrete. Constr Build Mater 2014;57:69–80. https://doi.org/10.1016/j.conbuildmat.2014.01.098.

[157] Wanasinghe D, Aslani F, Ma G. Effect of water to cement ratio, fly ash, and slag on the electromagnetic shielding effectiveness of mortar. Constr Build Mater 2020;256:119409. https://doi.org/10.1016/j.conbuildmat.2020.119409.

[158] Goto S, Roy DM. The effect of w/c ratio and curing temperature on the permeability of hardened cement paste. Cem Concr Res 1981;11:575–9. https://doi.org/10.1016/0008-8846(81)90087-9.

[159] Bu J, Tian Z, Zheng S, Tang Z. Effect of sand content on strength and pore structure of cement mortar. J Wuhan Univ Technol-Mater Sci Ed 2017;32:382–90. https://doi.org/10.1007/s11595-017-1607-9.

[160] Kazmi SMS. Effect of different aggregate treatment techniques on the freeze-thaw and sulfate resistance of recycled aggregate concrete. Cold Reg Sci Technol 2020:9.

[161] Sun P, Wu H-C. Chemical and freeze–thaw resistance of fly ash-based inorganic mortars. Fuel 2013;111:740–5. https://doi.org/10.1016/j.fuel.2013.04.070.

[162] Mardani-Aghabaglou A, Yüksel C, Beglarigale A, Ramyar K. Improving the mechanical and durability performance of recycled concrete aggregate-bearing mortar mixtures by using binary and ternary cementitious systems. Constr Build Mater 2019;196:295–306. https://doi.org/10.1016/j.conbuildmat.2018.11.124.

[163] Zhao N. Study on the durability of engineered cementitious composites (ECCs) containing high-volume fly ash and bentonite against the combined attack of sulfate and freezing-thawing (F-T). Constr Build Mater 2020:14.

[164] Li Y, Wang R, Li S, Zhao Y, Qin Y. Resistance of recycled aggregate concrete containing low- and high-volume fly ash against the combined action of freeze–thaw cycles and sulfate attack. Constr Build Mater 2018;166:23–34. https://doi.org/10.1016/j.conbuildmat.2018.01.084.

[165] Jiang L, Niu D, Yuan L, Fei Q. Durability of concrete under sulfate attack exposed to freeze-thaw cycles. Cold Reg Sci Technol 2015:6.

[166] Ohama Y. Polymer-based admixtures. Cem Concr Compos 1998;20:189–212. https://doi.org/10.1016/S0958-9465(97)00065-6.

[167] Gong F, Takahashi Y, Segawa I, Maekawa K. Mechanical properties of concrete with smeared cracking by alkali-silica reaction and freeze-thaw cycles. Cem Concr Compos 2020;111:103623. https://doi.org/10.1016/j.cemconcomp.2020.103623.

[168] Taheri BM, Ramezanianpour AM, Sabokpa S, Gapele M. Experimental evaluation of freeze-thaw durability of pervious concrete. J Build Eng 2021;33:101617. https://doi.org/10.1016/j.jobe.2020.101617.

[169] Ma Z, Zhu F, Ba G. Effects of freeze-thaw damage on the bond behavior of concrete and enhancing measures. Constr Build Mater 2019;196:375–85. https://doi.org/10.1016/j.conbuildmat.2018.11.041.

[170] Zhang P, Wittmann FH, Vogel M, Müller HS, Zhao T. Influence of freeze-thaw cycles on capillary absorption and chloride penetration into concrete. Cem Concr Res 2017;100:60–7. https://doi.org/10.1016/j.cemconres.2017.05.018.

[171] Ren J, Lai Y, Gao J. Exploring the influence of SiO2 and TiO2 nanoparticles on the mechanical properties of concrete. Constr Build Mater 2018;175:277–85. https://doi.org/10.1016/j.conbuildmat.2018.04.181.

[172] Wang D, Zhang W, Ruan Y, Yu X, Han B. Enhancements and mechanisms of nanoparticles on wear resistance and chloride penetration resistance of reactive powder concrete. Constr Build Mater 2018;189:487–97. https://doi.org/10.1016/j.conbuildmat.2018.09.041.

[173] Li G, Zhou J, Yue J, Gao X, Wang K. Effects of nano-SiO2 and secondary water curing on the carbonation and chloride resistance of autoclaved concrete. Constr Build Mater 2020;235:117465. https://doi.org/10.1016/j.conbuildmat.2019.117465.

[174] Francioso V, Moro C, Martinez-Lage I, Velay-Lizancos M. Curing temperature: A key factor that changes the effect of TiO2 nanoparticles on mechanical properties, calcium hydroxide formation and pore structure of cement mortars. Cem Concr Compos 2019;104:103374. https://doi.org/10.1016/j.cemconcomp.2019.103374.

[175] Shahrajabian F, Behfarnia K. The effects of nano particles on freeze and thaw resistance of alkali-activated slag concrete. Constr Build Mater 2018;176:172–8. https://doi.org/10.1016/j.conbuildmat.2018.05.033.

[176] Mirgozar Langaroudi MA, Mohammadi Y. Effect of nano-clay on the freeze–thaw resistance of self-compacting concrete containing mineral admixtures. Eur J Environ Civ Eng 2019:1–20. https://doi.org/10.1080/19648189.2019.1665107.

[177] Alhusain M, Quayle TG, Al-Mayah A. Three-Dimensional Characterization of Naturally Corroded Steel-Reinforced Concrete Using Computed Tomography. In: Ilki A, Ispir M, Inci P, editors. 10th Int. Conf. FRP Compos. Civ. Eng., Cham: Springer International Publishing; 2022, p. 706–13. https://doi.org/10.1007/978-3-030-88166-5_61.

[178] Wang L, Liang Y, Ueda T. Numerical Simulation of Corrosion-Induced Cracking of Concrete Considering Rust Penetration into Cracks. J Mater Civ Eng 2021;33:04021183. https://doi.org/10.1061/(ASCE)MT.1943-5533.0003778.

[179] Alhusain M, Al-Mayah A. Three-Dimensional CT Imaging Analysis of Concrete: Effects of Water and Sand Contents on Pore Characteristics. In: Benmokrane B, Mohamed K, Farghaly A, Mohamed H, editors. 8th Int. Conf. Adv. Compos. Mater. Bridg. Struct., Cham: Springer International Publishing; 2023, p. 69–75. https://doi.org/10.1007/978-3-031-09409-5_8.

[180] Alhusain M, Al-Mayah A. Three dimensional imaging of reinforcement corrosion using micro-computed tomography: Literature review. Constr Build Mater 2021;284:122813. https://doi.org/10.1016/j.conbuildmat.2021.122813.

[181] Pereira da Costa FB, Haselbach LM, da Silva Filho LCP. Pervious concrete for desired porosity: Influence of w/c ratio and a rheology-modifying admixture. Constr Build Mater 2020:121084. https://doi.org/10.1016/j.conbuildmat.2020.121084.

[182] Almusallam AA, Beshr H, Maslehuddin M, Al-Amoudi OSB. Effect of silica fume on the mechanical properties of low quality coarse aggregate concrete. Cem Concr Compos 2004;26:891–900. https://doi.org/10.1016/j.cemconcomp.2003.09.003.

[183] Hino Junior JR, Balestra CET, Medeiros-Junior RA. Comparison of test methods to determine resistance to chloride penetration in concrete: Sensitivity to the effect of fly ash. Constr Build Mater 2021;277:122265. https://doi.org/10.1016/j.conbuildmat.2021.122265.

[184] Abdelrahman M, Xi Y. The effect of w/c ratio and aggregate volume fraction on chloride penetration in non-saturated concrete. Constr Build Mater 2018;191:260–9. https://doi.org/10.1016/j.conbuildmat.2018.10.013.

[185] Islam MM, Alam MT, Islam MS. Effect of fly ash on freeze–thaw durability of concrete in marine environment. Aust J Struct Eng 2018;19:146–61. https://doi.org/10.1080/13287982.2018.1453332.

[186] Lu Z, Feng Z, Yao D, Li X, Ji H. Freeze-thaw resistance of Ultra-High performance concrete: Dependence on concrete composition. Constr Build Mater 2021;293:123523. https://doi.org/10.1016/j.conbuildmat.2021.123523.

[187] Yazıcı H. The effect of silica fume and high-volume Class C fly ash on mechanical properties, chloride penetration and freeze–thaw resistance of self-compacting concrete. Constr Build Mater 2008;22:456–62. https://doi.org/10.1016/j.conbuildmat.2007.01.002.

[188] Bilal H, Chen T, Ren M, Gao X, Su A. Influence of silica fume, metakaolin & SBR latex on strength and durability performance of pervious concrete. Constr Build Mater 2021;275:122124. https://doi.org/10.1016/j.conbuildmat.2020.122124.

[189] Chalee W, Teekavanit M, Kiattikomol K, Siripanichgorn A, Jaturapitakkul C. Effect of W/C ratio on covering depth of fly ash concrete in marine environment. Constr Build Mater 2007;21:965–71. https://doi.org/10.1016/j.conbuildmat.2006.03.002.

[190] Li G, Wang D, Du J-M. Deterioration and Service Life Prediction of Concrete Subjected to Freeze–Thaw Cycles in Na_2SO_4 Solution. Am J Civ Eng 2016;4:104. https://doi.org/10.11648/j.ajce.20160403.17.

[191] Eskandari-Naddaf H, Kazemi R. Experimental evaluation of the effect of mix design ratios on compressive strength of cement mortars containing cement strength class 42.5 and 52.5 MPa. Procedia Manuf 2018;22:392–8. https://doi.org/10.1016/j.promfg.2018.03.060.

[192] Mahasneh BZ, Shawabkeh RA. Compressive strength and permeability of sand-cement-clay composite and application for heavy metals stabilization. Am J Appl Sci 2004;1:1–4.

[193] Bullard JW, Garboczi EJ. Defining shape measures for 3D star-shaped particles: Sphericity, roundness, and dimensions. Powder Technol 2013;249:241–52. https://doi.org/10.1016/j.powtec.2013.08.015.

[194] Tu Y, Liu D, Wang T, Yuan L. Evaluation on later-age performance of concrete subjected to early-age freeze–thaw damage. Constr Build Mater 2021;270:121491. https://doi.org/10.1016/j.conbuildmat.2020.121491.

[195] Wu H, Liu Z, Sun B, Yin J. Experimental investigation on freeze–thaw durability of Portland cement pervious concrete (PCPC). Constr Build Mater 2016;117:63–71. https://doi.org/10.1016/j.conbuildmat.2016.04.130.

[196] Richardson AE, Coventry KA, Wilkinson S. Freeze/thaw durability of concrete with synthetic fibre additions. Cold Reg Sci Technol 2012;83–84:49–56. https://doi.org/10.1016/j.coldregions.2012.06.006.

[197] Allahverdi A, Abadi MMBR, Anwar Hossain KM, Lachemi M. Resistance of chemically-activated high phosphorous slag content cement against freeze–thaw cycles. Cold Reg Sci Technol 2014;103:107–14. https://doi.org/10.1016/j.coldregions.2014.03.012.

[198] Girskas G, Skripkiūnas G. The effect of synthetic zeolite on hardened cement paste microstructure and freeze-thaw durability of concrete. Constr Build Mater 2017;142:117–27. https://doi.org/10.1016/j.conbuildmat.2017.03.056.

[199] Grinys A, Augonis A, Daukšys M, Pupeikis D. Mechanical properties and durability of rubberized and SBR latex modified rubberized concrete. Constr Build Mater 2020;248:118584. https://doi.org/10.1016/j.conbuildmat.2020.118584.

[200] Shang H, Song Y, Ou J. Behavior of air-entrained concrete after freeze-thaw cycles. Acta Mech Solida Sin 2009;22:261–6. https://doi.org/10.1016/S0894-9166(09)60273-1.

[201] Peng R, Qiu W, Teng F. Three-dimensional meso-numerical simulation of heterogeneous concrete under freeze-thaw. Constr Build Mater 2020;250:118573. https://doi.org/10.1016/j.conbuildmat.2020.118573.

[202] Li Z, Deng Z, Yang H, Wang H. Bond behavior between recycled aggregate concrete and deformed rebar after Freeze-thaw damage. Constr Build Mater 2020;250:118805. https://doi.org/10.1016/j.conbuildmat.2020.118805.

[203] Zhang S, Fan Y, Li N. Pore structure and freezing resistance of nanoclay modified cement based materials. Mater Res Innov 2014;18:S2-358-S2-362. https://doi.org/10.1179/1432891714Z.000000000434.

[204] Jin X, Yang H, Fan X, Wang Z, Shu X. Spherical and cylindrical cavity expansion models based prediction of penetration depths of concrete targets. PLOS ONE 2017;12:e0175785. https://doi.org/10.1371/journal.pone.0175785.

[205] Rao F, Zhang Z, Ye G, Liu J, Han J. Mesostructure of Foamed Cement Paste and Its Influence on Macromechanical Behavior. J Mater Civ Eng 2021;33:1–11.

[206] Sadowski Ł, Stefaniuk D, Różańska M, Usydus I, Szymanowski J. The Effect of Waste Mineral Powders on the Structure of Air Voids in Low-Strength Air-Entrained Concrete Floor Screeds. Waste Biomass Valorization 2020;11:2211–25.

[207] Ren J, Lai Y. Study on the durability and failure mechanism of concrete modified with nanoparticles and polypropylene fiber under freeze-thaw cycles and sulfate attack. Cold Reg Sci Technol 2021;188:103301. https://doi.org/10.1016/j.coldregions.2021.103301.

[208] Zhong R, Wille K. Material design and characterization of high performance pervious concrete. Constr Build Mater 2015;98:51–60. https://doi.org/10.1016/j.conbuildmat.2015.08.027.

[209] Wardhana K, Hadipriono F. Analysis of Recent Bridge Failures in the United States. J Perform Constr Facil 2003;17:144–50. https://doi.org/10.1061/(ASCE)0887-3828(2003)17:3(144).

[210] ElBatanouny MK, Mangual J, Ziehl PH, Matta F. Early Corrosion Detection in Prestressed Concrete Girders Using Acoustic Emission. J Mater Civ Eng 2014;26:504–11. https://doi.org/10.1061/(ASCE)MT.1943-5533.0000845.

[211] Al-Dulaijan SU, Maslehuddin M, Al-Zahrani MM, Sharif AM, Shameem M, Ibrahim M. Sulfate resistance of plain and blended cements exposed to varying concentrations of sodium sulfate. Cem Concr Compos 2003;25:429–37. https://doi.org/10.1016/S0958-9465(02)00083-5.

[212] Geng J, Easterbrook D, Li L, Mo L. The stability of bound chlorides in cement paste with sulfate attack. Cem Concr Res 2015;68:211–22. https://doi.org/10.1016/j.cemconres.2014.11.010.

[213] Adu-Amankwah S, Zajac M, Skoček J, Němeček J, Haha MB, Black L. Combined influence of carbonation and leaching on freeze-thaw resistance of limestone ternary cement concrete. Constr Build Mater 2021;307:125087. https://doi.org/10.1016/j.conbuildmat.2021.125087.

[214] Jin S, Zheng G, Yu J. A micro freeze-thaw damage model of concrete with fractal dimension. Constr Build Mater 2020;257:119434. https://doi.org/10.1016/j.conbuildmat.2020.119434.

[215] Ebrahimi Besheli A, Samimi K, Moghadas Nejad F, Darvishan E. Improving concrete pavement performance in relation to combined effects of freeze–thaw cycles and de-icing salt. Constr Build Mater 2021;277:122273. https://doi.org/10.1016/j.conbuildmat.2021.122273.

[216] Matalkah F, Soroushian P. Freeze thaw and deicer salt scaling resistance of concrete prepared with alkali aluminosilicate cement. Constr Build Mater 2018;163:200–13. https://doi.org/10.1016/j.conbuildmat.2017.12.119.

[217] Alhusain M, Al-Mayah A. Three-Dimensional μCT Imaging of Pore Morphology and Freeze-Thaw Damage Mechanisms of Different Concrete Mixing Proportions 2022.

[218] Liu T, Zou D, Teng J, Yan G. The influence of sulfate attack on the dynamic properties of concrete column. Constr Build Mater 2012;28:201–7. https://doi.org/10.1016/j.conbuildmat.2011.08.036.

[219] Martins MC, Langaro EA, Macioski G, Medeiros MHF. External ammonium sulfate attack in concrete: Analysis of the current methodology. Constr Build Mater 2021;277:122252. https://doi.org/10.1016/j.conbuildmat.2021.122252.

[220] Naik NN, Jupe AC, Stock SR, Wilkinson AP, Lee PL, Kurtis KE. Sulfate attack monitored by microCT and EDXRD: Influence of cement type, water-to-cement ratio, and aggregate. Cem Concr Res 2006;36:144–59. https://doi.org/10.1016/j.cemconres.2005.06.004.

[221] Mohan A, Mini KM. Strength and durability studies of SCC incorporating silica fume and ultra fine GGBS. Constr Build Mater 2018;171:919–28. https://doi.org/10.1016/j.conbuildmat.2018.03.186.

[222] Haufe J, Vollpracht A. Tensile strength of concrete exposed to sulfate attack. Cem Concr Res 2019;116:81–8. https://doi.org/10.1016/j.cemconres.2018.11.005.

[223] al-Swaidani AM. Use of micro and nano volcanic scoria in the concrete binder: Study of compressive strength, porosity and sulfate resistance. Case Stud Constr Mater 2019;11:e00294. https://doi.org/10.1016/j.cscm.2019.e00294.

[224] Gaze ME, Crammond NJ. The formation of thaumasite in a cement:lime:sand mortar exposed to cold magnesium and potassium sulfate solutions. Cem Concr Compos 2000;22:209–22. https://doi.org/10.1016/S0958-9465(00)00002-0.

[225] Caneda-Martínez L, Kunther W, Medina C, Sánchez de Rojas MI, Frías M. Exploring sulphate resistance of coal mining waste blended cements through experiments and thermodynamic modelling. Cem Concr Compos 2021;121:104086. https://doi.org/10.1016/j.cemconcomp.2021.104086.

[226] Taheri S, Ams M, Bustamante H, Vorreiter L, Bevitt JJ, Withford M, et al. Characterizing concrete corrosion below sewer tidal levels at chemically dosed locations. Water Res 2020;185:116245. https://doi.org/10.1016/j.watres.2020.116245.

[227] Planel D, Sercombe J, Le Bescop P, Adenot F, Torrenti J-M. Long-term performance of cement paste during combined calcium leaching–sulfate attack: kinetics and size effect. Cem Concr Res 2006;36:137–43. https://doi.org/10.1016/j.cemconres.2004.07.039.

[228] Wu M, Zhang Y, Ji Y, She W, Yang L, Liu G. A comparable study on the deterioration of limestone powder blended cement under sodium sulfate and magnesium sulfate attack at a low temperature. Constr Build Mater 2020;243:118279. https://doi.org/10.1016/j.conbuildmat.2020.118279.

[229] Arzola S, Palomar-Pardavé ME, Genesca J. Effect of resistivity on the corrosion mechanism of mild steel in sodium sulfate solutions. J Appl Electrochem 2003;33:1233–7. https://doi.org/10.1023/B:JACH.0000003855.95788.12.

[230] Kunther W, Lothenbach B, Skibsted J. Influence of the Ca/Si ratio of the C–S–H phase on the interaction with sulfate ions and its impact on the ettringite crystallization pressure. Cem Concr Res 2015;69:37–49. https://doi.org/10.1016/j.cemconres.2014.12.002.

[231] Rahman MM, Bassuoni MT. Thaumasite sulfate attack on concrete: Mechanisms, influential factors and mitigation. Constr Build Mater 2014;73:652–62. https://doi.org/10.1016/j.conbuildmat.2014.09.034.

[232] Cheng H, Liu T, Zou D, Zhou A. Compressive strength assessment of sulfate-attacked concrete by using sulfate ions distributions. Constr Build Mater 2021;293:123550. https://doi.org/10.1016/j.conbuildmat.2021.123550.

[233] Xiao QH, Cao ZY, Guan X, Li Q, Liu XL. Damage to recycled concrete with different aggregate substitution rates from the coupled action of freeze-thaw cycles and sulfate attack. Constr Build Mater 2019;221:74–83. https://doi.org/10.1016/j.conbuildmat.2019.06.060.

[234] ASTM International. C150/C150M-20 Standard Specification for Portland Cement. n.d.

[235] Alhusain M, Al-Mayah A, Quayle TG. 3D Investigation of Microstructural Sulfate Damage of Concrete Using Micro-Computed Tomography 2022.

[236] Lei Y, Guo Q, Zhang Z, Wang S. Numerical and parametric studies on out-of-plane flexural and shear behaviour of half steel-concrete slabs. J Build Eng 2022;46:103787. https://doi.org/10.1016/j.jobe.2021.103787.

[237] Gunawardena Y, Aslani F. Finite element modelling of concrete-filled spiral-welded stainless-steel tube columns under concentric and eccentric axial loading. Structures 2021;33:1119–43. https://doi.org/10.1016/j.istruc.2021.05.015.

[238] Zhang Z, Zhang Z, Wang X, Zhou C. Dynamic and static interfacial bonding properties of CFRP–concrete subjected to freeze–thaw cycles. Structures 2022;37:947–59. https://doi.org/10.1016/j.istruc.2022.01.049.

[239] Xu Y, Chen S. A method for modeling the damage behavior of concrete with a three-phase mesostructure. Constr Build Mater 2016;102:26–38. https://doi.org/10.1016/j.conbuildmat.2015.10.151.

[240] Quan W, Ma X, Li X, Dong Z. Efficient numerical model for effective thermal conductivity of concrete with aggregates of different morphologies and imperfect interfaces. Int J Heat Mass Transf 2022;185:122358. https://doi.org/10.1016/j.ijheatmasstransfer.2021.122358.

[241] Chen X, Yu A, Liu G, Chen P, Liang Q. A multi-phase mesoscopic simulation model for the diffusion of chloride in concrete under freeze–thaw cycles. Constr Build Mater 2020;265:120223. https://doi.org/10.1016/j.conbuildmat.2020.120223.

[242] Trofimov A, Mishurova T, Lanzoni L, Radi E, Bruno G, Sevostianov I. Microstructural analysis and mechanical properties of concrete reinforced with polymer short fibers. Int J Eng Sci 2018;133:210–8. https://doi.org/10.1016/j.ijengsci.2018.09.009.

[243] Pan T, Chen C, Yu Q. Three-dimensional micromechanical modeling of concrete degradation under multiphysics fields. Compos Struct 2017;175:7–18. https://doi.org/10.1016/j.compstruct.2017.05.008.

[244] Dong Y, Qiao P. CT image-based synthetic mesostructure generation for multiscale fracture analysis of concrete. Constr Build Mater 2021;296:123582. https://doi.org/10.1016/j.conbuildmat.2021.123582.

[245] Aho IM, Ndububa EE. Compressive and flexural strength of cement mortar stabilized with raffia palm fruit peel (RPEP). Glob J Eng Res 2015;14:1–7. https://doi.org/10.4314/gjer.v14i1.1.

[246] Yao W, Jiang S, Fei W, Cai T. Correlation between the Compressive, Tensile Strength of Old Concrete under Marine Environment and Prediction of Long-Term Strength. Adv Mater Sci Eng 2017;2017:1–12. https://doi.org/10.1155/2017/8251842.

[247] Narayan Swamy R. Dynamic Poisson's ratio of portland cement paste, mortar and concrete. Cem Concr Res 1971;1:559–83. https://doi.org/10.1016/0008-8846(71)90060-3.

[248] Skarżyński Ł, Nitka M, Tejchman J. Modelling of concrete fracture at aggregate level using FEM and DEM based on X-ray μCT images of internal structure. Eng Fract Mech 2015;147:13–35. https://doi.org/10.1016/j.engfracmech.2015.08.010.

[249] Qiu W, Fu S, Zhu J, Zeng C, Ye J. Meso-scale modelling of the thermo-mechanical response for concrete with complex-shaped aggregates in early age. Constr Build Mater 2022;323:126485. https://doi.org/10.1016/j.conbuildmat.2022.126485.

[250] Moghbeli A, Sharifi Y. New predictive equations for lateral-distortional buckling capacity assessment of cellular steel beams. Structures 2021;29:911–23. https://doi.org/10.1016/j.istruc.2020.12.004.

[251] Bolina FL, Rodrigues JPC. Numerical study and proposal of new design equations for steel decking concrete slabs subjected to fire. Eng Struct 2022;253:113828. https://doi.org/10.1016/j.engstruct.2021.113828.

[252] Gold LW. The elastic modulus of columnar-grain fresh-water ice. Ann Glaciol 1994;19:13–8. https://doi.org/10.3189/1994AoG19-1-13-18.

[253] Sinha NK. Effective Poisson's ratio of isotropic ice. vol. 4, Collection / Collection : NRC Publications Archive / Archives Des Publications Du CNRC: 1987, p. 189–95.

[254] Rhardane A, Al Haj Sleiman S, Alam SY, Grondin F. A quantitative assessment of the parameters involved in the freeze–thaw damage of cement-based materials through numerical modelling. Constr Build Mater 2021;272:121838. https://doi.org/10.1016/j.conbuildmat.2020.121838.

[255] Wang P, Zhou G. Frost-heaving pressure in geotechnical engineering materials during freezing process. Int J Min Sci Technol 2018;28:287–96. https://doi.org/10.1016/j.ijmst.2017.06.003.

[256] Tao Y, Chen JF. Concrete Damage Plasticity Model for Modeling FRP-to-Concrete Bond Behavior. J Compos Constr 2015;19:04014026. https://doi.org/10.1061/(ASCE)CC.1943-5614.0000482.

[257] Kmiecik P, Kamiński M. Modelling of reinforced concrete structures and composite structures with concrete strength degradation taken into consideration. Arch Civ Mech Eng 2011;11:623–36. https://doi.org/10.1016/S1644-9665(12)60105-8.

[258] Yu Y, Zheng Y, Xu J, Wang X. Modeling and predicting the mechanical behavior of concrete under uniaxial loading. Constr Build Mater 2021;273:121694. https://doi.org/10.1016/j.conbuildmat.2020.121694.

[259] Fisher JM, Kloiber LA. Steel Design Guide 1-Base Plate and Anchor Rod Design. AISC, 2006, p. 801–6.

[260] Rabbat BG, Russell HG. Friction Coefficient of Steel on Concrete or Grout. J Struct Eng 1985;111:505–15. https://doi.org/10.1061/(ASCE)0733-9445(1985)111:3(505).

[261] Robuschi S, Tengattini A, Dijkstra J, Fernandez I, Lundgren K. A closer look at corrosion of steel reinforcement bars in concrete using 3D neutron and X-ray computed tomography. Cem Concr Res 2021;144:106439. https://doi.org/10.1016/j.cemconres.2021.106439.

[262] Zhao Y, Dong J, Ding H, Jin W. Shape of corrosion-induced cracks in recycled aggregate concrete. Corros Sci 2015;98:310–7. https://doi.org/10.1016/j.corsci.2015.05.028.

[263] Chauhan A, Sharma UK. Crack propagation in reinforced concrete exposed to non-uniform corrosion under real climate. Eng Fract Mech 2021;248:107719. https://doi.org/10.1016/j.engfracmech.2021.107719.

[264] Amalia Z, Qiao D, Nakamura H, Miura T, Yamamoto Y. Development of simulation method of concrete cracking behavior and corrosion products movement due to rebar corrosion. Constr Build Mater 2018;190:560–72. https://doi.org/10.1016/j.conbuildmat.2018.09.100.

[265] Xu X, Zhao Y. Corrosion-induced cracking propagation of RC beams subjected to different corrosion methods and load levels. Constr Build Mater 2021;286:122913. https://doi.org/10.1016/j.conbuildmat.2021.122913.